الجمهورية الجزائرية الديمقراطية الشعبية
République Algérienne Démocratique Et Populaire
وزارة التعليم العالي والبحث العلمي
Ministère de L'Enseignement Supérieur et de La Recherche Scientifique
جامعة محمد بو ضياف المسيلة
Département d'Electronique, Faculté de Technologie, Université Mohamed Boudiaf M'sila

THESE

Présentée à l'Université Mohamed Boudiaf M'sila
Pour l'obtention du diplôme de

Doctorat en Sciences

Option : Electronique

Par:

Mr. CHEROUANA Abdelbaki

THÈME:

Conception et modélisation des composants photoniques Application : capteurs à guides d'onde photoniques

Devant le jury:

Mr. …….	Prof. Université de ……	Président
Mr. BOUCHAMA Idris	Prof. Université de M'sila	Rapporteur
Mr. BENCHEIKH Abdelhalim	MCA. Université de BBA	Co-encadreur
Mr. ……	……. Université de …….	Examinateur
Mr. ……	……. Université de …….	Examinateur

Soutenu le:

Remerciements

Ce travail ne se produit jamais de cette façon sans l'aide de tous ceux qui ont le collaboré de près ou de loin et qui méritent les remerciements suffisants.

Je tiens à remercier Monsieur BOUCHAMA Idris, Professeur en électronique, Faculté de Technologie, Université Mohamed BOUDIAF M'sila, mon directeur de thèse, qui m'a encadré tout au long de cette thèse et pour sa gentillesse.

Un grand remerciement est apporté à Monsieur Bencheikh Abdelhalim, Maitre de conférences classe A, université de BBA et Co-directeur de Cette thèse, non seulement pour son aide et ses nombreux conseils, mais aussi pour les encouragements qu'il m'a prodiguée pour inscrire à cette thèse et pour l'accomplir.

J'adresse mes vifs remerciements à M. ……., professeur à l'université de ……. qui m'a fait un grand honneur d'accepter de présider le jury de cette thèse.

J'adresse mes remerciements à Monsieur …….., Professeur à l'Université de ……..., ainsi qu'à Monsieur ……..., Professeur à l'Institut de ……..., de l'honneur qu'ils m'ont fait en acceptant d'être examinateurs de cette thèse.

Je remercie toutes les personnes avec qui j'ai partagé mes études et recherches, notamment ces années de thèse.

Table des matières

Chapter4: Planar Optical Sensor and Evanescent Wave Effects

General introduction

Photonic sensors are under extensive development world-wide combining multidisciplinary research. Optical sensors are a class of devices that use various forms of light–matter interactions to detect, interrogate, and quantify molecules for multiple applications, in industry, environmental monitoring, medicine and chemical analysis. Progress in materials, light sources, innovative solutions and detectors covering wider ranges of the electromagnetic spectrum, with higher sensitivity; allow the use of new techniques that some time ago would have been considered inappropriate. Photonic sensors are recent class of optical sensors. Hence, research in photonic structures and components has had a significant impact on sensor technology. Chemical and biochemical sensors represent the state of the art of photonic sensing, since they are expected to exhibit higher sensitivity and selectivity as well as high stability, immunity to electromagnetic interference, and product improvements such as smaller integration sizes and lower cost. In an intrinsic photonic bio-chemical sensor, the optical transducer is generally represented by an integrated optical waveguide (optical fiber, slot-waveguide, photonic crystal waveguide, photonic wire waveguide and slab waveguide). By this way, this photonic device has to satisfy different parallel functions. The first one consists in guiding the photonic signal from the optical source to the sensible area. Secondly, the photonic waveguide has the role of transducer, enhancing the interaction between the chemical/biochemical process and the optical signal. The formation of modes in optical waveguides could be exploited for sensing. In fact, when light propagates through the waveguide by total internal reflection, it senses the medium surrounding the waveguide through the evanescent tails of its electric field. When a light wave interacts with the biomolecules that are binding to the waveguide surface, some of its properties (wavelength, amplitude or polarization) change and by monitoring these changes the analyte can be detected. A variety of optical-sensing mechanisms exist, including luminescence, fluorescence, phosphorescence, absorbance, elastic scattering, Raman scattering, surface-Plasmon resonance, guided-wave resonance, interference, and reflection/ transmission microscopy. Optical variable has to be transformed into an analytically useful signal. To this purpose, several photonic integrated configurations have been proposed, comprising, integrated optical interferometers, microring resonators, Bragg grating resonators, directional couplers and photonic crystals optical sensors. Among integrated optical waveguides, slab optical waveguide based evanescent wave is widely used for chemical and biochemical sensing. The most advanced technology for fabricating waveguides is Ti: LiNbO3, Lithium

Niobate (LN) is widely used for integrated sensor applications due to its excellent optical, ferroelectrical, piezoelectrical, and thermoelectrical properties. Sensitivity is the most important parameter of a planar optical sensor. Thus, sensitivity enhancement of optical sensors based on evanescent wave interactions has attracted significant research interest.

This thesis is divided into four chapters. In the first chapter, we presented in detail the principle optical sources, photodetectors, integrated optical waveguide transducers used in integrated photonic sensors as well as different light-coupling methods.

In the second chapter, we described in detail principle sensing mechanisms and architectures employed in integrated optical chemical sensors.

The third chapter is divided in two parts. In the first part, an isotropic and anisotropic slab optical waveguides are modeled with two approaches, successively. The first is the optical ray approach, which allows us to determine the dispersion equation of the guided modes for an isotropic slab waveguide. The second is the electromagnetic approach used to determine the wave equations and their solutions, as well as, the solutions of electromagnetic field for an anisotropic slab waveguides. In addition, the influence of the physical and geometric parameters and the wavelength of the source on the propagating modes are studied. In the second part, the effective index method (EIM) is used for calculating the modal fields and the propagation constants in the Embedded-strip waveguide.

In the fourth chapter, after brief description of planar optical sensors principles, we have investigated sensitivity and evanescent field of a slab waveguide optical sensor constituted of Lithium Niobate as a guiding film. Hence, the influences of source, geometrical and physical parameters as well as the birefringence on the sensor sensitivity and on the evanescent field have been studied.

Chapter1: The Optical Sensor Components

1. Introduction

Monitoring of the various aspects of the environment, whether it be external or internal to ourselves and involving chemical, physical or biomedical parameters is an essential process for the well-being of mankind and of the individual. Optical sensor technology has a major part to play in this process, both to complement existing technologies and to promote new solutions to difficult measurement issues. Optical sensors are a class of devices that use various forms of light–matter interactions to detect, interrogate, and quantify molecules for multiple applications, in industry, environmental monitoring, medicine and chemical analysis. Optical sensors can measure physical or chemical quantities. Their development has been stimulated by advances in optoelectronic technology. The developments in new sources and detectors covering wider ranges of the electromagnetic spectrum, with higher sensitivity, allow the use of techniques that some time ago would have been considered inappropriate or lacking in sufficient sensitivity [1]. Photonic sensors are recent class of optical sensors. Photonic sensor technologies involve a lot of application fields like chemical, temperature, strain, biomedical, electrical, magnetic, rotation, pressure, position, acoustic and vibration sensors. Optical Lab-on-a-chip systems, based on chemical and biochemical sensors, represent the state of the art of photonic sensing, since they are expected to exhibit higher sensitivity and selectivity as well as high stability, immunity to electromagnetic interference, and product improvements such as smaller integration sizes and lower cost [2]. In an intrinsic photonic bio-chemical sensor, the optical transducer is generally represented by an integrated optical waveguide (e.g., optical fiber, slot-waveguide, photonic crystal waveguide, photonic wire waveguide). By this way, this photonic device has to satisfy different parallel functions. The first one consists in guiding the photonic signal from the optical source to the sensible area. Secondly, the photonic waveguide has the rule of transducer, enhancing the interaction between the chemical/biochemical process and the optical signal [3].

In this chapter we will present in detail the principle optical sources, photodetectors, integrated optical waveguide transducers used in integrated photonic sensors and different light-coupling methods.

2. The Optical Sensor components

Regardless of their working principles and purposes, all optical sensors have a common set of components: light sources, photodetectors, and optical components to guide the light in between. Somewhere along this light path, there will be the measurement object

whose static and dynamic properties will determine the signal on the photodetector and, thus, the sensor reading, Fig.1.

This part gives a summary of the different kinds of light sources, of the wide variety of commercially available detector elements, and provides examples of optical integrated waveguide that guide and manipulate light for sensing applications.

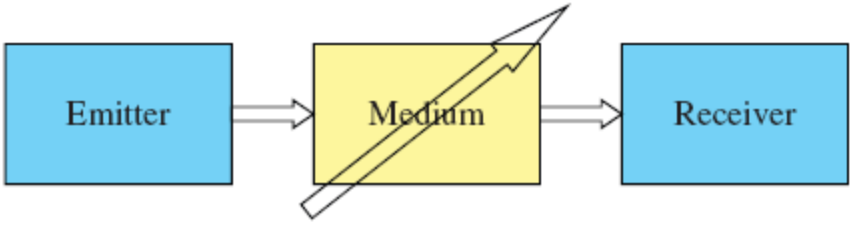

Figure 1: An optical sensor.

3. Light Sources

The light source is the very heart of an optical sensor. It not only provides the medium through which information is transferred, but it may also become a component of the detection circuit itself, for example, by a modulation of the emitted light. A light source is characterized in terms of, for example, its emission spectrum, degree of coherence, radiant intensity, power consumption, lifetime, and all other parameters decisive for the respective application. Due to the physical nature of their light generation process, they can be divided up into thermal light sources or continuous light sources, line sources, pseudo monochromatic light sources and monochromatic light sources.

3.1. Continuous light sources or thermal light sources

Thermal or incandescent light sources emit light as a result of their temperature. Every object with an absolute temperature T emits a continuous spectrum which is described by the spectral power density according to Planck's law of blackbody radiation [4]. One of the easiest embodiments of a radiating blackbody is an electrically heated, glowing piece of wire or a metal filament. In the presence of oxygen, such a filament would oxidize almost immediately. The filament is therefore surrounded by a glass vessel filled with an inert gas, for example, with a mixture of nitrogen and argon, or with even heavier noble gases like krypton or xenon. This is the basic principle of all incandescent lamps. Incandescent and gas discharge lamps are called white light sources because they emit light in a very broad spectral range. The comparison of spectral properties of typical continuous light sources, which are the

most frequently used in the chemical sensors, is presented in Figure 2. A xenon arc lamp seems to be the universal light source. It emits radiation starting from UV up to infrared but it is expensive and the optical power is not very stable. If a sensor needs to be excited only in the UV range, a deuterium lamp can give better results. This is a relatively short-lived lamp (1000-2000 h) and quite expensive. Tungsten halogen lamps are much cheaper than the previously mentioned types. Powered by a relatively simple power supply, they emit stable optical signal and have long lifetime.

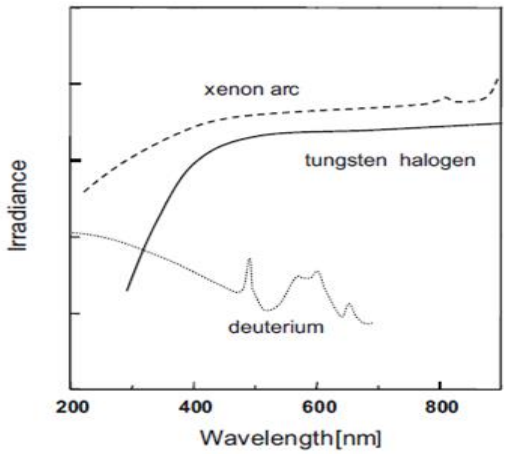

Figure 2: Emission spectra of continuous light sources used in sensors.

One of common disadvantages of these light sources is the necessity of using a wavelength-selecting device. Absorption filters, interference filters or monochromators are utilised to match the light to the sensor requirements. Furthermore, modulation of light is introduced to the system in order to increase the signal to noise ratio [5].

3.2. Line Sources

A discharge in a low - pressure gas does not emit a continuous spectrum, but a spectrum in which the intensity is concentrated in discrete and narrow wavelength intervals. When viewed with a spectrograph, these intervals become visible as single lines in the spectrum, which is therefore denoted by a line spectrum. The discrete distribution of emitted wavelengths is the consequence of the discrete energy levels of atomic orbits and the energy difference between them. As their emission is concentrated in a limited number of discrete wavelength intervals, discharges in a low - pressure gas do generally not emit white light, but show color effects:

- **Neon** has several emission lines in the visible spectrum, but also a dominant line at 632.8 nm. This is why neon tubes emit pink light.

• **Sodium** (Na) lamps emit yellow light because of the Na D lines, a narrow - spaced line doublet at 589.0 nm (D 2) and 589.6 nm (D 1). During power - up, however, they emit red light due to the neon added to the gas in the bulb.

• **Mercury** has a strong emission line at 253.7 nm. Mercury tubes, also called blacklight tubes, emit ultraviolet (UV) light. The ubiquitous fluorescent lamps are manufactured from these blacklight tubes by coating the insides of their glass vessels with phosphor substances that convert the UV to visible light.

The width of the emission lines depends on temperature and pressure. Higher temperatures lead to broader velocity distributions of the atoms and, thus, to broader frequency distributions, the so called Doppler broadening. Higher pressures, on the other hand, increase the collision rates between the atoms and, thus, lead to a decrease in the lifetimes of the upper states, which also leads to a line broadening.

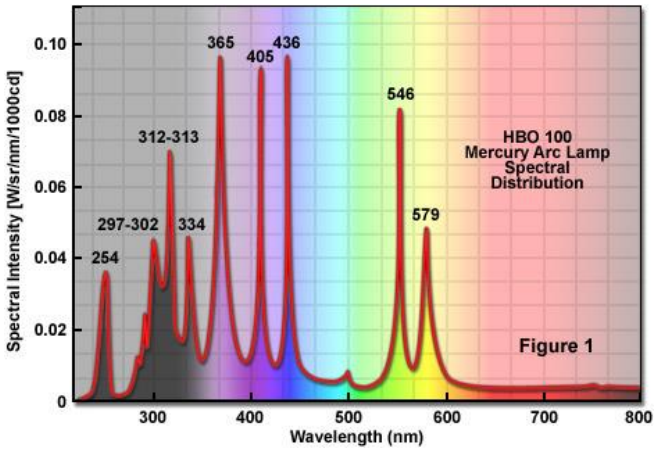

Figure 3: Spectrum of a mercury short - arc lamp. Black solid lines: line center positions.

3.3. Pseudo monochromatic light sources

3.3.1. Light Emitting Diodes (LEDs)

Light emitted by an LED is nearly monochromatic (pseudomonochromatic). LEDs are robust and their lifetimes are more than 100 000 hours. The actual light source in a semiconductor material is the pn - junction. An electronic transition from the lower edge of the conduction band to the upper edge of the valence band will lead to the emission of a light quantum, and its energy will equal the width of the energy gap. Light emitted from a pn - junction has a narrow – band spectrum. Indeed, a typical spectral bandwidth of LED is within the range of 20-50 nm. LEDs cover the whole visible range starting from 370 nm up to infra-red radiation. The radiation emitted by an LED depends on the semiconductor used for its

fabrication. III-V compounds from periodic system are used in LEDs fabrication. Their band-gap can be changed depending on the composition of the compound. Various compounds of gallium, arsenic and phosphorus with zinc, oxygen or nitrogen dopants produce radiation in the visible range, whereas gallium arsenide doped with either silicon or zinc gives infrared wavelengths (900-1020 nm). The emitted optical power can be stabilised or LED can operate in a pulse mode. Their long lifetime, low cost and small dimensions are additional advantages in designing the sensor. Figure 4 shows spectral profile of LEDs.

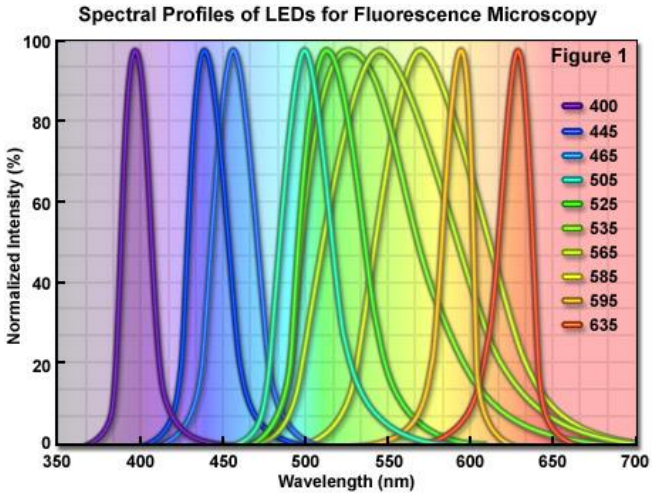

Figure 4: spectral profile of LEDs.

Because of the extremely small exit apertures with sizes of 0.01 to10 mm^2, light emission from an LED shows considerable, diffraction. For an optical designer, forming the light output from an LED is an important task, and manufacturers offer types with different radiation patterns, for example, Lambertian emitters that follow a cosine law for the radiated luminous intensity.

3.3.2. White - light LEDs

White - light LEDs are usually based on short - wavelength LEDs that are covered with a layer of photoluminiscent material. Their spectra show the narrow excitation peak in the blue or ultraviolet wavelength range, but also a broad emission covering the entire visible range, Figure 5**.** The spectral structure of this broad emission determines the color temperature of the emitted light. One major drawback is the low intensity emitted in the green part of the visible spectrum.

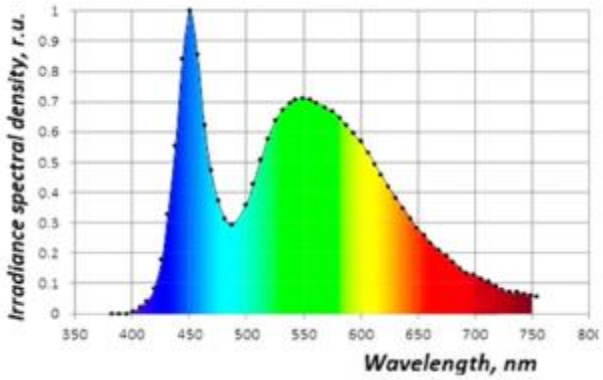

Figure 5: Spectrum of a white - light LED. Excitation peak at 445 nm, broadband emission with maximum at around 550 nm.

3.3.3. Superluminescent diodes (SLED s)

SLEDs are LEDs manufactured from semiconductor materials with high optical gains as they are actually used in diode lasers. In contrast to lasers, however, there is no resonator that feeds radiation back into the material so that there are basically two counterpropagating waves inside the active zone. The light from an SLED will thus be quite intensive, but it will have an LED - like bandwidth and therefore low coherence. In contrast to lasers, there will be no speckles across a spot that is illuminated by an SLED. With increasing temperature, the output power of an SLED will decrease significantly. SLEDs are preferred light sources in many fiber optical applications. Table 1 shows a collection of typical SLED specifications.

Table 1: Typical parameters of superluminescent diodes of Uncooled Single-Mode Free-Space (SLEDs) [6].

Wavelength (nm)	**FWHM (nm)**	**Output power (mW)**
670	7	Up to 15
796	15	20
840	25-30	Up to 100
920	30	20
960	45	90
1040	35-45	Up to 80

3.4. Monochromatic light sources

3.4.1 Diode lasers

Diode lasers are more convenient to use in sensor systems because of their size and their effectivity. In the structure, they are similar to LEDs but they have a resonant cavity where laser amplification takes place. A Fabry-Perot cavity is established by polishing the end facets of the junction diode (so that they act as mirrors) and also by roughening the side edges to prevent leakage of light from the sides of the device. The emitted light beam from diode lasers is coherent and highly monochromatic. In principle, diode lasers are highly – doped LEDs with donor and acceptor concentrations of more than 10^{19} cm^{-3}. As in LEDs, electron – hole recombination processes lead to the emission of light, but due to the high doping, population inversion builds up in the pn - junction. The laser diode package generally contains a photodiode that has one common electrode with the laser diode. This photodiode receives the laser radiation emitted backward from the laser crystal and is used as a sensor for the intensity stabilization of the laser. The main characteristic of diode lasers is the dependence of the light intensity on the injection current (Figure 6 (a)). For low - injection currents, the emitted intensity increases slowly. However, a threshold current, I_T , exists above which the intensity increases strongly.

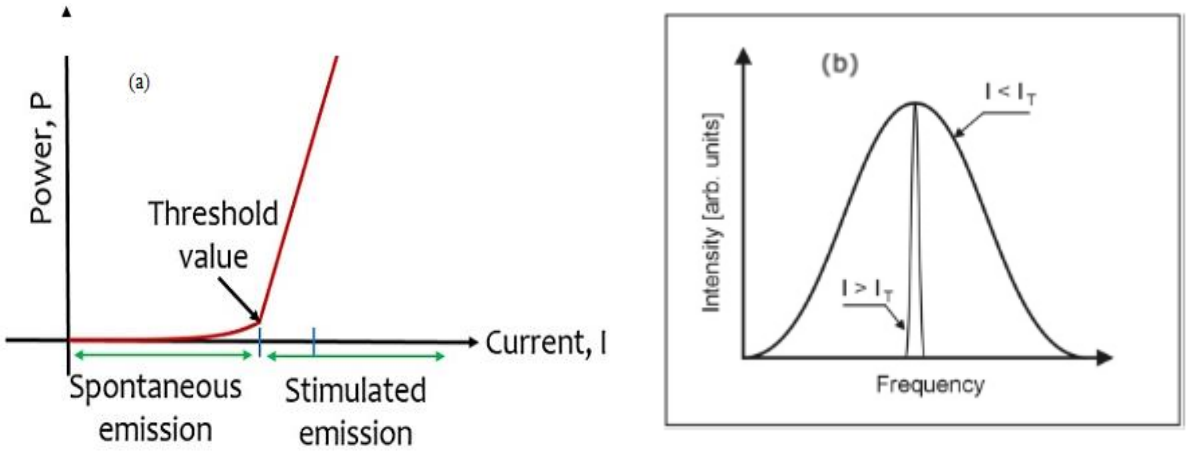

Figure 6: a) Dependence of laser diode power on the injection current.
b) Diode laser spectrum for currents below and above the threshold current.

Due to this strong increase, highly stable currents are required for applications in which highly stable intensities are required. For currents smaller than I_T , and in case of damage, the diode laser has the spectral properties of an LED, above the threshold current, the spectral width decreases due to increasing light amplification (Figure 6 (b)). The first commercial

diode lasers had emission wavelengths in the infrared and near infrared regions; in the meantime mass - produced diode lasers with red, green, and blue emission wavelengths have become available. Table 2 shows a collection of typical specifications of diode laser modules of different wavelengths.

Table 2: Typical parameters of diode lasers in the visible and infrared regions [7].

wavelengths	**Output Power**	**Operating Current**	**Beam Divergence**
405 nm	40 mW	70 mA	8x19
520 nm	25 mw	150 mA	7x22
670 nm	5 mw	30mA	8x32
780 nm	10 mw	24 mA	8x30
850 nm	10mw	20 mA	10x30
905 nm	10mw	50 mA	10x30

Diode lasers reach efficiencies of as high as 50% because electrical energy is directly transformed into radiation. For single laser diodes, the radiant power can reach some 10 mW. Due to this direct energy conversion, diode lasers can easily be modulated with frequencies up to the gigahertz range. Because diode lasers have a very small exit apertures, so diffraction effects cause high beam divergence and an elliptical beam profile. To form a parallel laser beam, a collimating lens is required, and circular beam profiles demand further optical corrections. Particularly for single - mode lasers, however, the collimating lens must be coated in order to avoid reflections back into the laser. As additional protections against back reflections, there are also so - called optical isolators that prevent light from travelling into the direction of the laser. These lasers are interesting light sources for spectroscopy. A special version of the diode laser is the vertical - cavity surface – emitting laser (VCSEL). Laser light is emitted perpendicular to the plane of the pn - junction, which makes it possible to run tests already in the wafer level of the production process. As a VCSEL has a higher exit aperture, its beam divergence is smaller, and its light output can more efficiently be coupled into an optical fiber. The resonator mirrors are formed by layers of different refractive indices, so - called Bragg reflectors. Their reflectivities can reach 0.99, and thus the laser threshold is significantly lower than that for the pn - type diode lasers. However, their radiant power is smaller.

3. 4. 2 Lasers

LASER is the acronym for Light amplification by stimulated emission of radiation. Stimulated emission is a quantum - mechanical process in which long – lived excited atomic states are quenched by radiation. These states are required to have lifetimes several orders of magnitude longer than the usual 10^{-8} s. Thus, it comes to a population inversion in the sense that more atoms are in excited states than in their ground states. As a consequence, one incoming quantum of light generates one additional quantum of outgoing light, and this, results in light amplification. The device becomes a signal source by feeding the output signal back to the input of the system. This feedback is usually accomplished by an optical resonator, a set of two parallel mirrors that contain the amplifying medium. The two mirrors have reflectance of more than 99% so that the light passes the medium more than once. The light waves traveling forward and backward inside the optical resonator interfere and form a standing wave. In the visible and ultraviolet ranges of the spectrum, the existence of longitudinal modes is a necessity for a domination of stimulated over spontaneous emission. As the emission is localized only on narrow frequency intervals, the laser emission is extremely monochromatic. Figure 7 illustrates how resonator modes and emission line profile determine the spectral output of a laser. Due to losses induced by diffraction, scattering, and absorption, a minimum gain, the so called laser threshold, is required for a mode to oscillate. The resonator mirrors must perfectly be aligned to ensure that the light waves be reflected exactly along the optical axis.

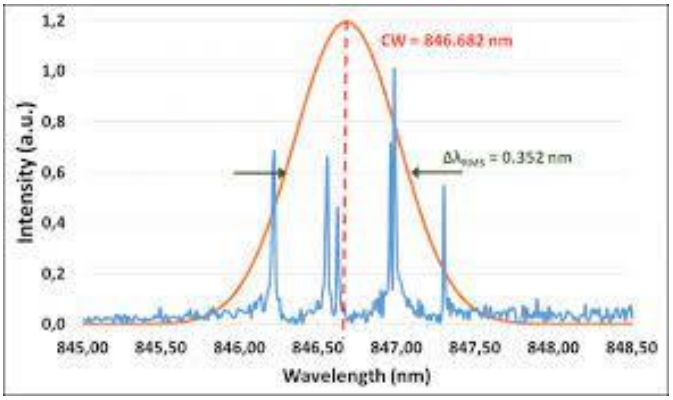

Figure 7: Output of a laser, resonator modes.

The intensity distribution across the beam profile is determined by the transversal modes TEM_{mn} transversal electromagnetic), where *m* and *n* are small integers and describe the number of horizontal and vertical lines with minimal intensity in the beam profile. The

preferred transversal mode is the fundamental TEM_{00} mode: its Gaussian - shaped beam profile has minimum diffraction losses, and the wave fronts are almost spherical [8].

Another important property of a laser is its coherence. The temporal coherence of a light source is determined by its spectral bandwidth. It means a strong correlation (fixed phase relationship) between the electric fields at one location but different times.

Spatial coherence means a strong correlation (fixed phase relationship) between the electric fields at different locations. It describes the surface area that a light source with circular area can illuminate coherently with the light cone of its 0th diffraction order in a distance *r* from the light source. Spatial coherence can thus be improved by increasing the distance to the source, and by reducing its size.

The amplifying medium of a laser may be solid, liquid, or gaseous. Solid – state lasers are based on ion - doped crystals or glasses, for example, Cr^{3+}, Nd^{3+}, Ho^{3+}.

3. 4.2. 1 The HeNe laser

The helium–neon laser was the first gas laser. The original laser transitions were in the near infrared, but the most commonly used transition is the red laser at a wavelength of 632.8 nm and a second infrared line is at 1.15 μm wavelength. This laser is available in sizes ranging from approximately 10 cm in length to over 100. It has continuous power outputs ranging from less than 1 mW to over 100 mW and has a lifetime of 50,000 h for some commercial units. The excitation mechanism involves electrons colliding with helium atoms to produce helium metastable atoms, which then transfer their energy to neon laser levels [9]. Although the size of the discharge tube prevents a significant miniaturization of the laser, HeNe lasers are easy to handle and, therefore, well suitable for sensor systems with no extreme downsizing demands. Although these lasers require high - voltage power supplies, these power supplies are therefore small and easy to use devices. Also, HeNe lasers have smaller line widths than diode lasers and, thus, longer coherence lengths. This is why they are still more suitable for interferometry applications than semiconductor lasers.

3.4.2.2. Supercontinuum light source

As we have seen, lasers are usually light sources of high spatial and temporal coherence. By coupling highly intensive, pulsed laser light into, for example, optical fibers, nonlinear processes inside the material lead to the generation of a wide continuous spectrum of light. The result is a laser system of low temporal, but still large spatial coherence, a so -

called Supercontinuum light source. A commercial model covers a spectral range between the UV and infrared parts of the spectrum (390 – 2400 nm) [10]. The repetition rate is 78 MHz, and the output visible power reaches 2000 mW. Potential applications cover chromatic - confocal sensors, white - light interferometers or multiwavelength fluorescence microscopy.

4. Photodetectors

Before any evaluation of the information that the received light carries can start, it has to be transformed into electrical signals. All processes in which light incident onto a surface produces a current or a voltage are therefore processes around which photodetectors can be designed. Therefore, the primary task of a photodetector in any optical sensor is to convertthe light carrying the information about the measurand into an electrical signal. The light, having interacted with the analyte or indicator, carries the information about the presence or concentration of the analyte. In fact, the process of conversion takes place in an optoelectronic interface as a whole optoelectronic system, because the photodetector is usually combined with optical elements (lenses, filters) and amplifiers. The work of optoelectronic interface can be synchronized by a modulation wave driving the light source. Key considerations in selecting a detector are the required sensitivity, the level of noise inherent in the detector (and thus the signal to noise ratio), spectral sensitivity, linearity, response time etc. The most important of these processes is the photoeffect upon which the working principles of different types of detectors are based.

4.1. Photomultiplier tube (PMT)

PMT being the most sensitive device is capable to detect single photons. The working principle of the photomultiplier is based on the external photoelectric effect [11]. The photon of incident light produces on the photocathode an electron, which is then accelerated towards first dynode where secondary electrons are generated. The process of electron generation and their acceleration continues up to the anode resulting in a huge number of electrons. In this way, a single photon, generating a single photoelectron at the first stage, is multiplied by a given factor with an arrangement as depicted in Figure 8 (a), a so called photomultiplier tube (PMT):an evacuated glass tube contains a photocathode, an anode, and several additional electrodes, the dynodes. When a photoelectron hits the first dynode after being accelerated by the first potential drop, secondary electrons will be released. Each of these will hit the second dynode and, in turn, release additional secondary electrons. This avalanche effect will lead to

a current amplification from stage to stage. The resulting anode current is transformed into a voltage across a resistor. This voltage is proportional to the light intensity incident on the photocathode. One of the major parameters of PMT is its quantum efficiency (QE). The QE shows the ratio of photons incident on the PMT to electrons emitted from the photocathode. The quantum efficiency can be calculated to [12]:

$$\eta(\lambda) = \frac{S_\lambda . 1240}{\lambda} 100\% \qquad (1)$$

Where S_λ is the spectral sensitivity of the photocathode and is λ is the wavelength.

The material used for manufacture of photocathode governs both thesensitivity and the spectral range of the PMT. PMT shave their maximum spectral sensitivities in the ultraviolet part of the electromagnetic spectrum. However, there are special materials, in particular multialkali cathodes (Sb – Na – K – Cs), with increased sensitivities in the visible and near infrared [12]. The spectral characteristics of PMTs are presented in Figure 8 (b).

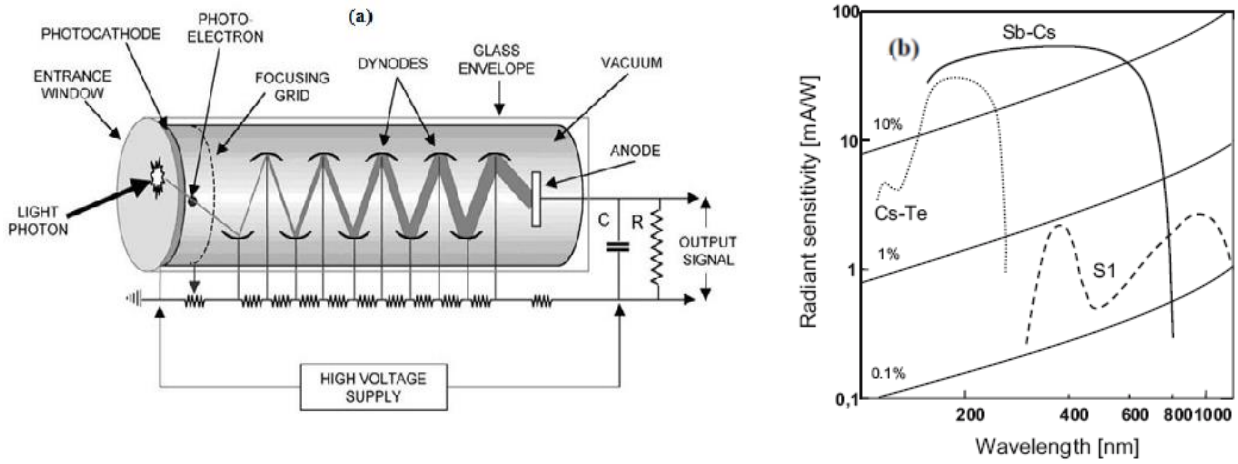

Figure 8: (a) Photomultiplier with resistor network.. b) Spectral characteristics of different PMTs (solid thin lines mark quantum efficiency) [5].

A PMT will yield an output current in the range of 1 pA even if it is kept in the dark. This dark current is caused by, for example, thermionic emission from the electrodes, field emission, and by radioactivity from the environment, cosmic rays, or from the materials used in the PMT. This dark current increases with increasing supply voltage. Photomultipliers exist in different designs, but with a mostly cylindrical tube.

4.2. Quantum photodetectors

Quantum photodetectors are based on the use of a semiconductor. Upon the light interaction, changes in conductivity or changes in generated voltage are observed. The most popular quantum device is a photodiode.

4.2.1. Photodiodes

Photodiodes require no high voltage and no special detector housing so that they are far easier to handle and operate than photomultipliers. They are, however, inferior in their noise characteristic that is typically three orders of magnitude higher than that of a PMT. when photons are absorbed, they create electron-hole pairs. As the charge carriers remain inside the material, this is called the internal photoeffect. An applied reverse voltage forces the charge carriers to drift toward the external electrodes, and this produces a photocurrent that is proportional to light intensity. Some of the charge carriers that travel across the pn junction will get lost due to recombination processes. Due to this recombination, bandwidths of pn diodes do not exceed values of about 10 MHz. In PIN photodiode (p doped, intrinsic, n doped semiconductor material), the charge carriers to travel faster across the junction provide higher reverse voltages. The electrical field across the intrinsic layer is constant and provides constant acceleration for the charge carriers. With these photodiodes, bandwidths in the GHz range have become possible.

4.2.2. Avalanche photodiode (APD)

APD was a response of the producers in competition between PMTs and semiconductor devices. It combines the benefits of both pin photodiodes and PMT, exhibiting the internal gain. A strong internal electrical field is created inside the APD by connecting it to a high reverse bias voltage. This field accelerates the electrons through the diode structure and thus secondary electrons are produced by impact ionisation. A special avalanching region can cause the increase of the gain factor up to several hundred. Apart from the architectures of the semiconductor material, also the sizes of the active areas determine the dynamic properties of photodiodes: the larger these areas are, the slower the response of the detector. The current/voltage (I / U) characteristic of photodiodes is:

$$I = I_S.\left(e^{U/U_T} - 1\right) - S_\lambda.P_L \qquad (2)$$

Where, P_L is the radiant power, I_s is the reverse current, $U_T = kT/e$, and S_λ is the spectral sensitivity. Equation (3) means that increasing light intensities shift the I/U curve down the current axis (Figure 9). The spectral properties of a photodiode depend on the material used for its fabrication. Typical characteristics are presented in Figure 6. Photodiodes are typically made of silicon or germanium. The spectral sensitivity of Si reaches from about 300 nm to 1100 nm and peaks at around 950 nm; they can be used in the whole visible range however their sensitivity drops by several times at the blue region.

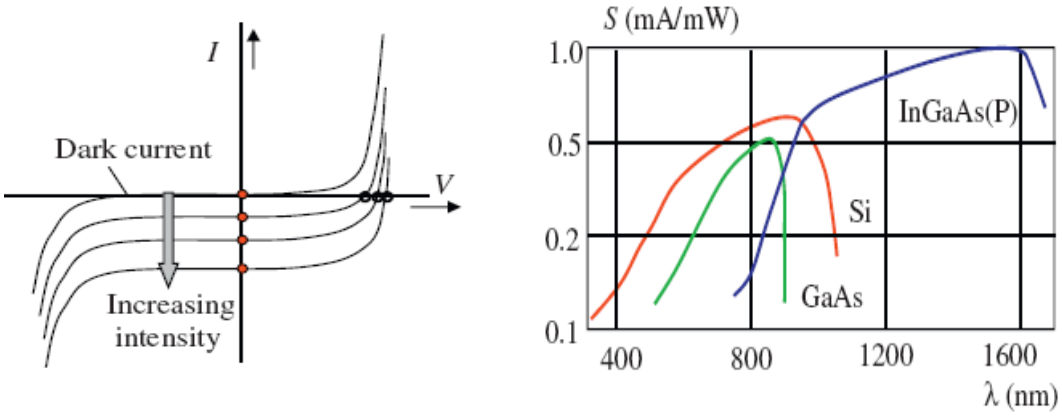

Figure 9: a) Current/voltage (I/U) characteristics of a photodiode in the photoamperic mode of operation. b) Spectral characteristics of photodiodes made from various semiconductors.

Special structures can be made with enhanced blue sensitivity (so-called blue or UV diodes). Whereas, the maximum spectral sensitivity of Ge is around 1450 nm and drops to zero at about 1800 nm. There are also semiconductor materials with increased sensitivities at larger wavelengths. One of these materials is indium gallium arsenide (InGaAs) with a spectral sensitivity range from about 900 nm to about 2500 µm, with its maximum at about 1650 nm wavelength. At the peak of their sensitivity curves, Si photodiodes have spectral sensitivities of about 0.5 A/W, while Ge photodiodes can reach values of 0.9 A/W and InGaAs photodiodes values of more than 1.0 A/W. Table 3 shows the specifications of three types of photodetectors: a Si PIN, a PMT and an APD [13].

Table 3: Comparison of different photodetector types: Si PIN photodiode, photomultiplier, APD

Photodetector type	**Gain**	**Useful spectral range (nm)**	**Quantum efficiency (%)**	**Response time (ns)**	**Multiplied dark current (nA)**
Si PIN	1	400-1150	60-90	0.3-3	-
Si APD	50-300	400-1150	70-80	0.5-5	0.1-1

Ge APD	10-100	800-1750	50-80	0.3-3	5-100
InGaAs PIN	1	900-1700	70-90	0.05-1	-
InGaAs APD	10-40	900-1700	60-90	0.1-1	0.5-5
Photomultiplier	105-107	160-850	30	0.15-13	10-200

4.3. Imaging Detectors

4.3.1. Charged coupling devices (CCD)

A CCD is an imaging detector which consists of linear or area arrays of pixels that produce potential wells from applied clock signals to store and transport electrons which are generated by the photoelectric effect from incident photons or from an internal dark signal. Basically, CCD consists of a light - sensitive area and a readout zone. The light - sensitive area is composed of single picture elements (pixels). A single pixel is a metal-oxide-silicon capacitor. After connecting a time variable voltage sequence, holes move away from the depletion region and thus a potential energy well is created. The incident light generates electrons, which are next accumulated in this well. The charge accumulated is proportional to the light detected. The readout zone basically consists of a shifting register that shifts the single charge packages sequentially from the pixels to a readout amplifier. The output of the CCD is intensity - proportional voltage. External electronics convert the output sequence of voltages into a two dimensional digital image. Three basic variations of CCD architecture are in common use for imaging systems: full frame**,** frame transfer**,** and interline transfer (Figure 10). The full-frame CCD, as referred to in the previous description of readout procedure, has the advantage of nearly 100% of its surface being photosensitive, with virtually no dead space between pixels. The imaging surface must be protected from incident light during readout of the CCD, and for this reason, an electromechanical shutter is usually employed for controlling exposures. Charge accumulated with the shutter open is subsequently transferred and read out after the shutter is closed, and because the two steps cannot occur simultaneously, image frame rates are limited by the mechanical shutter speed, the charge-transfer rate, and readout steps. Frame-transfer CCDs can operate at faster frame rates than full-frame devices because exposure and readout can occur simultaneously with various degrees of overlap in timing. They are similar to full-frame devices in structure of the parallel register, but one-half of the rectangular pixel array is covered by an opaque mask, and is used as a storage buffer for photoelectrons gathered by the unmasked light-sensitive portion. Following image exposure, charge accumulated in the photosensitive pixels is rapidly shifted to pixels on the storage side of the chip, typically within approximately 1 millisecond. Because the storage pixels are

protected from light exposure by aluminum or similar opaque coating, stored charge in that portion of the sensor can be systematically read out at a slower, more efficient rate while the next image is simultaneously being exposed on the photosensitive side of the chip. In the interline-transfer CCD design, columns of active imaging pixels and masked storage-transfer pixels alternate over the entire parallel register array. Because a charge-transfer channel is located immediately adjacent to each photosensitive pixel column, stored charge must only be shifted one column into a transfer channel. This single transfer step can be performed in less than 1 millisecond, after which the storage array is read out by a series of parallel shifts into the serial register while the image array is being exposed for the next image.

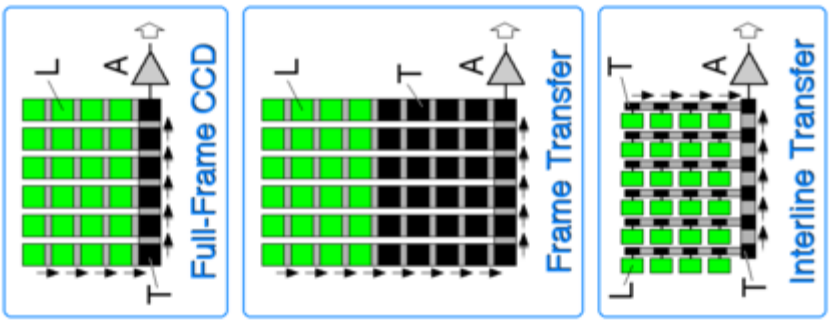

Figure 10: CCD readout techniques: full-frame CCD, Frame-transfer CCD and interline-transfer CCD. L - light sensitive pixel, T - transfer register, A - readout amplifier.

4.3.2. Electron - multiplying CCD s (EMCCD)

For very small light intensities, as they may have to be captured in fluorescence microscopy, cooled cameras with special CCD designs have become available. These electron multiplying CCDs (EMCCD s) are mostly designed like standard CCDs, but they feature an additional, multiplying register that follows the shifting register. Each cell of this multiplying register is supplied with a high voltage so that multiplication of the shifted charge occurs by way of impact ionization. EMCCDs can detect wavelengths between 250 and 1000 nm with quantum efficiencies of more than 90% and are thus capable of detecting single-photon events [14].

4.3.3. Complementary - metal - oxide - semiconductor (CMOS)

In contrast to CCDs, (CMOS) sensors feature current - to - voltage converters and amplifiers in every single pixel. Each pixel is read out without the need for shifting its signal as in a CCD; the additional circuitry, however, requires extra space. The fill factor, that is, the

ratio between the total light sensitive area to the total area of the chip, is thus reduced. This also implies that the overall light sensitivity of CMOS sensors is smaller than that of CCDs. Further miniaturization and microlenses on every pixel have helped to overcome these drawbacks. On the other hand, the power consumption of CMOS sensors is smaller than that of CCDs. CMOS sensors are widely used as image sensors in digital cameras, from single lens reflex (SLR) cameras to mobile phone cameras. In other spectral regions, they are less sensitive than CCDs, which generally renders them unsuitable for surveillance cameras that require high sensitivity in the infrared.

For both sensor types, resolution increases with increasing number of pixels, this always comes with decreasing pixel sizes. This means that for a given image, the intensity per pixel decreases as well so that the signal to noise ratio becomes smaller. Of course, more megapixels always mean higher resolution, but also a generally more adverse noise behavior. Also, with high camera resolutions, one should always try to estimate if the camera optics is indeed capable of providing the same optical resolution. If not, a high camera resolution would be completely useless. This is often the case with digital cameras in microscopy: here, the optical resolution of the objective is determined by its numerical aperture. A simple calculation shows that a camera with 1.3 megapixels and a ½ inch detector chip is sufficient for all detail that an objective with a numerical aperture of 0.65 can resolve.

Neither the pixels of a CCD sensor nor those of a CMOS sensor are color-sensitive; their output is proportional to light intensity only. However, recent innovation incorporates three image sensors stacked on top of each other, realized through the manufacturing process of the sensor array. Photons of different wavelengths have different penetration depths into the semiconductor material so that the blue ones are captured near the surface of the chip, the green ones in the central, and the red ones in the lowermost sensor array. Without the need to interpolate the color pixels, the images appear sharper than that with a Bayer filter [15].

5. Integrated waveguides for optical sensing

Optical waveguides initially developed for the advancement of the telecommunications. However, their efficient light-matter interactions, noise immunity, precise detection and dedicated flexible geometry make them suitable for sensing applications [16]. In principle, there are three types of widely used waveguides, namely strip waveguide, rib waveguide and slot waveguide. Depending on the application, it is necessary to choose an appropriate waveguide type. Rib waveguides show low optical losses at the cost of sensitivity.

In contrast, slot waveguides exhibit a large sensitivity but high optical loss at the same time. Strip waveguides, in contrast, offer a good compromise between loss and sensitivity [17]. Both the labeling-based and label-free sensing processes can be exploited by these exotic waveguide designs. They can be fabricated with standard lithographic techniques which results in low-cost mass production on a single-chip. Additionally, SOI based high index contrast waveguiding incorporates sensor integration with other electronic and optical components on the same chip. Moreover, the use of low refractive index (LI) materials (polymers) for realizing high sensitivity integrated optical sensors should have a number of advantages compared to high index (HI) dielectrics, especially: transparency in the visible range, great chemical flexibility and simple fabrication process [18]. The rib and strip waveguides confines the light wave in the high index core surrounded by low index medium. Here, the light guiding is based on the total internal reflection (TIR) and only a modest fraction of evanescent light tail interacts with the surrounded sensing analytes. However, the slot waveguide guide and strongly confine light in the low-refractive slot region, results in a strong light-matter interaction that makes this structure more attractive for extensive label-based, label-free and opto-mechanical sensing applications. The major sensing mechanism for integrated optical sensors is the detection of the refractive index RI change of analyte. Hence, integrated optical waveguides based RI sensors are commonly implemented by means of interferometers and microresonators [19]. In interferometers sensors such as directional couplers [20], Mach-Zehnder [21], Young (YI) interferometers [22], light-matter interaction introduces a corresponding phase change which is dependent on the difference between the effective indices of the sensor arm and the reference arm. In microresonator sensors, such as ring, disk and Bragg resonators, the resonating wavelength shift measures the refractive index changes that arise due to bio-chemical bindings [23, 24, 3].

5.1 Wire (Strip) waveguide

The wire waveguide consists of a silicon core and silica-based cladding, Figure 11(a).When the effective refractive index is larger than the cladding and smaller than the core, mode is guided in the waveguide, and guiding will be stronger for higher values of effective index n_{eff}. Each mode propagates through the waveguide with a phase velocity of c/n_{eff}, where c denotes the speed of light in vacuum and n_{eff} is the effective refractive index felt by that mode. The n_{eff} depends on the waveguide cross-section, waveguide materials, and the cladding material. Higher-order modes travel with a different propagation constant compared

to the lowest order modes and are less confined in the waveguides. Wire waveguides are advantageous as they provide a small bending radius and realization of ultra-dense photonic circuits. However, they have higher propagation losses.

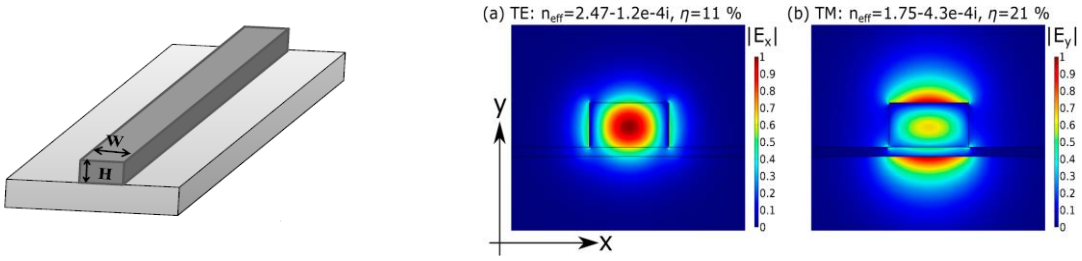

Figure 11: Basic schematic of Strip waveguide (in the left) [25]. (a) Field distribution of |Ex| for the fundamental quasi-TE mode; (b) Field distribution of |Ey| for the fundamental quasi-TM mode [26].

5.1.1. Sensing principle in strip waveguide

When the electromagnetic wave travels through the silicon strip waveguide, most of the energy is confined within the core. However, there is a part of light known as evanescent field extending to the substrate and cladding region as shown in Figure 11. If an absorbing medium is located in the vicinity of the waveguide, the evanescent field is absorbed and the total modal power decreases as the mode propagates along the waveguide, which is detected in terms of a reduced transmitted intensity. In waveguide -based sensing, two basic approaches are commonly used, which are compared in Fig. 12. For so-called homogeneous sensing, a bare WG core is exposed to a typically aqueous homogeneous target medium with its refractive index, Fig. 12(a). For surface sensing, a WG core is functionalized such that target molecules from an aqueous solution can bind to the core forming a surface layer with its effective thickness and refractive index, Fig. 12(b). The amount of the evanescent field, expressed in terms of the evanescent field ratio (EFR), depends on the cross section of the waveguide with respect to the wavelength of the propagating light, as well as on the optical properties of the used materials [26]. Evanescent field absorption gas sensing is a well-recognized approach. The light goes through power attenuation if the wavelength is properly selected with the absorption lines of the sensed gas. The absorption is widely dependent on the concentration of the gas under consideration. In these sensors two important parameters are generally investigated, which are the intrinsic losses and the evanescent field ratio, the latter determines the part of the EM mode that propagates in the gas region [27].The sensors with high EFR can interact more with the absorbing medium, which in turn improves the

sensitivity of the sensor. However, there is a drawback of a higher EFR: the mode is less confined in the waveguide, which leads to a higher spurious damping and leakage of the mode. The geometrical dependence of EFR, as well as propagation loss, provides a guideline for the design of optical waveguide for absorption sensing application [28].

Figure 12: Plain and functionalized strip WG on a buried silicon oxide (BOX) layer. (a) Homogeneous sensing. (b) Surface sensing [29].

In strip waveguide, both quasi-TE and quasi-TM modes are studied, because of the likely gas interaction with the evanescent field on the top and at the sidewalls of the waveguide **[**25, 26, 27]. Due to the electric displacement continuity condition the surface normal component of the electric field shows a distinct discontinuity on the side walls for the quasi-TE mode and on top and the bottom for the quasi-TM mode, Fig.11(a, b). For quasi-TE mode, the dominant electrical field is in the horizontal direction. As the waveguide dimensions are reduced, the mode gets compressed and the evanescent field can jump to even higher level. This, in turn, leads to an increase in the EFR. However, there is a limit on narrowing the dimensions of the waveguide. When *W* gets too small, the quasi-TE mode gets leaky and it is no longer supported as a guiding mode and all the energy is transferred to the cladding. EFR saturates for large *W* values because most of the energy is confined laterally in the silicon core and most of the evanescent field will be from the top wall interface. Moreover, in the vertical direction, EFR doesn't depend so much on the waveguide height *H*, but shrinkage of H_c an still enhance the EFR value [28]. In the case of quasi-TM mode propagation in a waveguide, the vertical electrical field is dominant. This is for the same reason as in the quasi-TE mode; the evanescent field is enhanced at the top cladding as shown in Fig.11 (b). The EFR is sensitive to waveguide height and it depends on *H* in a similar fashion as it does on *W* in the quasi-TE mode. Meanwhile, larger waveguide width affects the EFR value. Waveguide becomes leaky when *W* and *H* become too small [16]. In conclusion, the strip waveguide show a higher EFR for small waveguide dimensions, due to less confinement of the mode in the waveguide core. Nevertheless, intrinsic losses due to absorption in the lossy cladding or

leakage due to the surface roughness will increase with smaller dimensions as the mode is less confined in the core. Furthermore, if the dimensions get too small no guided mode can propagate.

5.2. Rib waveguide

Rib or ridge waveguides have been studied comprehensively over the years since they are commonly used for lasers, amplifiers, modulators, and switches as essential parts to deliver photons and provide host medium to light matter interaction [30]. The rib waveguides generally consist of three parts; a silica substrate, a thin silicon layer on top of the substrate and a rectangular silicon rib part. The index of the rectangular region must be larger than the surrounding medium for the rib in order to guide light, Fig.13. Although a rib waveguide can never truly be single mode, by optimizing the design, the power carried by the higher order modes will eventually leak out of the waveguide over a very short distance, thus leaving only the fundamental mode. For widths below 800 nm, silicon photonic rib waveguide willbe single mode for each polarization. Rib waveguides typically require bend radii >50 μm in SOI to ensure low bend losses, which eventually result in a larger device/circuit footprint [31].

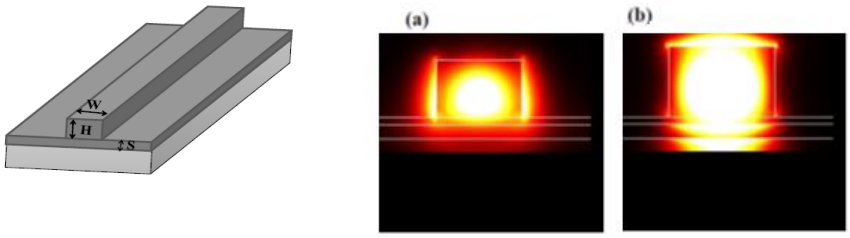

Figure 13: Basic schematic of Rib waveguides (in the left). a) TE mode distribution in a rib waveguide. b) TM mode distribution in a rib waveguide [25].

5.2.1. Sensing principle in rib waveguide

Rib waveguide-based optical sensors are used in a variety of applications such as label-free detection of chemical or biological analytes that specifically bind to functionalized waveguide (WG) surfaces and for detection of bulk refractive index changes in the WG cladding (homogeneous sensing). The sensor principle relies on an optical rib WG, guiding a mode which significantly extends into the cladding medium that surrounds the WG core. The interaction between the optical mode field and the varying surface layer properties or the refractive index of cladding medium, alters the effective refractive index of the mode and thus the optical phase shift accumulated during propagation [29]. For sensing applications, the

optical waveguide structures should be designed to offer a high sensitivity. That is, the sensor response for variations in the optical properties of the cover medium has to be as high as possible. The sensitivity depends on the strength and distribution of the evanescent field in the outer medium. The sensors with high EFR likely interact more with the absorbing medium, which improves the sensitivity of the sensor. However, there is a drawback of a higher EFR: the mode is less confined in the waveguide, which leads to a strong leakage of the mode. Rib waveguide provides a design freedom by inserting a slab layer which supports in waveguiding. Rib waveguide has an advantage over strip waveguide is that the attainable EFR can surpass that in the strip waveguide [25]. In rib waveguide, both TE and TM modes are considered because they are valuable for the field enhancement as shown in figure 13(a, b).The gas or analytes will interact with the evanescent field on the top and at the two side walls of the waveguide. TE mode in rib waveguide has a significant portion of field distributed in the two shoulders of the rib as can be seen in Fig.13 (a). It has been shown that the EFR is slightly dependent to the slab thickness. Moreover, EFR is much higher at larger waveguide width but this waveguide can suffer from high leaky modes. In the other hand, for TM polarization, Fig.13 (b), it has been shown that slab height has a strong impact on the EFR. The dependence of EFR on the waveguide geometry as well as propagation loss provides a standard for the design of optical waveguide for mid-IR absorption sensing application [25].

5.3. Slot waveguide sensor

Slot waveguide consists of two strips (rails) of high refractive index (n_H) separated by a low-index (n_S) region (slot) of width W_{slot}, Figure 14. This structure is able to guide and strongly confine light in a nanoscale low-refractive index material by using TIR at levels that cannot be achieved with conventional waveguides. The principle of operation of this structure is based on the discontinuity of the electric (E) field at a normal boundary between two materials, which results into higher amplitude in the low-index slot region. The amplitude is proportional to the square of the ratio between the refractive indices of the high-index material and the low-index slot material (air) [32]. When the width of the slot waveguides is comparable to the decay length of the field, electric field remains across the slot and the section has high-field confinement, which results into propagation of light in the slot section; unlike in a conventional strip waveguide, where the propagating light is confined mainly in the high-index medium. The advantage of a slot waveguide is the high-field confinement in the slot section, which normally cannot be achieved using a simple strip- or a ridge-based

waveguide, making it a potential candidate for applications that require light-matter interaction such as sensing [33] and nonlinear photonics [34]. In addition, slot-waveguides can be fabricated by employing CMOS compatible materials and technology, enabling miniaturization, integration with electronic, photonic and fluidic components in a chip, very low wavelength sensitivity and mass production. These advantages have made the use of slot waveguides for highly sensitive biochemical optical integrated sensors an emerging field [19]. RI sensors based on slot-waveguide are mainly implemented by means of interferometry configurations such as directional couplers [19], [35], Mach-Zehnder interferometers [36] and microring resonators [37, 38, 39]. They are highly efficient to make a very small measurement that is not possible by any other means.

Utilizing the remarkable field concentration in the slot region, an effective light-analyte interaction could be obtained in case of both surface and bulk sensing, Figure 15. The bulk sensing or homogeneous sensing refers to a sensitivity investigation when the cladding and the slot region are filled directly with analyte. Thus, the refractive index change of cover and slot regions are detected. In the surface sensing, an ultrathin adlayer of receptor molecules uses on guiding material to immobilize the targeted analyte. The binding interaction between the target analyte and adlayer changes the complete (adlayer + analyte) sensing layer thickness that influences the effective index of the guided optical mode [16].

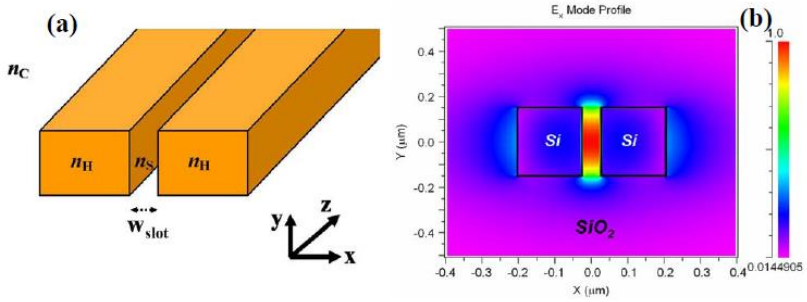

Figure 14: (a) Schematic view of a slot-waveguide. (b) Calculated Ex profile of the quasi-TE eigen mode in a Si (n_H = 3.45)/SiO2 (n_S = n_C = 1.44) slot-waveguide at a wavelength of1.55 µm. E-field is enhanced in the nanoscale slot-region of refractive index n_S [19].

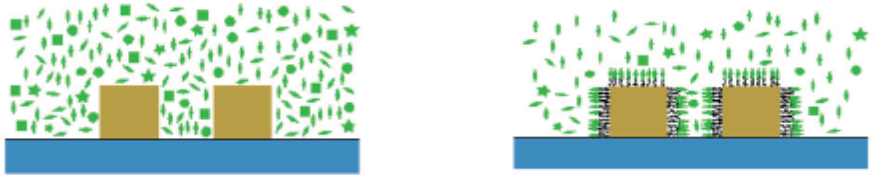

Figure 15: Schematic homogenous sensing and surface sensing principle. The receptor molecules (antibody) are located on top of slot waveguide surface [40].

In case of homogeneous sensing, slot waveguide sensitivity is defined as [18]:

$$S = \frac{\partial n_{eff}}{\partial n_c} = \frac{2n_c^0}{\eta_0 P} \iint_R |E(x,y)|^2 dxdy \quad (3)$$

Where: n_{eff} is the propagating mode effective index, $\eta_0$is the free space impedance, E and H are the electric and magnetic field vectors, respectively, $n_c^0$is the unperturbed value of cover medium refractive index. *P* is the Poynting vector calculated over the entire simulation domain and *R* is the integration domain (unless differently specified, the integral has been calculated over both the top cladding layer and the slot region).

In case of surface sensing, slot waveguide sensitivity can be written as [41]:

$$S = \frac{\partial n_{eff}}{\partial \rho} \quad (4)$$

Where: ρis the molecular adlayer thickness and $n_{eff}$is the propagating mode effective index.

Using an optimized set of geometrical parameters, a sensitivity exceeding the unity can be obtained. This sensitivity value is significantly larger than those obtained by other nanometer guiding structures, although highly sensitive, such as Si-wires [41]. A slot waveguide SWG can be realized in two geometrical configurations that differ by the orientation of the low index region, either vertically etched at a rectangular WG centre, horizontally sandwiched between two high index layers or a combination of both, forming a cross-slot. In case of both vertical and horizontal slot waveguides, the dominant electric field components (*Ex* and *Ey*) of the quasi-TE and TM mode, respectively, encounters discontinuities at the material interfaces. Thus, a peculiar (remarkable) field concentration is showed in the low refractive index region.

5.3.1. The vertical slot waveguide

In this waveguide, the slot region is vertically aligned between the two strips waveguide, Fig.16. Where n_1 refers to the high index region while n_2 indicates the low index region (slot region) and n_3 depicts the cladding region, which surrounds the slot waveguide. From Fig.16(a, b) it is evident that the TE mode has stronger confinement in the slot region than TM mode due to the discontinuity of the normal component (x-component in this case) of the electric field at the high index contrast interface. The cladding and the slot region are filled directly with analyte (bulk sensing) or first, the waveguide is coated by an ultra-thin receptor to immobilize the target.

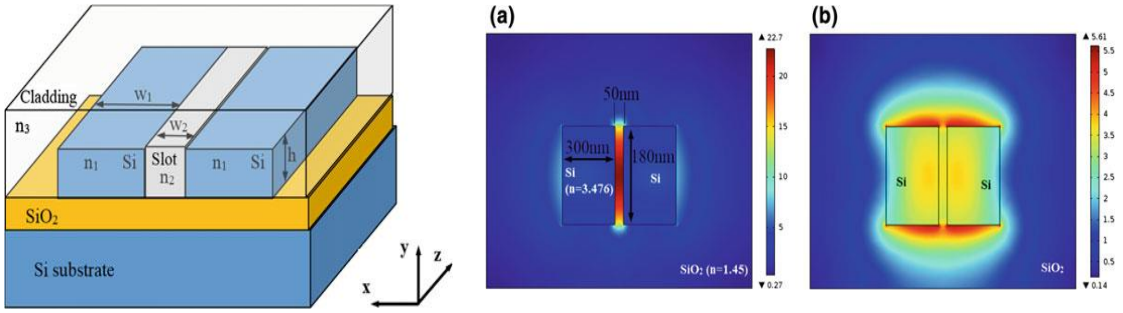

Figure 16: Slot waveguide based on SOI (in the left). Norm of the E-field distribution at wavelength 1550 nm for (a) TE mode and (b) TM mode [16].

5.3.2. The horizontal slot waveguide

The horizontal slot waveguide shown in Figure 17(a) is used to obtain a strong confinement in the slot region for TM mode [42]. In this regard, the strong light confinement mode is the TM mode because the normal component of the electric field now becomes the y-component. Figure 17(b) depicts the norm of the electric field distribution of the TM mode for the SOI horizontal slot waveguide atλ= 1550 nm. Such a horizontal slot can be fabricated on SOI substrate, where a low index slot channel is sandwiched by two high index silicon slabs. For applications towards bio-chemical or gas sensing, the slot region should be filled by the desired target analytes.

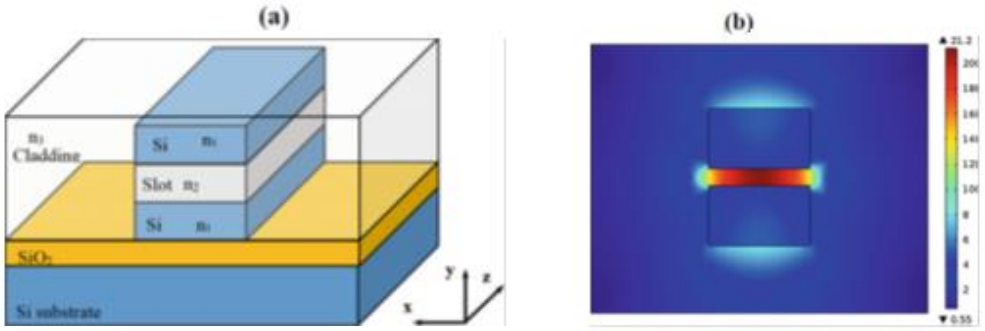

Figure 17: (a) Horizontal slot waveguide based on SOI. (b) Norm of the E-field distribution at wavelength 1550 nm for TM mode [16].

5.4. SWG based photonic biosensors

Subwavelength grating (SWG) waveguide is a periodic arrangement of silicon blocks, Figure 18. The geometrical parameters describing this structure are the waveguide width (W), the silicon layer height (H), the period or pitch(Λ) and the duty cycle (DC =L_{Si}/Λ). Depending

on the size of the period (Λ) compared to the free-space wavelength (λ_0), three different operating regimes exist [43]; i) Subwavelength, where the pitch is small enough to suppress diffraction effects ($\Lambda < \lambda_0/2*n_{eff}$) and the structure behaves as a lossless waveguide whose core can be modeled as an homogeneous anisotropic material. ii) Bragg or photonic band gap, where the incoming light is completely reflected backwards ($\Lambda = \lambda_0/2*n_{eff}$). iii) Diffraction, where the light is gradually radiated as it travels through the periodic waveguide.

In all cases, the electromagnetic field solutions supported by the structure can be rigorously described by the Floquet-Bloch modes formalism [44]. Operation in the subwavelength regime is very attractive in the field of photonics integrated circuits because, by using a single etch-depth and judiciously choosing the aforementioned geometrical parameters, it is possible to control the properties of the Floquet-Bloch mode. Not only is it feasible to tailor its effective index, and consequently its mode shape, but also its wavelength dependence or dispersion and even its birefringence [43]. Figure 18 shows a cut of the fundamental TE Floquet-Bloch mode. Due to the segmentation, a significant delocalization of the electric field in comparison with a photonic wire of same dimensions takes place. Furthermore, apart from the field enhancement that occurs at the sidewalls (like in a photonic wire waveguide), the field is also enhanced between the silicon blocks. This enhanced light-matter interaction is the cause of the high sensing capabilities of SWG waveguides. It has been showed that in bulk and surface sensing, significant enhancement can be achieved by optimizing the waveguide geometry for sensitivity [43].

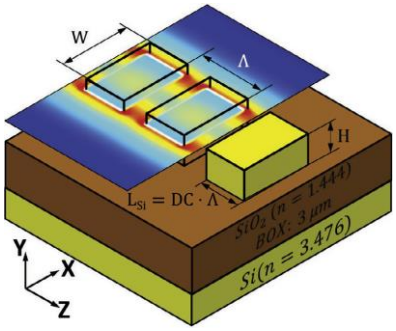

Figure 18: Schematic representation of a SWG waveguide. The electric field intensity distribution in the XZ plane is shown at half-height of the silicon blocks [43].

5.6. Photonic Crystal for Chemical/Biochemical Sensors

Photonic sensors continue to be high on the agenda because of the ever-increasing demand for sensing applications in areas such as healthcare, defense, security, environment and food quality control, with a particular emphasis on miniaturised and personalised

technologies [45]. A particular photonic structure that can be used for sensing is a photonic crystal (PhC). Photonic crystals are the periodic dielectric structures that can control and guide the photons. They can be categorized into three main groups as one-dimensional (1D), two-dimensional (2D), and three-dimensional (3D) structures [44]. An intrinsic property of PC structure is Photonic Band Gap (PBG) introduced by the periodicity of dielectric constant which prohibits a certain range of frequencies from propagating within the materials. The wavelength range of propagation in PC depends upon PBG structure which in turn is controlled by periodicity and refractive index of material. In fact, a little change in the periodic structure, which is called as defect, can create a new frequency range in the band gap, displaying particular resonant dips/peaks in the spectral signature [44]. In the lattice of air holes in silicon, defects can be formed by reducing or increasing the radius of one or more air holes; even defects can be shaped by filling holes. Point defect creates microcavities and line defect creates waveguides in photonic crystals [46]. The main PC property exploited for sensing is the dependency of the width and position of the defect peak on the periodicity and on the refractive index of the surrounding materials. In addition, light can be localized in avery small volume, leading to strong light–analyte interactions. Sensing mechanism in the most photonic crystal sensors is based on the refractive index (RI) change mechanism. By binding the chemical or biochemical molecules to active sensing surface, the refractive index will be changed. So, the resonant wavelength or the intensity of the transmission spectrum is changed. This process can be used as a way to measure the concentration of the molecules [47]. In photonic crystals, the sensor can be formed by simply illuminating the structure with a incandescent lamp, LED or Laser. Miniature, sturdy and low cost instrumentation for measuring properties of photonic crystals, with the addition of the ability to fabricate photonic crystal structures inexpensively has made them suitable for sensor applications in multidisciplinary field.

5.6.1. Architectures of photonic crystals

Several architecture of photonic crystals have been investigated and employed in photonic sensors to achieve high performance e.g., simple photonic crystal, microcavities, waveguides, ring resonators, photonic crystal fibers, slotted photonic crystals, slotted waveguides, slotted ring resonators, interferometry structures [48].

5.6.1.1. W1 photonic crystal waveguides

One of the most common defects is realized by removing a single row of holes along a symmetry direction of the crystal, thus creating a W1 waveguide, Figure 19. This creates the defect modes in the photonic band structure. Forbidden frequencies can be guided by this defect Holes on either side of the line defect behave as very efficient mirrors for forbidden frequencies, and thus can be used to guide light. Photonic crystal waveguides can employ temporal light confinement mechanisms such as slow light [49, 50]. Physically, slow light behavior results from coherent backscattering at each unit cell of the photonic crystal forming slow moving interference patterns within the waveguide [49]. The main advantage of slow light is that it results in pulse length compression, which in turn leads to higher intensity and increased light-matter interactions. These linear defects are often employed to side-couple light into cavities by placing them in close proximity and allowing evanescent-wave coupling.

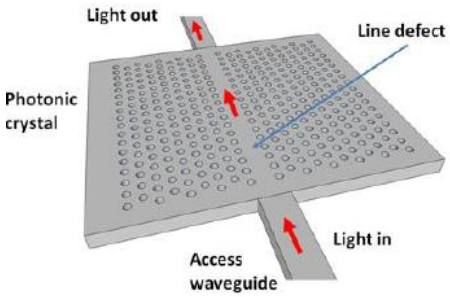

Figure 19: Schematic of a 2-D slab photonic crystal, with a W1 defect. Light is delivered to and from a photonic crystal via access waveguides [51].

5.6.1.2. Slot photonic crystal waveguides

Slot photonic crystal waveguides (SPCWs), are constructed by introducing a slot cut along the length of a standard PhC planar waveguide, Figure 20. These structures allow the confinement and guiding of light when it is polarized with the electrical field perpendicular to the slot. They are of interest for hybrid integration as they can enhance the light-matter interaction due to the combined slot and slow light effects [52, 53] with a low-index material filling the slot. Typical dimensions for a SPCW have been chosen to achieve proper fraction of electric-field energy density in the cladding region, especially the radius of holes in the first row (r_1) and the value of the slot width (W_{slot}).

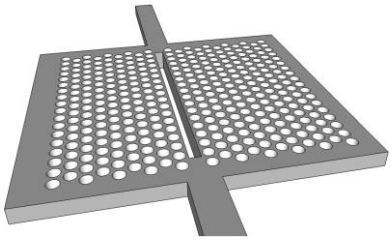

Figure 20. Sketch of slotted photonic crystal geometry. Slot waveguide defect introduced to guiding region of W1 photonic crystal [51].

5.6.1.3. Planar photonic crystal cavities

Confinement of light in photonic crystals can be achieved by introducing defects in the ordered arrangement of refractive index, such as removing holes or changing their radii. The result is the creation of available states for a narrow-band portion of radiation within the bandgap, which prevents radiation from propagating in neighboring regions. The performance of a cavity can be evaluated by a high quality factor *Q*, a concept determining how long the lifetime of photon confined in the cavity is, and a small cavity mode volume *V* defining the cavity ability of spatial mode confinement. Defects that form cavities in a two-dimensional slab can be classified in three main categories:

- They can be created by shifting several holes in the Γ-K direction to make "point-shift" of "zero-cell" cavity (H0), figure 21(a), or removing one hole from a triangular lattice of air holes (H1), Figure 21(a)**.**

- L*n* cavities represent line defects, whereby *n* adjacent holes are removed from the periodic lattice in order to localise light along a line, figure 22(a).

- Heterostructure cavities; the hole size and/or period is changed along a line defect similar to semiconductor heterostructures, figure 22(b).

- PhCs can also feature periodicity in only a single spatial direction, to form "nanobeam" cavities. Nanobeam cavities utilise refractive index guiding in the transverse directions and photonic crystal confinement in the direction of propagation; interestingly, this approach tends to achieve smaller mode volumes than those of cavities in 2D slabs, while 2D cavities achieve higher Q-factors. To form a nanobeam cavity, a row of air holes is typically etched into a single mode waveguide. Defects can be introduced by removing holes, altering their radii or by tapering their sizes and positions. Figure 22(c).

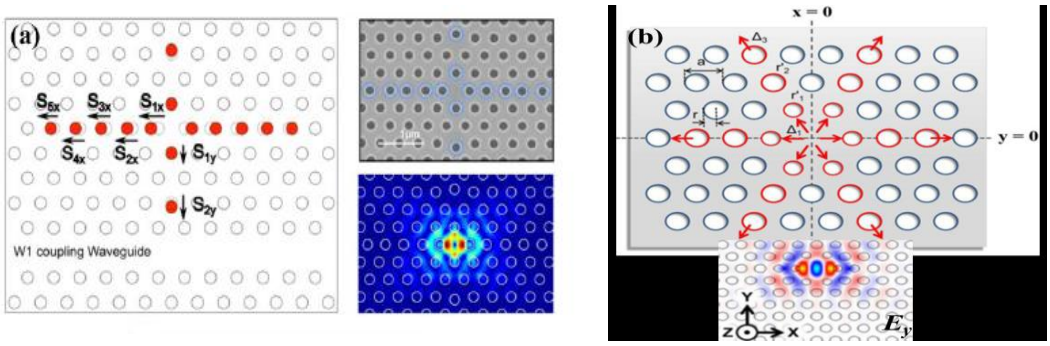

Figure 21: Different kinds of PhC cavities and the E_y profile of the dipole mode (a) H0 PhC cavity [54]. (b) H1 PhC cavity [55].

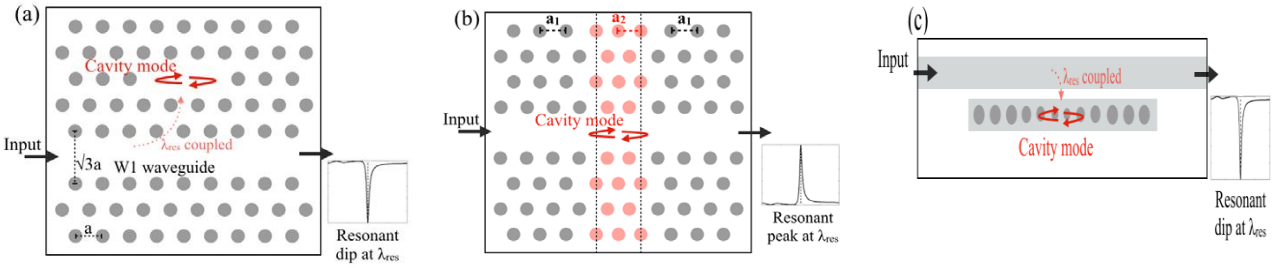

Figure 22*:* Examples of 2D photonic crystal cavity geometries. (a) Top view of a PhC cavity, consisting of 3 missing holes. (b) Schematic of a Heterostructure cavity obtained by altering the period of the PhC in a specific section. The result is a peak in the transmission spectrum, similar to a Fabry-Perot cavity. (c) Schematic of a side-coupled nanobeam cavity [45].

5.6.1.4. Slot photonic crystal cavities

An interesting variant of the photonic crystal cavity configuration is the slotted cavity [51], figure 23. Slotted cavities combine the concept of photonic crystal confinement with the slot waveguide [32] by adding an air slot at the center of the cavity; their main advantage is a strong spatial confinement of the mode within the air slot and the resulting larger overlap of the mode with the sensing medium, which increases sensitivity. Indeed, slotted devices show the best performance in terms of sensitivity and LOD within the class of PhC biosensors [45].In this sensor, the technological approach employed for realizing the microcavity does not consist in modifying the lattice constant or the hole radii characterizing the PhC, but in introducing a straight line defect in which a modified waveguide width acts as resonant cavity [56]. The waveguide region is obtained by removing a row of air holes in the middle of the structure. An air – slot is embedded in this line defect region. The width of the air slot is kept constant, except in the middle. A slit is made by increasing the width of air slot in the center. This increasing in slot width results in the formation of reflective barriers for traveling mode.

The cavity mode is strongly confined into the cavity region [3]. By this way, only resonant wavelengths can propagate inside the photonic cavity. The refractive index change (Δn) due to the sensor exposition to different analytes, causes a resonant wavelength shift ($\Delta\boldsymbol{\lambda}$). Consequently, it is possible to detect different analytes concentrations by monitoring the cavity transmission spectrum [3].

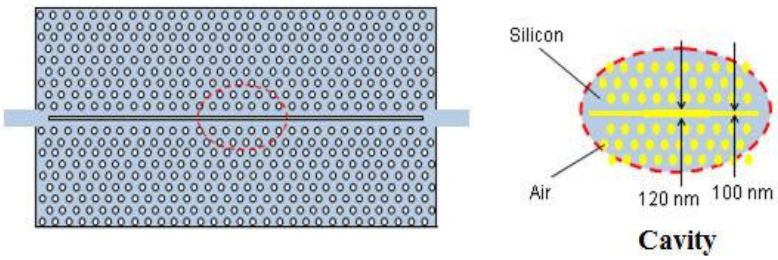

Figure 23: Air-slot PhC cavity with zoom of slit in the slot [3].

6. Light-coupling methods

Because of the small dimensions of thin-film waveguides, the coupling of light into an optical waveguide requires special attention. The application of the sensor system and the layout of the waveguide determine the appropriate light coupling method. Coupling the light out is easier and may employ the same means as that used to launch light into the waveguide. The three means most commonly used for coupling the light into the waveguide include end-firing, prism coupling, and grating coupling. Each method has advantages and disadvantages, depending on the design of the waveguide sensor.

6.1. End-firing coupling

End-firing is the most obvious method to excite a guided mode in a waveguide. It can be accomplished either by a lens focusing a collimated light beam onto the waveguide or by a waveguide illumination with an optical fiber, Fig.24.

Effective coupling requires well-prepared (e.g., polished) square edges of the waveguide and an exact alignment of the optical elements focusing the light beam. This ensures a maximal overlap integral, which is determined by the intensity distribution of the light and the distribution of the waveguide modes [57]. Although technically not demanding, End-firing coupling has the disadvantage of low robustness against vibrations in the sensor system, and it requires extensive alignment procedures to minimize variations in the coupling efficiency.

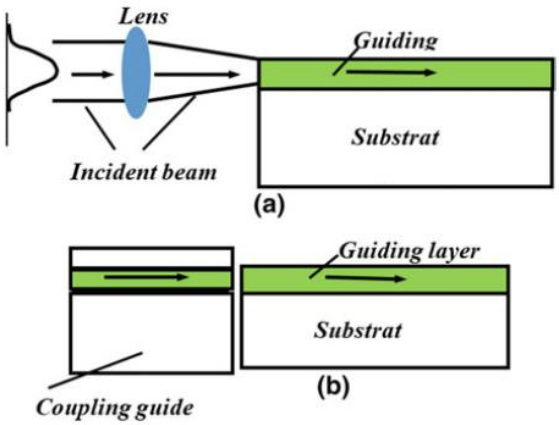

Figure 24: End-firing coupling technique using a) a direct coupling by focusing beam and b) a coupling guide [58].

6.2. Taper Coupling

In this configuration, where a tapered structure is created on the waveguide surface over a distance of 10 to 100 times the wavelength as shown in Fig.25. The incident light can be progressively coupled into or out from the waveguide throughout the tapered structure, while the cutoff thickness of the guided mode is reached. The taper allows a continuous variation of the reflection angle around the critical angle. This technique is of great interest with high-index thin films where it is difficult to find a high-index transparent prism [59]. However, the taper coupling has some drawbacks [60] it is a destructive method due to the created tapered structure on the surface of the guide; low coupling efficiency; and it is difficult to excite selective guided modes.

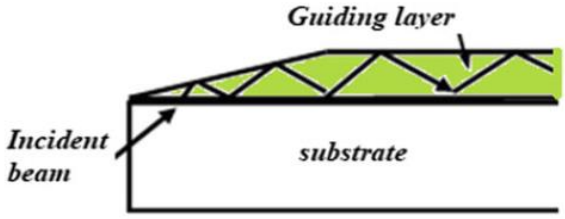

Figure 25: Taper coupling technique [58].

6.3. Prism Coupling

Prism coupling method is the most frequently technique for optical waveguide characterization. This method, in which a high refractive index prism is placed in intimate contact with the surface of the waveguide, permits highly efficient coupling of light into and out of a waveguide. Prisms such as heavy flint glass (n = 2.009) and rutile (no = 2.584) are commonly used. A bit of pressure and a scrupulously clean surface are necessary for good

contact. For light confinement within the guide, the longitudinal component of the wave vector should be equal to the guided mode propagation constant. Thus, the following condition should be satisfied:

$$\beta_m = k_0 n_{co} \sin\theta_m \geq k_0 n_s \geq k_0 n_c \qquad (5)$$

where cladding index *nc* is usually air. This condition cannot be satisfied if the beam is directly incident on the surface of the waveguide. In order to excite guided modes, it is necessary to use a high-index incident medium, Fig.26, a high-index prism is used to couple the laser beam into the waveguide. To maintain a very small air gap, (of order of half a wavelength) between the prism and the guide surface, spring-loaded clamps are used to press the prism onto the surface of the waveguide [58].

When the angle between the incident light and normal to the prism base exceeds the critical angle at the prism–air interface, total internal reflection occurs at the base of the prism and a stationary wave is formed inside the prism. In the air gap, an evanescent wave exists. If the phase matching condition is satisfied such that the propagation constant of the light passing through the prism is equal to the propagation constant of the guided mode, the coupling of the incident light into the guided mode is obtained. This can only occur when:

$$n_p \sin\theta_\psi = n_{co} \sin\theta_m \qquad (6)$$

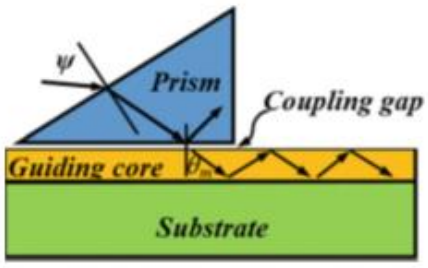

Figure 26: Prism coupling Technique [58].

Where n_p is the prism refractive index. The coupling efficiency mainly depends on the thickness of air gap which can be controlled by the pressure applied to the prism by the clamps, the incident beam profile and the incident beam section at the base of the prism, which are related to the optical setup and the used laser source.

If the waveguide is made to have additional modes, adjusting the angle ψ allows selecting and altering these individual modes. Also, such configuration can be used to characterize the waveguide by coupling the propagating light out of the guide. The use of prisms can find application when the sensing is conducted in air. However, this coupling method might not be

suitable for sensor systems used outside the laboratory, since the pressure of the prism on the waveguide needs to be reproduced with high precision.

6.4. Grating Coupler

The grating coupler is a periodic structure with alternating refractive indexes that is fabricated into the substrate or waveguide by embossing, etching, or by ion exchange. Gratings provide the option and advantage of having the light come in from the bottom of the waveguide, thus allowing for direct sensing of the environment, or the placement of the test cell and related fluidics on the sensing side. Gratings have less stringent alignment conditions than does the end-fire approach. The grating design allows waveguide chips to be routinely replaced, producing, a "plug and play" sensor. Gratings work well for slab waveguides but pose a more difficult task for channel waveguides. The narrow width of gratings on a channel waveguide limit the amount of light that can be coupled in, as well as making alignment a more difficult task. As with prism coupling, the coupling angle is determined by the effective refractive index of the waveguide. The grating structure allows only a very narrow range of coupling angles, depending on the spectral bandwidth of the light source. The position of the light beam on the grating influences the coupling efficiency to a large extent, along with grating parameters (structure depth). When linearly polarized light is used, the direction of polarization TE or TM mode is decisive [61]. In this technique, a periodic grating structure of period Ω is fabricated on the surface of the waveguide as shown in Fig.27.When a light laser beam with propagation vector β_o is incident on the grating region, the light is diffracted and components of a period 2π/Ω appear in the longitudinal component of the wave vector [62, 58]. These wave components have propagation constant,

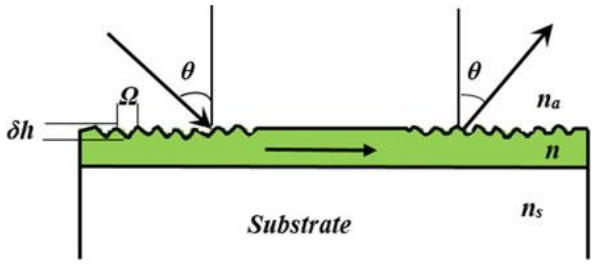

Figure 27: Excitation of guided modes using grating coupler [58]

$$\beta = \beta_0 + 2\pi\frac{\gamma}{\Omega} \qquad (7)$$

where γ is the diffraction order, integer: 0, +1, +2, +3, …

Thus, light can be coupled to guided modes *m* when the propagation vector of the guided mode βm fulfills the phase matching condition in relation (3). The coupling efficiency is optimal for specific values of the incident angle θ that are solutions of the phase matching relation. It depends on many factors: the grating structure (the grating period Ω and the grating depth Δh), the form of the incidental beam, and the zone of coupling [60].

6.5. Directional coupling

In the case of directional coupling, channel waveguides are brought in close proximity, so that a mode can be excited in a secondary waveguide via the evanescent field of a primary one [63], Fig.28. In other words, one of the two waveguides acts as the source for the second one. Whereby, the amount of the optical power transfer from the former to the later can be adjusted by geometrical means, like interaction length and their relative distance. The concept of directional coupling is mainly used for signal multiplexing or coupling into ring resonators, where this sophisticated and stable coupling mechanism is necessary, but it has the disadvantage that their production is technology-intensive and, analogue to the butt-end coupling, the light already needs to be coupled into one of the waveguides beforehand.

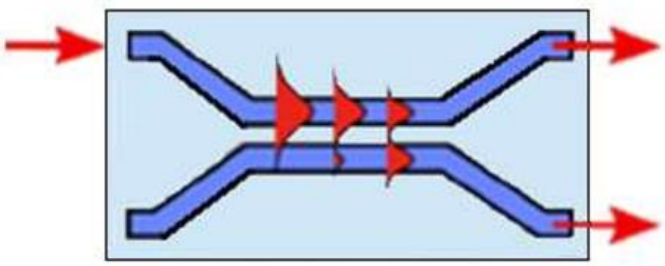

Figure 28: directional coupling [63].

7. Conclusion

In this chapter we have presented mainly, different photonic sensor components, including, light sources, photodetectors and photonic waveguides transducers. Hence, different kinds of light sources and their characteristics are described including, continuous light sources, pseudo monochromatic and monochromatic light sources. Moreover, parameters of diverse photodetectors are introduced comprising, photomultiplier tube, quantum photodetectors and imaging detectors. In the other hand, types of optical waveguides widely used in photonic sensors are designated as well as their sensing principles, containing,

strip waveguide, rib waveguide, slot waveguide and photonic crystal. In addition to that, methods of coupling light into the waveguides are specified, consisting of end-firing coupling, taper coupling, prism, coupling, grating coupling and directional coupling.

References

[1] K. T. V. Grattan and B. T. Meggitt: Optical Fiber Sensor Technology, Volume 4: Chemical and Environmental Sensing. © 1999 Springer Science+Business. Media Dordrecht.
[2] F. D. Leonardis & Passaro, V.M.N: Modeling and Performance of a Guided-Wave Optical Angular Velocity Sensor based on Raman Effect in SOI, *IEEE J. Lightwave Technol*., Vol.25, No.9, (2007), pp. 2352-2366.
[3] V. M. N. Passaro, B. Troia, M. L. Notte and F. D. Leonardis: Chemical Sensors Based on Photonic Structures. Advances in Chemical Sensors, Edited by Prof. Wen Wang, 2012.
[4] Hecht, E: Optics, Addison - Wesley, Bonn (2002).
[5] F. Baldini, A.N. Chester J, Homola and S. Martellucci: Optical-chemical-sensors. *© 2006 Springer.*
[6] Superlum (2009) Online Catalogue of Superlum Diodes, Moscow, Russia, www.superlumdiodes.com.
[7] Thorlabs laser diodes: https://www.thorlabs.com/newgrouppage9.cfm?objectgroup_id=9129.
[8] A. E. Siegman: Lasers, University Science Books (1986).
[9] Robert Allen Meyers (Editor): Encyclopedia of Physical Science and Technology - Aeronautics. Elsevier. 2001.
[10] The SuperK FIANIUM supercontinuum white light lasers. https://www.nktphotonics.com/lasers-fibers/product/superk-fianium-supercontinuum-lasers.
[11] F. P. Miller, A. F. Vandome, J. McBrewster: Photoelectric Effect. VDM Publishing, 2009.
[12] Hakamata , T. (ed.): Photomultiplier Tubes, Basics and Applications, Hamamatsu Photonics K. K. , Shizuoka - Ken, Japan (2006).
[13] David N Amanor, William W Edmonson, Awele I Anyanhun: Visible Light Communication System for Inter-satellite Communication of Small Satellites: Conference: Small Satellites Systems and Services - 4S Symposium, Valletta, Malta, 2016.
[14] Mark Stanford Robbins: Chapter 6 Electron-Multiplying Charge Coupled Devices – EMCCDs. From: Single-Photon Imaging. Seitz**,** Peter**,** Theuwissen, Albert J. P. (Eds.).(2011).
[15] Guttosch, R.J: *Investigation of Color Aliasing of High Spatial Frequencies and Edges for Bayer - Pattern Filters and Foveon X3 ® Direct Image Sensors* , Foveon Inc. , Santa Clara, CA . (2005).
[16] A. A. Rifat, R. Ahmed and B. B. Bhowmik: Chapter 16: SOI Waveguide-Based Biochemical Sensors. From: M. F., *Computational Photonic Sensors.* Mohamed Farhat O. Hameed and S. Obayya (eds.). *© Springer International Publishing AG, part of Springer Nature* 2019.
[17] S. Patrick, M. Hülsemann, B. Dietzel and A. Mai: Optical Biosensors Based on Silicon-On-Insulator Ring Resonators: A Review. J. Molecules. 2019 Feb; 24(3): 519.
[18] P. Bettotti , A. Pitanti, E. Rigo, F. D. Leonardis, V. M. N. Passaro and L. Pavesi: Modeling of Slot Waveguide Sensors Based on Polymeric Materials. *Sensors* 2011, 11, 7327-7340.
[19] C. A. Barrios: Optical Slot-Waveguide Based Biochemical Sensors. *Sensors* 2009, *9*, 4751-4765.
[20] Luff, B.J.; Harris, R.D.; Wilkinson, J.S.; Wilson, R.; Schiffrin, D.J. Integrated-optical directional coupler biosensor.*Opt. Lett.* 1996, *21*, 618–620.
[21] Heideman, R.G.; Kooyman, R.P.H.; Greve, J: Performance of a highly sensitive optical waveguide Mach-Zehnder interferometer immunosensor.*Sens. Actuat. B* 1993, *10*, 209–217.
[22] A. Ymeti, J. Greve, P.V. Lambeck, T.Wink, H. van, Beumer, R. R.Wijn, R. G. Heideman, V. Subramaniam, and J. S. Kanger, "Fast, ultrasensitive virus detection using a young interferometersensor," *Nano Lett.* 7(2), 394–397 (2007).
[23] Armani, A.M.; Kulkarni, E.P.; Fraser, S.E.; Flagan, R.C.; Vahala, K.J. Label-free, single molecule detection with optical microcavities. *Science* 2007, *317*, 783–786.
[24] S. Schmidt, J. Flueckiger, W. Wu, S. M. Grist, S. T. Fard, V. Donzella, P. Khumwan, E. R. Thompson, Q. Wang, P. Kulik, J. Kirk, K. C. Cheung, L. Chrostowski, and D. Ratner: Improving the performance of silicon photonic rings, disks, and bragg gratings for use in label-free biosensing. Proc. SPIE 9166, 91660M (2014).

[25] M. A. Butt, E. S. Kozlova : Optimization of silicon waveguides for gas detection application at mid-IR wavelengths. Proc. SPIE 10717, Saratov Fall Meeting 2017: Laser Physics and Photonics XVIII; and Computational Biophysics and Analysis of Biomedical Data IV, 1071704 (26 April 2018).
[26] C. Ranacher, A. Tortschanoff, C. Consani, M. Moridi, T. Grille and B. Jakoby: Photonic Gas Sensor Using a Silicon Strip Waveguide. J.*Proceedings* 2017, *1*, 547.
[27] C. Ranacher, C. Consani, N. Vollert, A.Tortschanoff, M.Bergmeister, T. Grille, B. Jakoby: Characterization of Evanescent Field Gas Sensor Structures Based on Silicon Photonics. IEEE Photonics Journal. V10, N° 5, 2018.
[28] M. A. Butt, S. A. Degtyarev, S. N. Khonina & N. L. Kazanskiy: An evanescent field absorption gas sensor at mid- IR 3.39 μm wavelength. Journal of Modern Optics. 2017, 1892-1897.
[29] J. Milvich, D. Kohler, W. Freude AND C. Koos: Surface sensing with integrated optical waveguides: A design guideline. OPTICS EXPRESS .Vol. 26, N^{o}. 16, 2018.
[30] N. Eti, I. Mahariq, and H. Kurt: Mode Analysis and Light Confinement of Optical Rib Waveguides in Various Air Slot Configurations. IEEE, 2015 17th International Conference on Transparent Optical Networks (ICTON), 2015.
[31] S. Selvaraja and P. Sethi: Chapter 6: Review on Optical Waveguides. From the Edited Volume : Emerging Waveguide Technology. Edited by Kok Yeow You.. Licensee IntechOpen, 2018.
[32] V. R. Almeida, Q. Xu, C. A. Barrios, and M. Lipson: Guiding and confining light in void nanostructure. *OPTICS LETTERS*. Vol. 29, No. 11. 2004.
[33] Passaro V, La Notte M: Optimizing SOI slot waveguide fabrication tolerances and strip slot coupling for very efficient optical sensing. Sensors 12.3. 2012:2436-2455.
[34] Wang Z, Zhu N, Tang Y, Wosinski L, Dai D, He S. Ultracompact low-loss coupler between strip and slot waveguides. Optics Letters. 2009;34(10):1498-1500.
[35] Passaro, V.M.N.; Dell'Olio, F.; Ciminelli, C.; Armenise, M.N: Efficient chemical sensing by coupled slot SOI waveguides. *Sensors* 2009, *9*, 1012–1032.
[36] Q. Liu et al., "Highly sensitive Mach–Zehnder interferometer biosensor based on silicon nitride slot waveguide," Sens. Actuators B Chem., 188 681 –688 (2013).
[37] Barrios, C.A.; Gylfason, K.B.; Sánchez, B.; Griol, A.; Sohlström, H.; Holgado, M.; Casquel, R. Slot-waveguide biochemical sensor. *Opt. Lett*. 2007, *32*, 3080 3082.
[38] P. H. FU, T. Y. CHIANG, N. C. CHENG, Y. F MA AND D.W. HUANG: Microring resonator composed of vertical slot waveguides with minimum polarization mode dispersion over a wide spectral range. Applied Optics . Vol. 55, N°. 13 / May 1 2016 .
[39] G. Yuan, L. Gao, Y. Chen, X. Liu, J. Wang, Z. Wang: Improvement of optical sensing performances of adouble-slot-waveguide-based ring resonator sensor onsilicon-on-insulator platform. Optik 125 (2014) 850– 854.
[40] S. Patrick: Chapter 10: Silicon-on-Insulator Slot Waveguides: Theory and Applications in Electro-Optics and Optical Sensing. From the Edited Volume : Emerging Waveguide Technology. Edited by Kok Yeow You.. Licensee IntechOpen, 2018.
[41] Dell'Olio, F.; Passaro, V.M.N: Optical sensing by optimized silicon slot waveguides. *Opt. Express* 2007, *15*, 4977–4993.
[42] E. Jordana, J.M. Fedeli, P. Lyan, J.P. Colonna, P. Gautier, N. Daldosso, L. Pavesi, Y. Lebour,P. Pellegrino, B. Garrido, J. Blasco, Deep-UV lithography fabrication of slot waveguides and sandwiched waveguides for nonlinear applications. in 2007 4th IEEE International Conferenceon Group IV Photonics (IEEE, Sept 2007), pp. 1–3.
[43] J. G.W. Pérez, A. H. ElHouati, A. S. Postigo, J. Leuermann, D. X. Xu, P. Cheben, A. O. Moñux, R. Halir and I. M. Fernández: Subwavelength structures for silicon photonics biosensing. Optics and Laser Technology 109 (2019) 437–448.
[44] J. Joannopoulos, S. Johnson, J. Winn, R. Meade: Photonic Crystals: Molding the Flow of Light. By Princeton University Press, 2008.
[45] Giampaolo Pitruzzello and Thomas F. Krauss: Photonic crystal resonances for sensing and imaging. Journal of Optics. Volume 20, Number 7. 2018.
[46] Y. Liu1, H. W. M. Salemink: Photonic crystal-based all-optical on-chip sensor. Optics Express 20(18), 19912-19920 (2012).

[47] C. Y. Chao, L. J. Guo: Design and optimization of microring resonators in biochemical sensing applications, Journal of Lightwave Technology 24, pp. 1395–1402, 2006.
[48] B. Troia, A. Paolicelli, F. D. Leonardis and V. M. N. Passaro: chapter11: Photonic Crystals for Optical Sensing: A Review. From, Advances in Photonic Crystals. Edited by Vittorio M. N. Passaro. 2013.
[49] Krauss, T.F: Slow light in photonic crystal waveguides. *J. Phys. D* 2007, *40*, 2666–2670.
[50] Krauss, T.F. Why do we need slow light? *Nat. Phot.* 2008, *2*, 448–450.
[51] Mark G. Scullion, Thomas F. Krauss and Andrea Di Falco: Slotted Photonic Crystal Sensors. *Sensors* 2013, *13*, 3675-3710.
[52] A. Di Falco, L. O'Faolain, and T. F. Krauss: Dispersion control and slow light in slotted photonic crystal waveguides," *Appl. Phys. Lett.*, vol. 92, p. 83501, 2008.
[53] J. Wu, C. Peng, Y.-P.Li, and Z.-Y. Wang: Light Localization in Slot Photonic Crystal Waveguide," *Chin. Phys. Lett.*, vol. 26, no. 1, p. 14209, 2009.
[54] U. P. Dharanipathy, M. Minkov, M. Tonin, V. Savona, and R. Houdré, "High-Q silicon photonic crystal cavity for enhanced optical nonlinearities," *Appl. Phys. Lett.*, vol. 105, p. 101101, 2014.
[55] H. Takagi, Y. Ota, N. Kumagai, S. Ishida, S. Iwamoto, and Y. Arakawa: High Q H1 photonic crystal nanocavities with efficient vertical emission. *Opt. Express*, vol. 20, no. 27, pp. 28292–28300, 2012.
[56] Jágerská, J.; Zhang, H.; Diao, Z.; Le Thomas, N. &Houdré, R. (2010): Refractive index sensing with an air-slot photonic crystal nanocavity.Optics Letters, (August 2010), 35(15), 2523-2525.
[57] H. Nishihara, M. Haruna and T. Suhara: Optical Integrated Circuits. McGraw Hill, USA (1985).
[58]: E. M. A. Elkaramany, M. Farhat O. Hameed and S. S. A. Obayya : Chapter 1: Introduction to Optical Waveguides in: *Computational Photonic Sensors.* Mohamed Farhat O. Hameed and S. Obayya (eds.). © *Springer International Publishing AG, part of Springer Nature* 2019.
[59]. P.K. Tien, R.J. Martin: Experiments in light waves in a thin, tapered film and a new light wave coupler. Appl. Phys. Lett. 18, 398–401 (1971).
[60] A. Boudrioua: Photonic Waveguides: Theory and Applications, *ISTE Ltd and Wiley* (2009).
[61] Arvind S. Vengurlekar: Polarization dependence of optical properties of metallodielectric gratings with subwavelength grooves in classical and conical mounts. J. Appl. Phys. 104, 023109 (2008).
[62] R. Petit: Electromagnetic Theory of Gratings, *Springer* (1980).
[63] P. Kozma, F. Kehl, E. hrentreich- Förster, C. Stamm, F. F. Bier: Integrated planar optical waveguide interferometer biosensors: a comparative review. *Biosensors and Bioelectronics*.2014.

Chapter2: Sensing Mechanisms and Architectures

1. Introduction

The evolution of science and technology of optical sensors has reached to a point that we can almost measure all physical parameters of interest and a broad range of biological and chemical quantities. The incorporation of optical waveguides in the sensing process adds an interesting twist to this field. For example, the formation of modes in optical waveguides could be exploited for sensing [1]. The optical waveguide sensors, known as Integrated Photonic Sensors, have shown the great advantages compared to the mechanical and electronic sensors such as quick response, high sensitivity, lower power consumption, free from electromagnetic interference, higher multiplexed configuration, small footprint eliminates the necessity of fluorescent labelling process for biosensing and facilities the label-free configuration, which make them promising in the sensing applications in different areas, especially in chemical and bio-chemical detection.[2]. Optical biochemical sensors, which provide detection and quantification of biochemical analytes, have emerged as a field of great interest because of the tremendous needs in early-stage disease diagnosis, pharmaceuticals, security, food quality control and environmental testing [3]. Using integrated photonic technologies, it is possible to fabricate very compact, high performing and low-cost chemical and biochemical sensors [4]. Light propagating through the waveguide is confined by total internal reflection, but 'senses' the medium surrounding the waveguide through the evanescent tails of its electric field. When a light-wave interacts with the biomolecules that are binding to the waveguide surface some of its properties (wavelength, amplitude or polarization) change and by monitoring these changes the analyte can be detected. A variety of optical-sensing mechanisms exist, including luminescence, fluorescence, phosphorescence, absorbance, elastic scattering, Raman scattering, surface-Plasmon resonance, guided-wave resonance, interference, and reflection/ transmission microscopy. The need to measure multiple parameters has been fulfilled by bundling several sensors together for multiplexing. Different configurations have been proposed for these devices, with characteristics suitable for different applications. Such as, integrated optical interferometers, microring resonators, Bragg grating resonators, directional couplers and photonic crystals optical sensors.

In this chapter we will describe in detail principle sensing mechanisms and architectures employed in integrated optical chemical sensors.

2. Optical Sensing Principles

Independently of the sensing region, different sensing mechanisms can be considered to achieve the detection of the analytes or substances of interest. In particular, it is convenient to distinguish different sensing mechanisms usually employed in label-free and labeled optical detection: optical absorption, fluorescence, Raman scattering and detecting of refractive index changes. It is well known that absorbance changes can be detected when light interacts with analytes. Although different wavelengths can be selected, UV-Vis absorption is one of the most employed light-based methods for chemical identification of analytes due to its universal nature, i.e. many analytes can be detected through their absorption changes in this region. Fluorescence is usually complementary to absorption spectroscopy, and it uses a beam of monochromatic light that excites the electrons in the molecules of the compounds and causes them to emit fluorescence, which is registered in the system. In contrast to absorption spectroscopy, this mechanism is much more selective but only valid when molecules present fluorescence properties. Raman spectroscopy is another typical optical sensing mechanism that also employs a monochromatic light from a laser to observe vibrational, rotational, and other low-frequency modes in a system. This sensing mode can provide a fingerprint for each chemical species, being therefore highly selective. Raman spectroscopy is gaining popularity over previous years in conventional analytical instrumentation and also in fiber-based chemical. However, the sensitivity of this mechanism is usually lower than the others due to the weak response of Raman signals. To enhance the signal intensity, surface-enhanced Raman spectroscopy (SERS) can be used [5]. The mechanism of detecting the refractive index changes consist of determining the changes in RI due to the presence of analytes that are in solution or adhered to the surface of the guiding structure in the sensing region. Despite possessing high sensitivity, many strategies can be performed to enhance the sensitivity of these systems. An interesting option for chemical sensing is the use of metallic nanoparticles. Surface plasmon resonance (SPR) based sensors have been widely used over previous years for obtaining an enhanced response to RI changes. The increase in sensitivity is achieved when the frequency of the incident light matches the frequency of the surface electrons of the nanoparticles. In this situation, the incident wavelength is strongly absorbed, creating a transmission dip in the sensor response. This resonant wavelength turns out to be highly sensitive to changes in the external RI and this property makes these systems ideal for chemical sensing applications. In addition, integrated optical sensors designed for the

quantification of angular velocity in gyro systems are based on Sagnac effect, exploited in fiber gyroscopes.

2.1. Optical absorption

Optical absorption is an important operating principle to be exploited in photonic chemical sensors. In fact, the absorption coefficient of the waveguide is a function of the operative wavelength, electronic and photonic properties of the material. In particular, several gases, organic and inorganic molecules are characterized by specific absorption spectra in the near- and mid-infrared (IR) wavelength regions. Hence, the frequency position of vibrational and rotational-vibrational transitions can provide information about the chemical composition of a monitored molecule. This principle is useful for optical sensing, since it is possible to connect the optical signal intensity to the gas or analyte concentration through the Beer-Lambert law:

$$\mathrm{I} = I_0 exp(-\alpha L) \quad (1)$$

Where I and I_0 are the light intensities at the end and at the beginning of waveguide path length, respectively, L is the optical path and αrepresents the absorption coefficient.

For liquids, the absorption coefficient can be expressed as the product of the so called molar absorptivity, $\varepsilon(\lambda)$, and the concentration, c , of the absorbers:

$$\alpha_{liquids}(\lambda) = \varepsilon(\lambda).c \quad (2)$$

The absorption coefficient of gases is usually expressed as the product of absorption cross section, $\sigma(\lambda)$, and the number density, N , of the absorbers:

$$\alpha_{gases}(\lambda) = \sigma(\lambda).N \quad (3)$$

Sensing mechanism consists in monitoring the optical signal intensity changes as a function of the absorption spectrum of the chemical specie to be detected. In particular, as shown in Equations (2, 3), the absorption coefficient α is dependent on I_0 and the concentration. Consequently, at the output of the waveguide it is possible to register sharp peaks in the transmission spectra at specific wavelengths corresponding to the molecule absorption lines. Fig.1, shows Absorption spectra of several gases and liquid solutions [6].

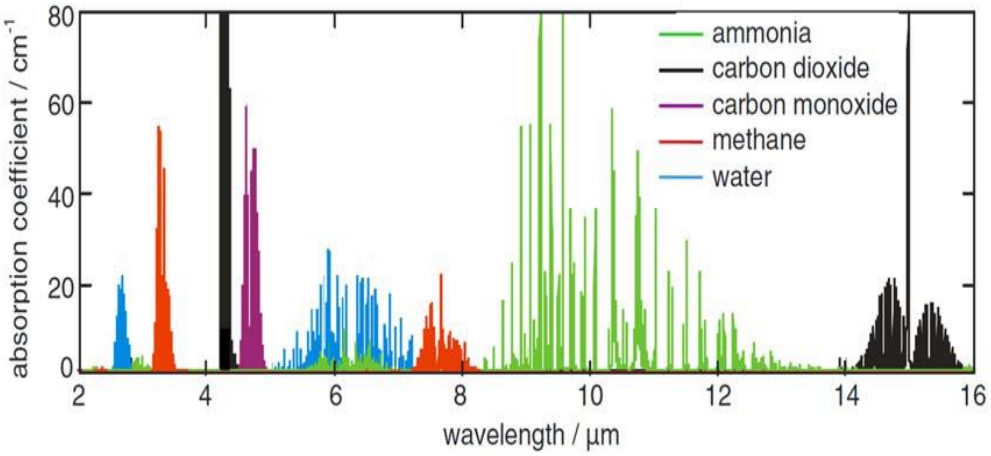

Figure 1: Absorption coefficients of five atmospheric gases at 100% vol concentrations [6].

2.2. Fluorescence

Fluorescence has many practical applications, including mineralogy, gemology, chemical sensors (fluorescence spectroscopy), fluorescent labelling, dyes, biological detectors, and, most commonly, fluorescent lamps. In fluorescence based detection the intensity of the fluorescence indicates the presence of the target molecules as well as their concentration. We can just measure the intrinsic fluorescence of the target analyte or a change in fluorescence of an indicator dye by the analyte, with the determined concentration, referred to as the quenching case [7]. In the latter case, the probe molecule can be immobilized onto the waveguide surface and placed in the evanescent field of the integrated optics sensor [4]. Fluorescence phenomena are related to an energetic transition from an excited state to a lower energy level producing photon emission. Energy levels in an organic molecule are shown by the so called Jablonskii diagram (Fig. 2). In this diagram, S_0,…,S_n and T_1,…, T_m represent the discrete electronic energy levels of a molecule (S_1,…, S_n are excited singlet states and T_1,…, T_m are excited triplet states). At equilibrium, molecules have the lowest possible energy S_0. When a molecule absorbs electromagnetic energy, it moves to an excited energy level (that usually is a singlet state). The energy level reached by the molecule absorbing electromagnetic energy depends on the incident radiation wavelength.

The intensity of the absorption (fraction of ground state molecules promoted to the electronic excited state) depends on the intensity of the excitation radiation (i.e., number of photons) and the probability of the transition with photons of the particular energy used. To characterize the intensity of an absorption band, a term often used is the oscillator strength *f*, which may be defined from the integrated absorption spectrum by the relationship [8].

$$f = 4.315 \times 10^{-19} . \int \varepsilon_v . dv \qquad (4)$$

where ε_υ is the molar extinction coefficient at the frequency υ . A molecule in an excited state tends to reach a lower energy level. Relaxation of the molecule from an excited state may occur in different manner. If relaxation takes place by emission of a photon without any change in spin multiplicity (from a singlet state to another singlet state), the transition is known as fluorescence. Emitted photon wavelength depends on loss energy by the molecule in the relaxation process. In most cases, the emitted light has a longer wavelength, and therefore lower energy, than the absorbed radiation. However, when the absorbed electromagnetic radiation is intense, it is possible for one electron to absorb two photons; this two-photon absorption can lead to emission of radiation having a shorter wavelength than the absorbed radiation. The emitted radiation may also be of the same wavelength as the absorbed radiation, termed "resonance fluorescence".

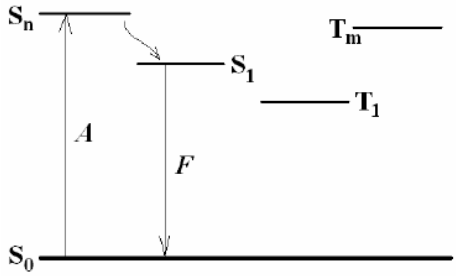

Figure 2: Jablonskii diagram.

The fluorescence quantum efficiency is defined as:

$$\emptyset_F = \frac{\mathrm{N}^0_{L-P}}{\mathrm{N}^0_{P-A}} \qquad (5)$$

Where
N^0_{L-P} is the number of luminescence photons, N^0_{P-A} is the number of absorbed photons.

An example of integrated optical fluorescence multichannel biosensor has been studied in [9].

2.3. Raman scattering

The Raman spectroscopy is one of the widely-used spectroscopic techniques and becoming increasingly important in a broad range of scientific disciplines categorized into distinct application areas such as materials science, biotechnology, pharmaceuticals, forensic science and photonic devices [10, 11]. Scattering of light by molecules can be elastic, *Rayleigh scattering*, or inelastic, *Raman scattering*. In the elastic scattering of light, the photon's energy and the state of the molecule after the scattering events are unchanged. Hence, Rayleigh scattered light does not contain much information on the structure of molecular states [12]. The incoming light photon at ground electronic state jumps up the

molecule to virtual electronic state and then, the outgoing light photon jumps down the molecule to ground electronic state, fig1. In inelastic scattering of light (*Raman scattering*), energy is transferred from the molecule to the photon or vice versa. In fact, incident and scattered photons have different energies and the energy lost by the incident field leads to creation of phonons, which modify the vibrational states of the medium. The inelastic scattering of light is separated into two cases, 'Anti-Stoke Raman scattering' and 'Stoke Raman scattering'. When the scattered photon has less energy than the incident photon, the process is referred to as Raman to Stokes scattering (Fig.3), thus, an incident photon $h\nu_0$ excites a molecular vibration $h\nu_{vib}$ and is then scattered with the corresponding difference in energy $h(\nu_0 - \nu_{vib})$ (red shift). When the scattered photon has more energy than the incident photon, the process is known as Raman to anti-Stokes scattering (Fig.4), thus, the photon acquires vibrational energy from the atoms/molecule and is scattered with a higher energy $h(\nu_0 + \nu_{vib})$ (blue shift). This shift provides information about vibrational, rotational, and other low frequency transitions in molecules. Raman spectroscopy can be used to study solid, liquid, and gaseous samples.

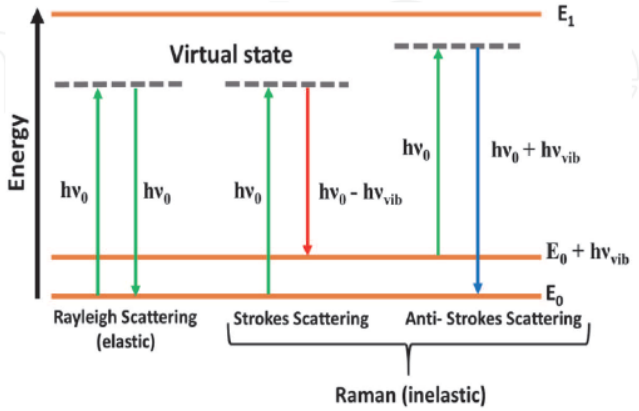

Figure 3: Energy level diagram for Rayleigh and Raman scattering, where $\Delta E = h\nu_{vib}$ represents the difference in vibration energy levels [13].

Light scattering can be measured either by the attenuation of the incident signal as light is scattered away from the beam path, or by measuring the intensity of the light scattered by the sample at a particular angle to the incident beam.

Raman signals are usually weak and require powerful sources and sensitive detectors. Therefore the Raman signal is very low from low concentrations of the analyte or poor Raman scatterers. Surface enhanced Raman spectroscopy (SERS) is all about amplifying Raman signals from molecules, by several orders of magnitude. SERS is a technique where molecules undergo much higher scattering efficiencies when adsorbed on metal colloidal nanoparticles or rough metal surfaces, represents a spectroscopic tool for non-invasive and non-destructive

detection of biochemical and chemical molecules [14]. Furthermore, when the intensity of the incident light is larger than a certain threshold value, variations of the optical properties of the medium lead to an enhancement of scattering process by several orders of magnitude, and photon emission can be stimulated by the presence of another photon, leading to optical gain, that is the Stimulated Raman scattering (SRS).In case of photonic sensors, stimulated emission is a fundamental effect since it can give rise to optical amplification and lasing [15, 16]. An example of optical waveguide Raman sensor is illustrated at fig.4. A laser beam through the aluminum nitride waveguide and illuminated a test sample containing a mixture of organic molecules. Upon examining the scattered light, the researchers found that they could discern each type of molecule within the sample based on the Raman spectra [17].

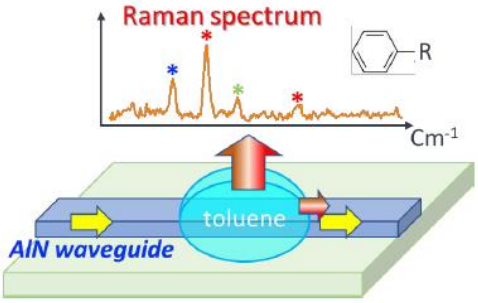

Fig. 4: Aluminum nitride optical waveguide carries the laser beam to a test sample. Scattered light reveals the sample's Raman molecular fingerprint [17].

2.4. Effective index change in guiding structures

Optical sensing of chemical species is typically based on the variation of waveguide optical properties in the presence of some target analyte near the sensor surface. In an optical guiding structure the variation of propagating optical mode effective index can be induced by two different physical phenomena (Fig. 5):

i) the change of thickness (equal to ρ) of an adlayer constituted by adsorbed or bound molecules which are transported (by convection or diffusion) from the gaseous or liquid medium, that serves as waveguide cover medium, to cover medium/guiding film interface.

ii) the change of refractive index n_c of the homogeneous liquid that serves as waveguide cover medium.

The principle of operation of optical guided-wave bio-chemical sensors in case of homogeneous and surface sensing can be described as follows [18]. When light propagates into an optical waveguide, a certain amount of power travels into the core, while the remainder is confined into the cladding and substrate regions. The effective index of the

propagating optical field also depends on the concentration of the specific analyte or gas localized in the cover medium, near the sensor surface. Consequently, the magnitude of the effective index change is related to the percentage of field interacting with the analyte, and thus to the confinement factor in the medium where the analyte is concentrated. Various gases and chemical species can be detected exploiting homogeneous sensing.

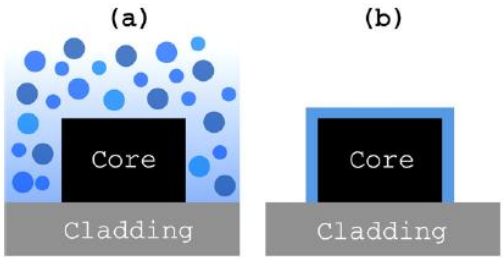

Figure 5: Sensing mechanisms: (a) homogeneous sensing; (b) surface sensing [3].

2.4.1. Homogeneous sensing

Homogeneous sensing (effective index change of guiding structure due to cover medium refractive index change) enables to measure concentration of a wide spectrum of chemical species as glucose or ethanol, usually present in a solution. Moreover, this kind of sensing mechanism allows estimating some gas concentration changes because some polymeric materials have the refractive index sensitive to specific gas concentrations. In all these cases, a chemical analyte concentration change induces the refractive index change in a solid or a liquid material serving as cover medium in the guiding structure. For example, when glucose concentration in an aqueous solution changes, a shift of the solution refractive index is induced. The dimensionless waveguide sensitivity, S_h, can be evaluated as [18]:

$$S_h = \frac{\partial n_{eff}}{\partial n_c}\bigg|_{n_c=n_c^0} = \frac{2n_c^0}{Z_0 P}\iint_C |E(x,y)|^2 dxdy = \frac{2n_c^0 \iint_\infty |E(x,y)|^2 dxdy}{Z_0 P}\Gamma_C' \qquad (6)$$

Where

$$P = \iint_\infty \left[(\vec{E} \times \overrightarrow{H^*} + \vec{E}^* \times \vec{H}).z\right] dxdy \qquad (7)$$

In Equation (1), $Z_0$is the free space impedance, n_{eff} is the effective mode index, ncis the solution refractive index, nc0is the aqueous solution refractive index in absence of the analyte, E and Hare the electric and magnetic field vectors, respectively, and Γ_C' is the optical field intensity confinement factor in the cladding region, defined as follows [18]:

$$\Gamma_C' = \frac{\iint_C |E(x,y)|^2 dxdy}{\iint_\infty |E(x,y)|^2 dxdy} \qquad (8)$$

The integration domain indices, *C* and ∞, stands for cladding cross section and whole computational domain, respectively.

2.4.2. Surface sensing

Unlike homogeneous sensing, surface sensing is based on the selective immobilization of receptor molecules on the functionalized waveguide surface. These molecules form a very thin adlayer on the waveguide surface. Consequently, the increase of themolecular adsorbed layer (adlayer) thickness causes the effective index change Δn_{eff} as [18]:

$$\Delta\, n_{eff} = \frac{n_m^2 - (n_c^0)^2}{Z_0 P} \iint_{\Sigma} |E(x,y)|^2 dxdy \tag{9}$$

Where n_m is the refractive index of the molecular adlayer and Σ represents the region in which the adlayer increases. Similarly to the definition of sensitivity given for homogeneous sensing, it is possible to define the surface waveguide sensitivity as follows [18]:

$$S_h = \left.\frac{\partial n_{eff}}{\partial \rho}\right|_{n_c = n_c^0} \tag{10}$$

Where ρ is the thickness of the molecular adlayer.

2.5. Sagnac Effect

The Sagnac effect has been widely employed in fiber optic based sensor for pressure, temperature and torsion monitoring [19, 20]. Moreover, it is the most exploited operating principle in optical gyroscopes [21]. Sagnac principle, as derivation of the general relativity theory, states that two counter-propagating optical beams propagating in a ring structure change their relative phase if the ring is rotating; thus, it is possible to relate the phase change to the angular speed of the ring. The two optical beams reciprocally interfered and produced a permanent wave, stationary with respect to an external inertial reference system. The stationary wave is composed by nodes and anti-nodes, whether the mirror is rotating or standing. A detector is mounted on the ring framework, solidly rotating with it, so that, during rotation, by counting nodes and anti-nodes of the standing wave through the detector, it is possible to evaluate the angular velocity of the ring. Indeed, the number of nodes is two times the length of the ring divided by the light wavelength. Knowing the number of counted nodes in the time unit through the detector, it is possible to calculate the angular velocity of the ring [22]. The following calculation demonstrates how it is possible to relate the effective path

length to angular velocity about an axis perpendicular to the plane containing the light path. In order to understand the working principle, Let us consider a disk of radius *R* that is rotating clockwise with an angular velocity Ω about an axis perpendicular to the plane of the disk as shown in Figure.6.

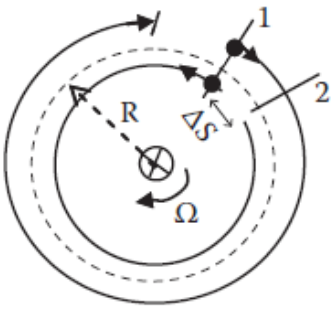

Figure 6: Functional principle of Signac interferometer for rotation sensing [1].

If we assume that, two identical photons are sent *cw* and *ccw* along the circumference starting at an arbitrary location 1. If the initial angular velocity is null, photons that travel at speed of light in vacuum c0 will arrive at starting point 1 after a trip length of 2πR in time t = 2πR/c. If the initial angular velocity is not null, photons that propagate in counter-clockwise direction, called CCW, will arrive at the starting point 2, due to the motion caused by the rotation, after a trip length of LCCW, shorter than 2πR, given by:

$$L_{ccw} = 2\pi R - R\Omega t_{ccw} = c_{ccw} t_{ccw} \qquad (11)$$

Where: RΩ is the tangential angular speed of the ring and t_{ccw} is the time to cover the distance L_{ccw}. In the same way, the clockwise photons, called CW, will arrive at the starting point 2, after a trip length of LCW, longer than 2πR, due to the motion caused by the rotation, given by:

$$L_{cw} = 2\pi R + R\Omega t_{cw} = c_{cw} t_{cw} \qquad (12)$$

t_{cw} is the time to cover the distance L_{cw}. Thus, the net time difference between the two counter propagating beams to cover $L_{cw,ccw}$ would be :

$$\Delta t = \frac{2\pi R}{c_{cw} - R\Omega} - \frac{2\pi R}{c_{cw} + R\Omega} \cong \frac{4\pi R^2}{c^2}\Omega = \frac{4A}{c^2}\Omega \qquad (13)$$

Where the area A enclosed by the path length is πR^2. We have assumed that in vacuum light velocity, *c*ccw = *c*cccw = *c* and the product $R^2\Omega^2$ is negligible relative to c^2. Equivalently, this time difference amounts to a path length difference of :

$$\Delta L = C\Delta t = \frac{4A}{c}\Omega \quad (14)$$

And to this path length difference corresponds a phase shift of:

$$\Delta\varphi = k_0\Delta L = \frac{8\pi A}{c\lambda_0}\Omega \quad (15)$$

3. Integrated optical sensors configurations

The well-developed silicon photonic integrated circuits (PICs) technology is one of the most promising. Due to the compatibility with complementary metal-oxide semiconductor (CMOS) foundry processes, silicon PICs can be manufactured with great efficiency at high volume. Moreover, the high refractive index contrast between silicon and silicon dioxide, or other surrounding media, enables the development of miniaturized compact sensing devices, with the additional possibility of fabricating multiple sensors on one single chip [23]. Among the various optical sensing devices, refractive index sensors have emerged as promising technology in the past few years. Refractive index sensors allow label-free, realtime and direct detection of the molecular interaction at a dielectric interface. In both homogeneous and surface sensing the optical transduction leads to the effective index change. This optical variable has to be transformed into an analytically useful signal. To this purpose, several photonic integrated platforms have been proposed in literature. Hence, numerous silicon photonic sensing devices, such as Mach–Zehnder interferometers (MZIs), microring resonators (MRRs), microdisk resonators, Bragg grating resonators, directional Couplers and photonic crystals (PhCs) have been developed over the past decades for biosensing applications. In particular, it is possible to distinguish between two different types of optical readout: the intensity and wavelength readout (power and wavelength interrogation, respectively). For example, photonic chemical sensors based on optical absorption are characterized by intrinsic intensity readout, because the change of the absorption coefficient is directly linked to the output optical intensity, according to the Beer-Lambert law [24]. However, Wavelength (or phase) interrogation and intensity interrogation are two common interrogation configurations applied to evanescent field biosensors such as Surface Plasmon Resonance (SPR) or planar waveguide based sensors.

3.1. Integrated optical interferometers

In a conventional interferometric biosensor, the guided light is split by a Y-junction into two single-mode waveguide paths, one containing the sample, which is regarded as a

sensing arm, and the other is used as a reference arm. The evanescent field of the sensing arm interacts with the sample and senses the RI change at the surface, resulting in an optical phase shift depending on the sensing arm effective index, *i.e.*, analyte concentration. After a certain distance, the beams recombine again and cause a constructive or destructive interference at the output. where the intensity modulation corresponds to the RI difference between sample and reference arms. Two standard configurations exist for interferometers integrated on a chip: the Mach–Zehnder interferometer (MZI) and the Young interferometer (YI), which is similar but out-couples the light in both arms allowing the light to interfere in free space, instead of using a junction on-chip.

3.1.1. Mach–Zehnder interferometers

A typical MZI-based sensing system only requires afixed-wavelength laser source and a PD/camera for data readout. Many types of Mach-Zehnder interferometers can exist according to the type of waveguides constituting the tow arms, stripe waveguide, rib waveguide, buried waveguide, slot waveguide, ect. In the case of a MZI sensor fig.7**,** if any optical phase delay is applied to the guided mode in the sensing arm, light will be combined at the output Y-branch exhibiting an output optical power equal to the input optical power. If an optical phase delay is applied in the sensing arm, the optical output power will be different from the input one. According to Eq. 16, the output intensity (I_{out}) is a periodically oscillating function of the phase change difference ($\Delta\varphi$) of the beams from two arms:

$$I_{out} = I_{in} \cos\left(\frac{\Delta\varphi}{2}\right)^2 \quad (16)$$

The phase difference caused by the variation of the effective index (Δn_{eff}) at the wavelength λ is calculated as:

$$\Delta\varphi = \frac{2\pi}{\lambda}\Delta n_{eff} L \quad (17)$$

Where: L is the effective detection length of the sensing arm. The sensitivity S of the Mach–Zehnder interferometer sensor can be expressed for homogeneous sensing as follows:

$$S = \frac{2\pi L}{\lambda}\left(\frac{\partial n_{eff}}{\partial n_c}\right) \quad (18)$$

However, for surface sensing, S is given by

$$S = \frac{2\pi L}{\lambda}\left(\frac{\partial n_{eff}}{\partial \rho}\right) \quad (19)$$

Where n_{eff} is the effective index of the propagating supported mode through the waveguide, ncis the cladding medium refractive index, and ρ is the thickness of molecular layer deposited

on guiding cover medium interface. The sensitivity of Mach–Zehnder-based sensor relies on sensing arm length, L.

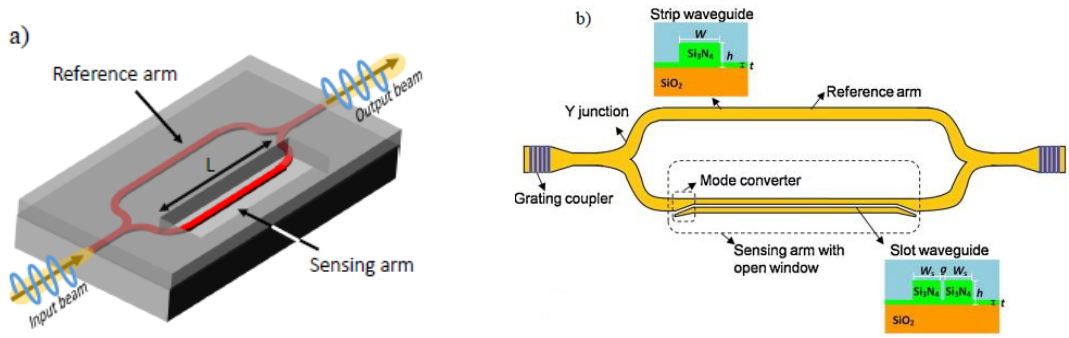

Figure.7: a) Interferometric PIC sensors. A standard MZI configuration. Light enters the interferometers on the left and is split into the sensing and reference arms, the arms are recombined in a Y-junction and the interference measured in the output is used to quantify the presence of an analyte in the sensing arm, from [25]. b) Highly sensitive Mach–Zehnder interferometer biosensor based on silicon nitride slot waveguide [26].

In the slot design, the sensing arm is split into two waveguides separated by a nanometer-scale, low-refractive index "slot" region for light confinement. This design greatly enhances the light–matter interaction yielding higher sensitivity to the refractive index of the analyte [26].

3.1.2. The BiMW configuration

Bimodal waveguides (BiMW) has been explored to improve sensor accuracy. Light from a coherent source in TE polarization is coupled into a ridge waveguide supporting a single transversal mode. After some distance this mode is coupled into another waveguide which supports two transversal modes. Due to the vertical asymmetry of the junction, the fundamental mode of the first waveguide splits in two, the fundamental and the first order mode, which are propagating until the output of the chip. The fundamental mode would act as the reference wave being only weakly influenced by the bio-interaction, while the first order mode will be strongly influenced by the refractive index changes occurring within the evanescent field [27].The modes propagate with different velocities and create an interference pattern at the exit, which intensity distribution depends on the physical parameters of the structure (width, thickness, rib height) and, in particular, on the refractive index of the cladding layer through the interaction with the evanescent field. This intensity distribution is monitored off chip using a photodetector array [28].

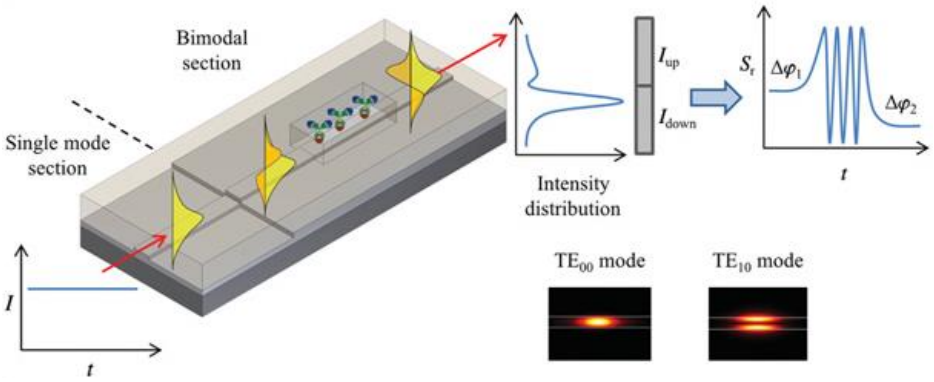

Figure .8: Working principle of the BiMW interferometer, highlighting the TE_{00} and TE_{10} mode profiles as well as the output detection scheme via a two-sectional photodiode [29], [28].

3.1.3. Young Interferometer

In the Young interferometer, a Y-junction splits the input waveguide into a sensing arm and a reference arm but, contrary to the MZI, there is no second Y-junction at the output. As depicted in Figure.9, the interference pattern is produced off-chip by projecting the output light from both arms onto a screen or CCD camera. The phase difference between the two interfering beams is given by:

$$\Delta\varphi(t) = \frac{2\pi}{\lambda}\left[\frac{d.x}{f} - \left(n_{eff,s}(t) - n_{eff,R}\right).L\right] \qquad (20)$$

Where: *d* is the distance between the two arms, *f* the distance between the sensor output and the camera, and *x* the position of the interference pattern on the screen. When a biomolecular interaction takes place in the sensing area, the $\Delta\varphi$ variation is deduced from the shift of the interference pattern on the screen.

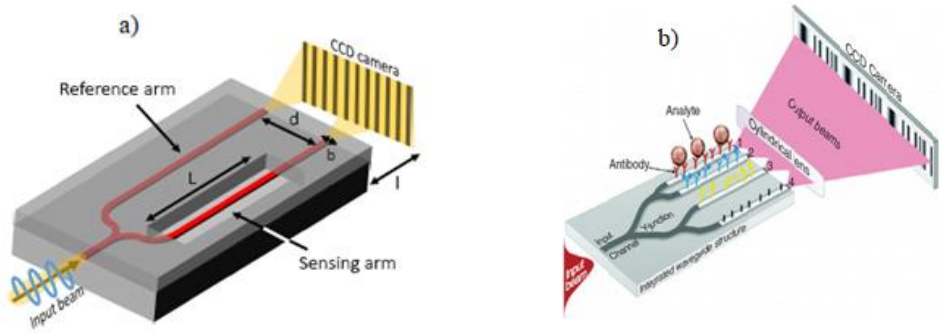

Figure 9: a) In the YI configuration, the light is not coupled, but is out coupled from sensing and reference arms and interfered in free space to create interference pattern. The presence of an analyte and its concentration is identified based on the interference pattern [25]. b) Four-channel Young interferometer [30].

Four-channel Young interferometer based on Si3N4/SiO2waveguides was developed and integrated with microfluidics to have independent measurements in each sensing arm (Fig. 9.b). This system is highly sensitive and has one of the lowest LODs reported until now. An example of a bioanalytical application of this device is the specific detection of herpes simplex virus 1 (HSV-1) [30].

3.1.4. Interferometry biosensor based on planar optical waveguide

Planar waveguides are integrated with diffraction gratings for in- and out-coupling of light but both the split and the recombination of the sensing and reference beams are produced off-chip, fig.10. The core of the system is a sensor chip consisting of a planar optical waveguide. Light coupled into the 154 nm thick Ta_2O_5 waveguide propagates with monomode behavior in the direction perpendicular to the propagation direction. The part of the electromagnetic field propagating above the waveguide is called evanescent field and is exponentially decaying with the distance from the waveguide. The interaction of the sample with the evanescent field is described in terms of an effective refractive index. The effective refractive index depends on the refractive indices of the waveguide, the glass substrate, the cover fluid and, in case of an adsorption of biomolecules, the refractive index of the adsorbate layer. A single channel evanescent field sensor is therefore sensitive both to bulk refractive index changes and to changes in surface coverage due to adsorption or binding of molecules [31].

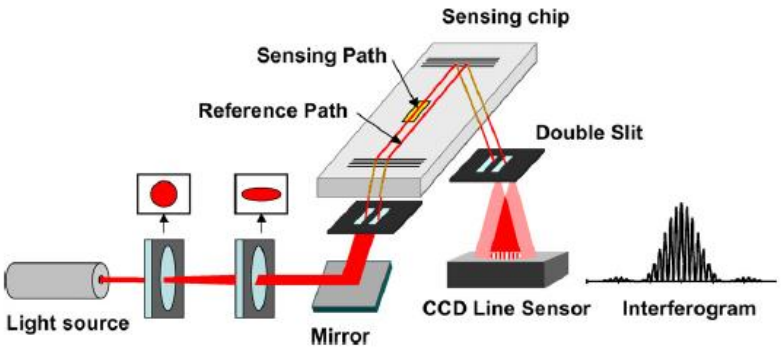

Figure 10: Optical setup of the interferometric biosensor system. Two beams of a superluminescent diode are coupled into a waveguide sensing chip, as sensing and reference branch. After outcoupling by a second grating they pass a double slit and overlap to an interference pattern that is recorded by a CCD sensor [31].

3.1.5. The birefringent waveguide biosensor

The birefringent waveguide biosensor is based on the interference between two orthogonally polarized beams (TE and TM) propagating in a straight birefringent waveguide. A birefringent waveguide biosensor with an integrated microfluidic channel has been implemented for the detection of pathogenic bacteria such as *Listeria monocytogenes* in food [32]. The waveguide biosensor system consists of a waveguide sensor platform where an antibody–antigen reaction occurs and a birefringence measurement system for signal detection and analysis. Fig. 11(a) shows the concept of utilizing an antigen–antibody reaction on the exposed core surface for biomolecular detection. When the antibody–antigen reaction occurs under the introduction of incident light, the difference in refractive index between the core and the sensing surface increases. This refractive index change in the waveguide in turn causes a change in birefringence between the two orthogonal polarizations (transverse electric, TE, and transverse magnetic, TM) induced from the light source. A phase difference between the two polarizations is converted into a phase delay by the birefringence measurement system. Continuous real-time monitoring of the phase delay allows us to determine the amount of antibody–antigen reaction taking place. The Phase differences for various injection amounts of L. monocytogenes is presented in Fig.11 b). Specificity was demonstrated as well as the capabilities of the device to perform detection in milk. However, this device is not extremely sensitive as the lowest detected concentration was of 10^6 CFU mL^{-1} in buffer *(CFU stands for colony-forming unit).*

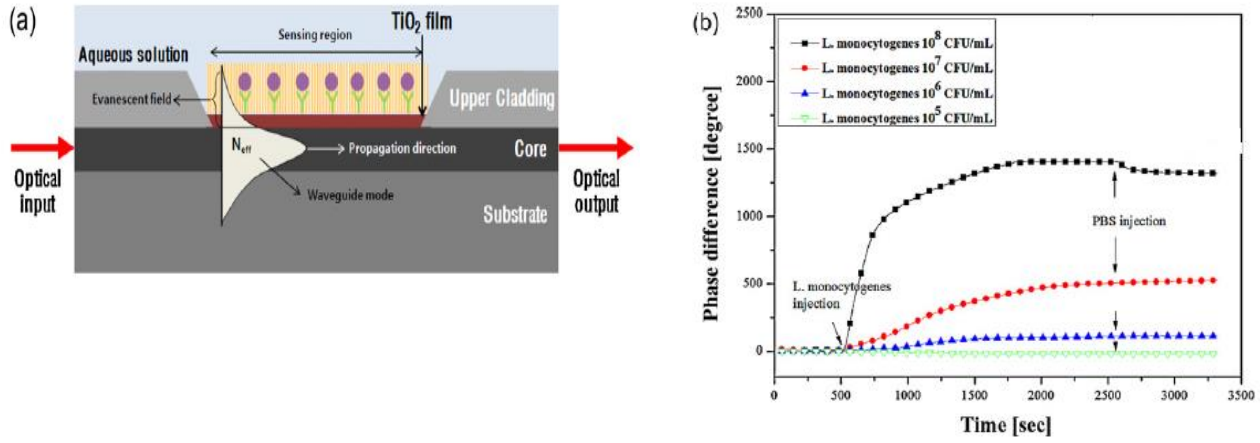

Figure.11: (a) Cross section of the waveguide sensor platform for antigen–antibody detection, consisting of a core and cladding with a microfluidic channel. TiO_2 film with a high refractive index is deposited on the core. (b) phase difference comparison between concentrations of 108, 107, 106, and 105 CFU/mL of L monocytogenes [32].

3.2. Grating-Coupler Sensors

A Bragg grating is characterised by a periodic perturbation of the waveguide refractive index along the propagating direction. Bragg gratings are usually employed to couple light into or out of an optical waveguide. More recent application of Bragg gratings is the realization of integrated optical sensors based on those structures. A propagation of the wave within the waveguide is observed, if the coupling condition (21) is fulfilled. The resonant coupling between the guided mode and a diffraction order of the grating is governed by the phase-matching condition as

$$n_{\text{eff}} = \sin\theta + m\frac{\lambda}{\Lambda} \qquad (21)$$

Where: θ is the incident angle of light, Λ the grating period, and m the diffraction order. To fulfill Eq. (21), submicronic grating periods are requested. As can be deduced from this equation, a variation of the effective refractive index, with the presence of different ambient gases or biochemical molecules, will affect the resonance angle or the resonance wavelength. Therefore, grating-based biosensors can be achieved with two optical configurations: the angular and the wavelength interrogation. Depending on the configuration, the grating can be defined at the interface core/substrate, at the interface core/cladding or at both interfaces.

3.2.1. Grating-based biosensors with angular configuration

In the angular approach, a scan of the resonance angle using a laser source of fixed wavelength is employed. Light is coupled into the waveguide via an input grating and then propagated until the output of the waveguide where it was detected by a standard photodetector. The sample can be rotated on a goniometer to find the coupling angle and to determine the shift of the resonance angle induced by the bioreactions occurring in the sensing area, fig.12. Optical sensors based on output grating couplers work in the opposite fashion. Light propagating in the waveguide is coupled out of the waveguide by means of a diffraction grating. The out coupling angle is proportional to the propagation constant of the waveguide mode. Changes in the refractive index at the sensor surface alter the propagation constant of the mode resulting in a change in the outcoupling angle.fig13. Here, light is coupled into the horizontally positioned waveguide and a position-sensitive photodetector, e.g., a CCD line sensor, monitors the coupling angle depending on the layer thickness or the effective refractive index, respectively. The detected signal then represents the position of the outcoupled light beam on the detector [33]. This configuration is employed in the Optical

Waveguide Light mode Spectroscopy (OWLS) configuration, which has been used in awide range of applications. Among them, the detection of Legionella pneumophila contamination in water samples [34] or, more recently, the detection of vitellogenin, a biomarker for assessing exposure to environmental endocrine disruptors [35].

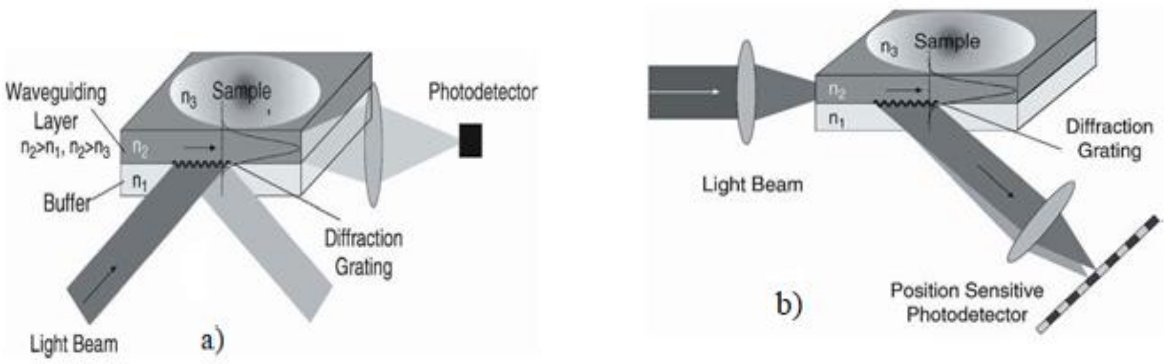

Figure 12: Input grating coupler sensor and Output grating coupler sensor [7].

Grating-based biosensors have also been developed using the grating as a reflector instead of a coupler, Fig.13 (a). In this case, light from a tunable laser is coupled into the waveguide by end-fire and a resonance wavelength is reflected back after interaction with the grating. A bioreaction on the grating surface results in a wavelength shift in the spectrum, Fig. 13. (b). An experimental sensitivity of 140 nm per RIU, corresponding to an LOD of 6 $\times 10^{-6}$ RIU, has been demonstrated using $Si/SiO_2/Si_3N_4$ waveguides [36]. Direct and label-free detection of the PepN enzyme was achieved with an experimental resolution of about 4 pm adlayer growth which is equivalent to the capture of 3 $\times 10^{9}$ mol cm^{-2}.

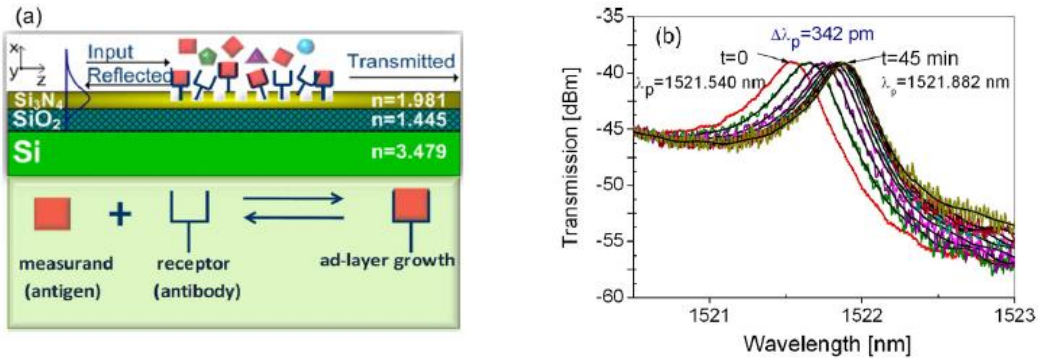

Figure 13: (a) Schematic 2D cross-section of the grating-based biosensor wavelength interrogation with grating as reflector for direct, label-free surface biosensing. (b) Transmission spectra of the label-free protein sensing of grating-based biosensor wavelength interrogation with grating as reflector [36].

3.2.2. Grating-based biosensors with the wavelength configuration

The wavelength-interrogated approach requires a tunable laser to scan the resonance wavelength at a fixed angle of incidence. The operating principle of the input grating coupler is shown in Fig. 14[37]. A collimated laser beam is incident at fixed angle θ onto a waveguide deposited on a transparent substrate. When the coupling conditions are satisfied, the light beam is coupled into the waveguide, propagates, and a detector is placed at the waveguide output to monitor the intensity of light as a function of the input laser wavelength. When the grating is exposed to the analytes, adsorption causes changes in the refractive index at the grating surface and results in a shift in the laser beam coupling conditions, detected as angular (θ) shift or wavelength (λ) shift.

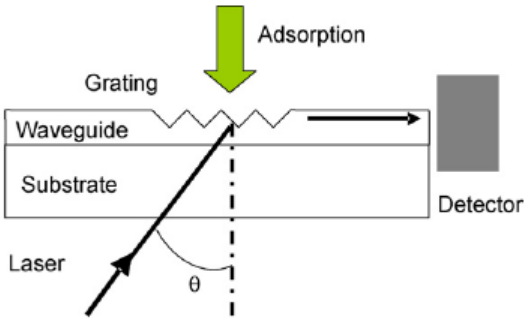

Figure 14: Schematic of the sensing principle of the input grating coupler with the wavelength-interrogated approach [37].

The Wavelength Interrogation Optical Sensor WIOS technology has been used for the detection of sulfonamides antibiotics in milk, but including an additional amplification step with a secondary antibody [38]. In the field of genomics, it has been employed to study the kinetics of covalent immobilizationof double-stranded oligonucleotides to evaluate the optimal hybridization efficiency after sequential denaturation [39].

3.3. Evanescent-Wave Sensors

Photonic-based biochemical sensors use light that is confined in its waveguide.As the light is reflected from the interface back into the waveguide, part of the electromagnetic field called evanescent field, extends beyond the surface into the external medium, where it can interact with analytes—this interaction is the fundamental mechanism of Photonic-based biochemical sensing.The evanescent field that is exponentially decays with distance, dependent on material properties and the physical design of the sensor(i.e., the length of the devices, the strength of the evanescent field, and its overlap with the optical cross section of

the analyte) [40]. In fact, the biochemical analytes perturb the evanescent field and modify the cladding refractive index and/or induce an additional optical absorption. The change in the cladding refractive index will primarily cause the shift of resonant peaks in photonic resonators, while the additional optical absorption reduces the light transmission intensity in waveguides [41].Accordingly, photonic biochemical sensors can be generally classified into RI-based sensors and absorption-based sensors.

3.3.1. Refractive index -based sensors

One major drawback of RI-based biochemical sensors is the lack of selectivity. Therefore, an additional process of sensor surface functionalization with specific receptors is required in order to realize selective adsorption. Hence, the target analytes can be identified, as illustrated in Fig.15.These sensors operate at a single wavelength that is chosen based on the absorption of the analyte. For applications requiring the analysis of a liquid sample (bulk or homogenous sensing), the sensing signal can be employed to determine the RI of the sample as compared to a reference sample. For biomolecule detection applications (surface sensing), the specific capture of biomolecules at the sensor surface results in a local change in RI which produces a sensing signal that enables quantification of the biomolecules in the sample. Hence, according to the different ways the target molecules interact with the sensors, two definitions for sensitivity are used in biochemical sensing applications. One is the bulk sensitivity (S_{bulk}), the other one is the surface sensitivity (S_{surf}). For RI-based sensors, the bulk sensitivity is defined as the slope of wavelength (or phase) shift versus bulk refractive index unit (RIU) change:

$$S_{bulk} = \frac{\Delta\lambda(\Delta\phi)}{\Delta n_{sample}} \tag{22}$$

The surface sensitivity is defined slightly differently by replacing the RI of the sample (n_{sample}) with the thickness of the adlayer on the sensor surface (t_{adlayer}):

$$S_{surf} = \frac{\Delta\lambda(\Delta\phi)}{\Delta t_{adlayer}} \tag{23}$$

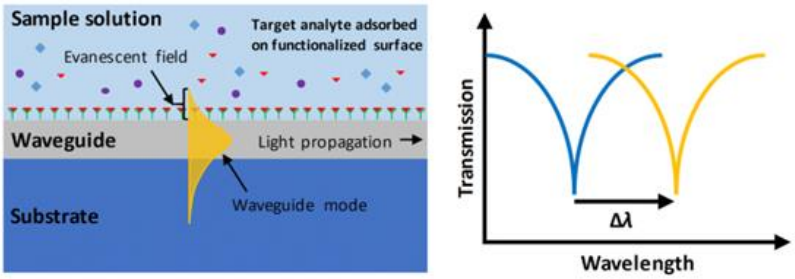

Figure 15: Schematic illustration of the sensing mechanisms of the RI-based sensor with its surface functionalized to selectively adsorb analyte. The optical signal change in the sensor, e.g., the resonant wavelength shift in a resonator, is known to be induced by the absorbed analyte [41].

3.3.2. Absorption-based sensors

Absorption-based sensors do not use a chemically specific receptor to capture a known analyte, in contrast to RI-based sensors**. I**nstead, the evanescent field of the optical mode probe the vibrational transitions of the surrounding environment directly**.** Optical absorption of the vibrational transitions, in accordance with the Beer–Lambert law, provides an absorption spectrum that can be used for spectroscopic identification; Fig.16.The output spectrum may have multiple features, which need to be deconvolved with known analytes in the environment in order to determine their concentrations. Measuring the IR absorption spectrum requires a broadband or tunable source, and Raman spectroscopy uses a monochromatic source to excite molecular vibrational transitions and identify them in a broadband optical output. This type of sensing is well-suited for environmental and air-quality monitoring, greenhouse-gas sensing, medical diagnostics, and standoff detection for chemical, biological, radiological, nuclear, and explosive (CBRNE) agents [40, 42].

For absorption-based sensors, the sensitivity refers to bulk sensitivity in most cases as no surface functionalization is implemented, and is defined as the change in absorbance R (or transmittance T) divided by the change in sample concentration C:

$$S_{bulk} = \frac{\Delta R(\Delta T)}{\Delta C_{sample}} \qquad (24)$$

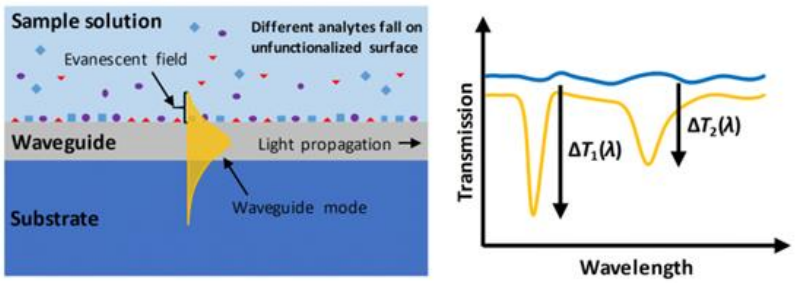

Figure 16: Schematic illustration of the absorption-based sensor without surface functionalization. The different analytes adsorbed on the sensor surface are distinguished by their induced characteristic absorption peaks at different wavelengths on the sensor transmission spectrum [41].

3.4. Surface Plasmon Resonance Sensors

Surface plasmon resonance (SPR) is a surface optical technique that measures minute changes in refractive index at a metal-coated surface. It has become increasingly popular in the study of biological and chemical analytes because of its label-free measurement feature. In addition, SPR allows for both quantitative and qualitative estimation of binding interactions in real time, making it ideally suited for probing weak interactions that are often difficult to study with other methods. Despite the obvious advantages of a label-free technique, SPR is a non selective detection because anything that binds to the surface will change the refractive index. Therefore, reproducible and well-understood surface chemistry to create a selective sensing interface is an important research area for understanding the nature of biological interactions [33]. SPR has applications in drug development, medical diagnostics, environmental monitoring, and food and water safety [43]. Surface plasmons (SPs) are surface electromagnetic waves that propagate parallel along a metal/dielectric interface. For this phenomenon to occur, the real part of the dielectric constant of the metal must be negative, and its magnitude must be greater than that of the dielectric. Thus, only certain metals such as gold, silver, and aluminum are usually used for SPR measurements. In SPR technique, a transverse magnetic-polarized light causes the excitation of oscillations of electron density at the metal-dielectric interface [44]. This oscillation of electrons produces a wave known as surface plasmon wave (SPW). When the incident light and the surface plasmon wave are matched, a conversion of light energy to surface plasmons occurs (resonance).the excitation of SPW corresponds to an attenuation of the reflected light intensity, which results in a sharp dip in the reflected light intensity. The incident angle, wavelength of the light, and the dielectric constant for both metal and substrate are the

parameters that affect the resonance condition. The sensing mechanism depends on the monitoring of the incident angle when the wavelength remains constant. The sharp dip occurs at the resonance angle. Similarly, the sensing mechanism can be through the monitoring of the wavelength while the incident angle remains constant. The resonance occurs at a specific wavelength. The dielectric media refractive index affects both the resonance incident angle and the resonance wavelength. So any variation in such refractive index will change the resonance wavelength or the resonance incident angle [2]. The Kretschmann geometry, depicted in Fig. 17(a), is the most common method for SPR. In this geometry, a monochromatic light wave passes through a high refractive index prism and is reflected at the prism-metal layer interface generating an evanescent wave penetrating the metal layer. For a certain angle of incidence, the component of the wave vector of the incident light parallel to the metal surface matches that of the surface plasmon and coupling between the light wave and the surface plasmon occurs:

$$\beta_{sp} = \sin\theta \frac{2\pi}{\lambda} n_{\mathrm{p}} \qquad (25)$$

Where λ is the incident wavelength, n_p is the prism refractive index, θis the incident angle, and β_{sp} is the propagation constant of the SPW. This coupling results in absorption of light and a characteristic dip in the angular spectrum of reflected light, Fig 17 (b). A change in the refractive index at the surface of the metal film gives rise to a change in the propagation constant of a surface plasmon. This change results in a change in the resonant angle and a shift in the angular position of the SPR dip.

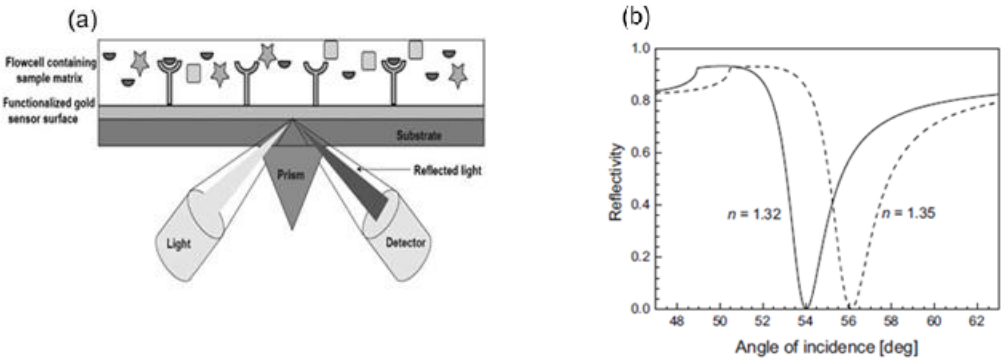

Figure 17: (a) Kretschmann configuration in SPR sensor depicting the conversion of energy from light waves to surface plasmons via a gold/dielectric interface [45]. (b) Reflectivity for the geometry Kretschmann, consisting of an SF14 glass prism, 50 nm thick gold layer, and a dielectric, as a function of the angle of incidence for two different refractive indices of the dielectric; wavelength = 682 nm. [7].

3.5. Ring Resonator Optical Sensors

3.5.1. Straight waveguide coupled to a ring resonator

Integrated optical resonant microcavities have been widely proposed for the realization of photonic chemical sensors with high sensitivity and low detection limits. In particular, resonant microcavities characterized by high quality factors Q and low level of optical noise, present some unique advantages with respect to other technological platforms. In particular, in resonant microcavities the interaction length is greater than the physical length of the device. Since, light propagates in multiple round trips into the resonant cavity. The sensing principle of a ring resonator optical sensor consists in monitoring the resonance wavelength shift as a consequence of the variations of the waveguide refractive index in the presence of the substance to be detected. The typical structure of optical microcavities includes a straight waveguide coupled to a ring resonator fig.18. Resonance wavelengths are determined as a function of the modal effective index of the optical mode propagating into the cavity. Consequently, by selecting the operative wavelength as one of the resonant wavelengths characterizing the ring resonator spectrum, variations of optical properties of the cover medium will induce an operating resonant wavelength shift $\Delta\boldsymbol{\lambda}$, small changes in refractive indexΔn_s of the solution can be determined. The wavelength shift can be calculated by [46]:

$$\Delta\lambda = \frac{\lambda_{res}}{n_g}.\Delta n_s.\Gamma_{clad} \qquad (26)$$

Where: Γ_{clad} is the field confinement factor in the cladding. Δn_s is the refractive index change, n_g is the group index and $\boldsymbol{\lambda}_{res}$ is the resonant wavelength of ring resonator.

$$n_g = n_{eff} - \lambda_0 \frac{\delta n_{eff}}{\delta\lambda} \qquad (27)$$

$$\lambda_0 = \frac{2\pi r n_{eff}}{m} \qquad (28)$$

Where: r is the ring radius of the ring, n_{eff} is the mode effective index and m is an integer.

The sensitivity S_{SR} of sensors based on single ring resonators can be connected to the sensitivity of the waveguide S_w (homogeneous S_h or surface S_s sensitivities) as:

$$S_{SR} = \mathrm{FSR}_S \frac{\lambda S_w}{n_g} \qquad (29)$$

Where FSR_s is the free spectral range of the sensing cavity (the period of the resonant spectrum) and n_g is the group index.

The effective length (L_{eff}) is related to the Q factor by:

$$L_{eff} = Q\frac{\lambda}{2\pi n} \qquad (30)$$

Where: λ is the wavelength and n the refractive index of the ring resonator. High Q factors indicate low optical losses and long photon lifetimes, which is translated into narrow line widths and high peak resolution (which means a high sensitivity) [48].

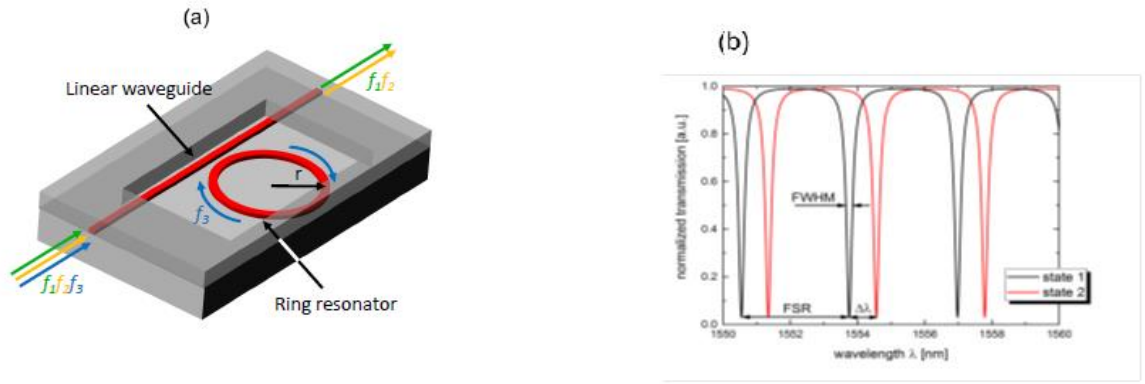

Figure 18: (a) Schematic of a ring resonator with one coupled bus waveguide. [25]. (b) Schematic of the sensor principle: The resonant peak is shifted due to a refractive index change in the cladding material. The resonance condition is changed. Wavelength shift $\Delta\boldsymbol{\lambda}$ is correlated to the analyte concentration [46]. The resonant wavelength can be calculated as [47].

3.5.2. Two cascaded ring resonators and the Vernier effect:

A relevant improvement of chemical sensor based on resonant cavities is the excitation of the Vernier effect, which significantly modifies the shape and the condition for resonance [49-52]. Photonic sensors based on such an effect are usually made by two cascaded ring resonators, figure 19(a). The former, referred to be the resonator acting as a filter, is covered by a proper cladding medium, while the latter, *i.e.*, the resonator acting as a sensor, is exposed to the analyte. The overall wavelength shift, the Low Detection Limit LOD and the sensitivity are strongly enhancing by the excitation of the Vernier effect, so that:

$$S_{DR} = \frac{FSR_S FSR_F}{|FSR_S - FSR_F|} \frac{\lambda S_w}{n_g} \qquad (31)$$

Where: FSR_F is the free spectral range of the filtering ring resonator [25]. Due to the different FSRs between the sensing and reference (filter) devices, a spectral response with a major peak plus some minor peaks will be presented at the output. As shown in Figure 19(b), the major peaks are located at the overlapped peaks of these devices, showing a Vernier FSR of the least common multiple of total FSR values, and the height of major peaks is determined by the

amount of overlap. When the RI above the sensing device changes, the major peak shifts ($\Delta\boldsymbol{\lambda}_{\max}$) discretely which equals to an integer multiple of the reference device's FSR [53]:

$$\Delta\lambda_{max} = \mathrm{m}\Delta\lambda_{FSR}^{ref} \tag{32}$$

In this way, the Vernier effect cascaded sensor system yields an ultra-high sensitivity which is given by Dai [53]:

$$\mathrm{S} = \left(\lambda_{maj}/n_{eff}\right)\left[\frac{\Delta\lambda_{FSR}^{ref}}{\left(\Delta\lambda_{FSR}^{ref}-\Delta\lambda_{FSR}^{sen}\right)}\right] = \mathrm{MS}_0 \tag{33}$$

Where λ_{maj} is the wavelength of the major peak, $\Delta\lambda_{FSR}^{ref}$ and $\Delta\lambda_{FSR}^{sen}$are the FSRs of reference and sensingdevices respectively, and $S_0$is the actual sensitivity of the single sensing device. Thus, the sensitivity of the optical sensor based on Vernier effect cascaded devices is M times improved than that of a single device, without requiring a narrow line width tunable light source or a high-resolution readout system [25].

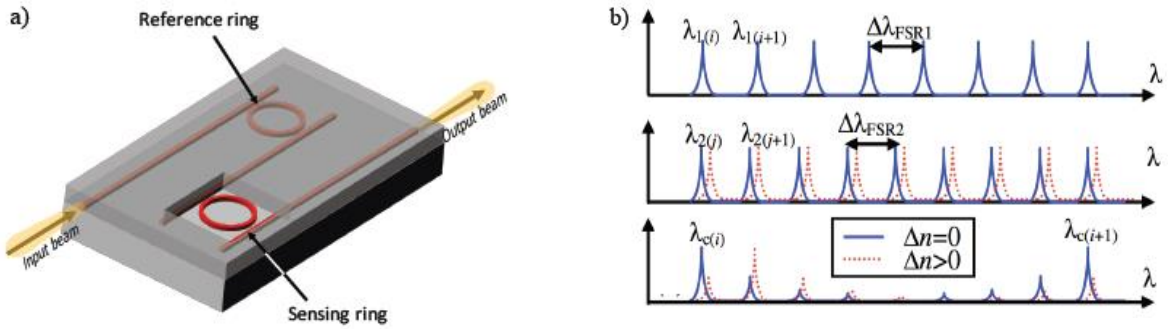

Figure 19: (**a**) Illustration of the Vernier effect sensing system consisting of two cascaded MRRs with different FSRs. The sensing ring is exposed to RI changes in its environment, while the reference ring iscovered by the cladding. (b) Illustrations of calculated transmission spectra of the reference device(D*l*FSR1), sensing device (D*l*FSR2), and cascaded system, respectively. Red-dashed lines represent transmission spectra after an RI change above the sensing device, showing an amplified wavelength shift in the cascaded system.[25].

3.5.3. Silicon slotted microring resonator sensor

Common silicon ring resonators are based on strip-waveguides, where the light is highly confined in the high-index silicon and exhibits low optical losses. This leads to a relatively low light-analyte-interaction. Ring resonators based on slot waveguides exhibit ultra-high performance for photonic bio-chemical sensing. In fact, by using slot waveguides it is possible to confine an extremely high optical field in the low refractive index region called

"slot region", where the chemical solution or gas will be detected [54]. by combining the enhanced light-matter interaction of the slot waveguide with the refractive index sensitivity of the microring resonator, [55] demonstrate the ability to detect small changes in the refractive index of surrounding medium. The transmission spectrum for the microring resonator, fig.21(a), in air (solid) and acetylene gas (dashed) at room temperature and atmospheric pressure show a resonance shift of approximately 0.2 nm, Fig.21(b).

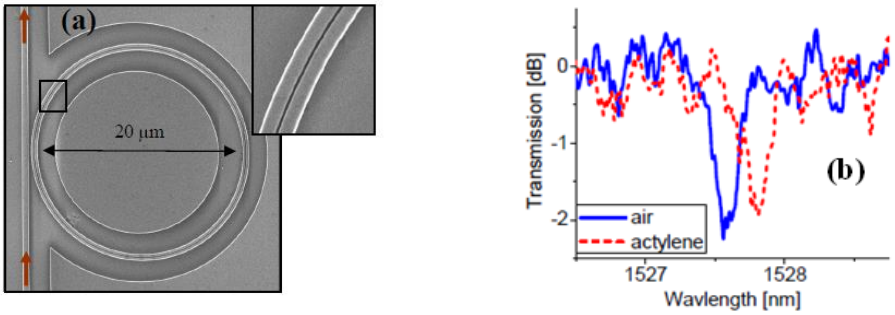

Figure 20: (a) SEM image of a silicon slotted microring resonator like the one used in our experiment. Inset shows the slot waveguide in the ring. (b) Transmission spectra for the microring resonator in the presence of air (solid) and acetylene gas (dotted) at room temperature and atmospheric pressure. The shift in resonance is due to the difference in refractive index between air and acetylene gas [55].

3.6. Photonic Sensors Based on Directional Couplers

Photonic sensors based on directional couplers, as shown in figure 21 a), are constituted of two collinear waveguides in the waist, with divergent inputs and outputs. Only one waveguide (waveguide 1), is directly exposed to the chemical test sample. The other one (waveguide 2) has to be isolated by using appropriate coatings. Generally, both waveguides have to be designed as symmetrical (e.g., identical geometries and contrast index Δn), in order to exhibit the same propagation features. The sensing principle of photonic sensors based on directional couplers is based on the power modulation at the output ports performed by the phase shift between the optical waves propagating into the two waveguides with respect to the synchronous condition. In particular, when optical propagation constants $\beta 1$ and $\beta 2$ characterizing optical modes propagating in the upper and lower arms, respectively, are equal, then the synchronous condition is verified (kL =π/2, 3π/2, 5π/2, etc) and the coupling mechanism is ensured with complete coupling efficiency ($P2 = P0$ and $P1 = 0$, at the end section x = L). The presence of any chemical analyte or gas in the coupling region (waveguide1)change the refractive index of the cover medium, causing change in the modal

effective index of the propagating mode neff1. Consequently, the synchronous coupling condition will not be ensured because β1 ≠β2 and P1 will be different to zero. By monitoring the change of coupler outputs P1 and P2, it is possible to detect a particular chemical target and estimate its concentration with high limit of detection. The sensitivity S can be calculated as follows:

$$S = n_{clad(REF)} \frac{\partial T}{\partial n_{clad}}\Big|_{n_{clad}=n_{clad}(REF)} \quad (34)$$

Where: T is the transmittance registered at the output of the reference waveguides, n_{clad} is the chemical analyte refractive index and $n_{clad(REF)}$ is the reference analyte refractive index value for which the derivative is calculated. The highest sensitivity can be achieved at the point of maximum slope of the main peak of the transmittance curve. Consequently, this condition indicates the operating point of the sensor. Obviously, the overall sensitivity depends on the waveguide sensitivity, S_W. In this context, the use of slot waveguides represents the best solution [24]. Multichannel directional couplers with slot waveguides have been also investigated and exploited for photonic chemical sensors [56]; [57]; figure 21 b). In particular, the sensing principle consists in the coupling coefficient change (Δk) as a function of the cover refractive index change (Δn_{clad}). The coupling coefficient k has an exponential dependence on analyte refractive index [57].

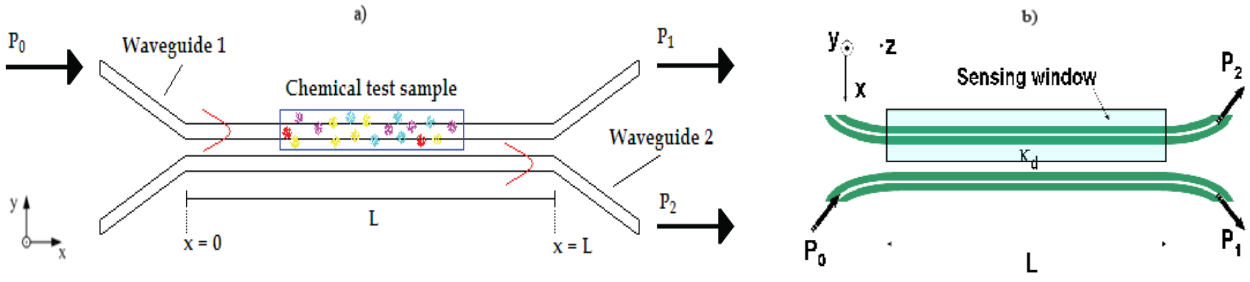

Figure 21: a) Schematic of directional coupler for sensing applications [24]. b) Schematic top view of a directional coupler formed by slot-waveguides [58].

3.7. Photonic Crystal Optical Sensors

Integrated Photonic Crystal (PhC)-based sensors represent one of the most popular class of photonic sensors, generally employed for physical and chemical/biochemical sensing. In this context, the principal advantages of these intriguing photonic sensor architectures are ultra-high light confinement in very small volumes, high wavelength selectivity, ultra high sensitivity and selectivity in sensing mechanism. Sensing mechanism in the most photonic

crystal sensors is based on the refractive index (RI) change mechanism. By binding the chemical or biochemical molecules to active sensing surface, the refractive index will be changed. So, the resonant wavelength or the intensity of the transmission spectrum is changed. This process can be used as a way to measure the concentration of the molecules. Several types of PhC-based sensor architectures are presented, focusing on employed sensing principles (i.e., opto-mechanical , nonlinear effects, optical absorption and refractive index (RI)-based sensor) [59].

3.7.1 Optomechanical sensors based on PhC

3.7.1.1. Force and strain sensors based on PhC

Strain sensor is an opto-mechanical sensor depends upon the variations of optical characteristics induced by the physical deformation of the PC-based device. A strain sensor [60] of dual-nano ring (DNR) channel drop filter on 2Dphotonic crystal with hexagonal lattice structure is presented to detect the deformation of physical structure, Figure 22 (a). In fact, Li et al. have demonstrated that the wavelength of the resonant peak at the backward drop port is strongly dependent on the ring size and separation distance *d* between the two rings. Consequently, when physical structure is deformed, a variation of the resonant wavelength can be detected. The application of an external force to the device induces a strain linearly proportional to the applied force located at the junction between cantilever and SOI substrate. The stronger the applied force, thus the strain induced to the sensor, the bigger the red shift of the resonant wavelength to be detected, Figure 22 (b).

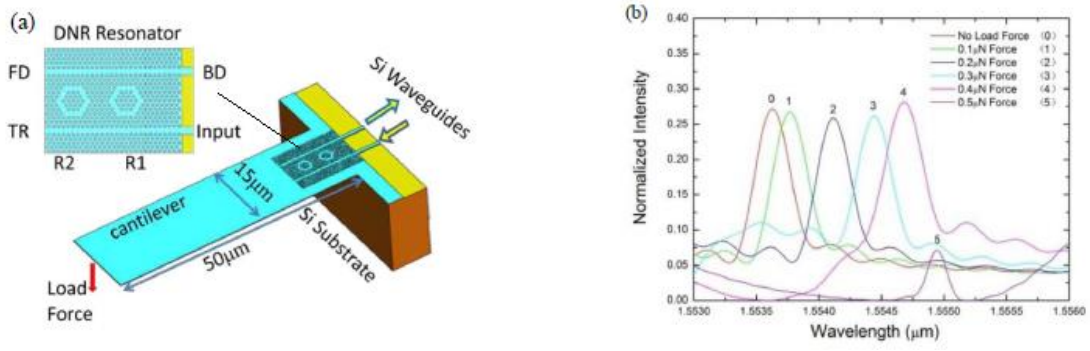

Figure 22: (a) Cantilever architecture with PC based dual-nano ring. (b) Resonant wavelength peak at the backward drop (BD) port under various force loads [60].

3.7.1.2 PhC micro-pressure sensor

Pressure sensor is an opto-mechanical sensor based on the principle of shifting of resonance wavelength, which occurs due to the change in PC's refractive index by the application of a hydrostatic pressure onto sensing surface [61]. A pressure sensor based on 2D PC microcavity structure is proposed with a linear resonant wavelength shift according to the applied pressure [62]. Another PhC micro-pressure sensor has been fabricated and characterized [63].The device is based on an air-bridged line-defect silicon slab PhC waveguide, Fig. 23.

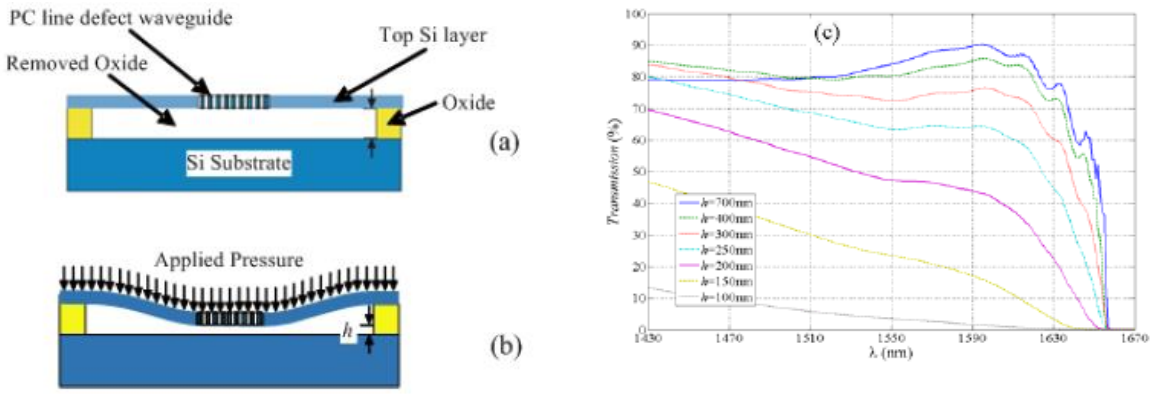

Figure 23: The basic photonic crystal sensor on a SOI platform in normal position and b) the same structure under uniform pressure. C) Transmission spectrum of the PC line defect waveguide at different bridge heights [63].

In case of TM polarization, the structure shows a band gap with its center at about 1550 nm. The basic operation of the device is based on the sensitivity of the waveguide transmission to the proximity of the surrounding material. By pushing the bridge nearer to the substrate, by the applied pressure (as shown in Figure. 23b), the evanescent field of the waveguide reaches the substrate, changing the transmission behavior of the bridge. Consequently, changes in the transmission spectrum are directly linked to the magnitude of the applied force. To this purpose, it is possible to define the device sensitivity as follows:

$$S = \frac{\delta T}{\delta P} = \frac{\delta T}{\delta h} \times \frac{\delta h}{\delta P} \qquad (35)$$

Where: T is the optical transmittance, P the applied pressure and h is the photonic crystal height over the substrate.

3.7.2. Integrated photonic crystal sensors based on nonlinear effect

Nonlinear photonic crystals (PhC) are periodic structures whose optical properties depend upon the intensity of the optical field that propagates into the crystal. In optically nonlinear media, index of refraction is modified by the presence of a light signal. But, such nonlinearities are extraordinarily weak, therefore slow light waveguide structures can be used to boost these nonlinear effects in which group velocity of light is decreased from vacuum speed of light [61], [64].The main nonlinear effects investigated in these photonic crystal structures are Kerr nonlinearities, Raman effect and harmonic generation. PC sensors based on nonlinear effects represent a new and intriguing approach in advanced sensing for ultra-high response of photonic crystal sensor. Such sensors are expected to be able to detect single particle in aqueous solutions, with very small dimensions comparable to that of virus or proteins [59]. An original nonlinear photonic crystals sensor is proposed [65], consisting in a PhC microcavity in which the Raman Effect related to the vibrational excitations mode in silica is excited. In fact, a photon of the incident field is scattered by a molecule of the medium in which the field propagates, resulting in the generation of a photon of lower energy (the Stokes wave). At the same time, the residual energy is absorbed by molecules via phonons. The Raman shift is then the frequency difference between the incident wave and the scattered one. The device proposed is characterized by a L6 PhC cavity, as sketched in Fig. 24. The device is designed in order to ensure the generation of Stokes wave into the cavity, away from the resonant wavelength of about 15,6 THz. This wavelength shift due to pump wave and resonant Stokes wavelength generated into the cavity is typical for silica.

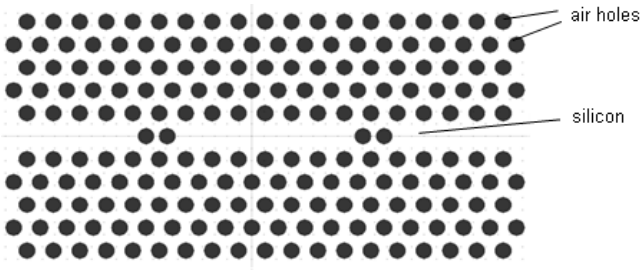

Figure.24: Schematic of L6 PhC cavity to generate Raman Effect [59].

3.7.3. Photonic crystal sensors based on optical adsorption

In IR absorption sensing, gases and liquid molecules that absorb radiation in near- and mid-infrared, are detectable by photonic crystal sensor by the study of peaks in absorption spectrum [59]. Molecules that bind to the surface of crystal structures interact with evanescent

field that is weak and exponentially decays with distance causing weak interaction. When the wavelength of an optical signal matches the natural frequencies or resonances of irradiated gas or molecules, the energy states of vibrating atoms change in discrete steps. The resonance frequencies or wavelengths depend on the number and mass of atoms in molecules as well as the number and strengths of chemical bonds. If the chemical structure of the molecules is complex, then a range of resonant vibrations characterize the optical absorption of molecules [59]. Fig. 25(a) present a photonic sensor based on a PhC slot waveguide proposed by [66].The PhC waveguide is a line defect with uniform lattice constant *a*. The device is designed for xylene and methane sensing. The sensing mechanism takes place by introducing analyte in the device sensible area through tygon tubes. For methane sensing, the absorbance peak selected occurs at 1665.5nm.In Fig. 25(b), absorbance magnitude at 1665.5nm is plotted versus methane concentration. The lowest experimentally determined concentration was 100ppm (parts per million) or 0.2% PEL. As observed in Fig. 5(b), the linear Beer-Lambert law is followed for low concentrations of methane. At higher concentrations, deviations from linearity are observed [66].

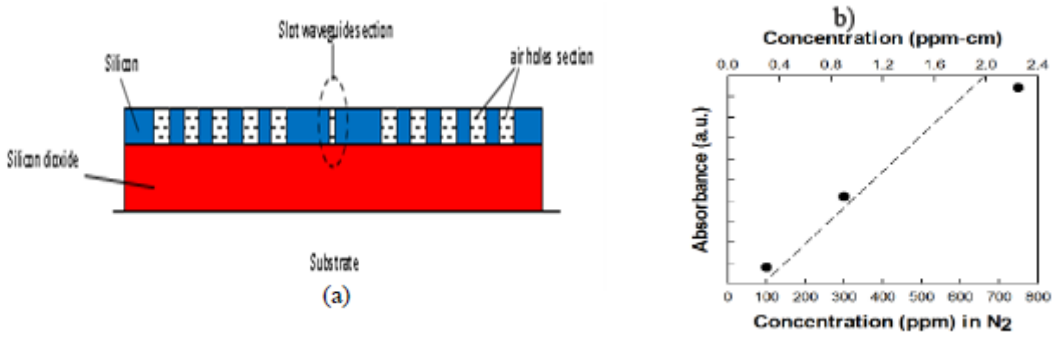

Figure 25: (a) Cross section of PhC slot waveguide based on optical adsorption [59]. (b)The absorbance magnitude of methane at 1665.5nm is plotted as a function of concentration obtained by direct absorption spectroscopy experimentally [66].

3.7.4. RI-based PhC sensors

RI sensing is most common form of sensing specifically used in chemical and bio sensing. RI-based PhC sensors present numerous advantages such as minimal sample preparation without fluorescence labeling, real–time detection, high sensitivity and selectivity. In particular, the sensing principle consists in measuring RI changes of a bulk solution due to the presence of chemical analytes or gases generally characterized by higher refractive indices. Applications in gaseous and aqueous environment have been studied to detect

concentrations of chemical and biological species [59]. RI sensing includes two fundamental sensing, i.e., surface sensing and homogeneous sensing. In surface sensing, PC holes are initially functionalized by receptor molecules properly chosen in order to selectively adsorb target analytes. Consequently,when the device is exposed to a sample, target molecules are trapped by receptors on the sensor hole inner surfaces inducing a localized refractive index change around the hole region. Homogeneous sensing involves optical mode propagation changes due to RI variations in bulk solution induced by gases or liquid samples where the photonic sensor is exposed. In fact, a large number of advanced architectures (e.g., integrated microcavities, waveguides, slotted cavities and interferometric configurations) employ the refractive index sensing for detection [61]. In the following, main architectures of PhC RI-based sensors are presented, focusing on their operating principles and performance.

3.7.4.1. PhC resonant microcavities sensors

The biosensing principle for these structures is the following; the defect hole of the PhC disturbs the PhC's period structure, leading to the formation of the defect mode in the band gap. Light resonates with the defect mode can propagate in the PhC. As a result, the defect mode appears as a sharp peak within the band gap on the transmission (or reflection) spectrum. The high electric field concentration results from Bragg reflection in the in-plane directions and total internal reflection(TIR) in the vertical direction makes the defect mode position highly sensitive to changes in the refractive index of the surrounding medium. Several photonic crystal resonant microcavities based sensors have been studied. Such as Biosensor-based PhC micro-resonator to detect small changes in the refractive index [67], PhC sensor based on air-bridge cavity [68], 1D-photonic crystal microcavity sensor [69], PhC device with one latex sphere in the central defect of microcavity [70] and biosensors based on photonic crystal nanocavity resonator [71, 72]. In [67], the sensor was suitable to detect many chemical or biochemical molecules. The micro-resonator was formed by decreasing the size of the air hole in the center of the structure. The general layout of the structure is represented in Figure 26(a).The transmission spectra of the sensor have a resonance wavelength within the wavelength range of 1.5 μm and the quality factor was equal to 400. The structure was responsive to changes in the refractive index in the range of 1–1.5. By changing the refractive index as 1.446, 1.448, 1.450, 1.452, and 1.454, the resonant peak is shifted to about 1500.2 nm, 1500.8 nm, 1501.2 nm, 1501.7 nm, and 1502.1 nm, respectively, as shown in Figure 26(b).

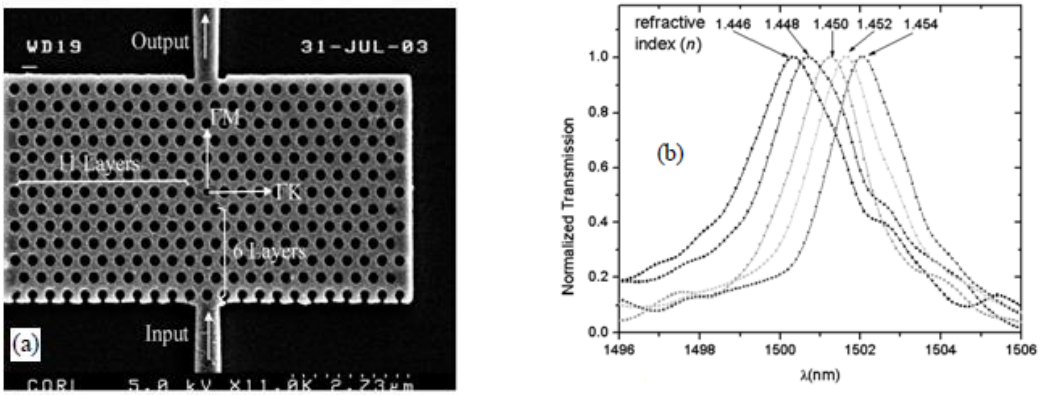

Figure 26: (a) Scanning electron microscope view of a photonic crystal microcavity integrated with two ridge waveguides. The regular hole diameter is *d* =0.58 *a*, the defect hole diameter is *d*0 =0.4 *a*, and *a* =440 nm is the lattice constant of the photonic crystal. (b) Normalized transmission spectra of the photonic crystal microcavity with five different ambient refractive indices ranging from *n* =1.446 to *n*=1.454 in 0.002 increments [67].

3.7.4.2. Biochemical sensor based on PhC LX resonator

This resonator is formed by removal of the successive air holes of structure which X represents the number of removed holes. In other words, X is the resonator length. For example, L3 resonator is obtained by removing three air holes in the photonic crystal structure. Some of the resonators, namely, L3, L4, L7, and L13, have been provided [73], [74]. In the later, photonic crystal (PC) microcavity biosensor consists of a linear photonic crystal microcavity coupled to a photonic crystal waveguide (PCW) in a silicon-on-insulator (SOI) platform. The PCW is a W1 line defect waveguide with uniform lattice constant a=400 nm. The linear L13 PC microcavities with 13 missing holes along Γ_K direction, are fabricated two periods away from the PCW, Fig 27 (a). Fig. 27 (b) shows experimental resonant transmission spectra observed when avidin binds to the target biotin at different concentrations (0 nM, 0.04 nM, 0.08 nM and 0. 1nM).A resonance wavelength shift of 0.03 nm was observed for each concentration.

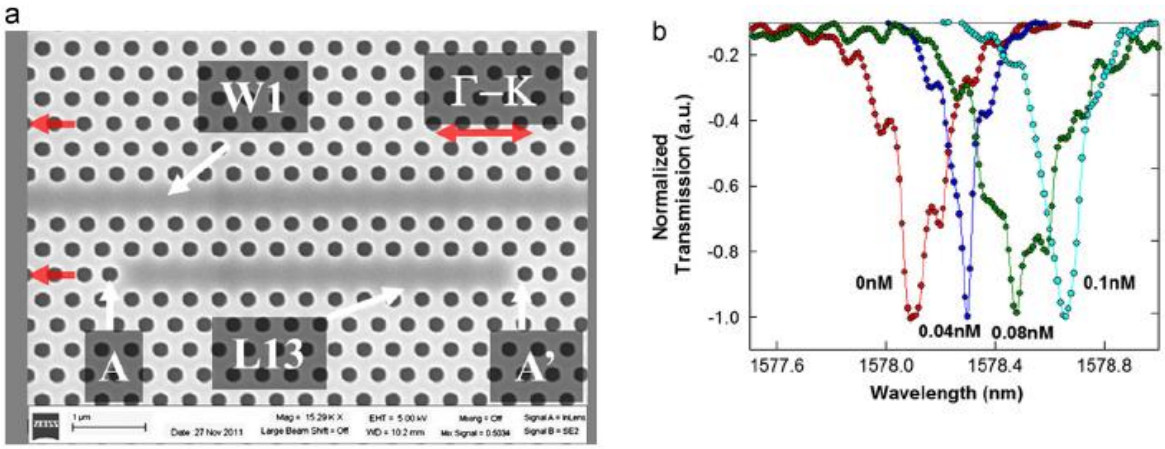

Figure 27: (a) Scanning electronmicrograph image of L13 PC microcavity coupled to W1 PC waveguide. The edge air holes are indicated by A and A0 and the direction of shift indicated by the red arrows. (b) Experimental transmission spectra showing the transmission drop resonance spectra f or the binding between Avidin and Biotin (K_d~10^{-15}M) between 0nM and 0.1nM [74].

3.7.4.3. Biochemical sensor based on Slot PhC cavities

Slotted photonic crystal cavities are advantageous for sensing applications as most of the field interacts with contents of the air slot. In conventional photonic crystal cavities and other devices such as ring resonators, most of the light is confined to the dielectric of the waveguide structure, and only the evanescent tail of the optical mode sees the analyte of interest. In the slotted photonic crystal case a change in the refractive index of the slot contents is felt by the majority of the modal field, altering the resonant wavelength of the system more strongly. An SEM image of the structure is shown in Figure 28 (a) [75]. As a first test different alcohols were introduced into the microchannel, as shown in Figure 28 (b) below. The cavity peak (around 1,532 nm for ethanol) is clearly distinguished from the bulk transmission of the mirror waveguide (above 1,540 nm for ethanol), and was found to shift significantly with the different alcohols. At 1,550 nm, Ethanol has a refractive index of approximately 1.354 and IPA has 1.378. Given that the shift in resonant wavelength is approximately 10 nm, this corresponds to a refractive index sensitivity of approximately 415 nm/RIU.

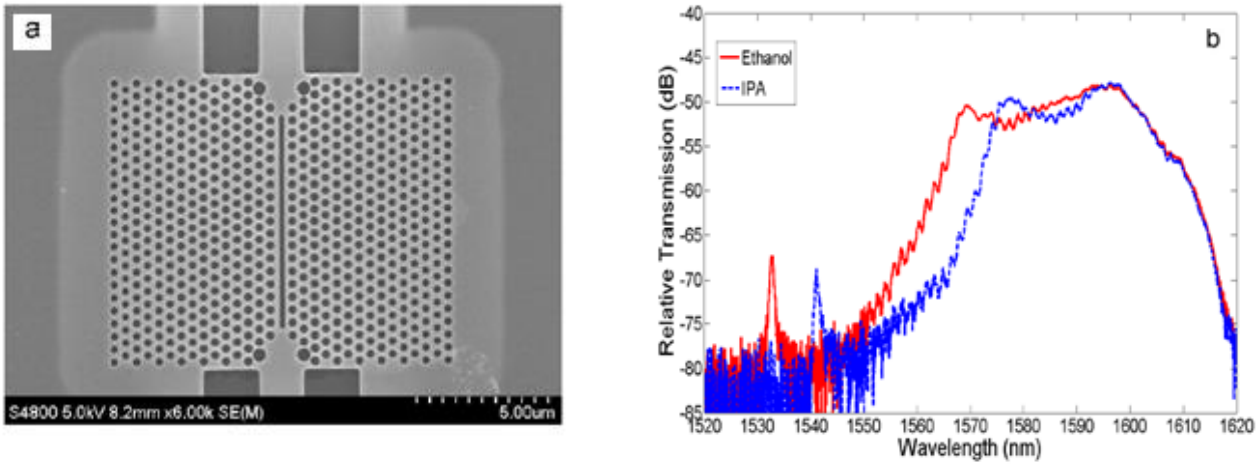

Figure 28: (a) SEM image of slotted photonic crystal cavity fabricated in SOI. **(b)** Transmission spectra of a slotted photonic crystal cavity with different alcohols injected into the integrated microchannel [75].

3.7.4.4. Photonic crystal ring resonator based sensors

The sensing mechanism of this biosensor or biochemical sensor is based on the measurement of the refractive index change. Thus, the resonance wavelength of the transmission spectrum shifts to longer wavelengths. Defects into the structures consist of a ring resonator of different shapes and two waveguides for input and output of light. For increasing the quality factor and sensitivity of the sensor, reduction of the radius of the ring can be very important. Several sensor based on photonic crystal ring resonator have been studied: nanoring resonator for both pressure and temperature sensing [76], diamond-shaped nanoring resonator for biochemical sensing [77, 78], Two-curve-shaped (TCS) photonic crystal ring resonator for biochemical sensor [79], biochemical sensor based on nano-ring resonator shaped by two consecutive curves [80]. Several parameters where studied in the purpose to obtain the better response of the sensor according to the refractive index changes caused by measurand, such as the shape of the ring resonators, defect holes radius, the end point of the waveguides, and the best holes for attaching chemical or biochemical molecules. In [78], Figure 29 (a), the red and green holes indicate position of end waveguide and air holes around the ring resonator for binding biochemical molecules, respectively. A waveguide to input light is located at the bottom of the structure. The light from top waveguide is detected by a photodetector. Figure **29 (**b) represents the normalized curve of the resonant wavelength shifts which is changed by the refractive index variation in the range of 1.33-1.55. This curve shows an approximately linear relationship between RI and resonant

wavelength shift. An acceptable linear relationship between refractive index and wavelength resonance will cause to measure more accurate of refractive index changes [78].

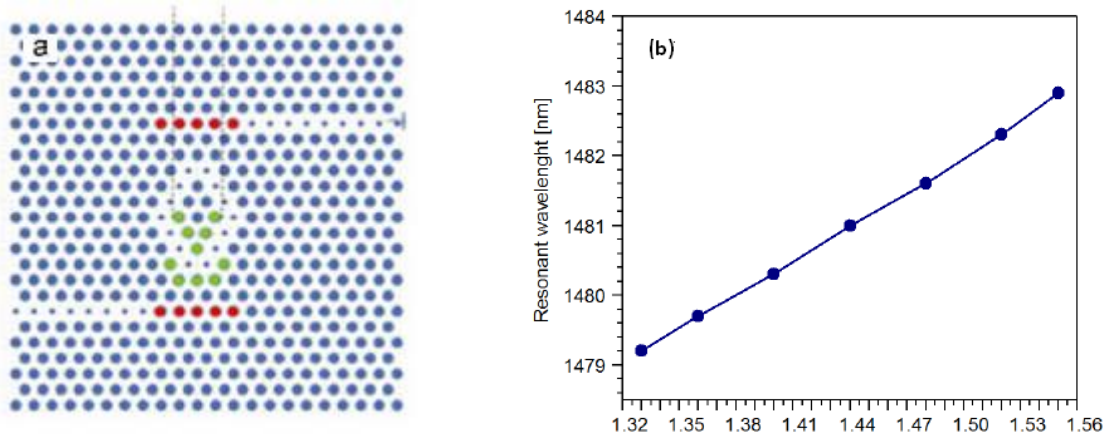

Figure 29: (a): Sketch of the biosensor based on photonic crystal diamond-shaped ring resonator for biochemical sensing applications [77]. b) The normalized curve of the resonant wavelength shifts which is changed by the refractive index variation in the range of 1.33-1.55. [78].

4. Conclusion

In this chapter, a variety of optical-sensing mechanisms were described, including optical absorption, fluorescence, Raman scattering, detecting of refractive index changes and The Sagnac effect. In the purpose to transform optical variable induced by such optical-sensing mechanism into an analytically useful signal, several integrated photonic sensors configurations have been described suitable for different applications, such as integrated optical interferometers, microring resonators, Bragg grating resonators, directional couplers and photonic crystals optical sensors.

References

[1] José Luís Santos Faramarz Farahi : Handbook of Optical Sensors. *CRC Press*. 2015.
[2] Ahmmed A. Rifat, Rajib Ahmed and Bishanka Brata Bhowmik: Chapter 16: SOI Waveguide-Based Biochemical Sensors. From: M. F., *Computational Photonic Sensors.* Mohamed Farhat O. Hameed and S. Obayya (eds.). © *Springer International Publishing AG, part of Springer Nature* 2019.
[3] M Gabalis, D Urbonas and R Petruskevicius: A perforated microring resonator for optical sensing applications. *J. Opt.* 16 (2014) 105003 (6pp).
[4] V. M. N. Passaro , F. Dell'Olio , B. Casamassima and F. De Leonardis : Guided-Wave Optical Biosensors. *Sensors* 2007, *7*, 508-536.
[5] U. S. Dinish, C. Y. Fu, K. S. Soh, R. Bhuvaneswari, A. Kumar, and M. Olivo : Highly sensitive SERS detection of cancer proteins in low sample volume using hollow core photonic crystal fiber. *Biosens. Bioelectron*. 33, 293–298 (2012).
[6] Andreas Hänsel and Martijn: Opportunities for photonic integrated circuits in optical gas sensors. *J. Phys. Photonics* 2, 012002 (2020).
[7] F. Baldini, A.N. Chester J, Homola and S. Martellucci: Optical-chemical-sensors. © *2006 Springer.*
[8] Vo-Dinh, T.; Cullum, B. M. "Fluorescence Spectroscopy for Biomedical Diagnostics, in chapter 5". Biomedical Photonics Handbook. Editor: Tuan Vo-Dinh. *CRC Press*, 2003.
[9] L. Liu1, X. Zhou1, J. S. Wilkinson, P. Hua, B. Song & H. Shi: Integrated optical waveguide based fluorescent immunosensor for fast and sensitive detection of microcystin-LR in lakes: Optimization and Analysis. *Scientific Reports 7*: *3655. 2017.*
[10] R.S. Das, Y.K. Agrawal.: Raman spectroscopy: Recent advancement, techniques and applications. *Vibrational Spectroscopy* 57 (2011) 163-176.
[11] *S. Kumar, P. Kumar, A. Das and C. S .Pathak* : Chapter, Surface-Enhanced Raman Scattering: Introduction and Applications. *Recent Advances in Nanophotonics-Fundamentals and Applications.* intechopen.92614. 2019.
[12] Weber WH, Merlin R.: Raman Scattering in Materials Science. Berlin, Heidelberg: *Springer*; 2000.
[13]: Smith E, Dent G: Introduction, basic theory and principles. In: Smith E, Dent G, editors. Modern Raman Spectrosopy—A Practical Approach. Vol. 5. 2005.
[14] Moskovits M: Surface-enhanced spectroscopy. Reviews of Modern Physics. 1985;57:783-826.].
[15] De Leonardis, F.; Passaro, V.M.N.: Modeling of Raman amplification in Silicon-on-Insulator optical microcavities. *New J. Phys.* 2007, *9*, 1–24.
[16] Liu, A.; Rong, H.; Jones, R.; Cohen, O.; Hak, D.; Paniccia, M :Optical amplification and lasing by stimulated Raman scattering in silicon waveguides. *J. Lightwave Technol*. 2006, *24*, 1440–1455.
[17] Benzene Derivatives Analysis Using Aluminum Nitride Waveguide Raman Sensors. M. Makela, P. Gordon, D. Tu, C. Soliman, G. L. Cote, K. Maitland, and P. T. Li. *American Chemical Society*. 2020.
[18] Dell'Olio, F.; Passaro, V.M.N: Optical sensing by optimized silicon slot waveguides. *Opt. Express* 2007, *15*, 4977–4993.
[19]: Chen, W.; Lou, S.; Wang, L.; Zou, H.; Lu, W.; Jian, S. : Highly sensitive torsion sensor based on Sagnac interferometer using side-leakage photonic crystal fiber. *IEEE Photon. Technol. Lett.* 2011, *23*, 1639–1641.
[20] Fu, H.Y.; Tam, H.Y.; Shao, L.Y.; Dong, X.; Wai, P.K.; Lu, C.; Khijwania, S.K. Pressure sensor realized with polarization-maintaining photonic crystal fiber-based Sagnac interferometer. *Appl. Opt.* 2008, *47*, 2835–2839.
[21 Sorrentino, C.; Toland, J.R.E.; Search, C.P. Ultra-sensitive chip scale Sagnac gyroscope based on periodically modulated coupling of a coupled resonator optical waveguide. *Opt. Express* 2012, *20*, 354–363.
[22] V. M. N. Passaro, A. Cuccovillo, L. Vaiani, M. D. Carlo and C. E. Campanella :Gyroscope Technology and Applications: A Review in the Industrial Perspective. *Sensors* 2017, 17, 2284.
[23] Soref, R. The past, present, and future of silicon photonics. IEEE J. Sel. Top. Quantum Electron. 2006, 12, 1678–1687.

[24]: Vittorio M. N. Passaro, Benedetto Troia, Mario La Notte and Francesco De Leonardis ; Chemical Sensors Based on Photonic Structures. Advances in Chemical Sensors, Edited by Prof. Wen Wang, 2012. ISBN 978-953-307-792-5.
[25] E. Luan , H. Shoman, D. M. Ratner, K. C. Cheung and L. Chrostowski, : Silicon Photonic Biosensors Using Label-Free Detection. *Sensors* 2018, 18, 3519.
[26] Q. Liu et al., "Highly sensitive Mach–Zehnder interferometer biosensor based on silicon nitride slot waveguide," Sens. Actuators B Chem., 188 681 –688 (2013).
[27] Cesar S. Huertas , Olalla Calvo-Lozano, Arnan Mitchell and Laura M. Lechuga : Advanced Evanescent-Wave Optical Biosensors for the Detection of Nucleic Acids: An Analytic Perspective. Frontiers in Chemistry, v 7, N 724 (2019).
[28] K. E. Zinoviev, A. B. Gonzalez-Guerrero, C. Dominguez, and L. M. Lechuga, "Integrated bimodal waveguide interferometric biosensor for label-free analysis," *J. LightwaveTechnol.* 29(13), 1926–1930 (2011).
[29] Daphn´e Duval and Laura M. Lechuga, chapter8: OPTICAL WAVEGUIDE BIOSENSORS, from, PHOTONICS Scientific Foundations, Technology and Applications, Biomedical Photonics, Spectroscopy, and Microscopy, Volume IV, *Edited by* DAVID L. ANDREWS; Copyright © 2015 by John Wiley & Sons, Inc.
[30] A. Ymeti, J. Greve, P.V. Lambeck, T.Wink, H. van, Beumer, R. R.Wijn, R. G. Heideman, V. Subramaniam, and J. S. Kanger, "Fast, ultrasensitive virus detection using a young interferometersensor," *Nano Lett.* 7(2), 394–397 (2007).
[31] K. Schmitt, B. Schirmer, C. Hoffmann, A. Brandenburg, and P. Meyrueis, "Interferometric biosensor based on planar optical waveguide sensor chips for label-free detection of surface bound bioreactions," *Biosens. Bioelectron.*22(11), 2591–2597 (2007).
[32] J. H. Sim, Y. H. Kwak, C. H. Choi, S.-H. Paek, S. S. Park, and S. Seo, "A birefringent waveguide biosensor platform for label-free live cell detection of Listeria monocytogenes," *Sens. Actuators B. Chem.* 173, 752–759 (2012).
[33] Zourob M., Lakhtakia A : Optical Guided-wave Chemical and Biosensors I., Vol. 7, 2010. Springer Series on Chemical Sensors and Biosensors. Methods and Applications. Series Editor: G. Urban.
[34] I. R. Cooper, S. T. Meikle, G. Standen, G. W. Hanlon, and M. Santin, "The rapid and specific real-time detection of *Legionella pneumophila*in water samples using optical waveguide lightmode spectroscopy," *J. Microbiol. Methods* 78(1), 40–44 (2009).
[35] N. Ad´anyi, K. Majer-Baranyi, A. Nagy, G.N´emeth, I. Szendr˝o, and A. Sz´ek´acs, "Optical waveguide lightmode spectroscopy immunosensor for detection of carp vitellogenin," *Sens. Actuators B. Chem.* 176, 932–939 (2013).
[36] S. V. Pham, M. Dijkstra, A. J. F. Hollink, L. J. Kauppinen, R. M. de Ridder, M. Pollnau, P. V. Lambeck, and H. J.W. M. Hoekstra, "On-chip bulk-index concentration and direct, label-free protein sensing utilizing an optical grated-waveguide cavity," *Sens. Actuators B. Chem.* 174, 602–608 (2012).
[37] Sonia Grego , Jonathan R. McDaniel, Brian R. Stoner : Wavelength interrogation of grating-based optical biosensors in the input coupler configuration. Sensors and Actuators B 131 (2008) 347–355.
[38] J. Adrian, S. Pasche, J.-M. Diserens, F. S´anchez-Baeza, H. Gao, M. P. Marco, and G. Voirin, "Waveguide interrogated optical immunosensor (WIOS) for detection of sulfonamide antibiotics in milk," *Biosens. Bioelectron.*24(11), 3340–3346 (2009).
[39] J. Razumovitch, K. de Franca, F. Kehl, M. Wiki, W. Meier, and C. Vebert, "Optimal hybridization efficiency upon immobilization of oligonucleotide double helices," *J. Phys. Chem. B* 113(24), 8383–8390 (2009).
[40] R. Chandrasekhar; Z. J. Lapin; A. Nichols; R. Braun; A. W. Fountain: Photonic integrated circuits for Department of Defense-relevant chemical and biological sensing applications, state-of-the-art and future outlooks, Optical Engineering Volume 58, Issue 2, February 2019.

[41] Yiming Ma , Bowei Dong, ChengkuoLee:Progress of infrared guided-wave nanophotonic sensors and devices, jurnal of *Nano Convergence* volume 7, Article number: 12 (2020).
[42] G. Ycas et al., "High-coherence mid-infrared dual-comb spectroscopy spanning 2.6 to 5.2 μm," Nat. Photonics 12, 202–208 (2018).
[43]: Homola J (2008) Surface plasmon resonance sensor for detection of chemical and biological species.Chem Rev 108:462–493.
[44] E. Stenberg, B. Persson, H. Roos, C. Urbaniczky, Quantitative determination of surface concentration of protein with surface plasmon resonance using radiolabeled proteins. J. Colloid Inter. Sci. 143, 513–526 (1991).
[45] Z. M., Lakhtakia A : Optical Guided-wave Chemical and Biosensors II., Vol. 8, 2010. Springer Series on Chemical Sensors and Biosensors. Methods and Applications. Series Editor: G. Urban.
[46] S. Patrick, C. Villringer, S. Pulwer, F. Heinrich, J. Bauer, B. Dietzel, C. Mai, A. Mai, M. Casalboni, and S. Schrader: Hybrid Waveguide Ring Resonator for Biochemical Sensing. *IEEE Sensors Journal ;* 17 ; 15 ; 4781 4790.2017.
[47]. Sun, Y.; Fan, X.: Optical ring resonators for biochemical and biochemical sensing. *Anal.Bioanal. Chem*, *399*, 205–211 (2011).
[48] M.-C. Estevez, M. Alvarez and L. M. Lechuga: Integrated optical devices for lab-on-a-chip biosensing applications. *Laser Photonics Rev*., 1–25 (2011).

[49] Passaro, V.M.N.; Troia, B.; De Leonardis, F.: A generalized approach for design of photonic gas sensors based on Vernier-effect in mid-IR. *Sens. Actuators B Chem.* 2012, *168*, 402 420.

[50] Claes, T.; Bogaerts, W.; Bienstam, P.: Experimental characterization of a silicon photonic sensor consisting of two cascaded ring resonators based on the Vernier-effect and introduction of a curve fitting method for an improved detection limit. *Opt. Express* 2010, *18*, 22747–22761.
[51] Jin, L.; Li, M.; He, J.: Highly-sensitive silicon-on-insulator sensor based on two cascaded micro-ring resonators with Vernier effect. *Opt. Commun. 284* (2011) 156–159.
[52] Dai, D. Highly sensitive digital optical sensor based on cascaded high-Q ring-resonators. *Opt. Express* 2009, *17*, 23817–23822.
[53] Dai, D. Highly sensitive digital optical sensor based on cascaded high-Q ring resonators. *Opt. Expresss* 2009, 17, 23817–23822.
[54] V. R. Almeida, Q. Xu, C. A. Barrios, and M. Lipson: Guiding and confining light in void nanostructure. *OPTICS LETTERS*. Vol. 29, No. 11. 2004.
[55] J. T. Robinson, L. Chen, and M. Lipson: On-chip gas detection in silicon optical microcavities. Optics Express. Vol. 16, Issue 6, pp. 4296-4301. 2008.
[56] McCosker, R.J. & Town, G.E. (2010a). Optical chemical sensor using a multi-channel directional coupler with slot waveguides. *International Conference on Photonics (ICP)*,ISBN: 978-1-4244-7186-7, July 5-7, 2010.[57]: McCosker, R.J. & Town, G.E. (2010b). Multi-channel directional coupler as an evanescent field sensor. (2010). *Sensors and Actuators B: Chemical*, Vol.150, No.1, (September2010), pp. 417-424.
[58] C. A. Barrios: Optical Slot-Waveguide Based Biochemical Sensors. *Sensors* 2009, *9*, 4751-4765.
[59] Benedetto Troia, Antonia Paolicelli, Francesco De Leonardis and Vittorio M. N. Passaro: chapter11: Photonic Crystals for Optical Sensing: A Review. From, Advances in Photonic Crystals. Edited by Vittorio M. N. Passaro. 2013.
[60] Li, B.; Hsiao, F.L. & Lee, C. (2011). : Computational Characterization of a Photonic Crystal Cantilever Sensor Using a Hexagonal Dual-Nanoring-Based Channel Drop Filter. *IEEE Transaction of Nanotechnology*, (July 2011), 10(4), 789-796.
[61] Sapna Dinodiya, B. Suthar and A. Bhargava: Photonic Crystal Sensors: Physics and Applications. *AIP Conference Proceedings* 1953, 060016 (2018). American Institute of Physics.

[62] Lee, C., Radhakrishnan, R., Chen, C.-C., Li, J., Thillaigovindan, J., Balasubramanian, N,"Design and Modeling of a Nanomechanical Sensor Using Silicon Photonic Crystals," *Journal of Lightwave Technology* 26(7), 839–846 (2008).
[63] Bakhtazad, A.; Sabarinathan, J. &Hutter, J.L. (2010). Mechanical Sensitivity Enhancement of Silicon Based Photonic Crystal Micro-Pressure Sensor. *International Symposium on Optomechatronic Technologies (ISOT)*, 978-1-4244-7682-4, (October 2010),1-5.
[64] M. Soljac˘ic, J. D. Joannopoulos,: Enhancement of nonlinear effects using photonic crystals. *Nature Materials* 3, 211-219 (2004).
[65] Van Leest, T.; Heldens, J.; Dan Der Gaag, B. & Caro, J. (2012). Photonic crystal cavities for resonant evanescent field trapping of single bacteria. *Proceedings of the SPIE*, (June 2012), art. 84270T, 8427.
[66] Chakravarty, S.; Lai, W.-C.; Zou, Y.; Lin, C.; Wang, X. & Chen, R.T. (2011a). Silicon nanomembrane- based photonic crystal nanostructures for chip-integrated open sensor systems. *Proceeding of SPIE*, (November 2011), art. 819802, 8198.]
[67] E. Chow, A. Grot, L. W. Mirkarimi, M. Sigalas, G. Girolami, "Ultracompact biochemical sensor built with two-dimensional photonic crystal microcavity", *Optics Letters* 29(10), pp. 1093–1095, 2004.

[68] Junhua, L.; Qiang, K.; Chunxia, W.; Baoqing, S.; Yiyang, X. &Hongda, C. (2011): Design of a photonic crystal microcavity for biosensing. *Journal of Semiconductors*, (March 2011), art.034008, 32(3).
[69] Mandal, S.; Goddard, J.M. & Erickson, D. (2009): A multiplexed optofluidic biomolecular sensor for low mass detection. *J. Lab on a Chip*, (July 2009), 9(20), 2924-2932.
[70] Lee, M.; Miller, B.L. &Fauchet, P.M. (2008): Two-dimensional photonic crystal microcavity sensor for single particle detection. *Lasers and Electro-Optics, and Conference on Quantum Electronics and Laser Science*, 978-1-55752-859-9, (May 2008).
[71] S. Olyaee, S. Najaf gholinezhad, "A high quality factor and wide measurement range biosensor based on photonic crystal nanocavity resonator", *Sensor Letters* 11, pp. 483– 488, 2013.
[72] S. Olyaee, S. Najafgholinezhad, "Computational study of a label-free biosensor based on a photonic crystal nanocavity resonator", Applied Optics 52(29), pp. 7206–7213, 2013.
[73]: D. Dorfner, T. Zabel, T. Hürlimann, N. Hauke, L. Frandsen, U. Rant, G. Abstreiter, J. Finley, "Photonic crystal nanostructures for optical biosensing applications", *Biosensors and Bioelectronics* 24, pp. 3688–3692, 2009.
[74] S. Chakravarty, Y. Zou, W. C. Lai, R. Chen, "Slow light engineering for high Q high sensitivity photonic crystal micro cavity bio-sensors in silicon", *Biosensors and Bioelectronics* 38, pp. 170–176, 2012.
[75] Mark G. Scullion, Thomas F. Krauss and Andrea Di Falco: Slotted Photonic Crystal Sensors. *Sensors* 2013, *13*, 3675-3710.
[76] R. Rajasekar1 & S. Robinson: Nano-Pressure and Temperature Sensor Based on Hexagonal Photonic Crystal Ring Resonator, *Springer Science+Business Media*, LLC, part of Springer Nature, 2018.
[77] S. Olyaee, H. Mohsenirad and A. Mohebzadeh-Bahabady: Photonic Crystal Chemical/Biochemical Sensors. Book: *Progresses in Chemical Sensor* (pp.37-56). Chapter: 3. InTech Editors: Wen Wang. 2016.
[78] S. Olyaee, A. Mohebzadeh-Bahabady, "A diamond-shaped bio-sensor based on two dimensional photonic crystal nano-ring resonator", *IEEE, IET 10th International Symposium on Communication Systems, Networks and Digital Signal Processing* (CSNDSP 2014), 23–25 July 2014.

[79] S. Olyaee, A. Mohebzadeh-Bahabady, "Two-curve-shaped biosensor using photonic crystal nano-ring resonators", *Journal of Nanostructures* 4, pp. 303–308, 2014.
[80] S. Olyaee, A. Mohebzadeh-Bahabady, "Designing a novel photonic crystal nano-ring resonator for biosensor application", *Optical and Quantum Electronics* 47(7), pp. 1881– 1888, 2015.

Chapter3: Photonic Waveguides Modeling

1. Introduction

The term photonics reflects the growing bind between optics and electronics. If electronics can be considered as the discipline that describes the flow of electrons, photonics deals with the control of photons. The term photonics also reflects the importance of the photon nature of light in describing the operation of many optical devices. Furthermore, integrated photonics refers to the fabrication and integration of several photonic components on a common planar substrate. These components include optical elements, sources and detectors. In turn, these can then be used as building blocks to fabricate more complex planar devices, which can perform a wide range of functions with applications in optical communication systems, optical signal processing and sensors [1]. The main goal pursued by integrated photonics is therefore the miniaturisation of optical systems; this is possible thanks to the small wavelength of the light, which permits the fabrication of circuits and compact photonic devices with sizes of the order of microns. The integration of multiple functions within a planar optical structure can be achieved by means of planar lithographic production used in microelectronics. Optical waveguides are the key elements of integrated photonic devices that perform not only guiding, but also coupling, switching, splitting, multiplexing and demultiplexing of optical signals.

In this chapter, firstly, slab optical waveguides will be studied with two approaches. The optical ray approach, witch allow us to determine the dispersion equation of the guided modes, and the Maxwell's equations approach, to determine wave equations and their solutions, as well as, the solutions of electromagnetic field. In addition, the influence of the physical and geometric parameters and the wavelength of the source on the propagation constants and the cutoff frequencies will be studied. Secondly, the effective index method (EIM) will be used for calculating the modal fields and the propagation constant in channel waveguides.

2. Photonic components characteristics

Systems based on integrated photonic technology have the following interesting characteristics [1]:

- Integrated photonic devices based on integrated optical circuits take advantage of the relatively short wavelength of the light in this range (0.5–2 μm), which allows the fabrication of miniature components using channel waveguides the size of microns.

- The technology required to fabricate planar optical circuit components of microns dimensions is therefore common in the well-established Micro-electronic technology, using the tools and techniques of the semiconductor industry. This technology makes mass production and reduces the quantity of material necessary to fabricate the photonic devices. Furthermore, this technology possesses important advantages in terms of choice of materials, design, fabrication and performance characteristics.
- The basic idea behind the use of photons rather than electrons to create integrated photonic circuits is the high frequency of light (200 THz), which allows a very large bandwidth for transporting and managing a huge amount of information.
- Because optical circuits and components are integrated in a single substrate, the alignment problem is avoided and the stability is assured.
- The key elements in an integrated optical device are monomode channel waveguides where the optical radiation propagates in a single mode, with width and depth typically of the order of microns; witch means weak dispersion and attenuation. Further, it is easier to control the optical radiation flux through the electro-optic, acousto-optic, thermo-optic or magneto-optic effects, or even by the light itself via non-linear interactions.
- The optical power density in a monomode channel waveguide is very high, due to the small cross-sectional area of the guide. This is of special relevance in the performance of devices requiring high radiation intensity, such as frequency converters or even optical amplifiers and lasers.
- Since the field distributions of surface acoustic waves (SAW) are located within a distance of a few wavelengths beneath the substrate surface (tens of microns), the SAW and the optical waveguide modes overlap strongly, giving rise to efficient acousto-optic interactions.
- For devices based on light control via the electro-optic effect, the short width of the channel waveguides allows one to drastically reduce the distance between the control electrodes. This implies that the voltage required to obtain certain electric field amplitude can be considerably reduced. Furthermore, the small size of the control electrodes implies low capacitance, and this allows for a faster switching speed and higher modulation bandwidth.

3. Basic integrated photonic components

All the optical components in integrated photonics are constructed with three building blocks. They are the straight waveguide, the bend waveguide and the power splitter. The optical elements that can be found in an optical chip can be classified according to their function as passive, active and non-linear. Passive optical elements have fixed input/output characteristics, which are determined when the photonic component is fabricated. Examples of these components are the straight and bend waveguides**,** the power splitter, waveguide reflector, directional coupler and polarizer [1, 2]. Active optical elements are photonic components which are driven by externally applied fields. Examples of this class are electro-optic TE/TM converter, frequency converter, intensity modulator, the phase modulator, integrated optical amplifier and the integrated laser. Finally, integrated optical non-linear devices make use of the non-linearity of certain materials to make frequency doubling or optical parametric oscillation [1].

4. Optical waveguides classification

An optical waveguide is a light conduit of dielectric material embedded in another dielectric material of lower refractive index. The light is transported through the inner medium by multiple total internal reflections at the boundaries without radiating into the surrounding medium. Optical waveguides can be classified according to their geometry, mode profile, refractive index distribution and the number of dimensions where the light is confined. Generally, dielectric waveguides are determined by the transverse profile of its dielectric constant $\varepsilon_r(x, y)$, which is independent on the longitudinal direction. In addition, optical waveguides can be classified based on mode structure as single mode and multiple modes. Optical waveguides can be classified based on the number of dimensions where the light rays are confined. The confinement of light takes place in a single direction (planar waveguides), in two directions (cannel waveguides) and in three directions (photonic crystals).According to their geometry, the optical waveguides can be categorized by three basic structures: planar or slab waveguide, cylindrical channel or fiber and rectangular channel (strip, rib, strip-loaded waveguide, Embedded-strip waveguide, Buried channel waveguide, Slot waveguide and arrow waveguide) [2, 3], figure 1.

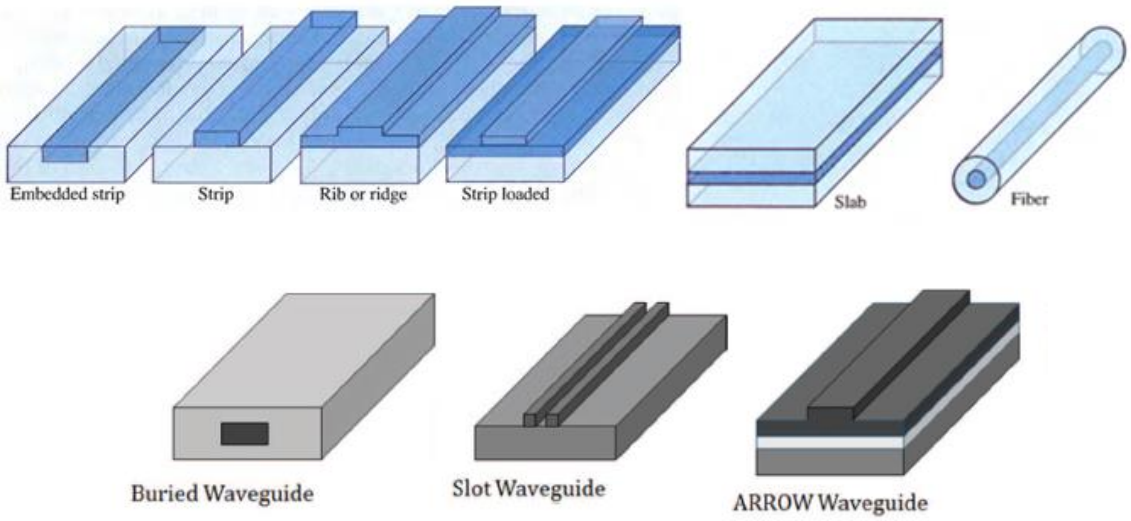

Figure 1: various waveguide geometries. The darker the shading, the higher the refractive index [2, 3]

5. Materials for integrated optical waveguides

The most advanced technology for fabricating waveguides is Ti:$LiNbO_3$. An embedded- strip waveguide is fabricated by diffusing titanium into a lithium niobate substrate to increase its refractive index in the region of the strip. GaAs strip waveguides are made by using layers of GaAs and AlGaAs of lower refractive index. Another semiconductor material that has recently gained importance in waveguides is InP. Glass waveguides are made by ion exchange. Polymer waveguides are also emerging as a viable technology. Waveguides can also be fabricated using silicon-on-insulator (Si-Si0 2 or SOl), and silicon and oxide etching tools, which are standards in the industry. This technology is also called silica-on-silicon. Since the refractive index of silica is ~ 3.5 and that of silica is less than 1.5, this combination of materials exhibits a large index-of-refraction difference Δn. Silicon processing and fabrication has been well developed by the microelectronics industry, and compatibility with CMOS fabrication technology is an important advantage [2].

6. Modeling of integrated optical waveguides

Generally, optical waveguides can be analyzed by solving Maxwell's equations or their reduced wave equation, with appropriate boundary conditions determined by their geometry and the materials properties. The main issue is to analyze the supported modes of the waveguide, which is an Eigen value problem. Analytical solutions of waveguides modes are only available in few simple cases such as slab waveguide which is invariant along the

waveguide axis. The most practical waveguides have usually complex geometries with non-uniform structure in the direction of wave propagation. Other examples are the waveguides with structures composed of nonlinear, anisotropic, or metamaterials. In these cases, numerical methods are needed for computing complex modes and to simulate the light wave propagation.

6.1. Guided modes in step-index planar waveguides

6.1.1. Ray approach

Consider the case of the guided mode propagating along an optical waveguide via series of total internal reflections at the core–substrate and core–cladding interfaces, as shown in Figure 2. The critical angle at the core–substrate interface is θ_{c1} and that at the core–cladding interface is θ_{c2}. Then, the angle θ must be greater than the critical angles at both interfaces ($\theta>\theta_{c1}$, θ_{c2}) to have total internal reflection. In this case, light is confined in the waveguide corresponding to a guided mode which propagates along the waveguide in a zigzag path. Rays making larger angles refract, losing a portion of their power at each reflection, and eventually vanish.

The condition for a guided mode is established on the basis of constructive interference, which implies that the total transversal phase shift in a complete round trip should be an integral number of 2π. Only a discrete number of angles fulfil that condition, and these will correspond to the propagation angles of guided modes. The phase shift encountered by the original wave in traveling from A to D must be equal to, or differ by an integer multiple of 2π, from that encountered when the wave reflects, travels from P to Q, and reflects once more. An additional phase shifts $\boldsymbol{\varphi}_{R1}$and $\boldsymbol{\varphi}_{R2}$ are associated with the internal reflections in the lower and upper interfaces. These phase shifts depend on the angle θ and on the polarization of the propagated wave.

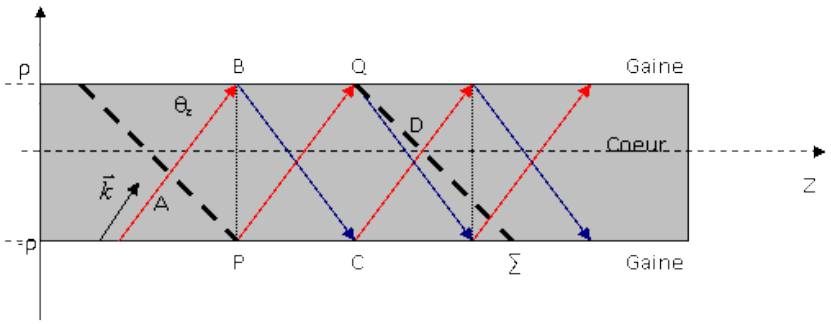

Figure 2: total reflection in the interfaces of an asymmetrical waveguide.

The difference in phase shifts for the two waves is described by [4]:

$$\varphi_{ABCD} - \varphi_{PQ} = 2\varphi_{AB} + \varphi_{R1} + \varphi_{R2} = 2m\pi \tag{1}$$

Where

$$\begin{aligned} \varphi_{AB} &= \varphi_{CD} = \left(\frac{2\pi}{\lambda} n_f\right)\left(2\rho \sin\theta_z\right) \\ \varphi_{BC} &= \varphi_{PQ} = \left(\frac{2\pi}{\lambda} n_f\right)\left(\frac{2\rho}{\sin\theta_z}\right) \end{aligned} \tag{2}$$

$$\begin{aligned} &\left(\varphi_R\right)_i = -2\arctan\left(g_i \frac{\sqrt{N^2 - n_i^2}}{\sqrt{n_f^2 - N^2}}\right) \quad ; \quad i = c(\text{cover}), s(substrate) \\ &g_i = 1 \quad : \quad for \quad TE \\ &g_i = \frac{n_f^2}{n_i^2} \quad : \quad for \quad TM \end{aligned} \tag{3}$$

Where: $N = n_f \cos\theta_z$

n_f , n_c and n_s are the core, cover and substrate indices, respectively.

We replace (2) and (3) in (1) by taking in consideration g_i, we get:

$$\left(\frac{4\pi\rho}{c} f\sqrt{n_f^2 - N^2}\right) - \arctan\left(\frac{\sqrt{N^2 - n_c^2}}{\sqrt{n_f^2 - N^2}}\right) - \arctan\left(\frac{\sqrt{N^2 - n_s^2}}{\sqrt{n_f^2 - N^2}}\right) - m\pi = 0 \tag{4}$$

For TE modes.

$$\left(\frac{4\pi\rho}{c} f\sqrt{n_f^2 - N^2}\right) - \arctan\left(\frac{n_f^2}{n_c^2}\frac{\sqrt{N^2 - n_c^2}}{\sqrt{n_f^2 - N^2}}\right) - \arctan\left(\frac{n_f^2}{n_s^2}\frac{\sqrt{N^2 - n_s^2}}{\sqrt{n_f^2 - N^2}}\right) - m\pi = 0 \tag{5}$$

For TM modes.

The dispersion equations describe discrete values of the effective refractive index *N* for guided modes corresponding to the mode number *m*, where the guided mode with *m = 0* is called the fundamental mode while those with *m ≠ 0* are called higher-order modes. The number of modes that can be supported by a slab waveguide depends on the thickness of the core, refractive indices and the wavelength of the source. Each mode has its cutoff frequency f_c below which waveguiding cannot occur.

Cut-off frequencies for TE modes

$$f_m = \frac{c\left(\arctan\left(\frac{\sqrt{n_s^2 - n_c^2}}{\sqrt{n_f^2 - n_s^2}}\right) + m\pi\right)}{\left(4\pi\rho\sqrt{n_f^2 - n_s^2}\right)} \quad (6)$$

Cut-off frequencies for TM modes

$$f_m = \frac{c\left(\arctan\left(\frac{n_f^2}{n_c^2}\frac{\sqrt{n_s^2 - n_c^2}}{\sqrt{n_f^2 - n_s^2}}\right) + m\pi\right)}{\left(4\pi\rho\sqrt{n_f^2 - n_s^2}\right)} \quad (7)$$

Where $n_s > n_c$

The optic-ray approach cannot be used to determine the guided mode electric field distribution, and hence, it is necessary to consider the Maxwell's equations approach.

6.1.2. Maxwell's equations approach

The study of photonic waveguides by the electromagnetic approach allows us to find the distribution of the E and M fields in each region of the waveguide, in addition to the information concerning the number of propagated modes, the cutoff frequency and the propagation constant of each mode.

We consider a slab waveguide constituted by three layers uniaxial crystals as presented in Figure 3. The core permittivity tensor is $\bar{\bar{\varepsilon}}_f$ with its optic axis in the direction of propagation z. The permittivity tensors of the media above and below the film guide are $\bar{\bar{\varepsilon}}_c$ and $\bar{\bar{\varepsilon}}_s$ respectively. We consider that the materials of the three layers are lossless and non-magnetic.

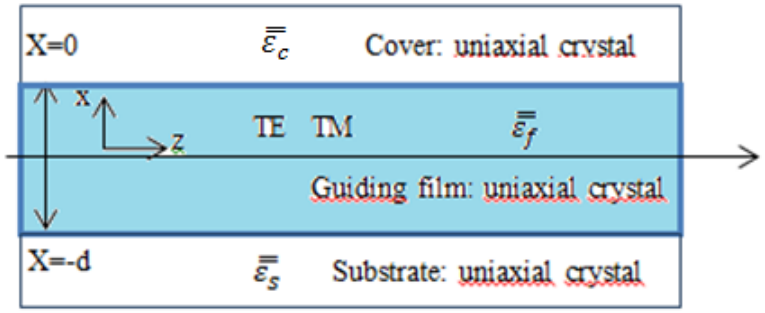

Figure 3: uniaxial anisotropic slab waveguide based sensor

Maxwell's equations can be written as follows:

$$\vec{\nabla} X \vec{E} = -j\omega\mu_0\vec{H} \tag{8}$$

$$\vec{\nabla} X \vec{H} = j\omega\varepsilon_0\varepsilon_i\vec{E} \tag{9}$$

Where

$$\varepsilon_i = \begin{bmatrix} \varepsilon_i & 0 & 0 \\ 0 & \varepsilon_i & 0 \\ 0 & 0 & \varepsilon_{iz} \end{bmatrix} = \varepsilon_0 \begin{bmatrix} n_i^2 & 0 & 0 \\ 0 & n_i^2 & 0 \\ 0 & 0 & n_{iz}^2 \end{bmatrix}$$

Notice that $\varepsilon_0$and $\mu_0$are the dielectric constant and the magnetic permeability of vacuum, i=c, f, s (cover, film, substrate).

We consider only time harmonic waves propagating in the z-direction with a propagation constant β, then:

$$\vec{E} = E(x).e^{j(\omega t-\beta z)} \tag{10}$$

$$\vec{\mathrm{H}} = H(x).e^{j(\omega t-\beta z)} \tag{11}$$

By using Cartesian coordinate system (x,y,z), equations (9) and (9) become:

$$\begin{cases} \frac{\partial E_z}{\partial y} - \frac{\partial E_y}{\partial z} = -j\omega\mu_0 H_x \\ \frac{\partial E_x}{\partial z} - \frac{\partial E_z}{\partial x} = -j\omega\mu_0 H_y \\ \frac{\partial E_y}{\partial x} - \frac{\partial E_x}{\partial y} = -j\omega\mu_0 H_z \\ \frac{\partial H_z}{\partial y} - \frac{\partial H_y}{\partial z} = j\omega\varepsilon_0\varepsilon_i E_x \\ \frac{\partial H_x}{\partial z} - \frac{\partial H_z}{\partial x} = j\omega\varepsilon_0\varepsilon_i E_y \\ \frac{\partial H_y}{\partial x} - \frac{\partial H_x}{\partial y} = j\omega\varepsilon_0\varepsilon_{iz} E_z \end{cases} \tag{12}$$

We simplify the description of the slab wave guide by assuming that there is no variation of the field in the y-direction.

$$\frac{\partial E_z}{\partial y} = \frac{\partial E_x}{\partial y} = \frac{\partial H_z}{\partial y} = \frac{\partial H_x}{\partial y} = 0 \tag{13}$$

The set of six equations become:

$$\begin{cases} -\frac{\partial E_y}{\partial z} = -j\omega\mu_0 H_x \\ \frac{\partial E_x}{\partial z} - \frac{\partial E_z}{\partial x} = -j\omega\mu_0 H_y \\ \frac{\partial E_y}{\partial x} = -j\omega\mu_0 H_z \\ -\frac{\partial H_y}{\partial z} = j\omega\varepsilon_0\varepsilon_i E_x \\ \frac{\partial H_x}{\partial z} - \frac{\partial H_z}{\partial x} = j\omega\varepsilon_0\varepsilon_i E_y \\ \frac{\partial H_y}{\partial x} = j\omega\varepsilon_0\varepsilon_{iz} E_z \end{cases} \quad (14)$$

6.1.2. 1.TE modes

In this case, electric field has only one component according the y axis, whereas, magnetic field component is zero according this axis.

$$\begin{cases} E_x = E_z = 0 \rightarrow \frac{\partial E_x}{\partial z} = \frac{\partial E_z}{\partial x} = 0 \\ H_y = 0 \rightarrow \frac{\partial H_y}{\partial z} = \frac{\partial H_y}{\partial x} = 0 \end{cases} \quad (15)$$

6.1.2.1.1. Wave equation of TE modes

We replace the simplifications above in the set of six equations above, we get:

$$j\beta E_y = -j\omega\mu_0 H_x \quad (16)$$

$$\frac{\partial E_y}{\partial x} = -j\omega\mu_0 H_z \quad (17)$$

$$-j\beta H_x - \frac{\partial H_z}{\partial x} = j\omega\varepsilon_0\varepsilon_i E_y \quad (18)$$

Where: $\frac{\partial}{\partial z} = -j\beta$

From equations of (16) and (17) we can obtain the magnetic field components in terms of the E_y component:

$$-\frac{\beta E_y}{\omega\mu_0} = H_x \quad (19)$$

$$\frac{j}{\omega\mu_0}\frac{\partial E_y}{\partial x} = H_z \quad (20)$$

Substituting H_x and $\frac{\partial H_z}{\partial x}$ into equation (18) we obtain the wave equations in each region:

$$\begin{cases} \frac{\partial^2 E_y}{\partial x^2} + \left(k_0^2 \varepsilon_f - \beta^2\right) E_y = 0; \quad film \\ \frac{\partial^2 E_y}{\partial x^2} - (\beta^2 - k_0^2 \varepsilon_c) E_y = 0; \quad cover \\ \frac{\partial^2 E_y}{\partial x^2} - (\beta^2 - k_0^2 \varepsilon_s) E_y = 0; \quad substrate \end{cases} \tag{21}$$

Where: $k_0^2 = \omega^2 \varepsilon_0 \mu_0$

Equation (21) is the wave equation of TE modes in each region (cover, film and substrate).

6.1.2.1.2. Solutions of the wave equations in the three regions for TE modes

Guided TE modes have exponentially decreasing behavior in the cover and substrate, and a sinusoidal behaviorin the film region. Then, solutions of the electric field in the three regions can be expressed as:

$$E_y = \begin{cases} Ae^{-\gamma_c x} & x \geq 0 \\ Be^{-j\gamma_f x} + Ce^{j\gamma_f x} & 0 > x > -d \\ De^{\gamma_s x} & x \leq -d \end{cases} \tag{22}$$

Solutions of the above wave equations must satisfy boundary conditions at the two dielectric interfaces, x=0 and x=-d. This requires that the tangential electric and magnetic fields (E_y and H_Z) be continuous at the dielectric discontinuities.

At x=0:

$$\begin{cases} E_{yc}(0) = E_{yf}(0) \\ H_{zc}(0) = H_{zf}(0) \end{cases} \tag{23}$$

At x=-d:

$$\begin{cases} E_{yf}(-d) = E_{ys}(-d) \\ H_{zf}(-d) = H_{zs}(-d) \end{cases} \tag{24}$$

This conditions giving place to four equations linear and homogenous that relate the constant parameters *A*, *B*, *C* and *D* and the propagation constant *β*:

$$\begin{cases} A - B - C + 0.D = 0 \\ -\gamma_c A + j\gamma_f B - j\gamma_f C + 0.D = 0 \\ 0.A + Be^{+j\gamma_f d} + Ce^{-j\gamma_f d} - De^{-\gamma_s d} = 0 \\ 0.A - j\gamma_f e^{+j\gamma_f d} B + j\gamma_f e^{-j\gamma_f d} C - \gamma_s De^{-\gamma_s d} = 0 \end{cases} \tag{25}$$

To have no trivial solutions of this set of equations, the determinant should be zero. After cumbersome calculation, the characteristic equation for TE modes is obtained:

$$k_0 d\sqrt{n_f^2 - N^2} = arctan\left(\sqrt{\frac{N^2-n_s^2}{n_f^2-N^2}}\right) + arctan\left(\sqrt{\frac{N^2-n_c^2}{n_f^2-N^2}}\right) + m\pi \qquad (26)$$

Where: $N = \frac{\beta}{k_0}$ is the effective refractive index of TE modes.

6.1.2.1.3. Field Distribution in each region for TE modes

By using the boundary conditions, we can determine the components of EM field E_y , H_x and H_z in each region function of A as follow:

$$E_y = \begin{cases} Ae^{-\gamma_c x} & x \geq 0 \\ A\left(cos\gamma_f x - \frac{\gamma_c}{\gamma_f} sin\gamma_f x\right) & 0 > x > -d \\ A\left(cos\gamma_f d + \frac{\gamma_c}{\gamma_f} sin\gamma_f d\right) e^{\gamma_s(x+d)} & x \leq -d \end{cases} \qquad (27)$$

$$H_x = \frac{\beta A}{\omega\mu_0} \begin{cases} e^{-\gamma_c x} & x \geq 0 \\ \left(cos\gamma_f x - \frac{\gamma_c}{\gamma_f} sin\gamma_f x\right) & 0 > x > -d \\ \left(cos\gamma_f d + \frac{\gamma_c}{\gamma_f} sin\gamma_f d\right) e^{\gamma_s(x+d)} & x \leq -d \end{cases} \qquad (28)$$

$$H_z = \frac{jA}{\omega\mu_0} \begin{cases} -\gamma_c e^{-\gamma_c x} & x \geq 0 \\ -\gamma_f\left(sin\gamma_f x + \frac{\gamma_c}{\gamma_f} cos\gamma_f x\right) & 0 > x > -d \\ \gamma_s\left(cos\gamma_f d + \frac{\gamma_c}{\gamma_f} sin\gamma_f d\right) e^{\gamma_s(x+d)} & x \leq -d \end{cases} \qquad (29)$$

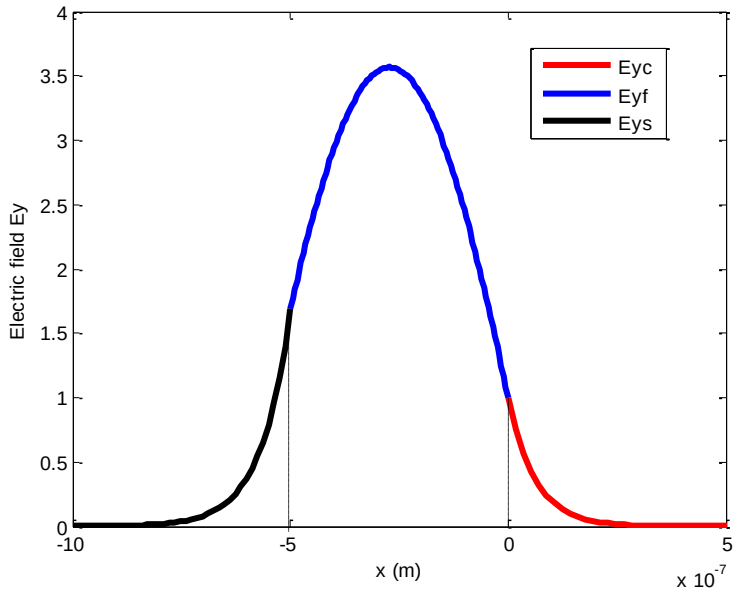

Figure 4: TE_0 magnetic field components (E_y) in three regions (cover, film and substrate) of slab waveguide (n_s= n_c =1.60, d=50 nm, $LiNbO_3$ as guiding film).

Figure 4 represent the dominant component E_y in each region of the slab waveguide, where we are considered that the cover and the substrate are isotropic. Red and black curves represent evanescent fields in the cover and substrate region, successively. However, blue curve represent electric field component in the core.

6.1.2.2. TM modes

In this case, magnetic field has only one component according the y axis, whereas, electric field component is zero according this axis.

$$\begin{cases} H_x = H_z = 0 \rightarrow \frac{\partial H_x}{\partial z} = \frac{\partial H_z}{\partial x} = 0 \\ E_y = 0 \rightarrow \frac{\partial E_y}{\partial z} = \frac{\partial E_y}{\partial x} = 0 \end{cases} \tag{30}$$

6.1.2.2.1. Wave equation for TM modes

The same steps from TE modes are followed. We get:

$$j\beta H_y = j\omega\varepsilon_0\varepsilon_i E_x \tag{31}$$

$$\frac{\partial H_y}{\partial x} = j\omega\varepsilon_0\varepsilon_{iz} E_z \tag{32}$$

$$-j\beta E_x - \frac{\partial E_z}{\partial x} = -j\omega\mu_0 H_y \tag{33}$$

From equations (31) and (32) we can obtain the electric field components in terms of the H_y component:

$$\frac{\beta}{\omega\varepsilon_0\varepsilon_i} H_y = E_x \tag{34}$$

$$\frac{-j}{\omega\varepsilon_0\varepsilon_{iz}} \frac{\partial H_y}{\partial x} = E_z \tag{35}$$

Substituting E_x and $\frac{\partial E_z}{\partial x}$ into equation (33) we obtain the wave equations of TM modes in each region:

$$\begin{cases} \frac{\partial^2 H_y}{\partial x^2} + \left(k_0^2\varepsilon_{fz} - \beta^2 \frac{\varepsilon_{fz}}{\varepsilon_f}\right) H_y = 0; \quad film \\ \frac{\partial^2 H_y}{\partial x^2} - \left(\beta^2 \frac{\varepsilon_{cz}}{\varepsilon_c} - k_0^2\varepsilon_{cz}\right) H_y = 0; \quad cover \\ \frac{\partial^2 H_y}{\partial x^2} - \left(\beta^2 \frac{\varepsilon_{sz}}{\varepsilon_s} - k_0^2\varepsilon_{sz}\right) H_y = 0; \quad substrate \end{cases} \tag{36}$$

Equation (36) is the wave equation of TM modes in each region (cover, film and substrate).

6.1.2.2.2. Solutions of the wave equations in the three regions for TM modes

In a similar way seen for TE modes, guided TM modes have exponentially decreasing behavior in the cover and substrate, and a sinusoidal behaviorin the film region. Then, solutions of the electric field in the three regions can be expressed as:

$$H_y = \begin{cases} Ae^{-\gamma_c' x} & x \geq 0 \\ Be^{j\gamma_f' x} + Ce^{-j\gamma_f' x} & 0 > x > -d \\ De^{\gamma_s' x} & x \leq -d \end{cases} \quad (37)$$

Where

$$\gamma_f' = \sqrt{k_0^2 \varepsilon_{fz} - \beta^2 \frac{\varepsilon_{fz}}{\varepsilon_f}} \quad (38)$$

$$\gamma_c' = \sqrt{\beta^2 \frac{\varepsilon_{cz}}{\varepsilon_c} - k_0^2 \varepsilon_{cz}} \quad (39)$$

$$\gamma_s' = \sqrt{\beta^2 \frac{\varepsilon_{sz}}{\varepsilon_s} - k_0^2 \varepsilon_{sz}} \quad (40)$$

Solutions of the above wave equations must satisfy boundary conditions at the two dielectric interfaces, x=0 and x=-d. This requires that the tangential electric and magnetic fields (H_y and E_Z) be continuous at the dielectric discontinuities.

At x=0:

$$\begin{cases} H_{yc}(0) = H_{yf}(0) \\ E_{zc}(0) = E_{zf}(0) \end{cases} \quad (41)$$

At x=-d:

$$\begin{cases} H_{yf}(-d) = H_{ys}(-d) \\ E_{zf}(-d) = E_{zs}(-d) \end{cases} \quad (42)$$

This conditions giving place to four equations linear and homogenous that relate the constant parameters *A, B, C* and *D* and the propagation constant *β*.

To have no trivial solutions of this set of equations, the determinant should be zero. After cumbersome calculation; the characteristic equation for TM modes is obtained:

$$k_0 d \frac{n_{fz}}{n_f} \sqrt{n_f^2 - N^2} = arctan \frac{n_{fz} n_f}{n_{cz} n_c} \sqrt{\frac{N^2 - n_p^2}{n_f^2 - N^2}} + arctan \frac{n_{fz} n_f}{n_{sz} n_s} \sqrt{\frac{N^2 - n_s^2}{n_f^2 - N^2}} + m\pi \quad (43)$$

Where: $N = \frac{\beta}{k_0}$ is the effective refractive index of TM modes.

6.1.2.2.3. Field Distribution of TM modes in each region

By using the boundary conditions, we can determine constants and different components of EM field as follow:

$$H_y = A\begin{cases} e^{-\gamma_c' x} & x \geq 0 \\ cos\gamma_f' x - \frac{n_f^2}{n_c^2}\frac{\gamma_c'}{\gamma_f'} sin\gamma_f' x & -d < x < 0 \\ \left(cos\gamma_f' d + \frac{n_f^2}{n_c^2}\frac{\gamma_c'}{\gamma_f'} sin\gamma_f' d\right) e^{\gamma_s'(x+d)} & x \leq -d \end{cases} \quad (44)$$

$E_x$andE_z can be determined from (10) and (11) respectively.

$$E_x = \frac{\beta A}{\omega\varepsilon_0\varepsilon_i}\begin{cases} e^{-\gamma_c' x} & x \geq 0 \\ cos\gamma_f' x - \frac{n_f^2}{n_c^2}\frac{\gamma_c'}{\gamma_f'} sin\gamma_f' x & -d < x < 0 \\ \left(cos\gamma_f' d + \frac{n_f^2}{n_c^2}\frac{\gamma_c'}{\gamma_f'} sin\gamma_f' d\right) e^{\gamma_s'(x+d)} & x \leq -d \end{cases} \quad (45)$$

$$E_z = \frac{-jA}{\omega\varepsilon_0\varepsilon_{iz}}\begin{cases} -\gamma_c e^{-\gamma_c' x} & x \geq 0 \\ -\gamma_f'\left(sin\gamma_f' x + \frac{n_f^2}{n_c^2}\frac{\gamma_c'}{\gamma_f'} cos\gamma_f' x\right) & -d < x < 0 \\ \gamma_s'\left(cos\gamma_f' d + \frac{n_f^2}{n_c^2}\frac{\gamma_c'}{\gamma_f'} sin\gamma_f' d\right) e^{\gamma_s'(x+d)} & x \leq -d \end{cases} \quad (46)$$

Where the dielectric constant ε_i differs from region to region, it is equal to ε_c in the cover region and to ε_s in the substrate region and ε_f in the film guide.

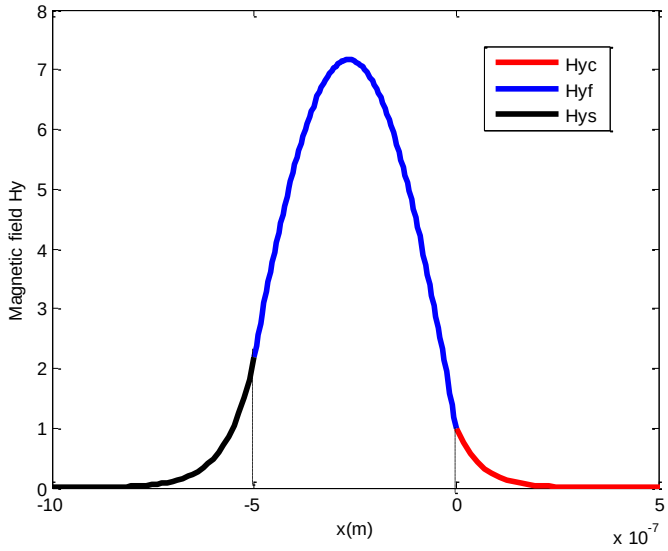

Figure 5: TM_0 magnetic field components (H_y) in three regions (cover, film and substrate) of slab waveguide (n_s= n_c =1.60, d=50 nm, $LiNbO_3$ as guiding film).

Figure 5 represent the magnetic field component H_y in each region of the slab waveguide, where we are considered that the cover and the substrate are isotropic. Red and black curves represent evanescent fields in the cover and substrate region, successively. However, blue curve represent magnetic field component in the core.

6.1.2.3. Solutions of the characteristic equations for both TE and TM modes

The characteristic equations link the propagation constants of modes with the different parameters of the waveguide. We developed a program in Matlab, based on the bisection method, which allowed us to calculate the propagation constants of both TE and TM modes (fundamental modes and higher order modes) as a function of the frequency, of the wavelength and the thickness of the waveguiding film. The developed program also allowed us to see the influence of the physical and geometrical parameters and the wavelength of source on the propagation constants and the cutoff frequencies of the propagated modes.

The slab waveguide consists essentially of a core of $LiNbO_3$ on a glass substrate; the wavelength of the source is 650 nm.

Figure 6 represents effective indices (propagation constants) versus frequency of TE_0, TE_1, TM_0 and TM_1 modes. The figure shows that, the effective indices of TE modes are greater than those of TM modes. Whereas, cut off frequencies of the latter, are greater than those of TE modes. On the other hand, the effective indices of fundamental modes are greater than those of higher order modes. Whereas, cut off frequencies of the latter, are greater than those of fundamental ones. If the slab waveguide is symmetric, we note that TE and TM have the same cut off frequencies, figure 7.

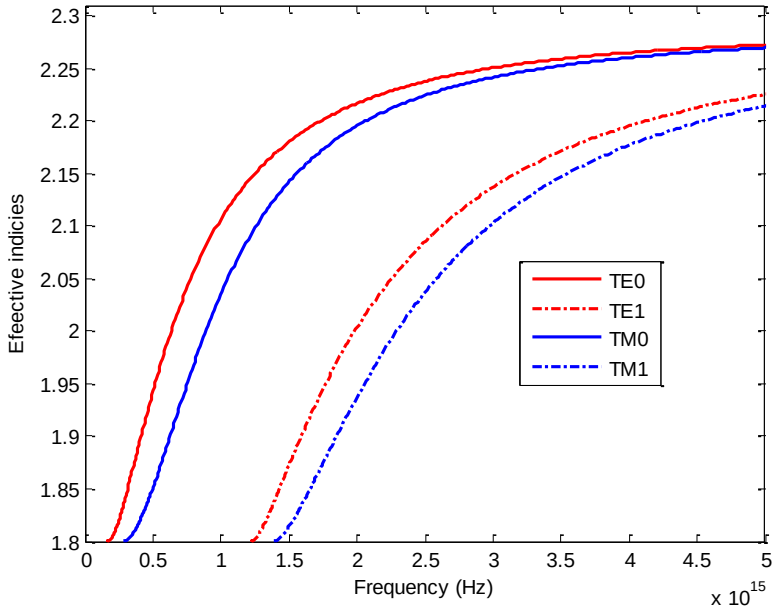

Figure 6: effective index versus frequency of TE and TM modes in asymmetric slab waveguide for (n_s=1.80, n_c =1.628, d=100 nm, $LiNbO_3$ as guiding film).

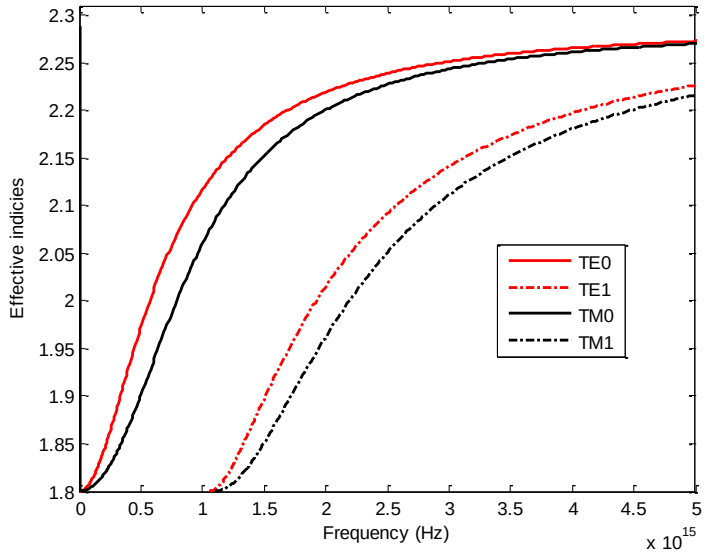

Figure 7: effective index versus frequency of TE and TM modes in symmetric slab waveguide for (n_s=1.80, n_c =1.628, d=100 nm, $LiNbO_3$ as guiding film).

6.1.2.4. The influence of the geometric parameter

Figures 8 and 9 show the propagation constants of fundamental modes (TE_0, TM_0) as well as modes of order one (TE_1, TM_1), function of the frequency for different core thicknesses. The figures show that the increase in the thickness of the core induces an increase

in the propagation constants of the modes as well as a decrease in their cut-off frequencies, especially for higher order modes. As a conclusion, the thickness of the core plays an important role in the choice of the frequency ranges of the propagated modes.

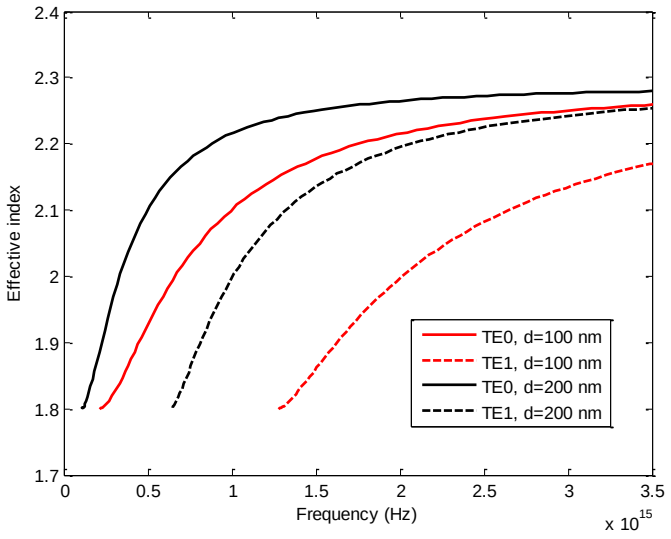

Figure 8: effective index versus frequency of TE_0 modes in slab waveguide for different core thicknesses, (n_s=1.80, n_c =1.628, $LiNbO_3$ as guiding film).

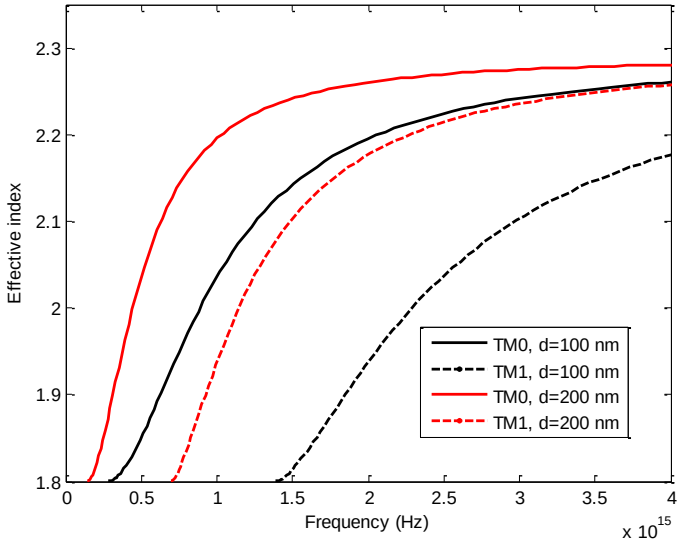

Figure 9: effective index versus frequency of TM modes in slab waveguide for different core thicknesses, (n_s=1.80, n_c =1.48, $LiNbO_3$ as guiding film).

6.1.2.5. The influence of the wavelength source

For different wavelengths source, we illustrate de propagation constants of (TE_0, TE_1, TM_0 and TM_1) modes function of the core thicknesses. As shown in figures (10, 11), the increase in the wavelength source induces a decrease in the propagation constants of the

modes as well as an increase in their cut-off thicknesses, especially for de modes of higher orders.

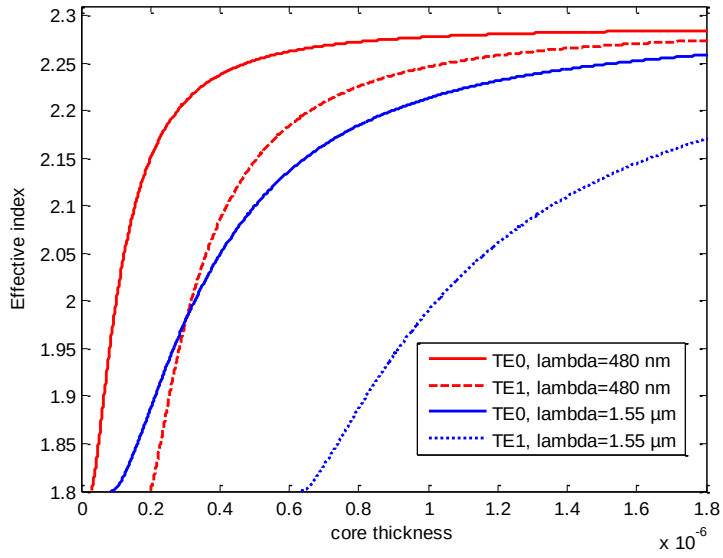

Figure 10: effective index versus core thickness of TE modes in slab waveguide for different wavelength source, (n_s=1.80, n_p =1.628, d=100 nm, $LiNbO_3$ as guiding film).

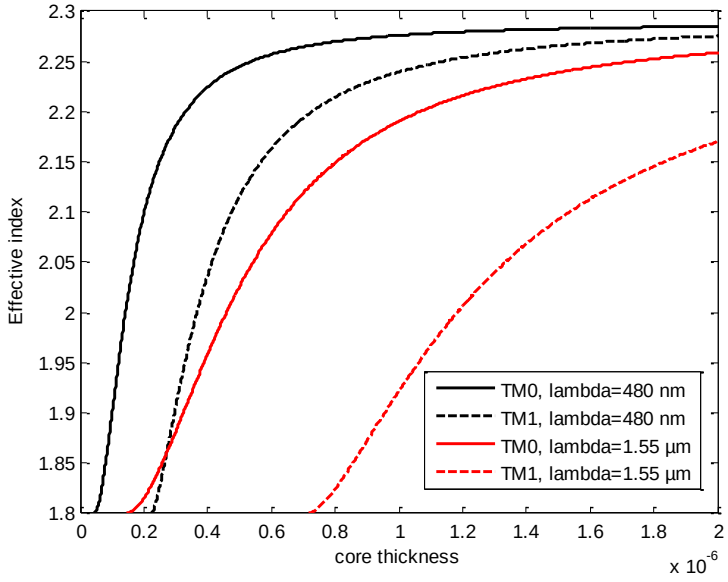

Figure 11: effective index versus core thickness of TM modes in slab waveguide for different wavelength source, (n_s=1.80, n_p =1.628, d=100 nm, $LiNbO_3$ as guiding film).

6.1.2.6. The influence of the physical parameters

6.1.2.6.1. The influence of cover refractive index

Changes in the cover index don't have great influence on the propagated modes, and especially for TM modes, figure 13. The increase of the cover index induces small decrease

in cut-off frequencies of modes and neglected increase in their propagation constants, figure 12.

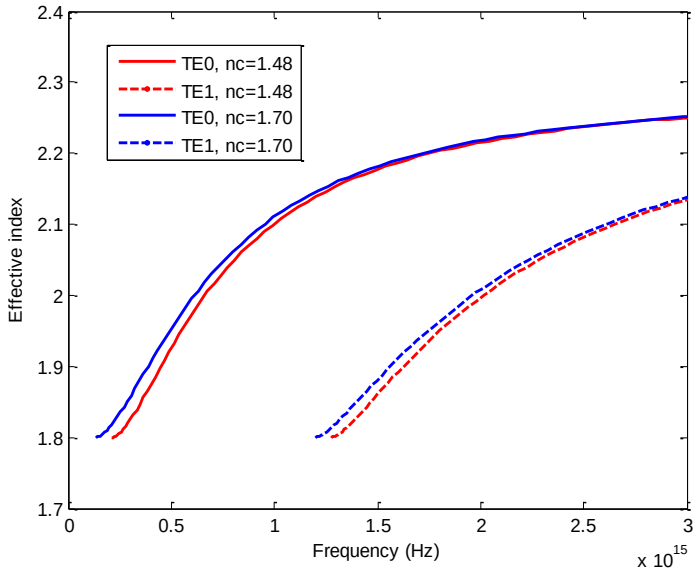

Figure 12: effective index versus frequency of TE0 modes in slab waveguide for different cover indices, (n_s=1.80, d =100 nm, $LiNbO_3$ as guiding film).

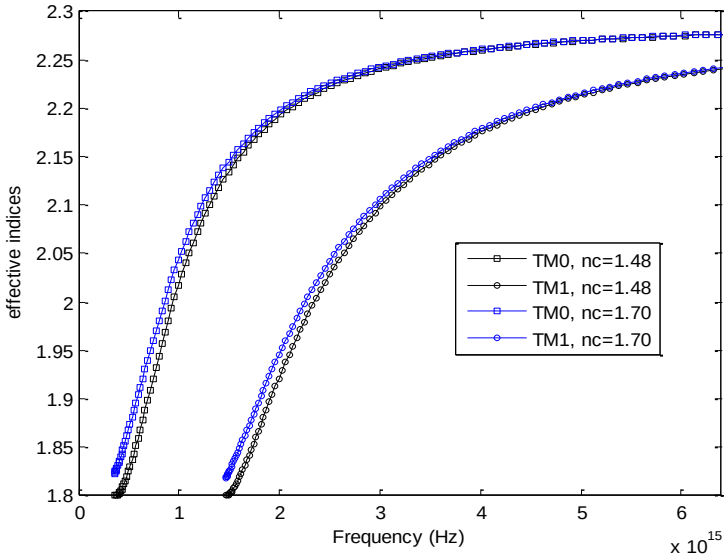

Figure 13: effective index versus frequency of TM modes in slab waveguide for different cover indices, (n_s=1.80, d=100 nm, $LiNbO_3$ as guiding film).

6.1.2.6.2. The influence of substrate refractive index

Substrate refractive index changes don't have great influence on the propagation constants in higher frequencies (far from cut-off frequencies). However, the increase of the Substrate refractive index induces an increase in the cut-off frequencies of the propagated

modes and their propagation constants near to the cut-off frequencies, in both TE and TM cases, figure (14, 15).

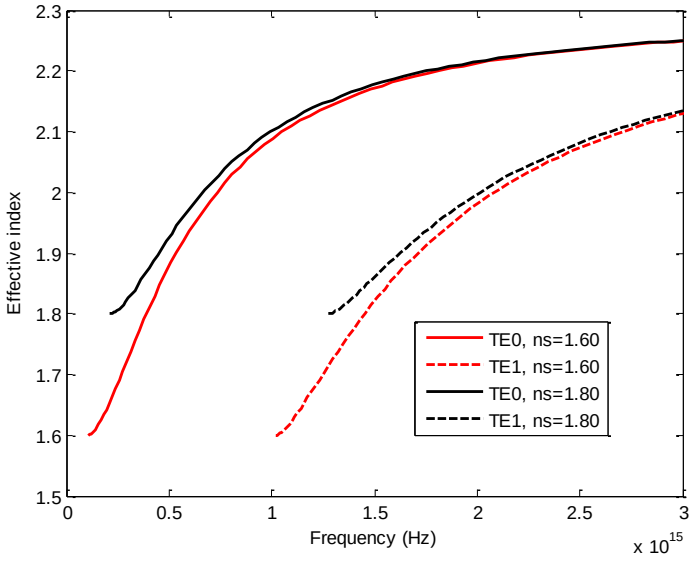

Figure 14: effective index versus frequency of TE0 modes in slab waveguide for different substrate indices, (n_p=1.48, d =100 nm, $LiNbO_3$ as guiding film).

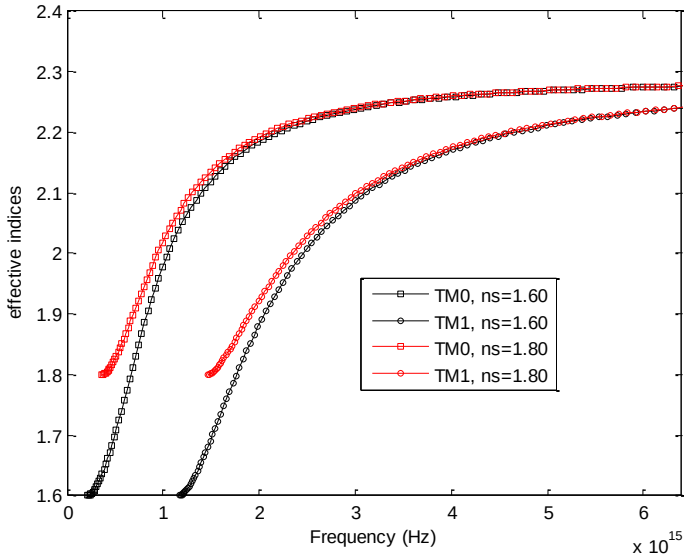

Figure 15: effective index versus frequency of TM modes in slab waveguide for different substrate indices, (n_c=1.48, d=100 nm, $LiNbO_3$ as guiding film).

6.1.2.6.3. The influence of core refractive index

Figures 16, 17 show very clearly that small changes in core refractive index induce great changes in the propagation constants of modes TE and TM and their cut off frequencies. In fact, the increase of the core refractive index induces an increase of the propagation

constants and a decrease in the cut off frequencies. Notice that, higher order modes are more sensitive to the core refractive index changes.

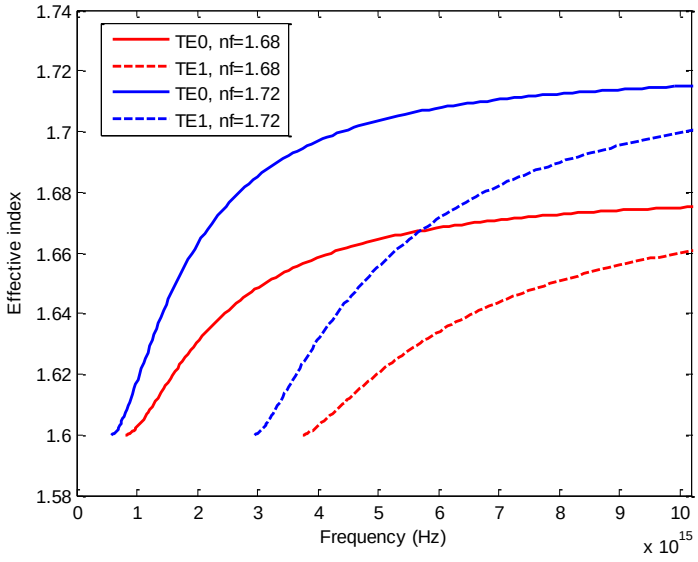

Figure 16: effective index versus frequency of TE modes in slab waveguide for different core indices, (n_c=1.48, n_s=1.60, d=100 nm).

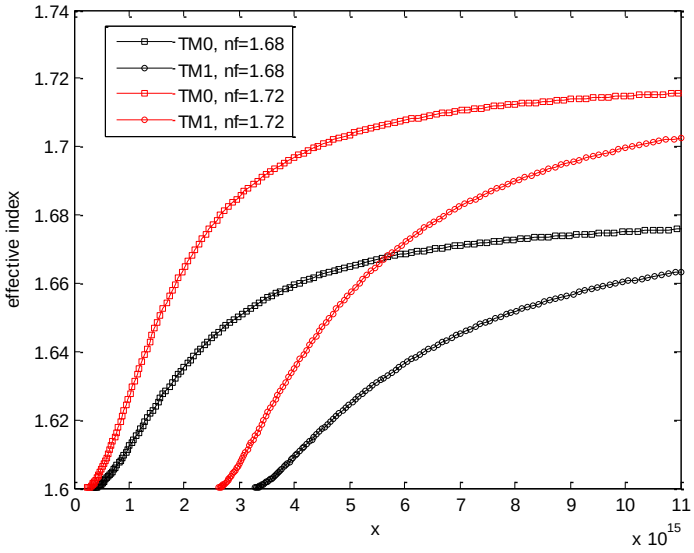

Figure 17: effective index versus frequency of TM modes in slab waveguide for different core indices, (n_c=1.59, n_s=1.60, d=100 nm).

6.2. Guided Modes in Channel Waveguides

When dealing with planar waveguides, whether step-index or graded index structures, light propagation can be described in terms of two mutually orthogonal polarisations, namely, the TE and TM propagating modes. In contrast, in channel optical waveguidesthere are no

pure TE or TM modes, but instead there are two families of hybridtransversal electromagnetic modes (TEM). Fortunately, the TEM modes that propagatein channel waveguides are strongly polarised along the *x* or *y* direction (*z* being thedirection of propagation of light), and therefore a classification can be made accordingto the major component of the electric field associated with the electromagnetic radiation. Optical modes having the main electric field component along the *x-axis* are called E_{mn}^{x} modes, and behave very similarly to the TM modes in a planar waveguide.For this reason, they are known as *quasi-TM modes*. The subscripts *p* and *q* denote the number of nodes of the electric field E_x in the *x* and *y* direction, respectively. Accordingly, the E_{mn}^{y} modes have E_y as the major component of the electric field, andare closely related to the TE modes in a planar waveguide, and can be considered as *quasi-TE modes* [1].

6.2.1. The effective index method

The effective index method (EIM) is an approximate analysis for calculating the modal fields and the propagation constant in channel waveguides having arbitrary geometry and index profiles. In this method, the propagation constant of the TM_{m-1} or $TE_{n-1,}$ (according to E_{mn}^{x} or E_{mn}^{y}), mode in the slab of thickness *a* is first calculated and used to define an effective index n_{eff}, which forms the refractive index of the second slab of thickness *b.* The propagation constant of the TE_{n-1} (TM_{m-1}) mode in the second slab then represents the propagation constant of the E_{mn}^{x} (E_{mn}^{y}) mode in the channel waveguide [5].

The EIM treats the channel waveguide as the superimposition of two 1D waveguides: planar waveguide I confines the light in the *x* direction, while planar waveguide II traps the light in the *y* direction [1], (Figure 18). The depth and width of the core waveguide are *a* and *b* respectively. The waveguide core with refractive index n_f is embedded in a substrate of refractive index of *ns* being the upper part delimited by the cover with refractive index n_c.

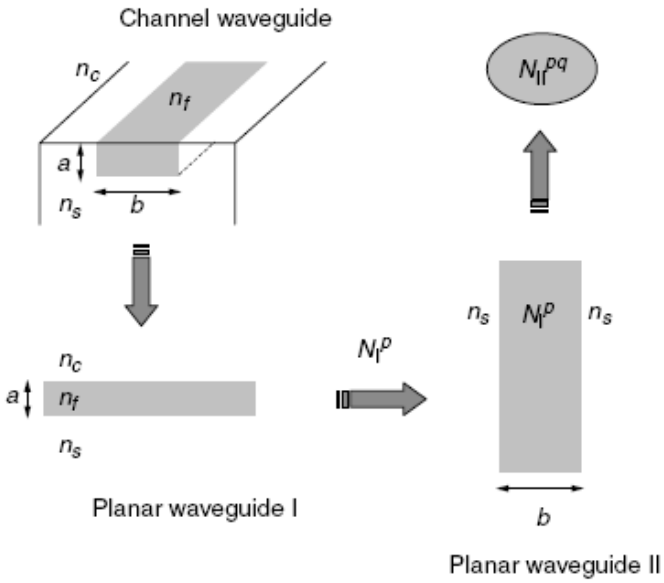

Figure 18: Scheme of the effective index method for solving the propagation constant of a step-index channel waveguide. Starting from a 2D waveguide, the problem is split into two step-index planar waveguides [1].

6.2.1. 1. E_{mn}^{x} Modes

For propagating modes polarised mainly along the *x* direction E_{mn}^{x} (m and n are integers), the field components are E_x, E_y, H_y, H_z and E_z, where the major field components are E_x, H_y (H_x=0). According to the Maxwell equations, the electromagnetic field representation and the wave equation are obtained as:

$$\begin{cases} E_x = \frac{\omega\mu_0}{\beta} H_y + \frac{1}{\beta\omega n_j^2 \varepsilon_0} \frac{\partial^2 H_y}{\partial x^2} \\ E_y = \frac{1}{\beta\omega n_j^2 \varepsilon_0} \frac{\partial^2 H_y}{\partial x \partial y} \\ E_z = -\frac{i}{\omega n_j^2 \varepsilon_0} \frac{\partial H_y}{\partial x} \\ H_z = -\frac{i}{\beta} \frac{\partial H_y}{\partial y} \\ H_x = 0 \end{cases} \quad (47)$$

A complete solution for the electromagnetic optical fields can be established once the solution for H_y is known.

$$\frac{\partial^2 H_y}{\partial x^2} + \frac{\partial^2 H_y}{\partial y^2} + \left(k^2 n_j^2 - \beta^2\right) H_y = 0 \quad (48)$$

In the EIM, we first express the solution of the wave Eq. (48) for the E_{mn}^{x} mode, by using the separation of variables, as:

$$H_y(x,y) = X(x)Y(y) \tag{49}$$

Substituting Eq. (49) into Eq. (48) and after taking in account the approximation used by the effective index method, which consists of assuming that the function *Y(x, y)* has a slowly variation respect to the *y* coordinate [6], we obtain a system of two differential equations:

$$\frac{\partial^2 X}{\partial x^2} + (k_0^2 n^2 - k_0^2 N_1(y)^2)X = 0 \tag{50}$$

$$\frac{\partial^2 Y}{\partial y^2} + (k_0^2 N_1(y)^2 - \beta^2)Y = 0 \tag{51}$$

6.2.1.1.1. Solution of the wave equation of E_{mn}^{x} Modes

The first step in the EIM procedure consists of solving the differential equation (50), using the *y* coordinate as a parameter. The eigenvalue solution of equation (50) gives an effective index profile $N_1(y)$, which depends explicitly on the *y* coordinate. Once the index distribution $N_1(y)$ has been obtained, we introduce this function in the second differential equation (51), thus performing the second step in the problem resolution.

If one considers the propagation in the asymmetric step-index planar waveguide I in figure 18, which consists of a film of width *a* and refractive index n_f, surrounded by a cover and a substrate, having refractive indices n_c and n_s respectively. One notices that the component of the field EM almost perpendicular to the plane of incidence is the most dominant component of the field H which is H_y. So this propagation is similar to the TM mode in this slab waveguide. The effective indices supported by this waveguide can be calculated by using one method solving step index planar structures. The wave equations in the three regions are:

$$\begin{cases} \frac{\partial^2 X}{\partial x^2} - (k_0^2 N_1(y)^2 - k_0^2 n_s^2)X = 0; \ \ substrate \\ \frac{\partial^2 X}{\partial x^2} - (k_0^2 N_1(y)^2 - k_0^2 n_c^2)X = 0; \ \ cover \\ \frac{\partial^2 X}{\partial x^2} + \left(k_0^2 n_f^2 - k_0^2 N_1(y)^2\right)X = 0; \ \ film \end{cases} \tag{52}$$

The solution of (52) is the solution of an asymmetric step-index planar waveguide for TM mode, and this is given by [7]:

$$X(x) = \begin{cases} A_1 cos(\gamma_{f1} a - \varphi) e^{-\gamma_{c1}(x-a)} & x > a \\ A_1 cos(\gamma_{f1} x - \varphi) & -a \le x \le a \\ A_1 cos(\gamma_{f1} a + \varphi) e^{\gamma_{s1}(x+a)} & x < -a \end{cases} \quad (53)$$

Where

$$\begin{cases} \gamma_{f1}^2 = k_0^2 n_f^2 - k_0^2 N_1(y)^2 \\ \gamma_{c1}^2 = k_0^2 N_1(y)^2 - k_0^2 n_c^2 \\ \gamma_{s1}^2 = k_0^2 N_1(y)^2 - k_0^2 n_s^2 \end{cases} \quad (54)$$

X(x) and $-\frac{i}{\omega n_j^2 \varepsilon_0} \frac{\partial X(x)}{\partial x}$ are continuous at the boundaries of core–cladding interfaces x=±a. after some calculation, we get:

$$\tan(\gamma_{f1} a - \varphi) = \frac{n_f^2}{n_c^2} \frac{\gamma_{c1}}{\gamma_{f1}} \quad (55)$$

$$\tan(\gamma_{f1} a + \varphi) = \frac{n_f^2}{n_s^2} \frac{\gamma_{s1}}{\gamma_{f1}} \quad (56)$$

From these two equations we deduce the characteristic equation of the asymmetric step-index planar waveguide for TM mode is given by:

$$2k_0 a \sqrt{n_f^2 - N_1^2} = arctan \frac{n_f^2}{n_c^2} \sqrt{\frac{N_1^2 - n_c^2}{n_f^2 - N_1^2}} + arctan \frac{n_f^2}{n_s^2} \sqrt{\frac{N_1^2 - n_s^2}{n_f^2 - N_1^2}} + m\pi \quad (57)$$

$$2\varphi = m\pi + arctan \frac{n_f^2}{n_s^2} \sqrt{\frac{N_1^2 - n_s^2}{n_f^2 - N_1^2}} - arctan \frac{n_f^2}{n_c^2} \sqrt{\frac{N_1^2 - n_c^2}{n_f^2 - N_1^2}} \quad (58)$$

Where

$\beta_1 = k_0 N_1$

Now the second step consists of considering a symmetric step-index planar waveguide (waveguide II) formed by a core film of thickness *b*, whose refractive index is the effective refractive index N_1 calculated previously. The film is surrounded on both sides by a medium with refractive index equal to the substrate refractive index n_s. If one considers the propagation in this slab waveguide, one notes that the component of the field EM almost perpendicular to the plane of incidence is the most dominant component of the field E which is E_x. therefore this propagation is similar to the mode TE. This new waveguide can easily be solved by conventional methods applied to planar structures. The effective refractive index *N* calculated by this planar waveguide corresponds to the modal effective index for the channel waveguide.

The wave equation (51) in the core and the substrate regions are given by:

$$\begin{cases} \frac{\partial^2 Y}{\partial y^2} + (k_0^2 N_1(y)^2 - k_0^2 N^2)Y = 0; \quad film \\ \frac{\partial^2 Y}{\partial y^2} - (k_0^2 N^2 - k_0^2 n_s^2)Y = 0; \quad substrate \end{cases} \tag{59}$$

The solution of (59) is the solution of a symmetric step-index planar waveguide for TE mode and this is given by:

$$\mathrm{Y(y)} = \begin{cases} A_2 \cos(\gamma_f b - \eta)\, e^{-\gamma_s (y-b)} & y > b \\ A_2 \cos(\gamma_f y - \eta) & -b \le y \le b \\ A_2 \cos(\gamma_f b + \eta)\, e^{\gamma_s (y+b)} & y < -b \end{cases} \tag{60}$$

Where

$$\begin{cases} \gamma_f^2 = k_0^2 N_1^2 - \beta^2 \\ \gamma_s^2 = \beta^2 - k_0^2 n_s^2 \end{cases} \tag{61}$$

Where

$\beta = k_0 N$

Y(x) and $\frac{\partial \mathrm{Y(x)}}{\partial x}$ are continuous at the boundaries of core–cladding interfaces x=±b. after some calculation, we get:

$$tan(\gamma_f b - \eta) = \frac{\gamma_s}{\gamma_f} \tag{62}$$

$$tan(\gamma_f b + \eta) = \frac{\gamma_s}{\gamma_f} \tag{63}$$

From these two equations we deduce the characteristic equation of the symmetric step-index planar waveguide for TE mode as:

$$2k_0 b\sqrt{N_1^2 - N^2} = 2arctan\left(\sqrt{\frac{N^2 - n_s^2}{N_1^2 - N^2}}\right) + m\pi \tag{64}$$

$$\eta = \frac{m\pi}{2} \tag{65}$$

6.2.1. 1.2. Field distribution of E_{mn}^x modes in each region

Figure 19, which consist of a central homogeneous high index core surrounded by four homogeneous low index regions. The waveguide core, referred to region I in the figure 19, has a rectangular cross-section with dimensions *a* and *b* in the *x* and *y* directions respectively, and a refractive index n_1. The central core is surrounded by homogeneous regions II, III, IV and V as indicated in Figure 19, which have refractive indices n_c and n_s respectively.

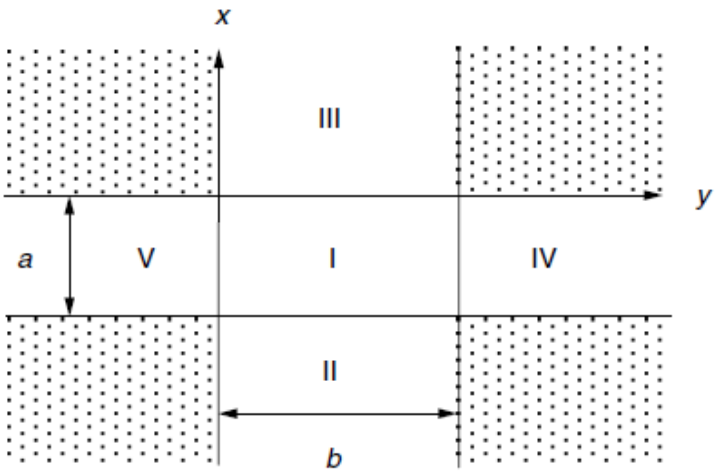

Figure 19: Three-dimensional rectangular waveguide. The dotted regions are not considered in this analysis [1].

The H_y components are obtained by multiplying (53) and (60) equations in each region as in [7]. The other components are obtained by replacing the derivatives $\frac{\partial H_y}{\partial x}$, $\frac{\partial H_y}{\partial y}$, $\frac{\partial^2 H_y}{\partial x^2}$ and $\frac{\partial^2 H_y}{\partial x \partial y}$ in the formula (47) in each region. After calculation, we get the complete field distribution of E_{mn}^x modes as fallow:

Region I

$$\begin{cases} H_y = A cos(\gamma_{f1} x - \varphi) cos(\gamma_f y - \eta) \\ E_x = A\left(\frac{\omega\mu_0}{\beta} - \frac{\gamma_{f1}^2}{\beta\omega n_f^2 \varepsilon_0}\right)\left(cos(\gamma_{f1} x - \varphi) cos(\gamma_f y - \eta)\right) \\ E_y = \frac{A\gamma_f \gamma_{f1}}{\beta\omega n_f^2 \varepsilon_0} sin(\gamma_{f1} x - \varphi) sin(\gamma_f y - \eta) \\ E_z = \frac{Ai\gamma_{f1}}{\omega n_f^2 \varepsilon_0} sin(\gamma_{f1} x - \varphi) cos(\gamma_f y - \eta) \\ H_z = \frac{Ai\gamma_f}{\beta} cos(\gamma_{f1} x - \varphi) sin(\gamma_f y - \eta) \\ H_x = 0 \end{cases} \quad (66)$$

Region II

$$\begin{cases} H_y = A\cos(\gamma_f y-\eta)\cos(\gamma_{f1}a+\varphi)e^{\gamma_{s1}(x+a)} \\ E_x = A\left(\frac{\omega\mu_0}{\beta}+\frac{\gamma_{s1}^2}{\beta\omega n_s^2\varepsilon_0}\right)\cos(\gamma_f y-\eta)\cos(\gamma_{f1}a+\varphi)e^{\gamma_{s1}(x+a)} \\ E_y = \frac{-A\gamma_{s1}}{\beta\omega n_s^2\varepsilon_0}\sin(\gamma_f y-\eta)\cos(\gamma_{f1}a+\varphi)e^{\gamma_{s1}(x+a)} \\ E_z = -\frac{iA\gamma_{s1}}{\omega n_s^2\varepsilon_0}\cos(\gamma_f y-\eta)\cos(\gamma_{f1}a+\varphi)e^{\gamma_{s1}(x+a)} \\ H_z = \frac{iA}{\beta}\sin(\gamma_f y-\eta)\cos(\gamma_{f1}a+\varphi)e^{\gamma_{s1}(x+a)} \\ H_x = 0 \end{cases} \quad (67)$$

Region III

$$\begin{cases} H_y = A\cos(\gamma_{f1}a-\varphi)\cos(\gamma_f y-\eta)e^{-\gamma_{c1}(x-a)} \\ E_x = A\left(\frac{\omega\mu_0}{\beta}+\frac{\gamma_{c1}^2}{\beta\omega n_c^2\varepsilon_0}\right)\cos(\gamma_{f1}a-\varphi)\cos(\gamma_f y-\eta)e^{-\gamma_{c1}(x-a)} \\ E_y = \frac{A\gamma_f\gamma_{c1}}{\beta\omega n_c^2\varepsilon_0}\cos(\gamma_{f1}a-\varphi)\sin(\gamma_f y-\eta)e^{-\gamma_{c1}(x-a)} \\ E_z = \frac{Ai\gamma_{c1}}{\omega n_c^2\varepsilon_0}\cos(\gamma_{f1}a-\varphi)\cos(\gamma_f y-\eta)e^{-\gamma_{c1}(x-a)} \\ H_z = \frac{iA\gamma_f}{\beta}\cos(\gamma_{f1}a-\varphi)\sin(\gamma_f y-\eta)e^{-\gamma_{c1}(x-a)} \\ H_x = 0 \end{cases} \quad (68)$$

Region IV

$$\begin{cases} H_y = A\cos(\gamma_f b-\eta)\cos(\gamma_{f1}x-\varphi)e^{-\gamma_s(y-b)} \\ E_x = A\left(\frac{\omega\mu_0}{\beta}-\frac{\gamma_{f1}^2}{\beta\omega n_s^2\varepsilon_0}\right)\cos(\gamma_f b-\eta)\cos(\gamma_{f1}x-\varphi)e^{-\gamma_s(y-b)} \\ E_y = \frac{A\gamma_{f1}\gamma_s}{\beta\omega n_s^2\varepsilon_0}\cos(\gamma_f b-\eta)\sin(\gamma_{f1}x-\varphi)e^{-\gamma_s(y-b)} \\ E_z = \frac{Ai\gamma_{f1}}{\omega n_s^2\varepsilon_0}\cos(\gamma_f b-\eta)\sin(\gamma_{f1}x-\varphi)e^{-\gamma_s(y-b)} \\ H_z = \frac{i\gamma_s A}{\beta}\cos(\gamma_f b-\eta)\cos(\gamma_{f1}x-\varphi)e^{-\gamma_s(y-b)} \\ H_x = 0 \end{cases} \quad (69)$$

Region V

$$\begin{cases} H_y = A\cos(\gamma_{f1}x-\varphi)\cos(\gamma_f b+\eta)e^{\gamma_s(y+b)} \\ E_x = A\left(\frac{\omega\mu_0}{\beta}-\frac{\gamma_{f1}^2}{\beta\omega n_s^2\varepsilon_0}\right)\cos(\gamma_{f1}x-\varphi)\cos(\gamma_f b+\eta)e^{\gamma_s(y+b)} \\ E_y = \frac{-A\gamma_s\gamma_{f1}}{\beta\omega n_s^2\varepsilon_0}\sin(\gamma_{f1}x-\varphi)\cos(\gamma_f b+\eta)e^{\gamma_s(y+b)} \\ E_z = \frac{iA\gamma_{f1}}{\omega n_s^2\varepsilon_0}\sin(\gamma_{f1}x-\varphi)\cos(\gamma_f b+\eta)e^{\gamma_s(y+b)} \\ H_z = -\frac{iA\gamma_s}{\beta}\cos(\gamma_{f1}x-\varphi)\cos(\gamma_f b+\eta)e^{\gamma_s(y+b)} \\ H_x = 0 \end{cases} \quad (70)$$

6.2.1. 2. E_{mn}^{y} Modes

The solutions for quasi-TE modes (E_{mn}^{y} polarised modes) are obtained in a similar manner to that carried out for quasi-TM modes. The field components are E_x, E_y, H_x, H_z and E_z, where the major field components are E_y, H_x (H_y=0). According to the Maxwell equations, the electromagnetic field representation and the wave equation are obtained as:

$$\begin{cases} E_x = -\frac{1}{\beta\omega n_j^2\varepsilon_0}\frac{\partial^2 H_x}{\partial x\partial y} \\ E_y = -\frac{\omega\mu_0}{\beta}H_x - \frac{1}{\beta\omega n_j^2\varepsilon_0}\frac{\partial^2 H_x}{\partial y^2} \\ E_z = \frac{i}{\omega n_j^2\varepsilon_0}\frac{\partial H_x}{\partial y} \\ H_z = -\frac{i}{\beta}\frac{\partial H_x}{\partial x} \\ H_y = 0 \end{cases} \quad (71)$$

A complete solution for the electromagnetic optical fields can be established once the solution for H_y is known.

$$\frac{\partial^2 H_x}{\partial x^2} + \frac{\partial^2 H_x}{\partial y^2} + \left(k^2 n_j^2 - \bar{\beta}^2\right)H_x = 0 \quad (72)$$

the solution of this wave equation by using the separation of variables, is:

$$H_x(x,y) = \bar{X}(x)\bar{Y}(y) \quad (73)$$

Where:

$$\frac{\partial^2 \bar{X}}{\partial x^2} + (k_0^2 n^2 - k_0^2 N_2(y)^2)\bar{X} = 0 \quad (74)$$

$$\frac{\partial^2 \bar{Y}}{\partial y^2} + \left(k_0^2 N_2(y)^2 - \bar{\beta}^2\right)\bar{Y} = 0 \quad (75)$$

6.2.1. 2.1. Solution of the wave equation of E_{mn}^{y} Modes

For E_{mn}^{y} modes, if one considers the propagation in the planar waveguide I, one notices that the component of the field EM almost perpendicular to the plane of incidence is the most dominant component of the field E which is E_y. So this propagation is similar to TE mode, solution of equation (74). If one considers the propagation in the plane guide of the thickness b, one notes that the component of the field EM almost perpendicular to the plane of incidence is the most dominant component of the field H which is H_x. so this propagation is similar to the TM mode, solution of equation (75).

The solutions of (74) are done as [7]:

$$\overline{\mathrm{X}}(\mathrm{x}) = \begin{cases} B_1 cos(\gamma_{f2} a - \bar{\varphi}) e^{-\gamma_{c2}(x-a)} & x > a \\ B_1 cos(\gamma_{f2} x - \bar{\varphi}) & -a \le x \le a \\ B_1 cos(\gamma_{f2} a + \bar{\varphi}) e^{\gamma_{s2}(x+a)} & x < -a \end{cases} \quad (76)$$

Where

$$\begin{cases} \gamma_{f2}^2 = k_0^2 n_f^2 - k_0^2 N_2(y)^2 \\ \gamma_{c2}^2 = k_0^2 N_2(y)^2 - k_0^2 n_c^2 \\ \gamma_{s2}^2 = k_0^2 N_2(y)^2 - k_0^2 n_s^2 \end{cases} \quad (77)$$

$\overline{\mathrm{X}}(\mathrm{x})$ and $\frac{\partial \overline{\mathrm{X}}(\mathrm{x})}{\partial x}$ are continuous at the boundaries of core–cladding interfaces x=±a. we get:

$$\gamma_{f2} a - \bar{\varphi} = atan\left(\frac{\gamma_{c2}}{\gamma_{f2}}\right) \quad (78)$$

$$\gamma_{f2} a + \bar{\varphi} = atan\left(\frac{\gamma_{s2}}{\gamma_{f2}}\right) \quad (79)$$

From these two equations we deduce the characteristic equation of the asymmetric step-index planar waveguide for TE mode is given by:

$$2k_0 a\sqrt{n_f^2 - N_2^2} = arctan\sqrt{\frac{N_2^2 - n_c^2}{n_f^2 - N_2^2}} + arctan\sqrt{\frac{N_2^2 - n_s^2}{n_f^2 - N_2^2}} + m\pi \quad (80)$$

$$2\bar{\varphi} = m\pi + arctan\sqrt{\frac{N_2^2 - n_s^2}{n_f^2 - N_2^2}} - arctan\sqrt{\frac{N_2^2 - n_c^2}{n_f^2 - N_2^2}} \quad (81)$$

Where

$\beta_2 = k_0 N_2$

The solution of (2) is the solution of a symmetric step-index planar waveguide for TM mode and this is given by:

$$\overline{\mathrm{Y}}(\mathrm{y}) = \begin{cases} B_2 cos(\bar{\gamma}_f b - \bar{\eta}) e^{-\bar{\gamma}_s(y-b)} & y > b \\ B_2 cos(\bar{\gamma}_f y - \bar{\eta}) & -b \le y \le b \\ B_2 cos(\bar{\gamma}_f b + \bar{\eta}) e^{\bar{\gamma}_s(y+b)} & y < -b \end{cases} \quad (82)$$

Where

$$\begin{cases} \bar{\gamma}_f^2 = k_0^2 N_2^2 - \bar{\beta}^2 \\ \bar{\gamma}_s^2 = \bar{\beta}^2 - k_0^2 n_s^2 \end{cases} \quad (83)$$

Where

$\bar{\beta} = k_0 \bar{N}$

$\overline{Y}(x)$; $\frac{i}{\omega n_f^2 \varepsilon_0} \frac{\partial \overline{Y}(x)}{\partial x}$ are continuous at the boundaries of core–cladding interfaces x=±b. We get the following equations:

$$\bar{\gamma}_f b - \bar{\eta} = atan\left(\frac{N_2^2}{n_s^2}\frac{\bar{\gamma}_s}{\bar{\gamma}_f}\right) \quad (84)$$

$$\bar{\gamma}_f b + \bar{\eta} = atan\left(\frac{N_2^2}{n_s^2}\frac{\bar{\gamma}_s}{\bar{\gamma}_f}\right) \quad (85)$$

From these two equations we deduce the characteristic equation of the symmetric step-index planar waveguide for TM mode as fallow:

$$2k_0 b\sqrt{N_2^2 - \bar{N}^2} = 2arctan\left(\frac{N_2^2}{n_s^2}\sqrt{\frac{\bar{N}^2 - n_s^2}{N_2^2 - \bar{N}^2}}\right) + m\pi \quad (86)$$

$$\bar{\eta} = \frac{m\pi}{2} \quad (87)$$

6.2.1. 2.2. Field distribution of E_{mn}^{y} modes in each region

We deduce H_x components by multiplying (76) and (82) equations in each region. The other components are obtained by replacing the derivatives $\frac{\partial H_x}{\partial x}$, $\frac{\partial H_x}{\partial y}$, $\frac{\partial^2 H_x}{\partial y^2}$ and $\frac{\partial^2 H_x}{\partial x \partial y}$ in the formula (71) in each region. After calculation, we get the complete field distribution of E_{mn}^{y} modes as fallow:

Region I

$$\begin{cases} H_x = Bcos(\gamma_{f2}x - \bar{\varphi})cos(\bar{\gamma}_f y - \bar{\eta}) \\ E_x = -\frac{1}{\beta\omega n_f^2 \varepsilon_0}\bar{\gamma}_f \gamma_{f2} Bsin(\gamma_{f2}x - \bar{\varphi})\sin(\bar{\gamma}_f y - \bar{\eta}) \\ E_y = B\left(\frac{\bar{\gamma}_f^2}{\beta\omega n_f^2 \varepsilon_0} - \frac{\omega\mu_0}{\beta}\right)cos(\gamma_{f2}x - \bar{\varphi})cos(\bar{\gamma}_f y - \bar{\eta}) \\ E_z = \frac{-i\bar{\gamma}_f B}{\omega n_f^2 \varepsilon_0}cos(\gamma_{f2}x - \bar{\varphi})sin(\bar{\gamma}_f y - \bar{\eta}) \\ H_z = \frac{i\gamma_{f2}B}{\beta}sin(\gamma_{f2}x - \bar{\varphi})cos(\bar{\gamma}_f y - \bar{\eta}) \\ H_y = 0 \end{cases} \quad (88)$$

Region II

$$\begin{cases} H_x = Bcos(\bar{\gamma}_f y - \bar{\eta})cos(\gamma_{f2} a + \bar{\varphi}) e^{\gamma_{s2}(x+a)} \\ E_x = \frac{\bar{\gamma}_f \gamma_{s2} B}{\beta \omega n_s^2 \varepsilon_0} sin(\bar{\gamma}_f y - \bar{\eta})cos(\gamma_{f2} a + \bar{\varphi}) e^{\gamma_{s2}(x+a)} \\ E_y = B\left(\frac{\bar{\gamma}_f^2}{\beta \omega n_s^2 \varepsilon_0} - \frac{\omega \mu_0}{\beta}\right) \cos(\bar{\gamma}_f y - \bar{\eta}) \cos(\gamma_{f2} a + \bar{\varphi})\, e^{\gamma_{s2}(x+a)} \\ E_z = \frac{-i\bar{\gamma}_f B}{\omega n_s^2 \varepsilon_0} sin(\bar{\gamma}_f y - \bar{\eta})cos(\gamma_{f2} a + \bar{\varphi}) e^{\gamma_{s2}(x+a)} \\ H_z = -\frac{i\gamma_{s2} B}{\beta} cos(\bar{\gamma}_f y - \bar{\eta})cos(\gamma_{f2} a + \bar{\varphi}) e^{\gamma_{s2}(x+a)} \\ H_y = 0 \end{cases} \quad (89)$$

Region III

$$\begin{cases} H_x = Bcos(\gamma_{f2} a - \bar{\varphi})cos(\bar{\gamma}_f y - \bar{\eta}) e^{-\gamma_{c2}(x-a)} \\ E_x = -\frac{\gamma_{c2} \bar{\gamma}_f B}{\beta \omega n_c^2 \varepsilon_0} cos(\gamma_{f2} a - \bar{\varphi})sin(\bar{\gamma}_f y - \bar{\eta}) e^{-\gamma_{c2}(x-a)} \\ E_y = B\left(\frac{\bar{\gamma}_f^2}{\beta \omega n_c^2 \varepsilon_0} - \frac{\omega \mu_0}{\beta}\right) \cos(\gamma_{f2} a - \bar{\varphi}) \cos(\bar{\gamma}_f y - \bar{\eta})\, e^{-\gamma_{c2}(x-a)} \\ E_z = \frac{-i\bar{\gamma}_f B}{\omega n_c^2 \varepsilon_0} cos(\gamma_{f2} a - \bar{\varphi})sin(\bar{\gamma}_f y - \bar{\eta}) e^{-\gamma_{c2}(x-a)} \\ H_z = \frac{i\gamma_{c2} B}{\beta} cos(\gamma_{f2} a - \bar{\varphi})cos(\bar{\gamma}_f y - \bar{\eta}) e^{-\gamma_{c2}(x-a)} \\ H_y = 0 \end{cases} \quad (90)$$

Region IV

$$\begin{cases} H_x = Bcos(\gamma_{f2} x - \bar{\varphi})cos(\bar{\gamma}_f b - \bar{\eta}) e^{-\bar{\gamma}_s(y-b)} \\ E_x = -\frac{\bar{\gamma}_s \gamma_{f2} B}{\beta \omega n_s^2 \varepsilon_0} sin(\gamma_{f2} x - \bar{\varphi})cos(\bar{\gamma}_f b - \bar{\eta}) e^{-\bar{\gamma}_s(y-b)} \\ E_y = -B\left(\frac{\bar{\gamma}_s^2}{\beta \omega n_s^2 \varepsilon_0} + \frac{\omega \mu_0}{\beta}\right) cos(\gamma_{f2} x - \bar{\varphi})cos(\bar{\gamma}_f b - \bar{\eta}) e^{-\bar{\gamma}_s(y-b)} \\ E_z = \frac{-i\bar{\gamma}_s B}{\omega n_s^2 \varepsilon_0} cos(\gamma_{f2} x - \bar{\varphi})cos(\bar{\gamma}_f b - \bar{\eta}) e^{-\bar{\gamma}_s(y-b)} \\ H_z = \frac{i\gamma_{f2} B}{\beta} sin(\gamma_{f2} x - \bar{\varphi})cos(\bar{\gamma}_f b - \bar{\eta}) e^{-\bar{\gamma}_s(y-b)} \\ H_y = 0 \end{cases} \quad (91)$$

Region V

$$\begin{cases} H_x = B\cos(\gamma_{f2}x - \bar{\varphi})\cos(\bar{\gamma}_f b + \bar{\eta})e^{\bar{\gamma}_s(y+b)} \\ E_x = \frac{\bar{\gamma}_s\gamma_{f2}B}{\beta\omega n_s^2\varepsilon_0}\sin(\gamma_{f2}x - \bar{\varphi})\cos(\bar{\gamma}_f b + \bar{\eta})e^{\bar{\gamma}_s(y+b)} \\ E_y = -B\left(\frac{\omega\mu_0}{\beta} + \frac{\bar{\gamma}_s^2}{\beta\omega n_s^2\varepsilon_0}\right)\cos(\gamma_{f2}x - \bar{\varphi})\cos(\bar{\gamma}_f b + \bar{\eta})e^{\bar{\gamma}_s(y+b)} \\ E_z = \frac{i\bar{\gamma}_s B}{\omega n_s^2\varepsilon_0}\cos(\gamma_{f2}x - \bar{\varphi})\cos(\bar{\gamma}_f b + \bar{\eta})e^{\bar{\gamma}_s(y+b)} \\ H_z = \frac{i\gamma_{f2}B}{\beta}\sin(\gamma_{f2}x - \bar{\varphi})\cos(\bar{\gamma}_f b + \bar{\eta})e^{\bar{\gamma}_s(y+b)} \\ H_y = 0 \end{cases} \quad (92)$$

7. Conclusion

In this chapter we have modeled slab and channel photonic waveguides. Firstly, isotropic and anisotropic slab waveguides were studied with the optical ray approach and the Maxwell's equations approach, successively. The former approach allowed us to calculate the dispersion equations of the guided modes whereas, the latter approach, enabled us to determine the wave equations, their solutions and the characteristic equations, as well as, the solutions of electromagnetic field in each region of the waveguide. In addition, we have studied the influence of geometrical, wavelength source and physical parameters on the propagation constants and the cutoff frequencies of modes. The results showed that, the increase in the thickness of the core induces an increase in the propagation constants of the modes as well as a decrease in their cut-off frequencies, especially for of higher order modes. Further, the increase in the wavelength source motivates the decrease of the propagation constants of modes as well as the increase of their cut-off thicknesses, especially for de modes of higher orders. Furthermore, changes of cover and substrate indices produce slight changes in the propagation constants of the modes and their cut-off frequencies. However, small changes in the core refractive index engender considerable changes in the propagation constants and cut-off frequencies of propagating modes.

Finally, the effective index method (EIM) is described in detail and used to calculating the propagation constants of quasi-TE and quasi-TM modes as well as their field distribution in each region of the Embedded-strip waveguide.

References

[1] G. Lifante: Integrated Photonics: Fundamentals. John Wiley & Sons Ltd, England (2003).
[2] B. e. a. Saleh, m. c. Teich: Fundamentals of photonics, wiley series in pure and applied optics. Editor: B. e. a. Saleh, published by john wiley& sons, inc, hoboken, new jersey(2007).
[3] S. K. Selvaraja and P. Sethi: Chapter 6: Review on Optical Waveguides. From: Emerging Waveguide Technology . IntechOpen (2018).
[4] J. OLIVIER **:** Cours d'optique guidée, Université Joseph Fourier, France (2005).
[5] K. S. Chiang**:** Dual effective-index method for the analysis of rectangular dielectric waveguides. APPLIED OPTICS. Vol. 25, N°. 13 (1986).
[6] J. Linares, V. Moreno and M.C. Nistal: Designing of Monomode Step-Index Channel Guides with Quasi-Exact Modal Solutions by the Effective Index Method, *Journal of Modern Optics*, **47**, 599–604 (2000).
[7] K. OKAMOTO: Fundamentals of Optical Waveguides. Elsevier Academic Press publications. USA (2006).

Chapter4: Planar Optical Sensor and Evanescent Wave Effects

1. Introduction

A broad range of planar waveguide based optical sensors exploit evanescent wave effects in their operation. Due to the exponential decay of the evanescent field in the external medium, only changes occurring in close proximity to the surface will be sensed. This feature makes evanescent wave chemical sensors and biosensors particularly attractive for use with reduced sample volumes and consequently reduced auxiliary reagent volumes as well. Evanescent-wave biosensors enable monitoring of biomolecular interactions in real-time and can contribute to a more concrete disease diagnosis. With these types of sensors, it would be possible to, selectively, sense an almost limitless range of analytes just by selecting the appropriate biological receptor [1]. Currently, Plasmonic and silicon photonics based biosensors are among the most employed evanescent-wave biosensors for the analyses of NAs with potential applicability in clinical diagnosis [2, 3]. In addition, Lithium Niobate (LN) is widely used for integrated sensor applications due to its excellent optical, ferroelectrical, piezoelectrical, and thermoelectrical properties [4]. Sensitivity is the most important parameter of a planar optical sensor. Sensitivity enhancement of optical sensors based on evanescent wave interactions has attracted significant research interest. Therefore, a normalized analysis for the design of evanescent wave sensors was carried out, and the condition for the maximum achievable sensitivity was derived for both linear TE and TM waveguide sensors [5]. In addition to that, a new highly sensitive evanescent field sensor using silicon-on-insulator (SOI) photonic wire waveguides was demonstrated [6]. Furthermore, sensitivity analysis of the nonlinear asymmetric metal-clad planar waveguide-based sensor was reported [7], it has been shown that the introduction of the nonlinear material in the cover media not only improves the sensitivity but also provides additional parameters to increase the sensitivity. Recently, binary and ternary photonic crystal with left-handed material (LHM) layers and multi-layer slab waveguides comprising LHMs with different configurations, have been investigated as optical sensors. It has been found that the sensitivity of the proposed structures can be significantly improved by the optimization of physical and geometrical parameters of the LHM layers [8, 9, and 10].

In this chapter, after brief description of planar optical sensors principles, we have investigated sensitivity and evanescent field of a slab waveguide optical sensor constituted of Lithium Niobate as a guiding film, where the influence of different parameters of the waveguide on the sensor sensitivity have been studied.

2. Planar waveguide-Based Optical Sensors

Figure 1 illustrates a typical planar optical sensor platform based on multimode slab waveguide configuration. Light is coupled into the waveguide and propagates along its length where it is then out coupled to an appropriate detector. When light undergoes total internal reflection at the interface between two dielectric materials, an evanescent field is generated. The basic IO sensor effect is caused by interaction of the evanescent wave of the guided mode with the sample. The evanescent field senses the changes in the refractive index distribution near the waveguide surface. Thus, changes in the effective refractive indices of the guided modes are induced. The effective refractive index changes (ΔN) can be induced by different effects, such as:(i) The formation of an adlayer of thicknessd_F, transported from the bulk of the sample to the waveguide surface. (ii) Changes Δn_c of the refractive index n_c of the homogeneous (liquid) sample C covering the waveguide surface and (iii) the adsorption or desorption of molecules in pores of the wave guiding film F of refractive index n_F. When all the effects are present, the resulting effective refractive index changes are as follows [11]:

$$\Delta N = \left(\frac{\partial N}{\partial D_F}\right) d_F + \left(\frac{\partial N}{\partial n_c}\right) \Delta n_c + \left(\frac{\partial N}{\partial n_F}\right) \Delta n_F \qquad (1)$$

Where the last summand can be omitted for nonporous waveguides.

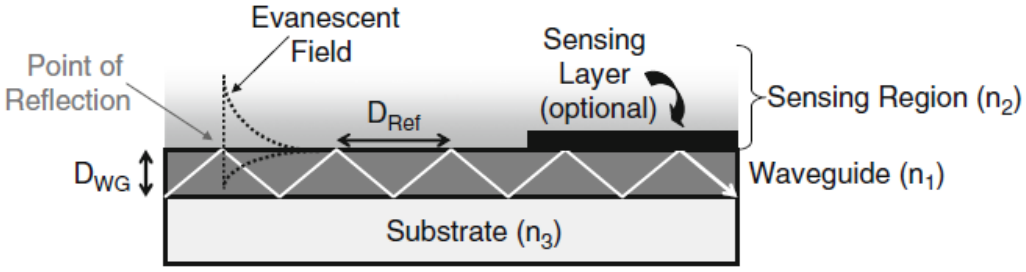

Figure 1: Schematic illustration of the principle of total internal reflection, generating an evanescent wave at the point of reflection[12].

Exponentially decaying evanescent tail extends into both cover and substrate layers over a distance that is characterised by the penetration depth, dp, it is typically of the order of the wavelength of the propagating light [1, 13]:

$$d_p = \frac{\lambda_0}{2\pi n\sqrt{\sin\theta^2 - \sin\theta_c^{\,2}}} = \frac{\lambda}{2\pi\sqrt{N^2 - n_c^{\,2}}} \qquad (2)$$

Here, $\boldsymbol{\lambda}_0$ is the wavelength of the interrogating light, n is the refractive index of the waveguide, θis the angle of incidence of the propagating light at the waveguide – cover layer

interface and θ_c is the critical angle defined by the refractive indices of the waveguide and cover layer. N is the effective refractive index of the core, and n_c refractive index of the cladding region. It is clear from the equation that the penetration depth is tuneable and depends on the choice of incident angle, interrogating wavelength and the material refractive indices, which dictate the value of the critical angle, θc. Typical penetration depths range between 50 and 700 nm, depending mainly on the wavelength and on the contrast between the refractive indices of the core and the cladding.

Both transverse electric (TE) and transverse magnetic (TM) polarized guided light can be used in the evanescent wave detection mechanism. However, TM modes usually have larger evanescent field, which means greater sensitivity than TE modes.

2.1. Absorption-Based Optical Sensors

A typical planar platform for absorption-based optical sensing is depicted in Figure 4, which consists of a planar waveguide on top of which a thin sensing layer has been deposited. Light propagates along the waveguide by total internal reflection. The sensing layer is doped with an analyte-sensitive dye whose absorption properties change upon exposure to the target analyte. The analyte diffuses into the sensing layer where it causes a change in the extinction coefficient, ε, of the layer. The evanescent field of the propagating light interrogates the sensing layer. Therefore, changes in the optical absorption of the layer result in a modulation of the detected light intensity, which is related to the analyte concentration, thereby providing the basis for the sensor. The output intensity can be written as [1]:

$$I = I_0 exp(-r\varepsilon C L_{int}) \quad (3)$$

Where L_{int} is the interaction length of the waveguide and r is the ratio of the optical power present in the evanescent field to the total guided optical power. In this configuration, sensitivity is proportional to the product of rand Lint.

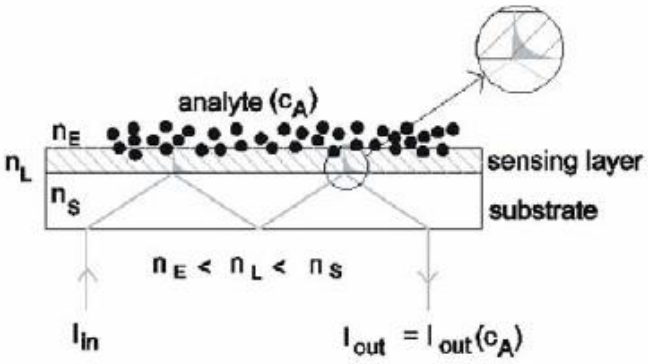

Figure 2: A planar, evanescent-wave absorption-based sensor platform [1].

2.2. Fluorescence-Based Optical Sensors

The utilization of fluorescence dyes for analytical measurements enhances the sensitivity for the detection of the molecules of interest. Contrary to the label free refractive-index sensors where the mass of the molecule of interest is crucial, the sensitivity of the evanescent field fluorescence depends, in addition to the number of capture sites and affinity constants, especially, on the fluorescence dye. The higher the molar extinction coefficient and the number of fluorescent reporter molecules, the more sensitive is the fluorescence detection system [4]. The platform consists of a multimode slab waveguide on the upper surface of which antibodies have been immobilized, Figure 5. These antibodies selectively bind the target analyte, which, in this case, is a specific antigen present in the sample solution that is passed over the platform using the required fluidics. A second solution containing fluorescently labelled antibodies similar to those bound to the surface of the waveguide is subsequently passed over the platform. These antibodies again bind selectively to the surface-bound antigens. Light from a suitable source is coupled to the glass slide and propagates along its length by total internal reflection. The evanescent field of the light extends above the surface of the waveguide where it excites fluorescence from the bound, labelled antibodies. The fluorescence from the upper surface is imaged using a CCD camera and the recorded fluorescence is correlated to antigen concentration. The fluorescence could be also separated via the out coupling grating and detected by a photodiode. The tuneable nature of the evanescent field penetration depth is critical to the effective operation of this sensor as it facilitates surface-specific excitation of fluorescence. This means that only those fluorophores attached to the surface via the antibody-antigen-labelled antibody recognition event. Hence, those within the distance defined by the penetration depth of the evanescent field are excited, permitting discrimination between surface binding events and fluorescence from the bulk solution.

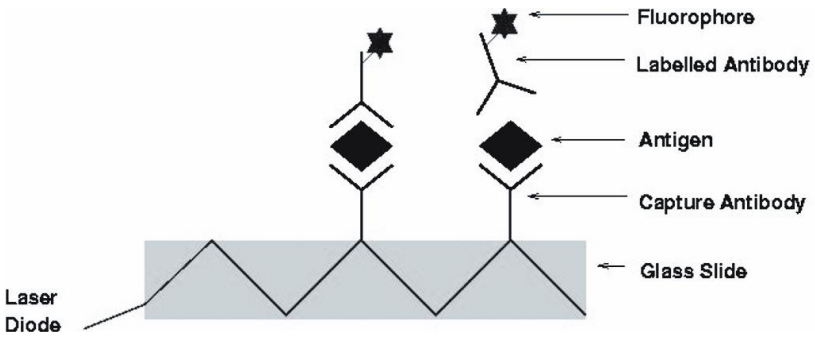

Figure 3: A planar platform for evanescent-wave excitation of fluorescence [1].

2.3. Performance parameters of optical sensors

Optical sensor performance is determined by a number of parameters [14] suchas sensitivity, limit of detection (LOD), limit of quantization (LOQ), response time, Resolution, dynamic range, specificity/selectivity and other parameters that are summarized as follows:

Resolution: is the smallest change that can be observed in the output signal. It is a critical performance parameter for detecting analytes at low concentration or molecules at low weight and depends on transducer, read-out technique, overall noise level, and data processing.

Limit of quantization (LOQ): An additive figure used to describe the smallest concentration of a measurand, if a numerical concentration is required, is the limit of quantitation, and is typically five times higher than the LOD. It is defined as the lowest concentration at which not only the analyte can be reliably detected, but also at which some predefined goals concerning measurement errors, i.e., bias and imprecision, are met.

The dynamic range: is the range of the measured values detectable by the sensor. It is lower limited by the LOD and upper limited by the saturation of the sensing signal sensor or by the physical limitation such as sensor breakage or unpredictable changes of the sensitivity. A wide dynamic range is desired to detect a broad interval of the analyte concentration.

Selectivity or Specificity: In addition to being able of producing an output signal related to the presence of an analyte, a sensor must also be able to distinguish between the analyte and any other substance. This capability is named selectivity or specificity, which is difficult to be measured due to the very large number of possible substances that do not generate an output signal. In fact, the sensor selectivity becomes particularly important when trying to detect an analyte at low concentration in an environment containing a high concentration of other materials, many of which cannot specifically bind to the sensor and therefore can produce an anomalous signal. Selectivity depends on the inherent binding capabilities of the bioreceptor. Thus, nonspecific binding of matrix molecules to the sensing layer leads to false positive signals causing an error in the measurement values. Many biosensors exploit complex, specific binding interactions provided by nature, such as antibody–antigen, nucleic acid hybridization, biotin–streptavidin, and enzyme–substrate interactions. Other substances such as aptamers have been artificially developed for the same purpose.

The response time: is the time required by the transducer to convert a change at the transducer surface such as analyte binding into a variation of the output signal.

Sample Volume: The sample volume is the least requested volume to make a consistent measurement.

The reproducibility: is the ability of the biosensor to reproduce output response when the same analyte concentration is applied in the same conditions.

Stability: Often, a regeneration of the sensor surface is desirable so that several samples can be measured with the same sensor surface. Therefore, regeneration solutions for stringent washing of the surface are applied, for example solutions with low pH or a considerable amount of detergents. The comparability between the assays performed with the identical sensor surface requires a sufficient stability against these chemical conditions.

Portability: refers to the possibility to easily carry the biosensors. It is important for real-time detection when time and location are critical aspects, such as in the case of difficult transportation of the sample to the laboratory.

Sensor Sensitivity: Sensitivity is the change of the sensor output signal in response to unit change in a property of the sensor (e.g., the concentration of an analyte deposited on the sensor surface). It is a parameter that defines the ability of a sensor to transduce an input signal to an output one. It depends on the nature of the analyte and on the type of transducer. According to the different ways the target molecules interact with the sensors, two definitions for sensitivity are used in biochemical sensing applications. One is the bulk sensitivity, referring to the response of the sensor to a uniform change in the cladding, where the sensor surface is mostly not functionalized. The other one is the surface sensitivity, which assesses the sensor response to light–matter interactions at the adsorbed molecule layer on the sensor surface, where the adsorption is normally assisted by a receptor layer through the surface functionalization.

3. Sensitivity study of a birefringence slab waveguide evanescent-wave sensor

Many integrated sensor applications use crystalline film guides with anisotropic optical properties. The simplest types of anisotropic materials are the uniaxial anisotropic crystals known as birefringent materials. Lithium Niobate (LN) is a birefringent material widely used for integrated sensor applications due to its excellent optical, ferroelectrical, piezoelectrical, and thermoelectrical properties [4]. Especially after the fabrication of $LiNbO_3$thin film crystals having an optical quality and electrooptical coefficients comparable to bulk crystals [15].Thing that allowed the production of a $LiNbO_3$slab waveguide structure, where the coupling of TE and TM modes into such waveguide was observed [16].

In this part, we investigate mainly, the sensitivity and the evanescent fields of uniaxial anisotropic slab waveguide sensor. The core of the waveguide, media above and below the

guiding film, are constituted of uniaxial anisotropic crystals. Firstly, the expressions of the sensitivity will be derived from the characteristic equations of TE and TM modes calculated in the previous chapter, in the case where the material above the guide film is isotropic. Secondly, the influence of light source parameters, physical and geometrical parameters of the waveguide, on the sensor sensitivity and the evanescent fields, will be studied in detail for the two kinds of modes. Finally, the influence of E-field induced birefringence of the wave guiding film constituted by $LiNbO_3$, on the sensor sensitivity, will be investigated for the two fundamentals modes.

3.1. Theoretical modeling

3.1.1 Characteristic equations calculation

Planar optical waveguides are the basic element in building integrated optical sensors. In following, we consider a slab waveguide constituted by three layers uniaxial crystals as presented in Fig. 1.We consider that the materials of the three layers are lossless and non-magnetic. The core permittivity tensor is$\bar{\bar{\varepsilon}}_f$withits optic axis in the direction of propagation z. The permittivity tensors of the media above and below the film guide are $\bar{\bar{\varepsilon}}_c$ and $\bar{\bar{\varepsilon}}_s$respectively, where

$$\bar{\bar{\varepsilon}}_i = \begin{bmatrix} \varepsilon_i & 0 & 0 \\ 0 & \varepsilon_i & 0 \\ 0 & 0 & \varepsilon_{iz} \end{bmatrix} = \varepsilon_0 \begin{bmatrix} n_i^2 & 0 & 0 \\ 0 & n_i^2 & 0 \\ 0 & 0 & n_{iz}^2 \end{bmatrix} \qquad (4)$$

Notice that ε_0 is the dielectric constant of vacuum, i=c, f, s (cover, film, substrate),$n_i = n_{ix} = n_{iy}$,n_{iz} are, respectively, the ordinary and the extraordinary refractive indices of each layer.

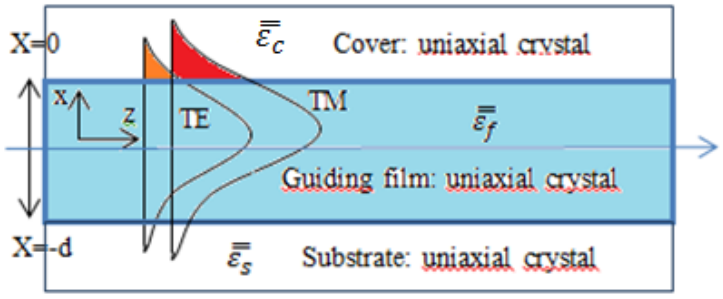

Figure 4: Uniaxial anisotropic slab waveguide based sensor

Two waves are propagated separately in the core of such slab waveguide, the ordinary wave, considered as a TE wave and the extraordinary wave considered as a TM wave [17]. Using

Maxwell's equations, constitutive relations and boundary conditions, the characteristic equations of TE and TM waves are obtained (detailed calculation can be found in the previous chapter) as follows:

For TE modes it's given by

$$k_0 d\sqrt{n_f^2 - N^2} = arctan\left(\sqrt{\frac{N^2-n_s^2}{n_f^2-N^2}}\right) + arctan\left(\sqrt{\frac{N^2-n_c^2}{n_f^2-N^2}}\right) + m\pi \quad (5)$$

For TM modes it is

$$k_0 d\frac{n_{fz}}{n_f}\sqrt{n_f^2 - N^2} = arctan\frac{n_{fz}n_f}{n_{cz}n_c}\sqrt{\frac{N^2-n_c^2}{n_f^2-N^2}} + arctan\frac{n_{fz}n_f}{n_{sz}n_s}\sqrt{\frac{N^2-n_s^2}{n_f^2-N^2}} + m\pi \quad (6)$$

Where: N is the effective refractive index, m is the mode order, d is the core thickness and $k_0$is the free-space wavenumber.

3. 1.2. Sensitivity of uniaxial anisotropic planar waveguide sensor

The sensitivity is defined as the rate of change of the modal effective refractive index relative to the cover refractive index,$S = \left(\frac{\partial n_p}{\partial N}\right)^{-1}$, (we consider that the cover layer is isotropic, that's means: $n_c = n_{cz}$. By differentiating the characteristics equations (5) and (6)with the last consideration, and after long algebra we found the sensor sensitivity or TE and TM modes, by taking into account the normalization as in [18]:

For TE modes, the sensitivity is given by

$$S_{TE} = \sqrt{\frac{1-a_c}{1-X}}\frac{X}{a_c}\frac{1}{\sqrt{a_c-X}}\frac{1}{\left[T+\frac{1}{\sqrt{a_s-X}}+\frac{1}{\sqrt{a_c-X}}\right]} \quad (7)$$

In the same maner, the sensitivity for TM modes is given by

$$S_{TM} = \frac{\frac{X(1-2X+a_c)\sqrt{1-a_c}}{\sqrt{1-X}\sqrt{a_c-X}[a_c(1-X(1-Xa_{cz}))-Xa_{cz}]}}{\left[T'K+\frac{a_c(1-a_c)}{\sqrt{(a_c-X)}[a_c(1-X(1-Xa_{cz}))-Xa_{cz}]}+K\sqrt{\frac{1-a_{sz}}{1-a_s}}\frac{a_s(1-a_s)}{\sqrt{(a_s-X)}[a_s(1-X(1-Xa_{sz}))-Xa_{sz}]}\right]} \quad (8)$$

Where

$$T = \frac{arctan\sqrt{\frac{a_s-X}{X}}+arctan\sqrt{\frac{a_c-X}{X}}+m\pi}{\sqrt{X}} \quad (9)$$

$$T' = \frac{arctan\frac{1}{\sqrt{1-a_c}\sqrt{1-a_{cz}}}\sqrt{\frac{a_c-X}{X}}+arctan\frac{1}{\sqrt{1-a_s}\sqrt{1-a_{sz}}}\sqrt{\frac{a_s-X}{X}}+m\pi}{\sqrt{X}} \quad (10)$$

$$a_s = 1 - \frac{n_s^2}{n_f^2} \quad (11)$$

$$a_c = 1 - \frac{n_c^2}{n_f^2} \quad (12)$$

$$X = 1 - \frac{N^2}{n_f^2} \quad (13)$$

$$a_{sz} = 1 - \frac{n_{sz}^2}{n_{fz}^2} \quad (14)$$

$$a_{cz} = 1 - \frac{n_c^2}{n_{fz}^2} \quad (15)$$

$$K = \frac{n_{fz}}{n_f} \quad (16)$$

4. Influence of waveguide and source parameters on the sensor sensitivity and evanescent fields

As we have seen previously, sensitivities expressions and evanescent field components are functions of the waveguide and the light source parameters. We developed a program in Matlab that allowed us to calculate the sensitivities of both TE and TM modes (fundamental modes and higher order modes) as a function of the frequency, of the wavelength and the thickness of the waveguiding film. The program calculates also, the electric and magnetic fields components in each region of the waveguide. The developed program allowed us to see the influence of physical, geometrical and the source parameters on the sensitivities of both TE and TM modes as well as their influence on the evanescent fields in the cover of waveguide especially. The slab waveguide consists essentially of a core of $LiNbO_3$ on a glass substrate; the wavelength of the source is 650 nm.

Figure 5 shows the sensitivity variation of both TE and TM modes, for an asymmetrical slab waveguide sensor as a function of frequency. The core of the waveguide sensor is $LiNbO_3$ (n_{fx}=2.2880, n_{fz}=2.2030), the refractive index of the substrate is n_s=1.80, whereas, the cover refractive index is n_c=1.628. For the first look on the graph, it is clear that sensitivities of TM modes (red curves) are more important than those of TE modes (blue curves). Further, sensitivities of fundamental modes (TM_0 and TE_0) are greater than those of higher order modes. Furthermore, maximum sensitivities of all modes are situated near the cut off frequencies, where those of higher order modes are situated in higher frequencies, in comparison with those of fundamental modes. We note also that, maximum sensitivities of TE modes are shifted towards lower frequencies in comparison with maximum sensitivities of

TM modes. In the other hand**,** for a symmetrical slab waveguide sensor, we note that maximum sensitivities of TE and TM modes are equals and they are situated in the cut off frequencies, however, sensitivities decrease quickly in higher frequencies, especially for TE modes, figure 6. A comparison of sensitivities of fundamental modes, for both symmetrical and asymmetrical slab waveguide sensors is represented in figure 7. It is clear that sensitivities of symmetrical slab waveguide sensor are more important than those of asymmetrical slab waveguide sensor. Furthermore, for TM_0 mode, the sensitivity is maximal for wide band of frequency, in comparison with maximum sensitivities of TE_0 mode.

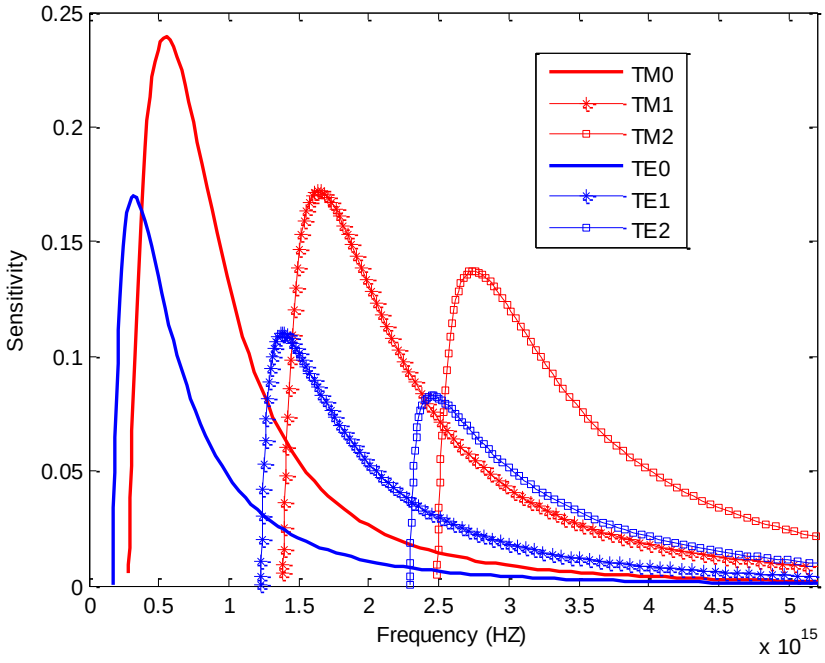

Figure 5: Sensitivities as a function of the frequency for the first three TE and TM modes of an asymmetric slab waveguide (n_c=1.628, n_s=1.80,d=100 nm and $LiNbO_3$as guiding film).

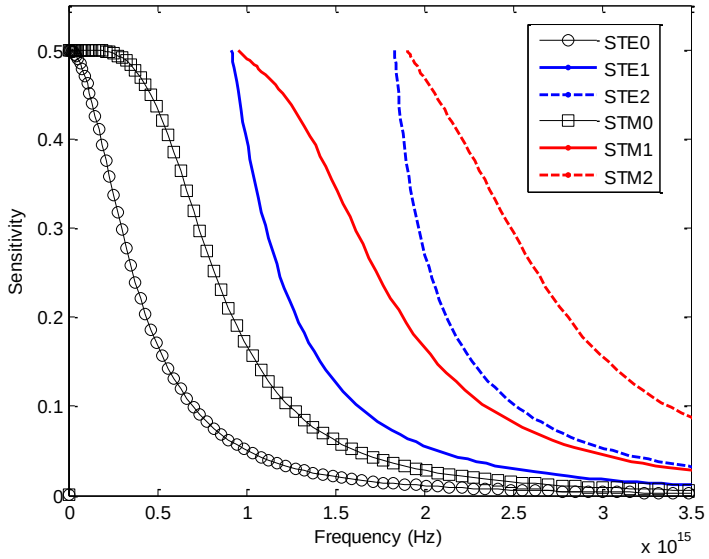

Figure 6: Sensitivities as a function of the frequency for TE0and TM0 modes of a symmetric slab waveguide (n_c=n_s=1.60, d=100 nm and $LiNbO_3$as guiding film.

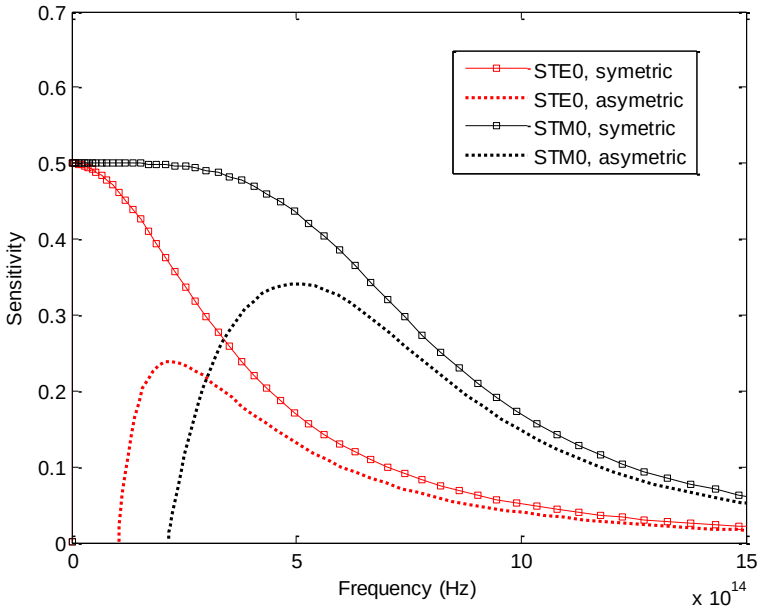

Figure 7: Sensitivities comparison as a function of the frequency for $TE_0$and TM_0modes of a symmetric and asymmetric slab waveguide (n_c=n_s=1.60, d=100 nm and $LiNbO_3$as guiding film.

In figures 8 and 9 we represent electric and magnetic fields components in the cover region for both TE and TM polarizations. For TE mode, H_z and H_x components are very small in comparison with E_y. However, for TM mode, the dominant components are E_x and E_z, H_y is unimportant. For this reason, small components are not represented in the next figures. We note that amplitudes of evanescent field components of TM modes are more important than

those of TE modes, for this reason, sensitivity of TM modes are always greater than that of TE modes. The expressions of electric and magnetic fields components are presented in the previous chapter. The intensities of these evanescent fields are responsible of sensing biochemical substances in optical slab waveguide sensors. We notice that all previous remarks are available in the rest of this chapter.

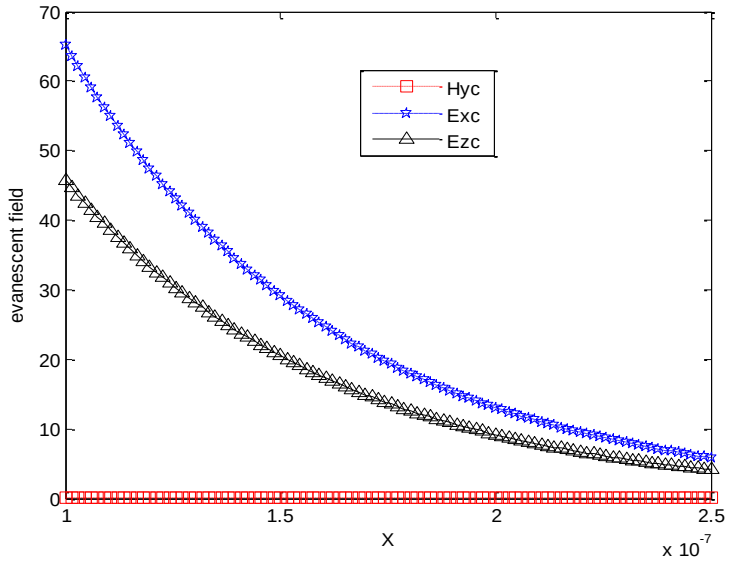

Figure 8: evanescent field components in the cover versus x of TM_0 mode, (n_s=1.80, n_p=1.628, $LiNbO_3$as guiding film, d=100 nm).Hy is very small in comparison with Ez and Ex.

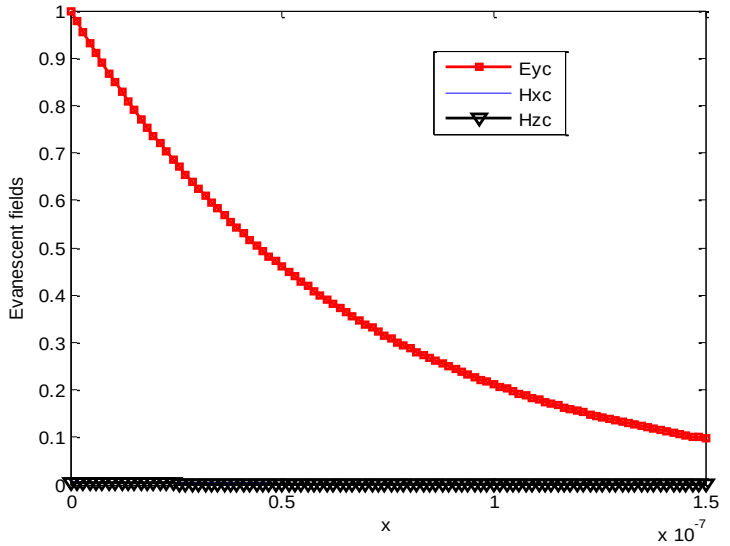

Figure 9: evanescent field components in the cover versus x of TE_0 mode, (n_s=1.80, n_p=1.628, $LiNbO_3$as guiding film, d=100 nm).H_z and H_x are very small in comparison with E_y.

4.1. Influence of the source parameters

4.1.1. Influence of field amplitude

Obviously, the greater the intensity of the evanescent field is, the more sensitive the sensor, both in TE and TM modes, will be. The expression of the sensitivity as a function of evanescent field intensity is defined as in [18]:

$$S = \Gamma_s \left[\sqrt{\frac{1-a_c}{1-X}} + 2\mathrm{P} \left(\sqrt{\frac{1-X}{1-a_c}} - \sqrt{\frac{1-a_c}{1-X}} \right) \right] \quad (17)$$

Where P=0 for TE polarization. However, P=1 for TM polarization,

The intensity of the evanescent field can be represented by the confinement factor Γ_s, which is the ratio of the electric field intensity in the sensitive region or the sensitive layer to the entire mode distribution of the guiding mode [19], defined as:

$$\Gamma_s = \frac{\iint_s |E(x,y)|^2 dxdy}{\iint_\infty |E(x,y)|^2 dxdy} \quad (18)$$

Where, the intensities of the electric and magnetic evanescent fields are function of their amplitudes.

Figures 10 and 11 illustrate, respectively, the sensitivity as a function of the frequency for TE_0 and TM_0 modes for different fraction of modal power located in the cover. The two graphs show that, the sensitivity increase when the fraction of modal power located in the cover increase. However, for TE_0, the sensitivity is maximal for the lower frequencies and it decreases for the higher frequencies. Whereas, for TM_0, the sensitivity is minimal for the lower frequencies and it is maximal for the higher frequencies. The increase of the sensitivities by increasing the modal power located in the cover can be explained by the increasing of evanescent field amplitudes in such region, as it is illustrated in figures 12 and 13.

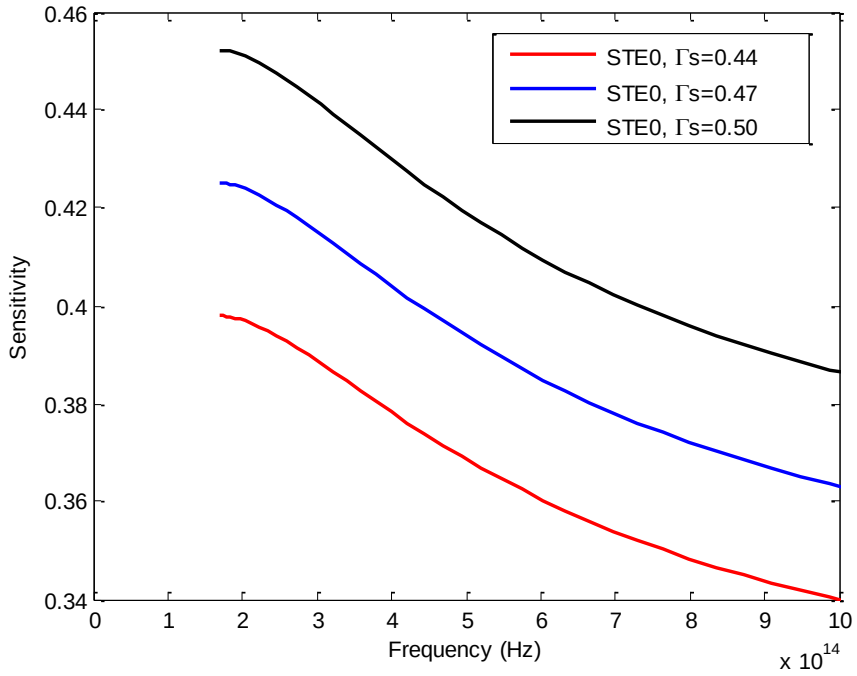

Figure 10: Sensitivity as a function of the frequency for TE_0modesfor different fraction of modal power located in the cover layer, (n_s=1.80, n_p=1.628, d=100 nm, $LiNbO_3$as guiding film).

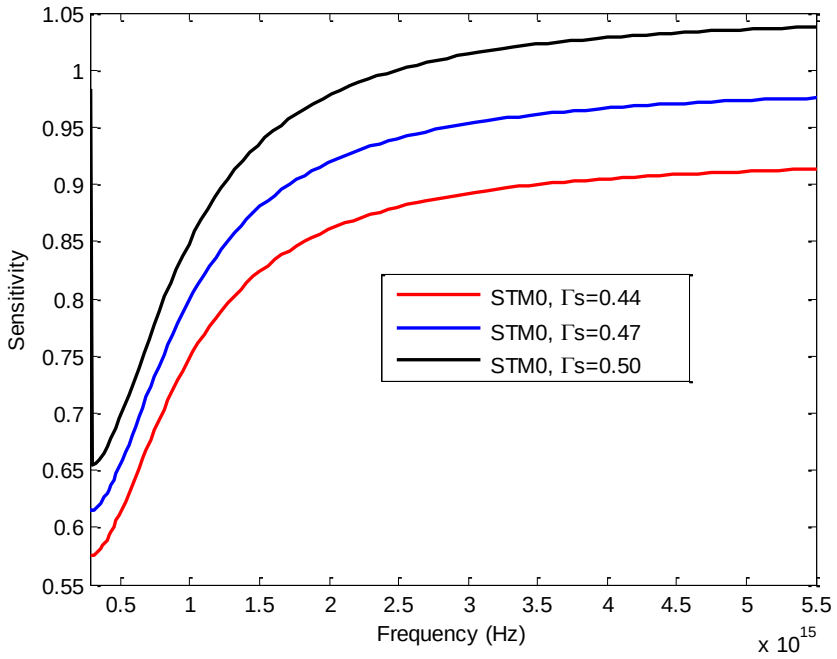

Figure 11: Sensitivity as a function of the frequency for TM_0modesfor different fraction of modal power located in the cover layer, (n_s=1.80, n_p=1.628, d=100 nm, $LiNbO_3$as guiding film).

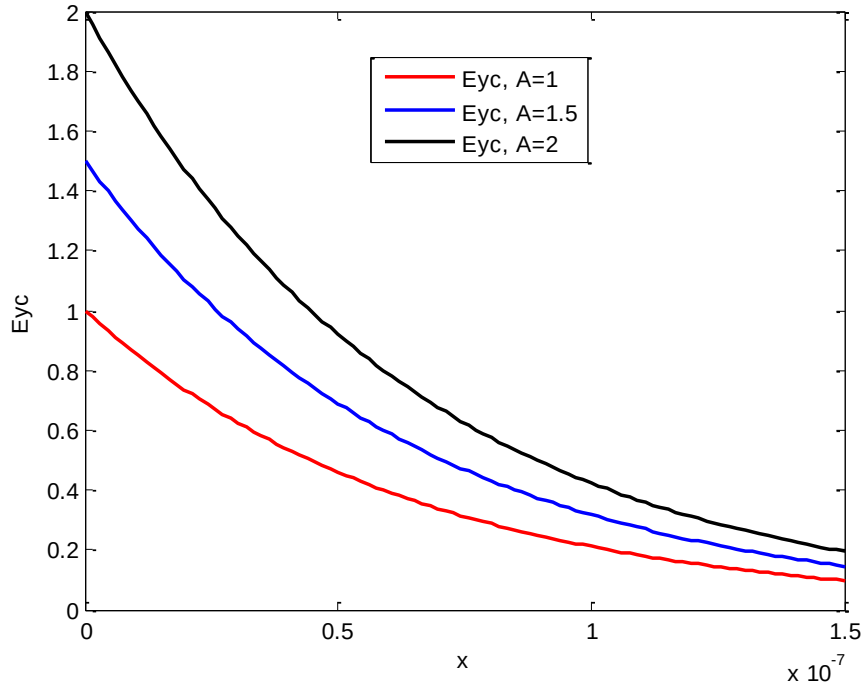

Figure 12: Evanescent field component Eyc in the cover versus x of TE_0 mode for different amplitude of field, (n_s=1.80, n_p=1.628,d=100 nm, $LiNbO_3$as guiding film).

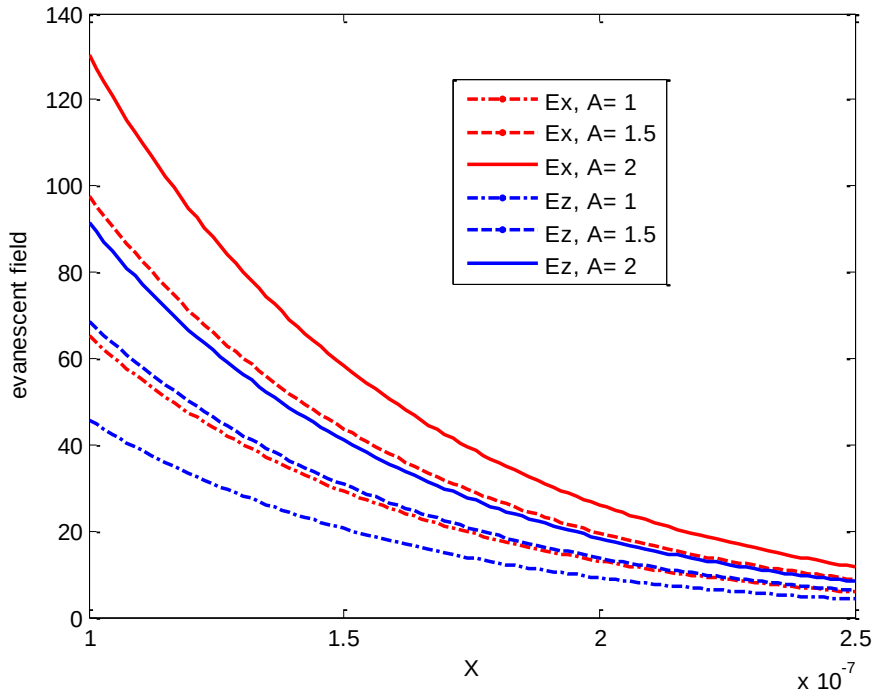

Figure 13: Evanescent field components (Ex, Ez)in the cover versus x of TM_0 mode for different amplitude of field, (n_s=1.80, n_p=1.628,d=100 nm, $LiNbO_3$as guiding film).

4.1.2. Influence of the source wavelength

Sensitivity as a function of the frequency for TE_0 and TM_0 modes, are presented in figures 14 and 15, respectively, for different wavelength source. The curves show that, the sensitivity of the slab waveguide sensor increases by increasing the wavelength source, however, the curves shift towards higher core thicknesses. This implies that, for longer wavelength source, maximal sensitivity is obtainable for longer core thicknesses and vice versa. The increase of the sensitivity for longer wavelength source can be explained by the increase of the evanescent fields intensities caused by increasing of their amplitudes, as illustrated in figures 16 and 17.

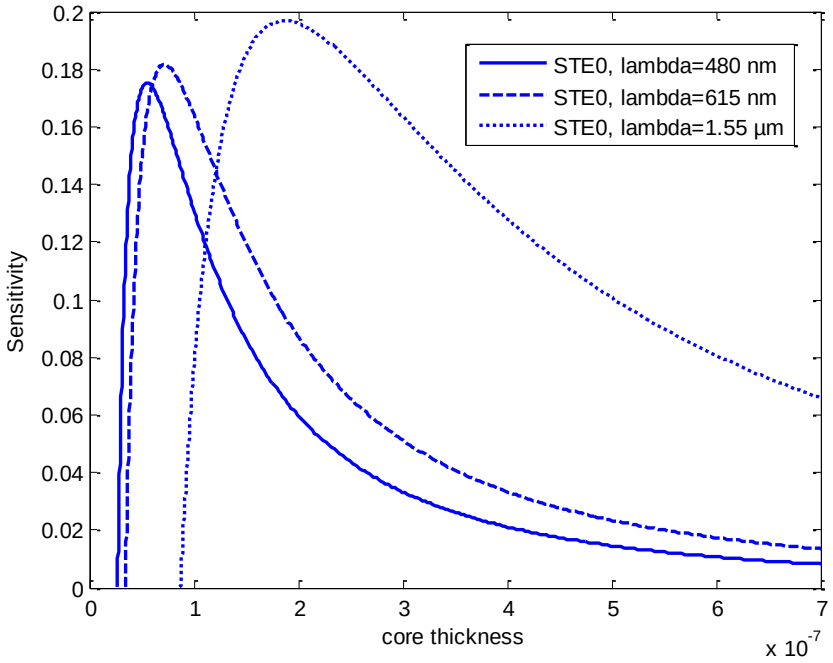

Figure 14: Sensitivity as a function of the frequency for TE_0modesfor different wavelength source, (n_s=1.80, n_p=1.628,d=100 nm, $LiNbO_3$as guiding film).

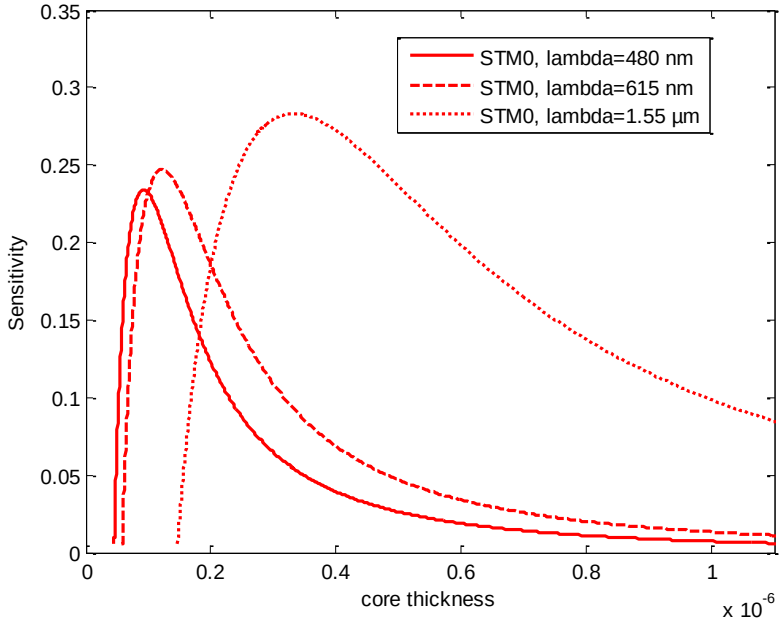

Figure 15: Sensitivity as a function of the frequency for TM_0modesfor different wavelength source, (n_s=1.80, n_p=1.628,d=100 nm, $LiNbO_3$as guiding film).

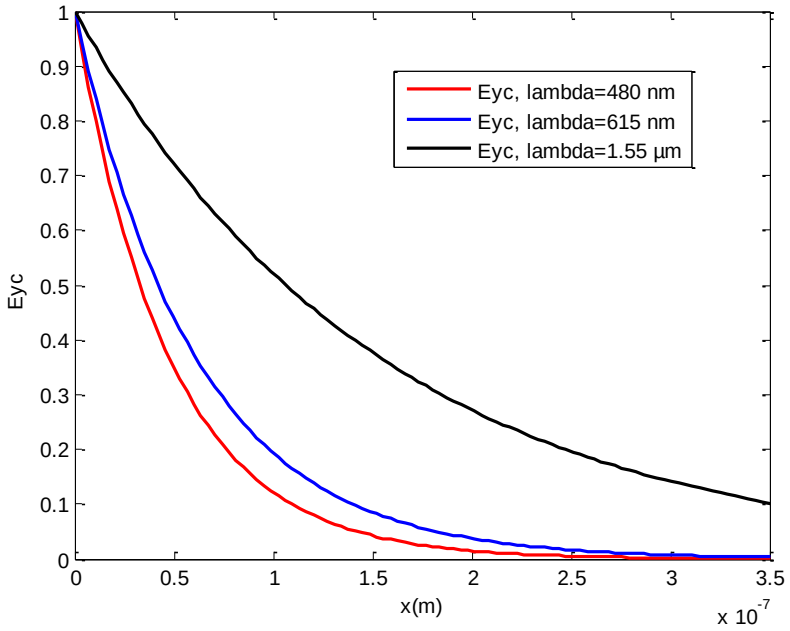

Figure 16: Evanescent field components Eycin the cover versus x of TE_0 mode for different source wavelengths, (n_s=1.80, n_p=1.628,d=100 nm, $LiNbO_3$as guiding film).

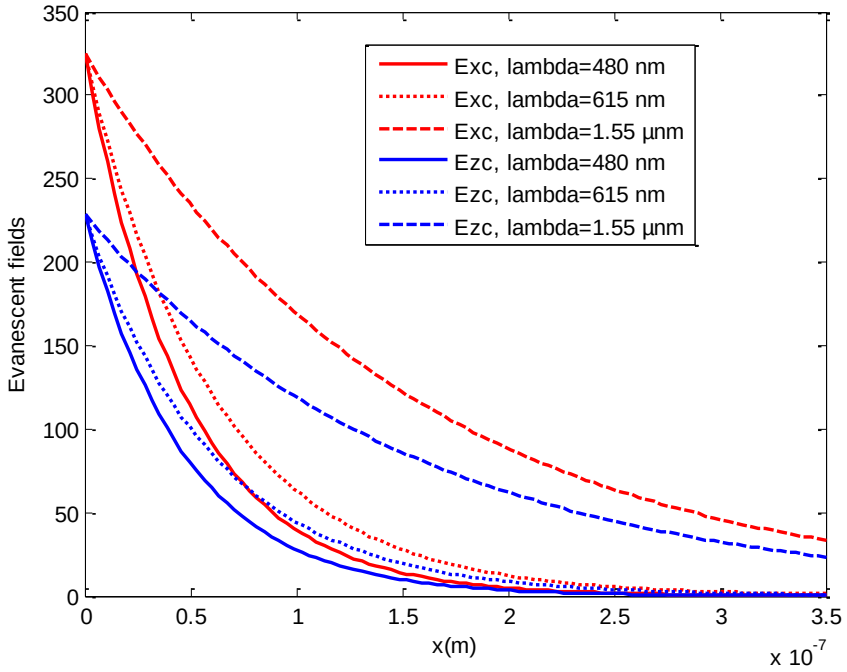

Figure 17: Evanescent field components (Ex, Ez) in the cover versus x of TM_0 mode for different source wavelengths, (n_s=1.80, n_p=1.628, d=100 nm, $LiNbO_3$as guiding film).

4.2. Influence of the geometrical parameter

Figures 18 and 19 illustrate, respectively, the sensitivity as a function of the frequency for TE_0 and TM_0 modes for different core thicknesses. The figures show that, by increasing the core thickness, the sensitivity of the waveguide sensor decreases and the curves shift towards the lower frequencies. The decrease of the sensitivity is due to the decrease of the sensing area limited by the evanescent fields, the normal to the waveguide at z=0 and the super surface of the waveguide (x=0). Hence, the decrease of the evanescent fields intensities in the cover. In fact, when increasing the core thickness, great part of optical signal enter in the core of the waveguide in the form of propagating energy and hence, the evanescent field intensities decrease, as illustrated in figures 20 and 21.

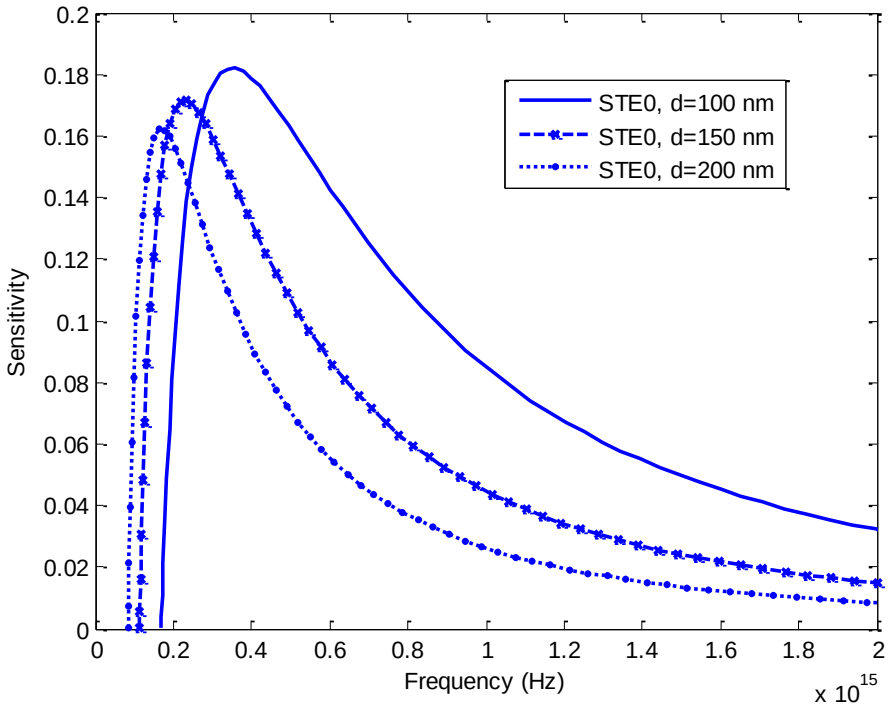

Figure 18: Sensitivity as a function of the frequency for TE_0modesfor different core thicknesses, (n_s=1.80, n_p=1.628, $LiNbO_3$as guiding film).

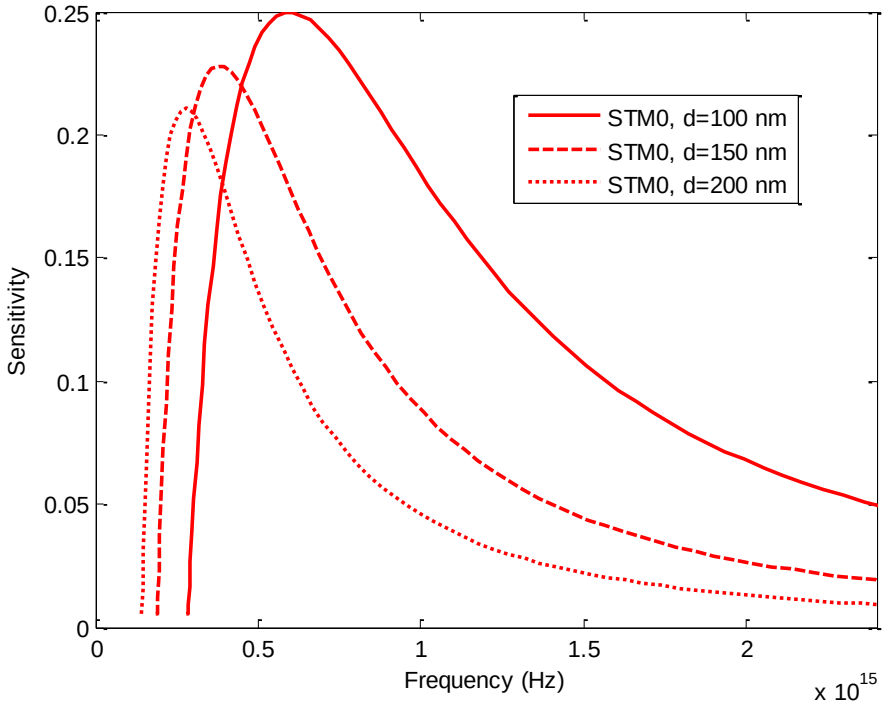

Figure 19: Sensitivity as a function of the frequency for TM_0modesfor different core thicknesses, (n_s=1.80, n_p=1.628, $LiNbO_3$as guiding film).

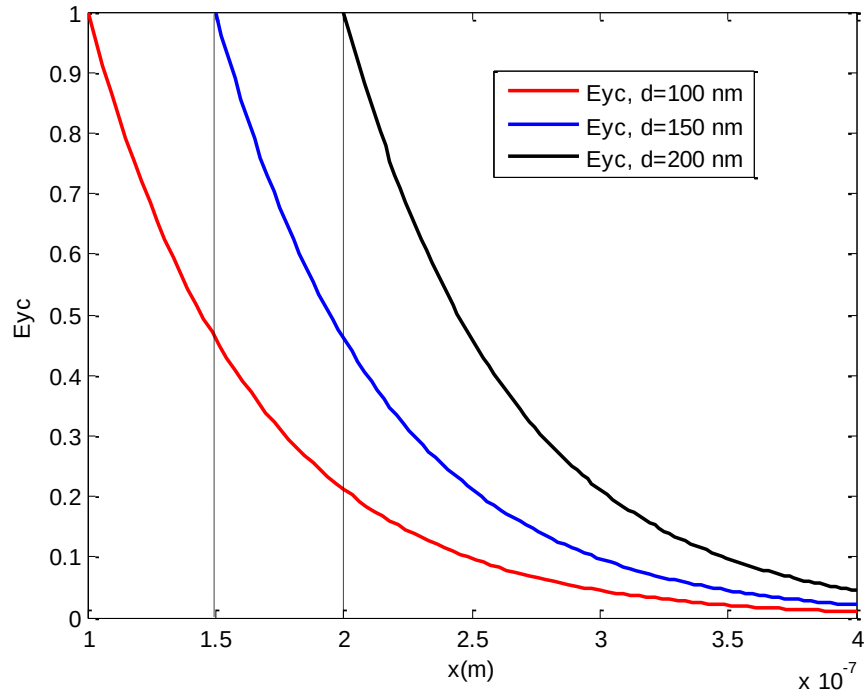

Figure 20: Evanescent field component Eyc in the cover versus x of TE_0 mode for different core thicknesses, (n_c=1.628, ns =1.80, $LiNbO_3$as guiding film).

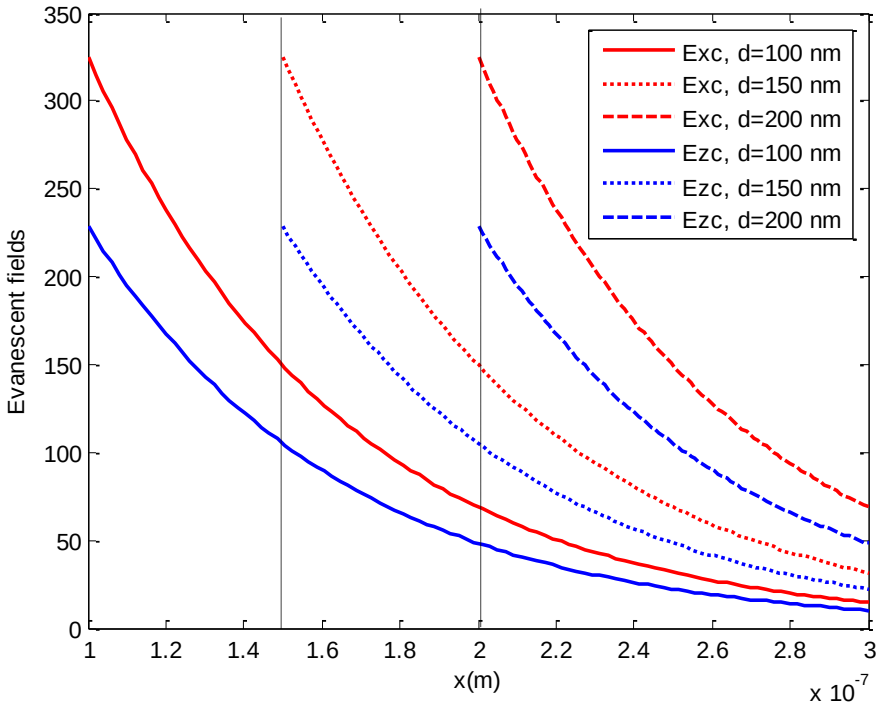

Figure 21: Evanescent field components in the cover versus x of TM_0 mode for different core thicknesses, (n_c=1.628, ns =1.80, $LiNbO_3$as guiding film).

4.3. Influence of the physical parameters

From expressions of sensitivities (4) and (5), we would know how physical parameters of the waveguide influence the sensitivity of the sensor. Physical parameters are refractive indices of the cover, the substrate and the core of the waveguide.

4.3.1. Influence of the cover refractive index

TE and TM modes sensitivities as a function of the frequency are presented in figures 22 and 23, respectively, for different cover refractive index. Whereas, figure 24 and 25, illustrate the sensitivities of TE_0 and TM_0 modes as a function of the effective refractive index, for different cover refractive index. The graphs give us the values of maximal sensitivities and their corresponding frequencies as well as their corresponding effective refractive index. For TE_0, maximal sensitivities are 0.11 and 0.225 corresponding to 1.48 and 1. 70 cover refractive index, respectively; while their corresponding frequencies are 3.0E14 Hz and 2.25E14 Hz; whereas their corresponding effective refractive index is 1.85. However, for TM_0, maximal sensitivities are 0.175 and 0.29 corresponding to1.48 and 1.70 cover refractive index, respectively; while their corresponding frequencies are 6.E14 Hz and 4.45E14 Hz; whereas their corresponding effective refractive index is1.86. The curves show that, the sensitivity of the slab waveguide sensor increases by increasing the cover refractive index for both TE and TM modes. In addition to that, the position of the maximal sensitivities exhibit small shifts toward lower values. As cover refractive index must be always less than substrate refractive index, we can conclude that, for both TE and TM modes, the sensitivity of the sensor increases by making the cover refractive index closer to that of the substrate. We can conclude that, changes of the cover refractive index, induces changes in the value of maximum sensitivity and changes in their corresponding frequencies.

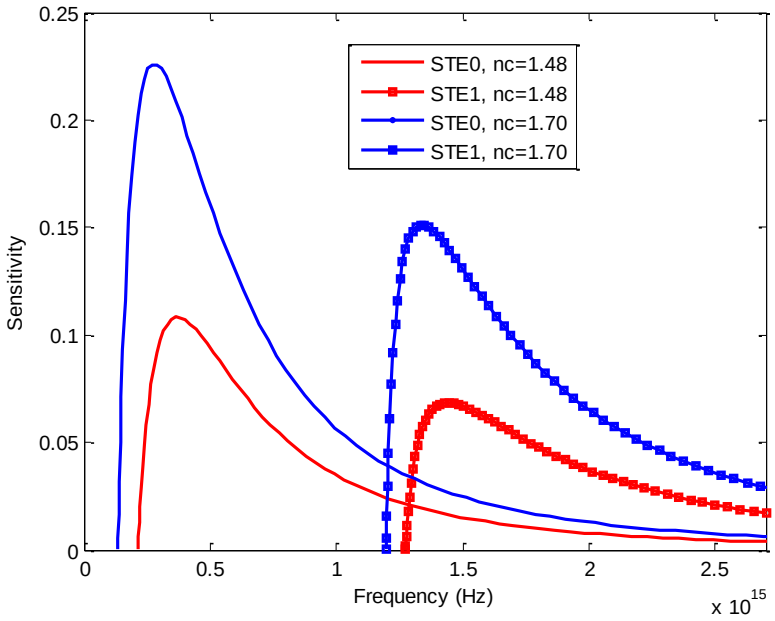

Figure 22: Sensitivity as a function of the frequency for TE modes for different refractive index of the cover material n_c, lines curves for TE_0 modes and square markers linked lines curves for TE_1 modes, (n_s=1.80, d=100 nm, $LiNbO_3$as guiding film).

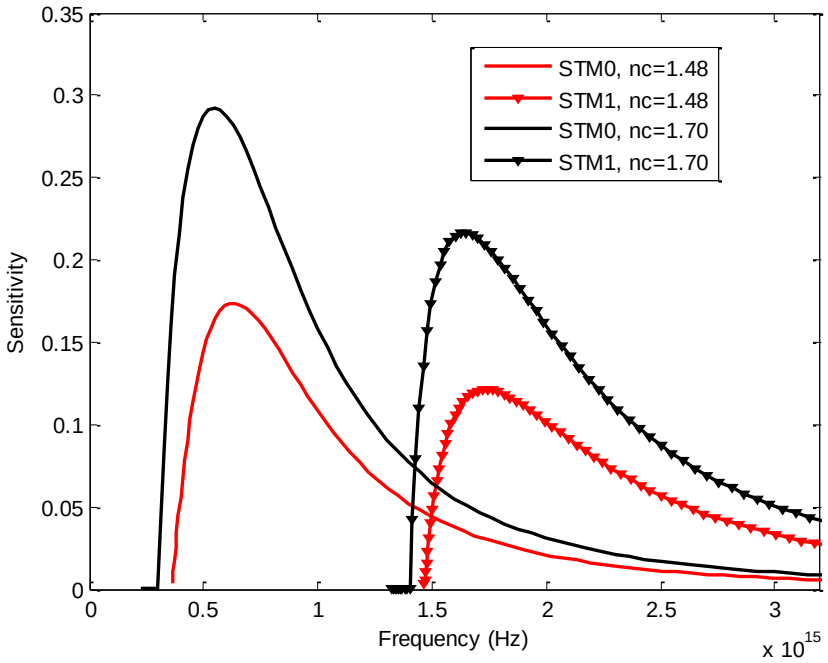

Figure 23: Sensitivity as a function of the frequency for TM modes for different refractive index of the cover materials n_c, lines curves for TM_0 modes and square markers linked lines curves for TM_1 modes, (n_s=1.80, d=100 nm, $LiNbO_3$as guiding film).

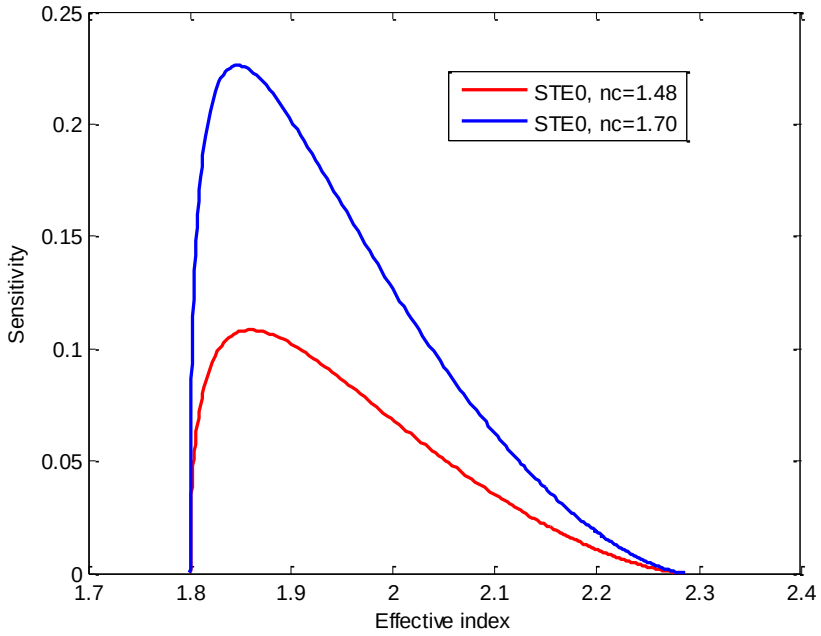

Figure 24: Sensitivity as a function of the effective index for TE_0 modes for different refractive index of the cover material n_c, (n_s=1.80, d=100 nm, $LiNbO_3$as guiding film).

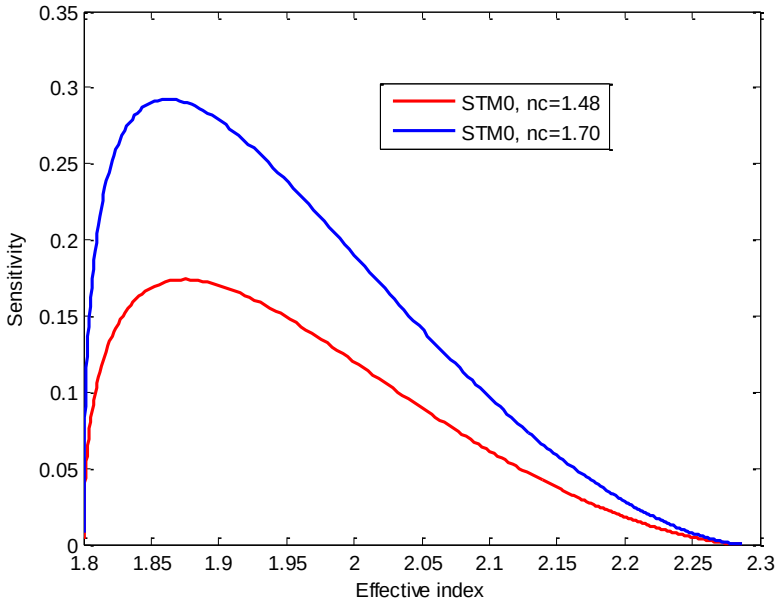

Figure 25: Sensitivity as a function of the effective index for TM_0 mode for different refractive index of the cover materials n_c, (n_s=1.80, d=100 nm, $LiNbO_3$as guiding film).

Figures 26, 27 represent evanescent field components in the cover of TE_0 and TM_0 modes, respectively, for different cover refractive indices. The curves show small changes in the evanescent field components in the cover near to the cut off frequencies. These changes are caused by small changes of the effective refractive indices of TE_0 and TM_0 modes induced

by changes of core refractive index, figure 28. These small changes of the evanescent field components in the cover, near to the cut off frequencies, have neglected influence on the sensitivity of the slab waveguide sensor.

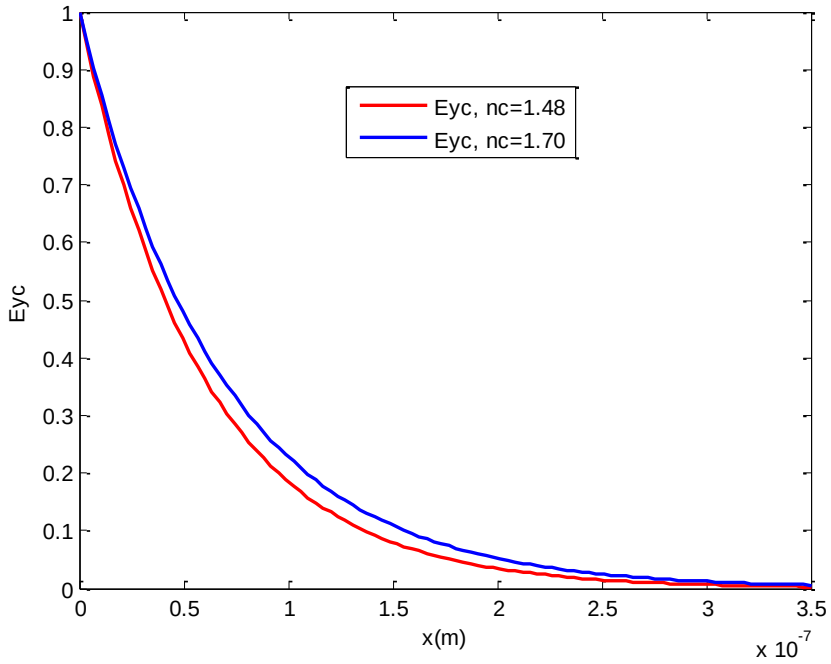

Figure 26: Evanescent field components E_{yc} in the cover versus x of TE_0 mode for different cover refractive indices, (n_s=1.80, d=100 nm, $LiNbO_3$as guiding film). loin de fc.

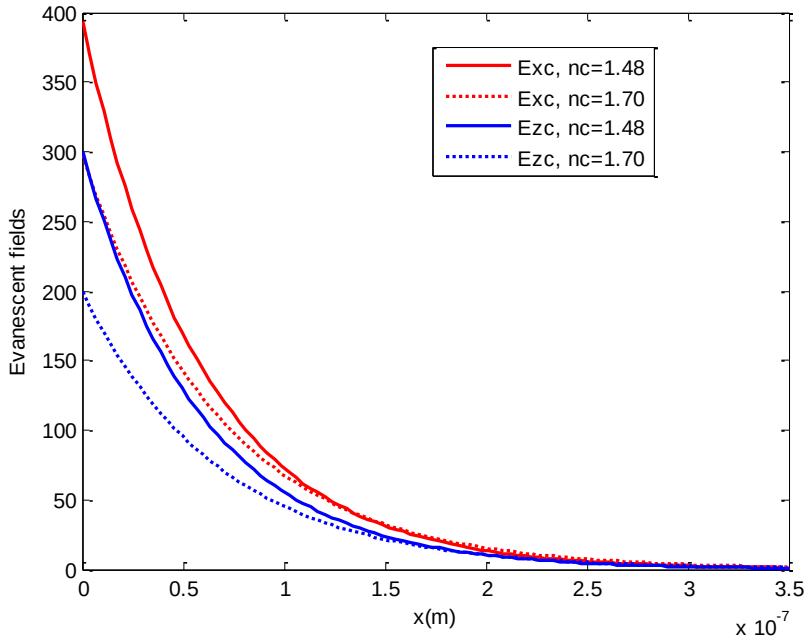

Figure 27: Evanescent field components (E_{xc}, E_{zc}) in the cover versus x of TM_0 mode for different cover refractive indices, (n_c=1.48, d=100 nm, $LiNbO_3$as guiding film).

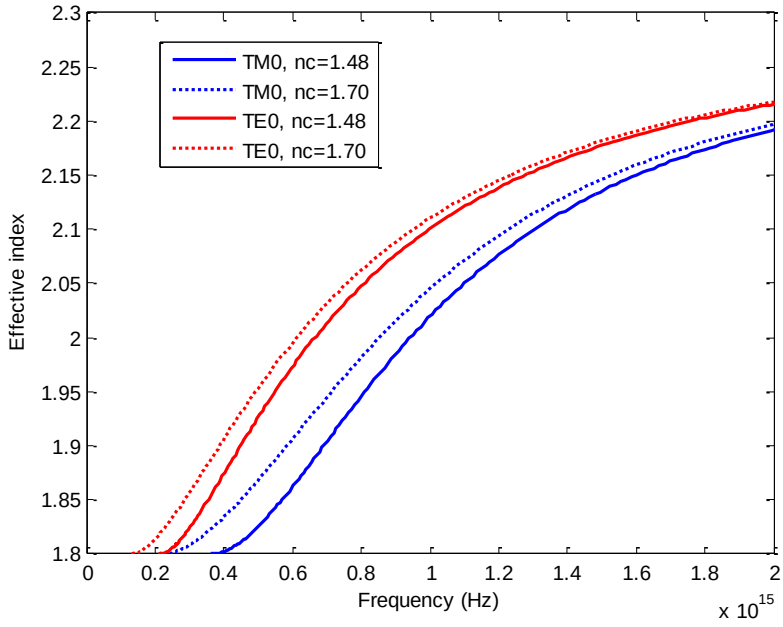

Figure 28: Effective index versus frequency of TE_0 and TM_0 modes in slab waveguide for different cover indices, (n_s=1.80, d=100 nm, $LiNbO_3$as guiding film).

4.3.2. Influence of the substrate refractive index

In figures 29, 30, we illustrate sensitivities as a function of the frequency of TE and TM modes, respectively, for different substrate refractive index. Whereas, figure 31 and 32, present the sensitivities of TE_0 and TM_0 modes as a function of the effective refractive index, for different substrate refractive index. As in the case of the cover refractive index changes, the first two graphs give us the values of maximal sensitivities and their corresponding frequencies, however, the last two graphs give us the values of maximal sensitivities and their corresponding effective refractive index. For TE_0, maximal sensitivities are 0.245 and 0.11corresponding to, 1.60 and 1.80 substrate refractive index, respectively; while their corresponding frequencies are 2.E14 Hz and 3.E14 Hz; whereas their corresponding effective refractive indices are 1.65 and 1.85 successively. However, for TM_0, maximal sensitivities are 0.34 and 0.175 corresponding to, 1.60 and 1.80 substrate refractive index, respectively; while their corresponding frequencies are 5.E14 Hz and 6.E14 Hz; whereas their corresponding effective refractive indices are 1.7 and 1.86 successively. The curves show that, the sensitivity of the slab waveguide sensor decreases by increasing the substrate refractive index for both TE and TM modes. Further, the position of the maximal sensitivities exhibit shifts toward higher frequencies, figures 29, 30, and considerable shifts toward higher values of effective

refractive indices, figure 31, 32. We can conclude that, changes of substrate refractive index, induces changes in the value of maximum sensitivity and changes in its position.

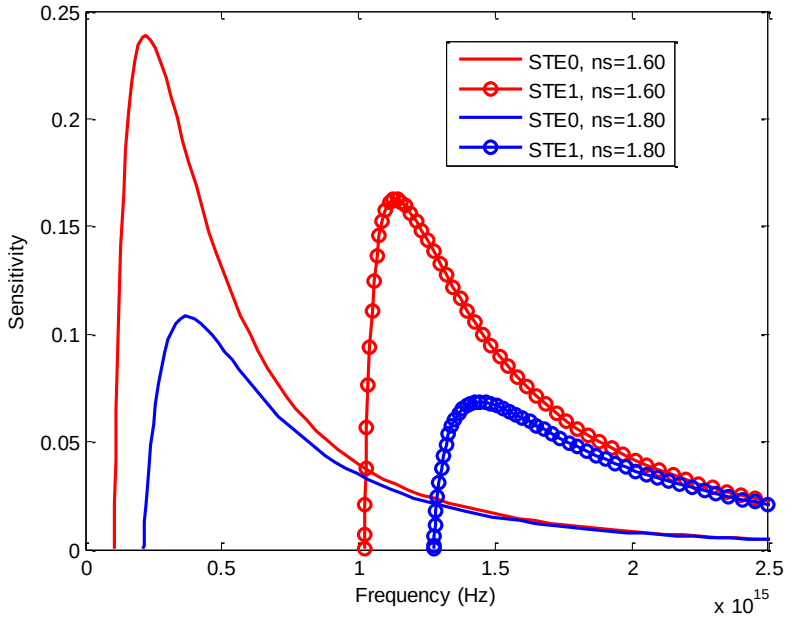

Figure 29: Sensitivity as a function of the frequency for TEmodes for different refractive index of the substrate materials n_s, lines curves for TE_0 modes and circle markers linked lines curves for TE_1 modes, (n_c=1.48, d=100 nm, $LiNbO_3$as guiding film).

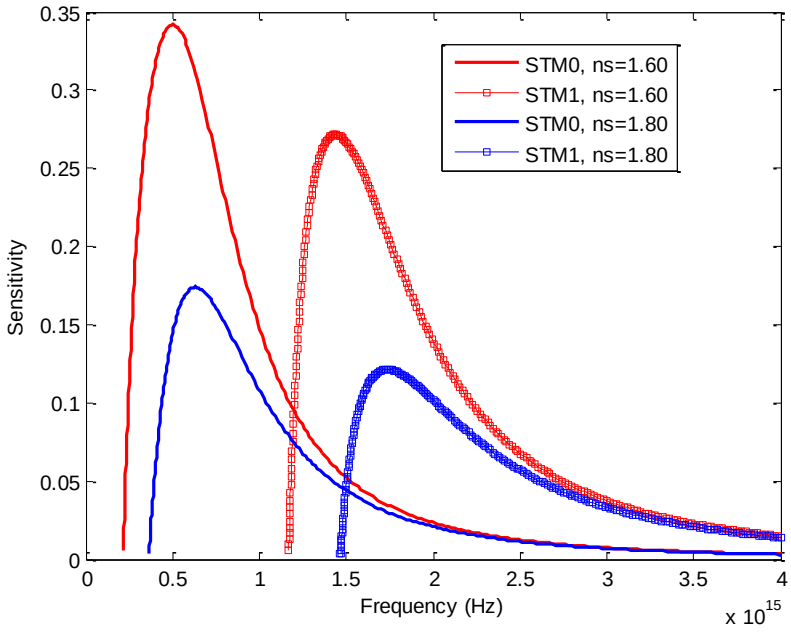

Figure 30: Sensitivity as a function of the frequency for TM modes for different refractive index of the substrate materials n_s, lines curves for TM_0 modes and circle markers linked lines curves for TM_1 modes, (n_c=1.48, d=100 nm, $LiNbO_3$as guiding film).

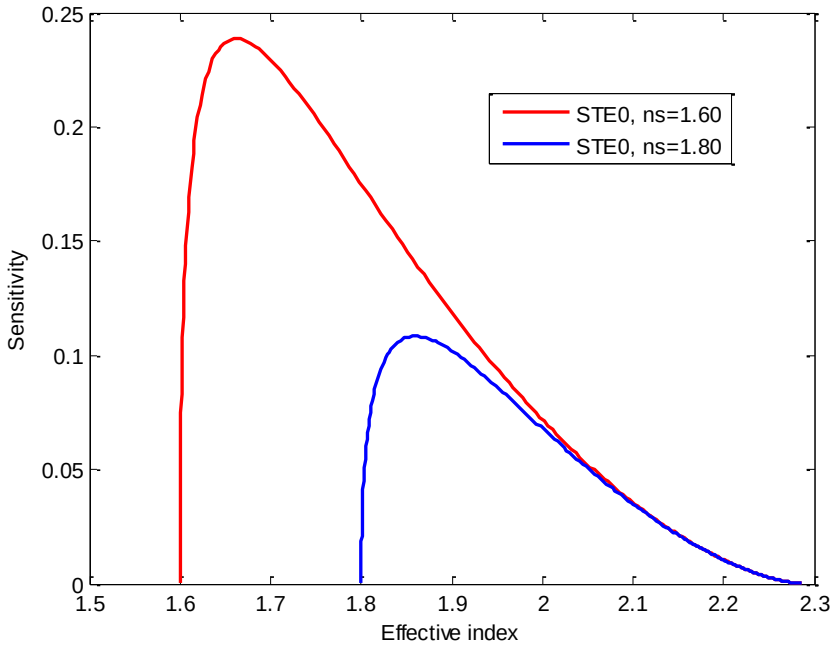

Figure 31: Sensitivity as a function of the effective index for TE_0 mode for different refractive index of the substrate n_s, (n_c=1.48, d=100 nm, $LiNbO_3$as guiding film).

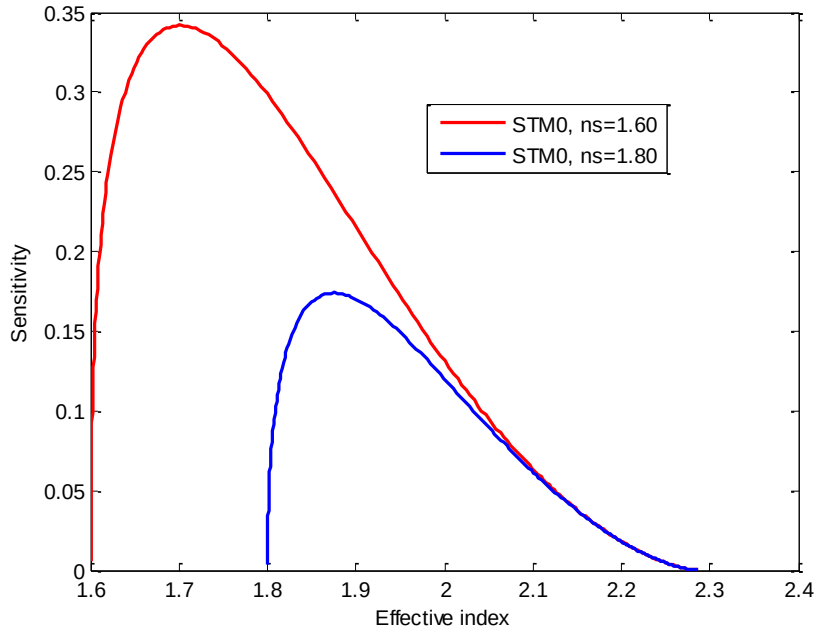

Figure 32: Sensitivity as a function of the effective index for TM_0 mode for different refractive index of the substrate n_s, (n_c=1.48, d=100 nm, $LiNbO_3$as guiding film).

Figure 33and 34 represent evanescent field components in the cover of TE_0 and TM_0 modes, for different substrate refractive indices, respectively. The curves show small changes in the evanescent field components caused by changes of substrate refractive index; in

addition, these small changes occur near the cut off frequencies of each mode. Far from these later, there are no changes of evanescent field components at all. The same thing for evanescent field components in the substrate, figures 35 and 36. There are small increases of E_{ys} and small decreases of E_{xs}, E_{zs} in the substrate resulting from increasing substrate refractive index. These small changes of the evanescent field components in the cover and in the substrate, near to the cut off frequencies, are caused by small changes of the effective refractive indices resulting from substrate refractive index changes, figure 37. Thus, changes of the evanescent field components in the cover have neglected influence on the sensitivity of the slab waveguide sensor, where there are important changes caused by changes of substrate refractive index, as we have seen in figures 31 and 32.

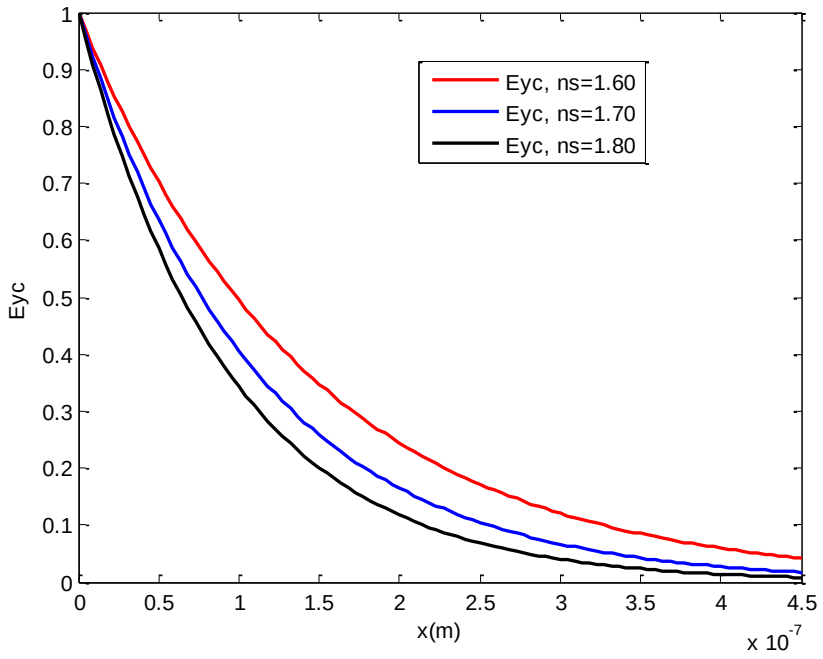

Figure 33: Evanescent field components E_{yc} in the cover versus x of TE_0 mode for different substrate refractive indices, (n_c=1.48, d=100 nm, $LiNbO_3$ as guiding film).

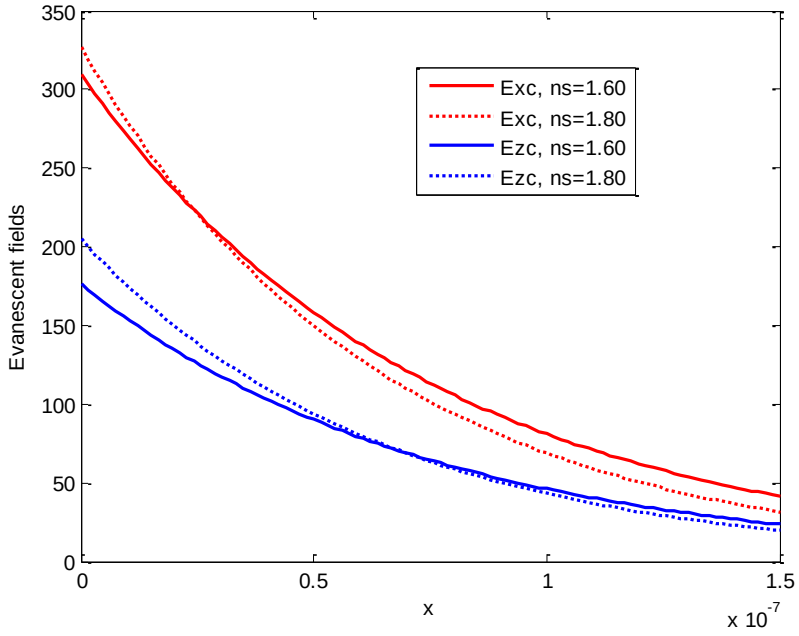

Figure 34: Evanescent field components (Ex, Ez) in the cover versus x of TM_0 mode for different substrate refractive indices, (n_c=1.48, d=100 nm, $LiNbO_3$as guiding film).

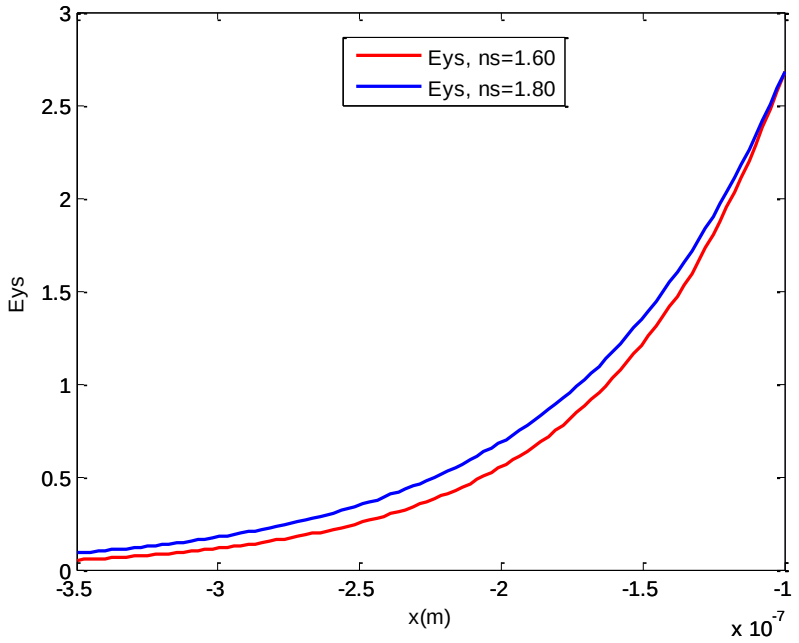

Figure 35: Evanescent field components E_{ys} in the substrate versus x of TE_0 mode for different substrate refractive indices, (n_c=1.48, d=100 nm, $LiNbO_3$ as guiding film).

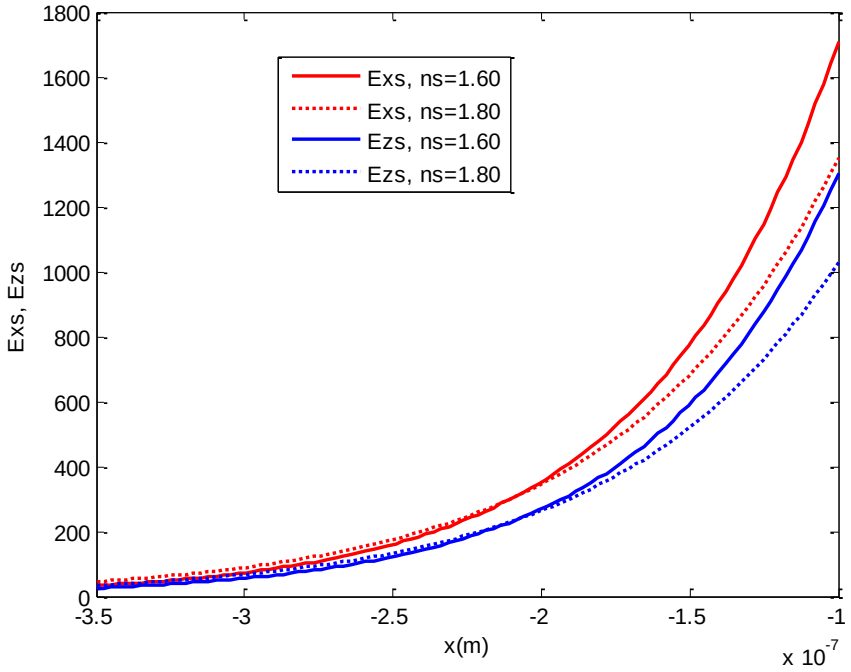

Figure 36: Evanescent field components (E_{xs}, E_{zs}) in the substrate versus x of TM_0 mode for different substrate refractive indices, (n_c=1.48, d=100 nm, $LiNbO_3$as guiding film).

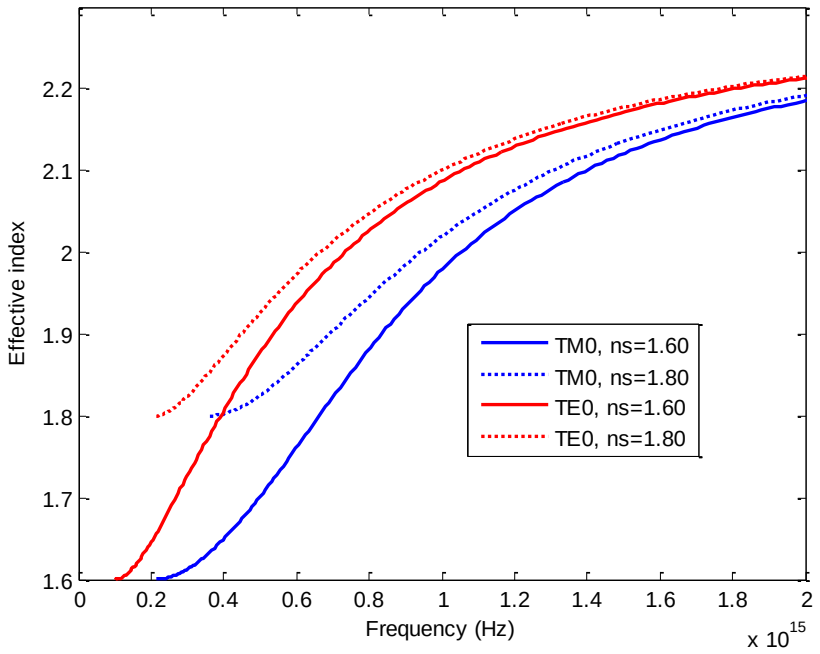

Figure 37: Effective index versus frequency of TE_0 and TM_0 modes in slab waveguide for different substrate indices, (n_c=1.48, d=100 nm, $LiNbO_3$as guiding film).

4.3.3. Influence of the core refractive index

Figures 38, 39, represent sensitivities as a function of the frequency of TE and TM modes, respectively, for different core refractive index. Whereas, figure 40 and 41, illustrate the sensitivities of TE_0 and TM_0 modes as a function of the effective refractive index, for different core refractive index. For TE_0, maximal sensitivities are 0.125 and 0.24 corresponding to 1.80 and 2.2880 core refractive index, respectively; while their corresponding frequencies are 6.6E14 Hz and 2.E14 Hz; whereas their corresponding effective refractive indices are 1.62 and 1.65 successively. However, for TM_0, maximal sensitivities are 0.15 and 0.34 corresponding to, 1.80 and 2.2880 substrate refractive index, respectively; while their corresponding frequencies are 8.5E14 Hz and 5.0E14 Hz; whereas their corresponding effective refractive indices are 1.63 and 1.71 successively. The curves show that, the sensitivity of the slab waveguide sensor increases by increasing the core refractive index for both TE and TM modes. In addition to that, the position of the maximal sensitivities exhibit shifts toward lower frequencies, figures 38, 39, and shifts toward higher values of effective refractive indices, figure 40, 41. Thus, as in the cases of cover and substrate refractive indices, changes of core refractive index, induces changes in the value of maximum sensitivity and changes in their corresponding frequency and effective refractive index.

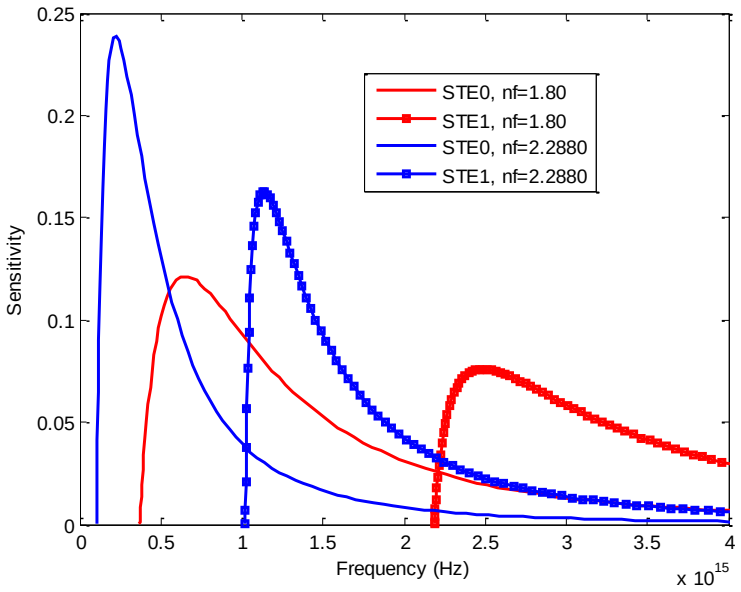

Figure 38: Sensitivity as a function of the frequency for TE modes for different refractive index of the cover materials n_f, lines curves for TE_0 modes and square markers linked lines curves for TE_1 modes, (n_c=1.48, d=100 nm, ns=1.60).

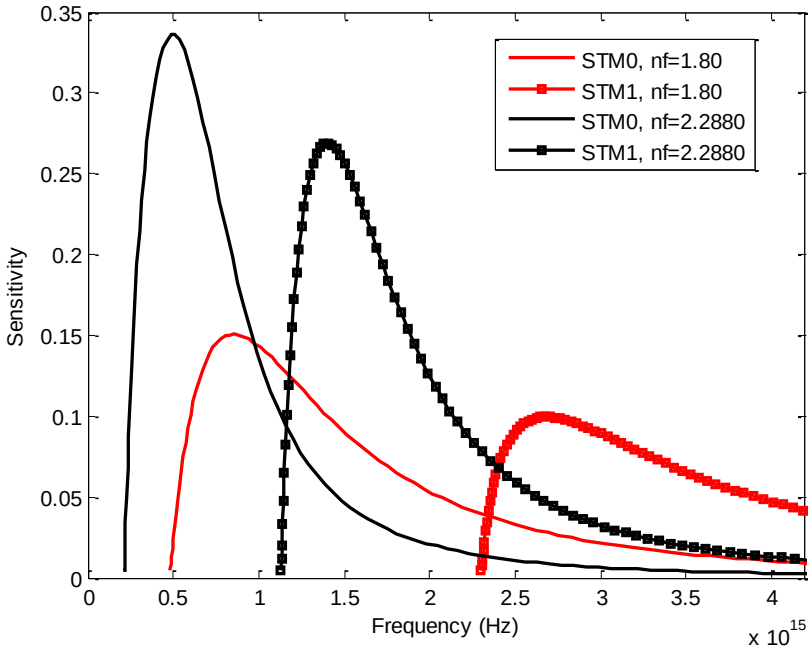

Figure 39: Sensitivity as a function of the frequency for TM modes for different refractive index of the cover materials n_f, lines curves for TM_0 modes and square markers linked lines curves for TM_1 modes, (n_c=1.48, d=100 nm, ns=1.60).

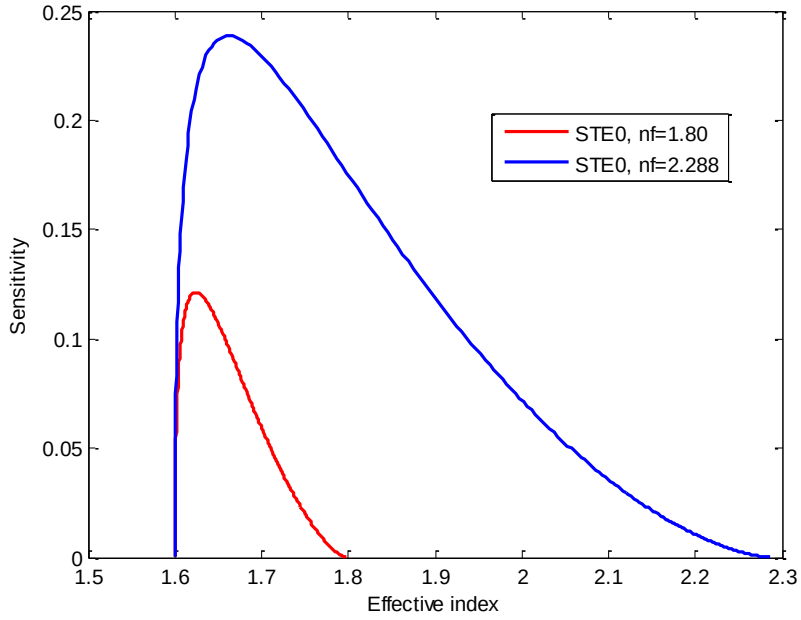

Figure 40: Sensitivity as a function of the effective index for TE_0 mode for different refractive index of the core n_f, (n_c=1.48, n_s=1.60, d=100 nm,).

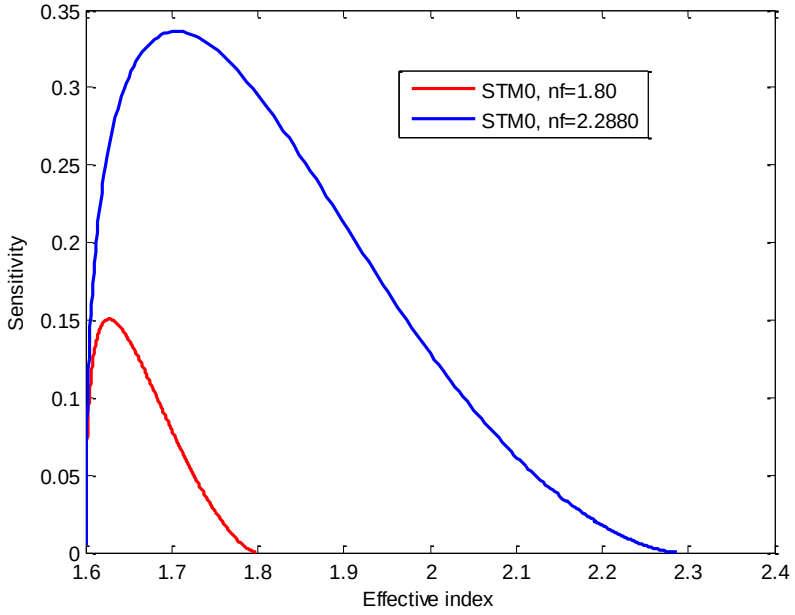

Figure 41: Sensitivity as a function of the effective index for TM_0 mode for different refractive index of the core n_f, (n_c=1.48, n_s=1.60, d=100 nm,).

Figure 42and 43 represent evanescent field components in the cover of TE_0 and TM_0 modes, for different core refractive indices, respectively. The curves show middle changes in the evanescent field components caused by changes of core refractive index; in fact, these changes occur far from the cut off frequencies of each mode. Near to these later, there are small changes of evanescent field components. These changes are caused by the change of effective refractive indices of TE_0 and TM_0 modes induced by changes of core refractive index, figure 44. These changes of the evanescent field components in the cover, far from the cut off frequencies, have neglected influence on the sensitivity of the slab waveguide sensor, since the peaks of sensitivities are situated near the cut off frequencies.

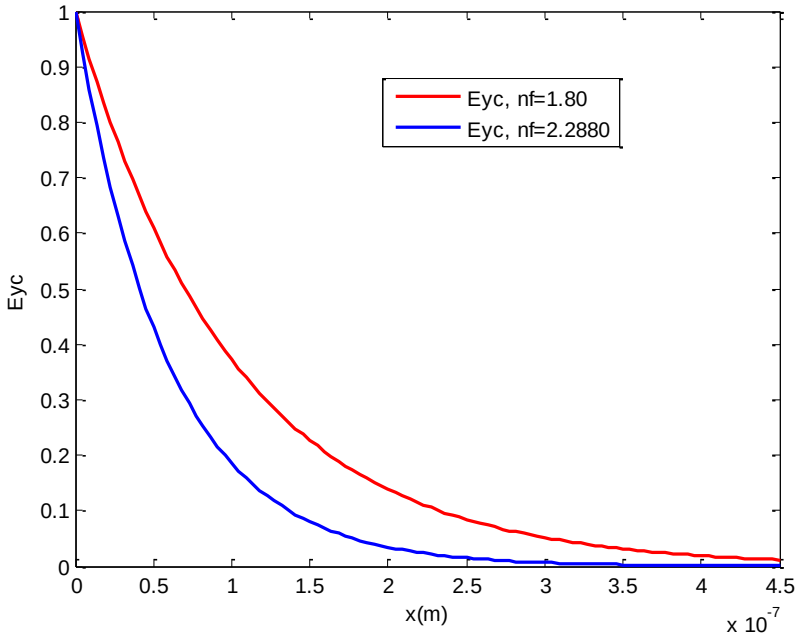

Figure 42: Evanescent field component E_{yc} in the cover versus x of TE_0 mode for different core refractive indices, (n_s=1.60, n_c=1.48, d=100 nm).Loin de fc.

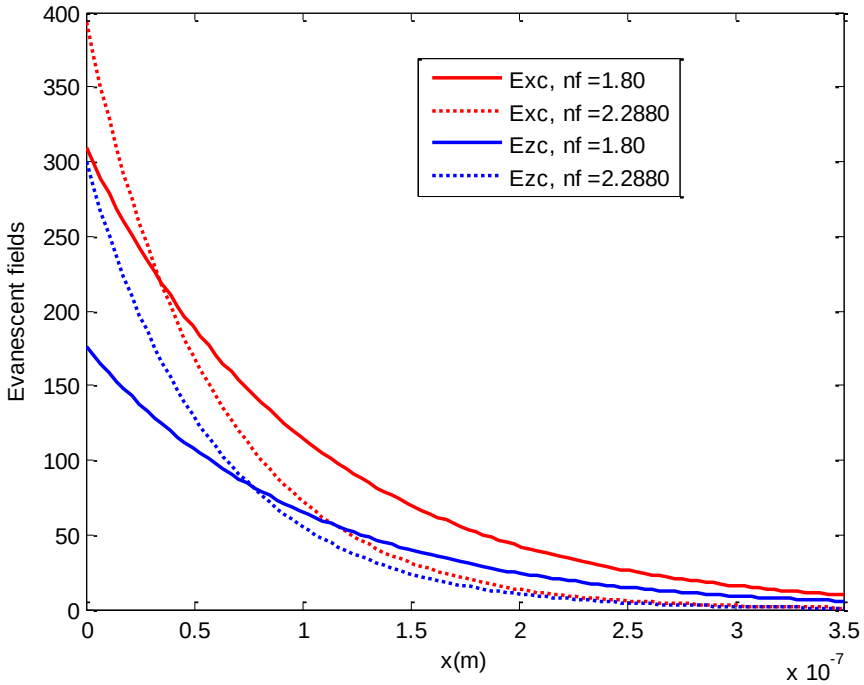

Figure 43: Evanescent field components (E_{xc}, E_{zc}) in the cover versus x of TM_0 mode for different core refractive indices, (n_s=1.60, n_c=1.48, d=100 nm).

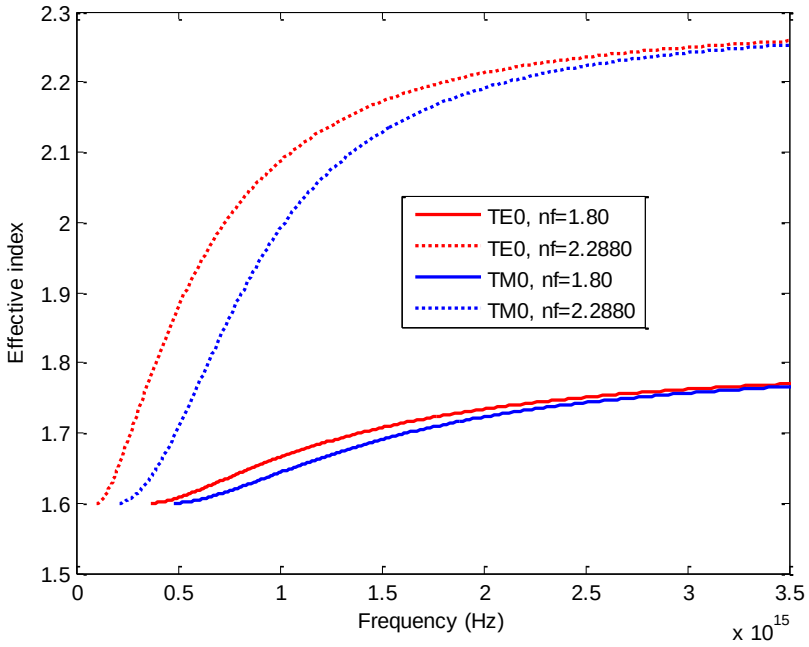

Figure 44: effective index versus frequency of TE_0 and TM_0 modes in slab waveguide for different core indices, (n_c=1.48, n_s=1.60, d=100 nm).

4.4. Electric-field-induced birefringence of uniaxial crystals

It is well known that electric fields can alter the refractive index of certain materials via the Pockels effect. When an electric field E is applied along (or opposite) the optic axis (c) of Trigonal 3m uniaxial Crystals (as $LiNbO_3$), the crystal remains uniaxial with the same principal axes, but its refractive indices are modified. We distinguish two cases according to the direction of the applied electric field. If the electric field is applied along the optic axis (+c), then refractive indices are modified as [20]:

$$n_0(E) \approx n_0 - \tfrac{1}{2} n_0^3 r_{13} E \qquad (19)$$

$$n_e(E) \approx n_e - \tfrac{1}{2} n_e^3 r_{33} E \qquad (20)$$

However, if the electric field is applied opposite to the optic axis (-c) of such uniaxial crystal, its refractive indices are modified as

$$n_0(E) \approx n_0 + \tfrac{1}{2} n_0^3 r_{13} E \qquad (21)$$

$$n_e(E) \approx n_e + \tfrac{1}{2} n_e^3 r_{33} E \qquad (22)$$

Where: $n_0$and n_e are the ordinary and extraordinary refractive indices of the uniaxial crystal without the application of electric field$E$,$n_0(E)$and $n_e(E)$ are respectively the modified ordinary and extraordinary refractive indices of the uniaxial crystal with the application of electric field,r_{13}andr_{33} are the linear electro-optic coefficients of the medium.

For this trigonal 3m uniaxial Crystal ($LiNbO_3$), the total birefringence as defined by [21] is given as:

$$\Delta n(E) = \left| n_{high}(E) - n_{low}(E) \right| \tag{23}$$

For a positive applied electric field (according +c), the corresponding total birefringence is:

$$\Delta n(E) = \left| n_0 - n_e + \tfrac{1}{2}E\left(n_e^3 r_{33} - n_0^3 r_{13} \right) \right| \tag{24}$$

We know that all Pockels media have r_{33} greater than $r_{13}(r_{33} > r_{13})$. This means that total birefringence $\Delta n(E)$is a linear increasing function of E.

For negative applied electric field (according -c), the corresponding total birefringence is

$$\Delta n(E) = \left| n_0 - n_e + \tfrac{1}{2}E\left(n_0^3 r_{13} - \tfrac{1}{2}n_e^3 r_{33} \right) \right| \tag{25}$$

While $r_{33} > r_{13}$This means that total birefringence $\Delta n(E)$is a linear decreasing function of E.

Noting that, typical optical properties of $LiNbO_3$are given in table.1 below:

n_0	n_e	$r_{13}(10^{-12}\ mV^{-1})$	$r_{33}(10^{-12}\ mV^{-1})$
2.2880	2.2030	10	32.2

Tab.1 Optical properties of $LiNbO_3$ at 632.8 nm

4.4.1. Influence of E-field induced birefringence on the sensor sensitivity

As we have seen previously, the naturel anisotropy of $LiNbO_3$birefringent material, changes with the application of an external electric field. Indeed, if the applied electric field is positive (according +c), the total birefringence is an increasing function of E(Eq.24). While, if the applied electric field is negative (according -c), the total birefringence is a decreasing function of E (Eq.25). To see the influence of birefringence variation on the sensor sensitivity for both positive and negative applied electric field, theoretically, we take arbitrary three values of $\Delta n(E)$ for each case; the values of $n_0(E)$ and $n_e(E)$ are deduced from their

corresponding equations. We have traced the sensitivities of the sensors as a function of frequency for the three values of $\Delta n(E)$.

The slab waveguide sensor characteristics are (d =100nm, n_p=1.628, n_s=1.72, LiNbO3as guiding film).

Figure.45 and figure.46 present respectively, fundamental modes sensitivities as a function of the frequency for different values of total birefringence induced by different values of positive and negative electric field. The curves of sensitivities, for TE_0 or TM_0, show two different behaviors; the first behavior occurs before the frequencies 3.1e14 Hz and 6.2e14 Hz for TE_0 andTM_0 modes successively, whereas, the second behavior occurs beyond these two frequencies. For positive applied E-field (Fig.45) and before the mentioned frequencies (in the left of vertical dashed lines), the increase the electric field induces an increase in the total anisotropy, which causes the decrease of the sensor sensitivity particularly around the maximum. However, for negative applied E-field (Fig.46), the increase of the absolute values of electric field induces a decrease in the total anisotropy, which causes an increase in the sensor sensitivity on the vicinity of the maximum. On the other hand, beyond the previous frequencies (in the right of vertical dashed lines), the increase of the electric field induces an increase in the sensor sensitivity (positive E-field case), while, the increase of absolute values of electric field induces a decrease in the sensor sensitivity (negative E-field case).Our interest focuses on the intervals where the sensitivities are maximal, which means, the near infrared domain for TE_0 mode and the visible frequency domain for TM_0 mode.

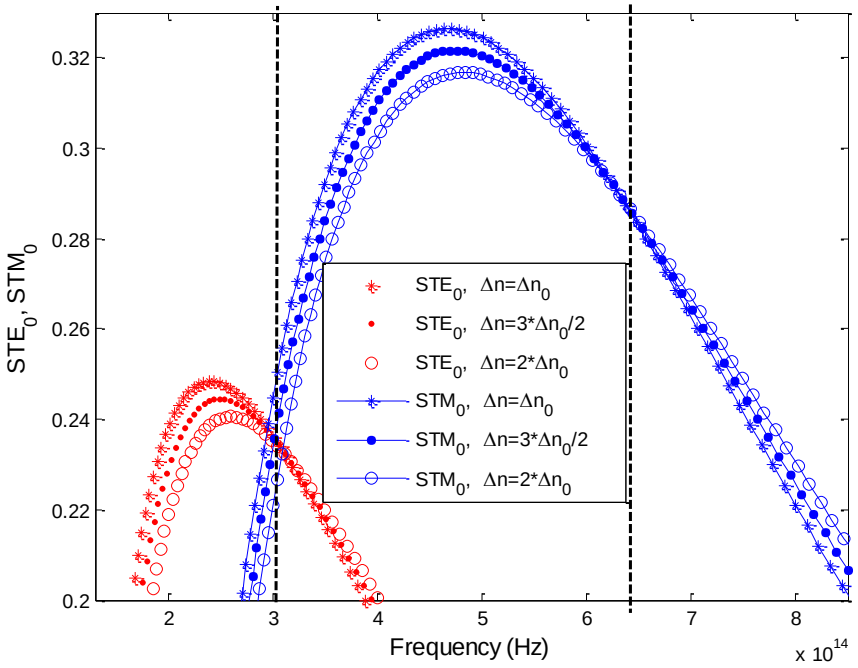

Fig. 45: TM_0 and TE_0 modes sensitivities as a function of the frequency for different value of increasing total birefringence Δn induced by different values of positive applied electric field, , blue curves for TM_0 mode and red curves for TE_0 mode.

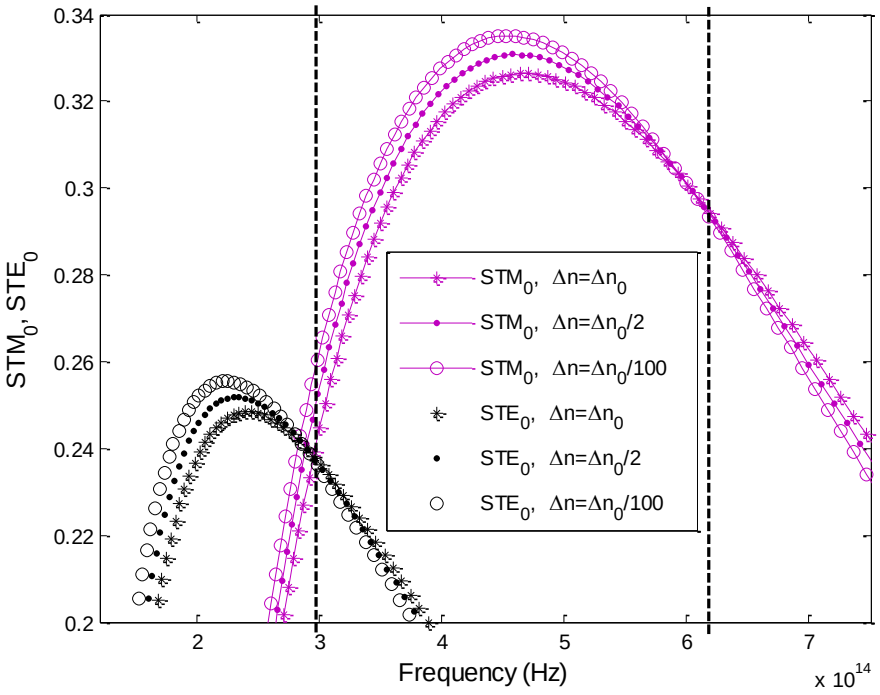

Figure 46: Sensitivities as a function of the frequency for different value of decreasing total birefringence Δn induced by different values of negative applied electric field, magenta curves for TM_0 mode and black curves for TE_0 mode.

Fig.47 and 48 present maximum fundamental modes sensitivities changes as a function of total birefringence Δn for positive and negative applied E-Field, respectively. The fig. 47 shows the decreasing of maximum sensitivity according to the increasing of anisotropy. Whereas, fig. 48 shows the increasing of maximum sensitivity according to the decreasing of anisotropy. Further, the figures show well that the sensitivities of TM_0 mode (blue and magenta lines), are greater than those of TE_0 mode (red and black lines). Moreover the sensitivities in the case of negative electric field are more important than those in the case of positive electric field. The difference between the two maximum sensitivities corresponding to the two extremes values of Δn are approximately 7.5e-3 and 9.0e-3 for TE_0 and TM_0 modes, respectively, for both positive and negative applied electric field. Hence, the maximum sensitivity changes as a function of anisotropy for TM_0 mode are greater than those of TE_0 mode.

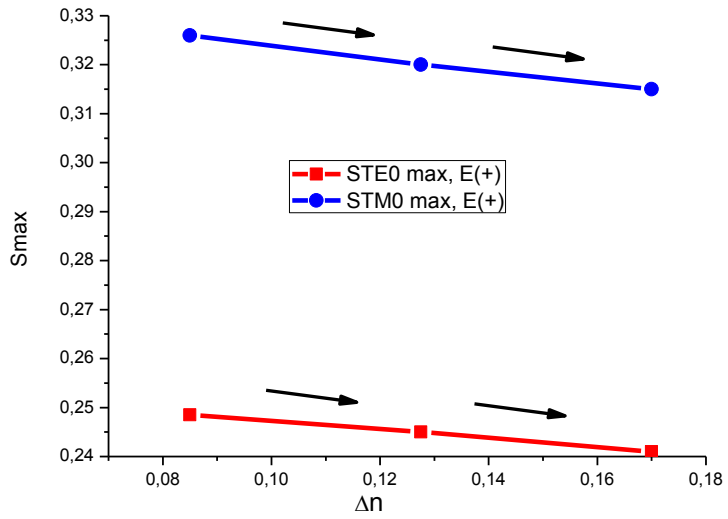

Figure 47: Maximum sensitivity variation as a function of total birefringence Δn for positive applied E-Field, red line for TE_0 mode and blue line for TM_0 mode.

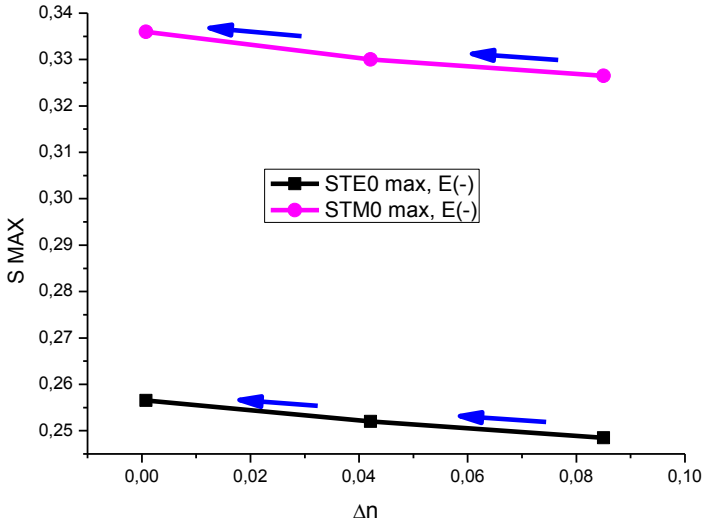

Figure 48: Maximum sensitivity variation as a function of total birefringence Δn for negative applied E-Field, black line for TE_0 mode and magenta line for TM_0 mode.

Figure 49 and 50 represent TE_0 and TM_0 effective refractive index changes as a function of the frequency for different value of increasing and decreasing total birefringence Δn, induced by different values of positive and negative applied electric field, respectively. Figure 49 shows that, the increase of the birefringence induces a decrease in the effective refractive index of both TE_0 and TM_0 modes. While, Figure 50 shows that, the decreasing of the birefringence induces an increase in the effective refractive index of both TE_0 and TM_0 modes.

From the curves of effective refractive index (figure 49, 50) and the curves of the sensitivities (figure 45, 46), we can beforehand, conclude that the evanescent fields changes induced by the birefringence have no or neglected influence on the sensitivity changes induced by this birefringence. This conclusion is explained as follow: for the reason that, evanescent field components are functions of effective refractive index, in the other hand, for the frequencies where the sensitivity changes are maximal (vertical dashed line in figures 49, 50), we show that the effective refractive index changes are minimal, hence, evanescent fields changes will be minimal. Thus, sensitivity changes are due to the birefringence itself.

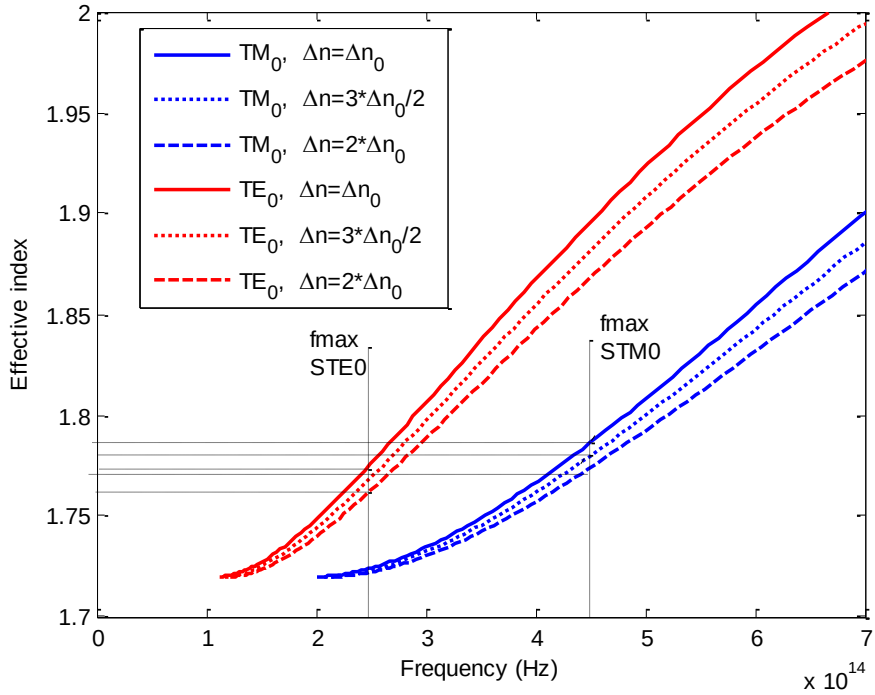

Figure 49: Effective refractive index as a function of the frequency for different value of increasing total birefringence Δn induced by different values of positive applied electric field, blue curves for TM_0 mode and red curves for TE_0 mode.

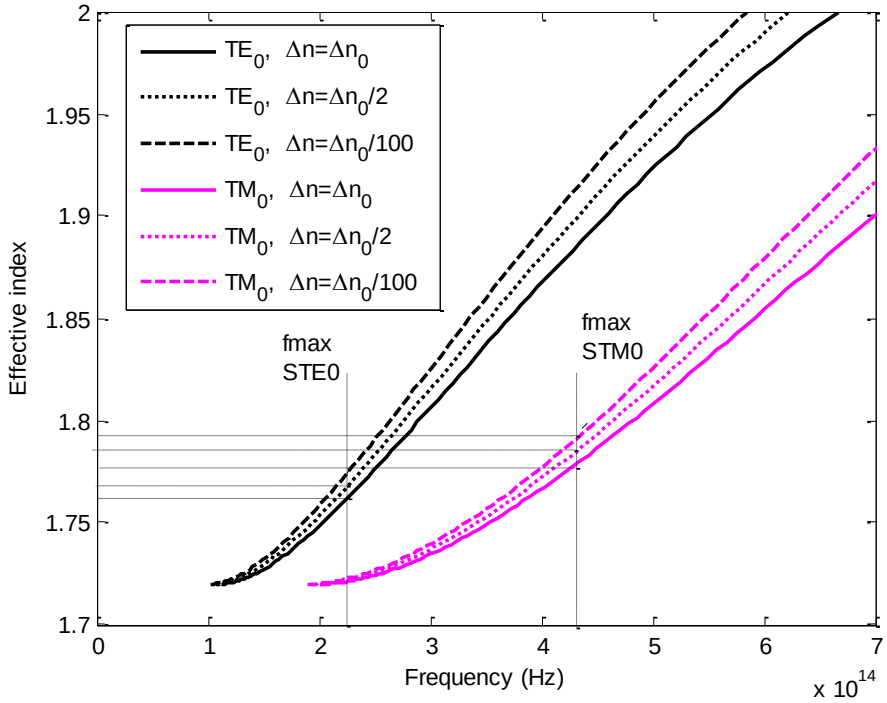

Figure 50: Effective refractive index as a function of the frequency for different value of decreasing total birefringence Δn induced by different values of negative applied electric field, magenta curves for TM_0 mode and black curves for TE_0 mode.

5. Conclusion

In this chapter, we have studied the sensitivity and the evanescent field of a slab waveguide sensor based on evanescent wave interactions constituted by uniaxial birefringent materials. We have calculated the sensor sensitivity formulas for the two kinds of modes propagating simultaneously in its waveguide. Then, we have studied the influence of the source, geometrical and physical parameters of the planar waveguide on the sensor sensitivity and the evanescent field. The results show that, in all cases, the maximal sensitivities of TM modes and their corresponding frequencies are greater than those of TE modes. In addition, the increase of the amplitude and wavelength light source, induce the increase of both the maximal sensitivity and the evanescent field in the cover. Further, the increase of the core thickness induces the decrease of the sensitivity of the sensor, in the reason of the decrease of the evanescent field in the cover. Furthermore, we have found that, the increase of the cover and the core indices induces the increase of the sensor sensitivity. On the contrary, the increase of the substrate index induces the decrease of the sensor sensitivity. Is worth to note that, changes of physical parameters of the waveguide sensor have no or neglected influence on the evanescent fields in the cover.

On the other hand, we have studied the influence of E-field induced birefringence of the wave guiding film ($LiNbO_3$), on the sensitivity of the studied sensor for TE_0 and TM_0 modes. In our study we have distinguished between two different cases**.** The first case when the electric field is applied along the optic axis (+c) of the $LiNbO_3$ wave guiding film (positive electric field); the second case when the electric field is applied opposite to the optic axis (-c) of such uniaxial crystal (negative electric field).The obtained results showed that, for positive electric field, the increase of electric field induces an increasing of the total anisotropy which causes a decreasing on the sensor sensitivity particularly around the maximum. However, for negative electric field, the increase of absolute values of negative electric field induces the decrease of the total anisotropy which causes an increasing on the sensor sensitivity on the vicinity of the maximum.

References:

[1] F. Baldini, A.N. Chester J. Homola and S. Martellucci: Optical Chemical Sensors edited by: Springer (2006).
[2] Ermini M. L., Mariani S., Scarano S., Minunni M: Bioanalytical approaches for the detection of single nucleotide polymorphisms by Surface Plasmon Resonance biosensors. Biosens. Bioelectron. 61, 28–37(2014).
[3] González A. B., Maldonado J., Herranz S., Lechuga L. M: Trends in photonic lab-on-chip interferometric biosensors for point-of-care diagnostics. Anal. Methods 8, 8380–8394(2016).
[4] Kovalevich, T., Belharet, D., Robert, L., Kim, M.S., Herzig, H. P., Grosjean, T., and Bernal, M.P.: Experimental evidence of Bloch surface waves on photonic crystals with thin-film LiNbO3 as a top layer. Photonics Research. 5 (6), 649-653 (2017)
[5] Parriaux, O., Dierauer, P.: Normalized expressions for the optical sensitivity of evanescent wave sensors. Opt. Lett.. 19(20), 1665–1665 (1994)
[6] Densmore, A., Xu, D.X., Waldron, P., Janz, S., Cheben, P., Lapointe, J., Delâge, A., Lamontagne, B., Schmid, J. H. and Post, E.: A silicon-on-insulator photonic wire based evanescent field sensor. IEEE Photon. Technol. Lett. 18(23), 2520–2522 (2006)
[7] Kumar, D., Singh, V.: Theoretical modeling of a nonlinear asymmetric metal-clad planar waveguide based sensors. Optik. 122(20), 1872–1875 (2011)
[8] Taya, S.A., and S. A. Shaheen: Binary photonic crystal for refractometric applications (TE case). Indian J. Phys. 92(4), 519–527 (2018)
[9] Taya, S.A.: Ternary photonic crystal with left-handed material layer for refractometric application. Opto-Electron Rev. 26(3), 236-241 (2018).
[10] Alkanoo, A. A. and Taya, S.A.: Theoretical investigation of five-layer waveguide structure including two left-handed material layers for refractometric applications. J. Magn.Magn.Mater.449(1), 395-400 (2018)
[11] Tiefenthaler K, Lukosz W: Sensitivity of grating couplers as integrated-optical chemical sensors. J Opt Soc Am B 6:209–220 (1989).
[12] M. Zourobl A. Lakhtakia :Optical Guided-wave Chemical and Biosensors. Springer Series on Chemical Sensors and Biosensors, Series Editor: G. Urban. Springer-Verlag Berlin Heidelberg 2010.
[13] Kasap SO: Optoelectronics and photonics. Prentice Hall, Canada (2001).
[14] D'Amico A, Natale CD: A contribution on some definitions of sensors properties. IEEE Sens J 1(3):183–190 (2001).
[15] Levy, M., Osgood, R. M., Jr., Liu, R., Cross, L. E., Cargill III, G. S., Kumar, A., and Bakhru,H., : Fabrication of single-crystal lithium niobate films by crystal ion slicing.APPL. PHYS. LETT. 73(16), 2293-2295 (1998)
[16] Rabieia, P. and Gunter, P.: Optical and electro-optical properties of submicrometer lithium niobate slab waveguides prepared by crystal ion slicing and wafer bonding. Appl. Phys. Lett. 85 (20), 4603-4605 (2004)
[17] Jalaleddine, A. M.: Guided waves propagating in isotropic and uniaxial anisotropic slab waveguide. Dissertation, Ohio University U.S.A (1982)
[18] Veldhuis, G. J., Parriaux, O., Hoekstra, H. J. W. M., and Lambeck, P. V.: Sensitivity enhancement in evanescent optical waveguide sensors. J.LightwaveTechnol. 18(5), 677–682 (2000).
[19] Passaro, V.M.N.; Dell'Olio, F.; Ciminelli, C.; Armenise, M.N: Efficient chemical sensing by coupled slot SOI waveguides. *Sensors* 2009, *9*, 1012–1032.
[20] Saleh E. A., Teich, M. C.: Electro-optics. In:Saleh E. A., Teich, M. C. (Eds.): Fundamentals of Photonics, pp. 696-736. John Wiley & Sons, Inc, U.S.A (1991).
[21] Timtere, P., Usman, A., Ododo, J. C.**:** The phenomenon of nonlinear optical birefringence in uniaxial crystals. Lat. Am. J. Phys. Educ. 5(2), 432-437 (2011).

General conclusion

During this thesis we modeled two kinds of optical waveguides, including, slab and embedded-strip waveguides. The modeling of the slab waveguide, allowed us the modeling and simulation of a slab optical sensor constituted by three layers of uniaxial crystals, as well as the investigation of the sensor parameters influencing its sensitivity and evanescent field.

In the first chapter we have presented mainly, different photonic sensor components, including, light sources, photodetectors and photonic waveguides transducers. Hence, different kinds of light sources and their characteristics are described including, continuous light sources, pseudo monochromatic and monochromatic light sources. Moreover, parameters of diverse photodetectors are introduced comprising, photomultiplier tube, quantum photodetectors and imaging detectors. In the other hand, types of optical waveguides widely used in photonic sensors are designated as well as their sensing principles, containing, strip waveguide, rib waveguide, slot waveguide and photonic crystal. In addition to that, methods of coupling light into the waveguides are specified, consisting of end-firing coupling, taper coupling, prism, coupling, grating coupling and directional coupling.

In the second chapter, a variety of optical-sensing mechanisms were described, including optical absorption, fluorescence, Raman scattering, detecting of refractive index changes and The Sagnac effect. Moreover, several integrated photonic sensors configurations have been presented suitable for different applications, such as integrated optical interferometers, microring resonators, Bragg grating resonators, directional couplers and photonic crystals optical sensors.

In the third chapter, we have modeled slab and channel photonic waveguides. Firstly, isotropic and anisotropic slab waveguides were studied with the optical ray approach and the Maxwell's equations approach, successively. The former approach allowed us to calculate the dispersion equations of the guided modes whereas, the latter approach, enabled us to determine the wave equations, their solutions and the characteristic equations, as well as, the solutions of electromagnetic field in each region of the waveguide. In addition, we have studied the influence of wavelength of source, geometrical and physical parameters on the propagating modes. The results showed that, the increase in the thickness of the core induces an increase in the propagation constants of the modes as well as a decrease in their cut-off frequencies, especially for of higher order modes. Further, the increase in the wavelength source motivates the decrease of the propagation constants of modes as well as the increase of

their cut-off thicknesses, especially for de modes of higher orders. Furthermore, changes of cover and substrate indices produce slight changes in the propagation constants of the modes and their cut-off frequencies. However, small changes in the core refractive index engender considerable changes in the propagation constants and cut-off frequencies of propagating modes. Finally, the effective index method (EIM) is described in detail and used to calculating the propagation constants of quasi-TE and quasi-TM modes as well as their field distribution in each region of the Embedded-strip waveguide.

In last chapter, we have studied the sensitivity and the evanescent field of a slab waveguide sensor based on evanescent wave interactions constituted by uniaxial birefringent materials. We have calculated the sensor sensitivity formulas for the two kinds of modes propagating simultaneously in its waveguide. Then, we have studied the influence of the source, geometrical and physical parameters on the sensor sensitivity and the evanescent field. The results show, in all cases, that, the maximal sensitivities of TM modes and their corresponding frequencies are greater than those of TE modes. In addition, the increase of the amplitude and the wavelength of light source, induce the increase of both the maximal sensitivity and the evanescent field in the cover. Further, the increase of the core thickness induces the decrease of the sensitivity of the sensor, in the reason of the decrease of the evanescent field in the cover. Furthermore, we have found that, the increase of the cover and the core indices induces the increase of the sensor sensitivity. On the contrary, the increase of the substrate index induces the decrease of the sensor sensitivity. It is worth to note that, changes of physical parameters of the waveguide sensor have no or neglected influence on the evanescent fields in the cover.

On the other hand, we have studied the influence of E-field induced birefringence of the wave guiding film ($LiNbO_3$), on the sensitivity of the studied sensor for TE_0 and TM_0 modes. In our study we have distinguished between two different cases**.** The first case when the electric field is applied along the optic axis (+c) of the $LiNbO_3$ wave guiding film (positive electric field); the second case when the electric field is applied opposite to the optic axis (-c) of such uniaxial crystal (negative electric field).The obtained results showed that, for positive electric field, the increase of electric field induces an increasing of the total anisotropy which causes a decreasing on the sensor sensitivity particularly around the maximum. However, for negative electric field, the increase of absolute values of negative electric field induces the decrease of the total anisotropy which causes an increasing on the sensor sensitivity on the vicinity of the maximum.